UNIVERSITY OF SOUTHAMPTON

Faculty of Natural and Environmental Sciences

Ocean and Earth Sciences

Understanding Tropical Cyclone induced changes in upper ocean temperature and salinity

by

Rafael Jaume Catany


https://orcid.org/0000-0002-3561-5596

Thesis submitted for the

Degree of Doctor of Philosophy

March 2019

UNIVERSITY OF SOUTHAMPTON

ABSTRACT

FACULTY OF NATURAL AND ENVIRONMENTAL SCIENCES

OCEAN AND EARTH SCIENCES

Doctor of Philosophy

UNDERSTANDING TROPICAL CYCLONE INDUCED CHANGES IN UPPER OCEAN TEMPERATURE AND SALINITY

Rafael Jaume Catany

Tropical Cyclones (TC) induce changes in both ocean temperature and salinity. This thesis uses available ocean in situ data to detect and quantify temperature and salinity changes for various TCs and determine the robustness of previous works. First, we present the Composite Tropical cyclone Footprint method (CTCFP), a new methodology developed during this thesis to compute the composite TC induced ocean response across multiple TC events. The method is applied to two case studies taken from the 2011 and 2014 TC seasons in the North Atlantic. Results show that the CTCFP mitigates the poor spatial and temporal representation of upper ocean state linked to the scarcity of in situ data within a given TC location. The CTCFP also proves to be a versatile tool amenable also to: 1) study TC induced changes at one TC location; 2) perform analyses of TC induced ocean response on local, regional and global scales; and 3) apply the same method to different data sources. The application of CTCFP to Argo data for TC Katia (2011) over the Amazon plume confirms a cooling of over 2˚C and an INCREASE of salinity up to 1 psu, in line with changes reported by previous studies. Similar effects are found also for TC Gonzalo (2014). However, CTCFP reveals other cases where the surface cooling after the passage of the TC is accompanied by cooling and salinity DECREASE. These results indicate that, whilst thermal TC induced changes seem always negative (cooling), the TC induced changes in salinity can be both positive (increased salinity) or negative (decreased salinity). Next, the CTCFP is applied to Argo temperature and salinity profiles from 2005 to 2015 to examine the composite signatures of TC with time and depth (top 400 m) in the North Atlantic. Results show that TC up to category 2 induce a cooling of -0.5˚C on average and a thermal recovery time between 20-25 days. Our observation-based analyses also confirm that slow moving TCs induce larger surface cooling. On average, TC induce changes in salinity of the order of 0.1 psu salinity increase, but TC induced changes in salinity are less clearly related to TC intensity than thermal changes. Finally, the CTCFP is applied to output from the data-assimilating FOAM system, indicating that while models capture the ocean thermal response to TCs relatively well, the TC induced salinity effects are generally not properly represented in today's data-assimilating ocean models.

Table of Contents

List of Tables

List of Figures

DECLARATION OF AUTHORSHIP

I, Rafael Eduardo Jaume Catany

declare that this thesis and the work presented in it are my own and has been generated by me as the result of my own original research.

Understanding Tropical Cyclone induced changes in upper ocean temperature and salinity.....

.....

I confirm that:

1. This work was done wholly or mainly while in candidature for a research degree at this University;
2. Where any part of this thesis has previously been submitted for a degree or any other qualification at this University or any other institution, this has been clearly stated;
3. Where I have consulted the published work of others, this is always clearly attributed;
4. Where I have quoted from the work of others, the source is always given. With the exception of such quotations, this thesis is entirely my own work;
5. I have acknowledged all main sources of help;
6. Where the thesis is based on work done by myself jointly with others, I have made clear exactly what was done by others and what I have contributed myself;
7. [Delete as appropriate] None of this work has been published before submission [or] Parts of this work have been published as: [please list references below]:

Signed:.....

Date:.....

Acknowledgements

Today is the day of writing this note of thanks, which is the finishing touch ground of my thesis. This has been a period of intense learning for me not only in my scientific development, but also on a personal level. Writing this thesis has had a big impact on me and I would like to thank all those who stand behind me to support me through this period.

I would like to first thank my main supervisors Christine Gommenginger and Christopher Banks who without you It would be not possible neither to start neither to finish this work. Thank you for believing in me, for your friendship and for helping me to get this far. Thanks Christine. Thanks Chris.

I would also like to thank a number of people who had helped me along the way. Thank you to both the University of Southampton and to the NOC MPOC family for partly sponsoring this PhD and for being an inspiration to me by displaying all the science and big achievements of this great science hub. Thank you for always keeping the doors open for all the motivating conversations. Thank you in particular to the satellite team (I include here Paolo Cipollini, Andrew Shaw and Francisco Mir Calafat) for always having a moment for science discussion and helping a colleague debugging that coding trouble. Thank you to ARGANS for providing me the opportunity to continue working with salinity from space community including Jacqueline Boutin (LOCEAN), Nicolas Reul (IFREMER), Antonio Turiel, Justino Martinez, Caro, Cristina, Vero and Estrella Olmedo (BEC), Simon Yue and Tony Lee (JPL), Frederic Bingham (UNCW), Eric Bayler (NOAA) and a long etc.!

I would like to thank my office mates, Mat, Carl, Colette Couves, Ryan Gallager, Michelle, Konstantina Rizopoulou, Daniela and specially Xiaolong Xu with whom I spend countless hours in the office day and day out. Thank you to all my friends in NOC and to the Spaniard gang María Azpiroz (also amazing House mate!) Himar Falcón, Héctor Marín, Marc Rius, Miguel Botí, Claudio Lo Iacomo, Veerle Huvenne, Anna, Christian Buckingham, for pushing me to continue writing even when I did not want too. Thanks to the lunching group Jaume, Lidia, Fatma, Irene, Vi and Miros.

My life in Southampton would not be the same if I would not find the Crossfit Solent community. So I own my respect to the morning crew for the training sessions in the early morning times when the city still sleeps. I can tell that some good science inspiration comes when you are that exhausted and you have no time to feel sorry for yourself. Thanks to my coaches and specially to Duncan and Oly who took me on board and help me to chip in the hardest times of an AMRAP. Thank you John, Jonhy and to Eleni Anagnoustou for joining me in the morning WODs, all that coffee and sharing your science plans with me (even though I have no clue of boron, corals or biochemistry!).

Of course I am not closing this section, to say thank you to my family. This includes you Carmen Catany I Miquel Jaume (es meus estimats pares), I Toni Jaume. Moltes gràcies per el vostre support incondicional. Gracias Marce Conroy, Leo, Fer, Zarco, Yuri. Thank you for your uncondicional love that was there even when I was away.

Finally. I know you were looking for these lines to come. Thank you for waiting for me and for your understanding when I got that late at home (thanks to the security guy kicking me out of the office). I have no words to make justice to the feeling of gratitude for having you by my side. You are my light and life. Thank you Eva Nedbalová! My wife and my best friend. Thank you also Tristan. One day you may read this line and you must know that you are very much loved. You are the future and our generation owns to yours we work this hard to preserve your future. Your planet.

I am aware that some of you are missing in this acknowledgement section. But believe me I do have you all with me. Thank you all.

Definitions and Abbreviations

Acronym	Definition
ACE	Accumulated Cyclone Energy
BL	Barrier Layer
BLT	Barrier Layer Thickness
CCI	Climate Change Initiative
CI	Cooling Inhibition (Index)
CTCFP	Composite Tropical Cyclone Footprint
ENP	East North Pacific
FOAM	Forecast Ocean Assimilation Model
GHRSST	Group High Resolution Sea Surface Temperature
ILD	Isothermal Layer Depth
ITCZ	Inter Tropical Convergence Zone
JCOMM	Joint Technical Commission on Oceanography and Marine Meteorology
JTWC	Joint Typhoon Warning Center
ML	Mixed Layer
MLD	Mixed Layer Depth
NA	North Atlantic
NEMO	Nucleus for European of the Ocean
NH	North Hemisphere
NHC	National Hurricane Center
NI	North Indian
OGCM	Ocean General Circulation Model
OHC	Ocean Heat Content
RMW	Radius of Maximum Wind
ROCI	Radius of the Outmost Isobar
SH	South Hemisphere
SMOS	Soil Moisture and Ocean Salinity
SP	South Pacific
SSD	Sea Surface Density
SSHWS	Saffir-Simpson Hurricane Wind Speed
SSS	Sea Surface Salinity
SST	Sea Surface Temperature
TC	Tropical Cyclone
WNP	West North Pacific
WP_i	Wind Power Index

Chapter 1

Introduction, Motivation & Overview

Tropical cyclones (TCs) are large atmospheric phenomena that are amongst the most energetic and hazardous geophysical events in nature, featuring extreme winds and high precipitation over large areas. TCs are major natural hazards that frequently pose direct and immediate threats to life, habitats and infrastructures, with the financial cost of individual TCs reaching billions of US dollars a year. Understandably, TCs attract the attention of the general public, the media and the environmental research community. The 2017 TC season attracted particular attention as the most active TC season in the last decade. In September 2017, TC-Irma hit the Virgin Islands and Cuba and continued its destructive path as it moved along the coast of Florida with wind speeds exceeding 70 m s^{-1} (252 km h^{-1}). In the following weeks, TC-Jose and TC-Maria closely followed the same path as Irma. The 2017 TC season proved that TCs are some of the most destructive natural disasters in terms of the loss of human life and economic damage. Although hurricane forecasting has made significant progress, better understanding of TC intensification and evolution is needed to improve the ability to estimate with confidence the hazard levels associated with a developing atmospheric system like Irma and subsequent storms. Such knowledge would give more certainty and more time to competent authorities to implement and to apply appropriate mitigation plans.

TC track forecasting has improved significantly over the last three decades, partly due to enhanced observational capabilities and improvements of numerical models. Over the same period, there has been little progress in predicting TC intensity, a factor most directly related to potential damage.

TC winds exert a frictional force over the ocean surface resulting in transfer of large amounts of kinetic energy that induces vertical turbulent mixing and upwelling. At the same time, the influence of ocean temperature (T) and ocean heat content (OHC) on TCs is now widely recognised as a dominant factor in TCs intensity evolution. The TCs induced "cold-wake", a reduction in upper ocean temperature after the passage of a TC, has been observed many times in satellite sea surface temperature images (SST) and in situ T profiles [e.g. *K Emanuel and Rotunno*, 2012; *K Emanuel and Sobel*, 2013; *Leipper*, 1967]. TC induced ocean surface cooling has subsequently been linked to TC de-intensification (a reduction in TC intensification) through a negative feedback that limits the transfer of energy (heat) from the ocean to the atmosphere.

The role of ocean salinity (S) in TC-ocean interactions is much less well documented, and thus less well understood and recognised. From a TC perspective, there is a priori no reason to think that salinity should play a role at all, since the input from the ocean to the TC is predominantly in the form of latent heat. Some studies suggest however that TC can also induce changes in salinity structure of the ocean that may extend throughout the top 200 m of the water column [*K Emanuel*, 2007] and that these changes in S could indirectly affect TCs by changing the availability of ocean heat. This points at a second potential feedback mechanism, linked this time to S, whereby the ocean salinity response to a TC could in some instances stimulate the intensification of passing storms by limiting cold water upwelling. Available evidence of TC induced changes in salinity does tend to correspond to ocean regions with fresh waters at the surface and strong vertical salinity gradients associated with freshwater river plumes (e.g. Amazon, Bay of Bengal). In these regions, the ocean is known to offer more resistance to TC induced surface cooling [*Balaguru et al.*, 2012]. It remains an open question whether this salinity-driven feedback is relevant solely for TCs in freshwater plume regions, or if the effect can be observed also more widely elsewhere in the ocean. TCs changes in salinity and their potential feedback have been ignored by most authors aiming to understand the interactions between the ocean and TCs formation and evolution [*K Emanuel et al.*, 2004]. Consolidating the evidence through a more systematic evaluation of available data should yield better understanding of the mechanisms linking TC induced changes in both T and S with, ultimately, positive implications for improved TC forecasting.

1.1 Motivation

On the basis of general consensus view about ocean thermal regulation of TC intensity, this thesis sets out the to study TC induced changes of both T and S, and to explore their links to TC intensification. The starting point of this research is the 2011 TC-Katia event, where large changes

in both T and S were observed as the TC moved over the Amazon plume in the Atlantic Ocean [e.g. *Androulidakis et al.*, 2016; *Grodsky et al.*, 2012; *Reul et al.*, 2014]. A key motivation of the work in this thesis is to determine whether these previous findings are robust, and if they are representative of similar processes occurring for other TC events and other ocean conditions. By considering a collection of TCs rather than individually hand-picked events, this thesis seeks to determine whether general principles can be drawn from the available observations about the role of ocean salinity in TCs-ocean feedback mechanisms.

Up to now, there has been no standard methodology to synthetize available observations in the vicinity of TC to estimate TC induced changes, and previous research utilised different approaches to capture the ocean changes resulting from the passage of a storm. The lack of established methodology increases the complexity of comparing results, since in some cases, there are issues linked to the sparsity or representativeness of the data close to TCs (e.g. in situ, satellites or model outputs). Thus, this thesis starts by devising and implementing a new method to collate observations in an objective and systematic manner, a method which is used later in the thesis to investigate aspects of TC induced changes in the ocean and feedbacks between the storm and the underlaying ocean. The **Composite Tropical Cyclone Foot Print (CTCFP)** method developed in this thesis provides a new objective tool by which observations are accumulated in both time (e.g. -20 to +20 days from the passage of the storm) and in space (e.g. radius of 400 km from the TC centre). The method is independent of the nature of the observations and provides the means to accumulate observations of any variable in both space and time in a TC reference frame. When applied to 2D horizontal fields, the method provides insights into the location of the TC impact relative to the TC centre and track. When applied to vertical T and S profiles (e.g. from Argo floats), the method makes it possible to evaluate the ocean response along observing dimensions corresponding to time and depth. The need to establish an objective method to capture TC induced changes in the ocean, and enable comparisons across basins and different ocean stratification states, represents a key driver for this work.

Finally, it is worth recalling that the original motivation of this research stemmed from the launch in 2010 of the Soil Moisture and Ocean Salinity (SMOS) satellite, the first mission to ever attempt to measure sea surface salinity (SSS) from space. Whilst the retrieval of SSS from space remains challenging, particularly in high wind conditions, this new spaceborne observing capability is providing uniquely detailed spatial and temporal oceanographic information about the variability of SSS thanks to global observations every 3 days. Thus, another motivation to better understand the magnitude and space-time character of TC induced changes in salinity is to determine to what

extent spaceborne SSS sensors can capture TC induced changes in salinity in a given spatial location within days from the passage of the storm, and thus contribute to improving TC forecasting.

1.2 Research Questions and Scope of the thesis

There are many research questions arising from the points raised in the previous section that require answering in order to improve our understanding of the role of salinity in TC formation, intensification and pathways. Not all of these questions can be addressed in one thesis though. Here, we identify six research questions that will provide the framework for the work in this thesis:

RQ 1. Is it possible to devise a method to objectively and systematically compute TC-induced changes in T and S, that can be applied to multiple TCs in any ocean basin, any ocean conditions, and which is independent of the sources of the data (e.g. Argo, model, satellite)?

RQ 2. Are TC induced changes in T always accompanied by changes in S, and if so, what is the nature of the observed changes in S? How robust are previous findings of temperature decreases and salinity increases for TCs crossing over freshwater river plumes?

RQ 3. Is it possible to detect the TC induced ocean response using satellite SST and SSS data?

RQ 4. Can we overcome the spatial and temporal limitations of in situ data to understand the ocean response to TC in similar ocean conditions but different basins?

RQ 5. How are TC induced changes in T and S related to ocean mixed layer depth? And barrier layers?

RQ 6. How are TC induced changes in S represented in data-assimilating model systems, and is data assimilation able to overcome the sampling limitations of in situ observations?

Given the wide range of issues to be considered, a number of choices had to be made to keep the scope of this work within what is achievable in a thesis. Thus, a large part of the study focuses on the North Atlantic where TCs are frequent and where there are a long and well-documented historical records. Furthermore, the North Atlantic comprises the Amazon freshwater plume that displays high inter-annual variability in its meridional and zonal spread. It is therefore possible to assume at the start of the study that the North Atlantic region provides a good balance of cases of TC observations over, and away from, freshwater plumes i.e. the opportunity to observe TCs over ocean conditions with and without barrier layer to determine how this might be affecting TC intensification. However, given the aim of putting the findings from the North Atlantic into a more global context, some of the analyses are then repeated in three other basins by applying the CTCFP method to TCs in the North-East Pacific, North-West Pacific and the North Indian basins.

Other choices made to control the scope of this thesis were to restrict analyses to TCs with a 1-minute maximum wind speed of at least 33 m s^{-1} (i.e. TC category 1-5 in the Saffir-Simpson Hurricane Wind Speed scale; SSHWS), that occur in the open ocean (i.e. further than 200 km from land) and in the North Hemisphere only between latitudes 0˚- 45˚ N. These restrictions, informed by the TC-ocean feedbacks reported in the literature, mean that Tropical Storms (i.e. wind speed ≤30 m s^{-1}) and Extratropical Storms (i.e. latitudes > 50˚) were not considered in this thesis.

Finally, the CTCFP method is applied in Chapter 8 to output from a data-assimilating model system to determine the ability of today's data assimilation schemes to represent TCs induced changes in ocean T and S. The analyses are based on output from the FOAM NEMO model run by the UK MetOffice, which is taken to be broadly representative of the capabilities of today's operational systems. Comparing the output and performance of different assimilating model systems was not within the scope of this thesis.

1.3 Structure of the thesis

The remaining chapters of this thesis are organized as follows: Chapter 2 presents a literature review of material relating to atmosphere-ocean interactions during TCs. This chapter presents the background of the thesis about current understanding of TC induced changes in T and S.

Chapter 3 provides descriptions of all datasets and data source used in the thesis.

Chapter 4 estimates the natural ocean variability in the North Atlantic in terms of monthly maps of T and S. These serve to establish the baseline against which the impact of TCs is later assessed.

Chapter 5 illustrates the Composite Tropical Cyclone Foot Print (CTCFP) method, a new approach to objectively estimate TC induced changes in ocean T and S. This chapter includes step by step descriptions of how to apply the method and one example of application to Argo float data and it is further developed in the following chapter.

Chapter 6 demonstrates the validation of the CTCFP method by showing its application to two case studies in the North Atlantic, and compares estimated TC induced ocean changes with those reported in previous work.

Chapter 7 sees the application of the new CTCFP method to different ocean basins and shows how the method serves to overcome the sampling limitations of in situ data to provide more general appraisal of TC induced ocean response in different regions and ocean conditions.

Chapter 8 presents the application of the new CTCFP method to output from a data assimilation model system to evaluate the ability of operational systems to represent TC induced changes in ocean T and S.

Chapter 9 gives a summary of the main findings and conclusions of this thesis. This chapter brings the thesis to an end with some thoughts and suggestions for further research and future work.

Appendix A contains a copy of the MATLAB code of the CTCFP following the steps described in the in this thesis (Chapter 5). All the scripts are also available upon request to the author or via GitHub platform (after thesis publication).

Chapter 2

A review of atmosphere-ocean interactions during Tropical cyclones conditions

This chapter presents a comprehensive literature review of the interactions between the ocean and the atmosphere in Tropical cyclone (TC) conditions. TC are extreme atmospheric events that are commonly studied in meteorology but feature strong interactions with the ocean that have only become recognised over the last decade. This chapter identifies the main aspects needed to understand feedback mechanisms between the atmosphere and the ocean that may nurture or inhibit the formation and intensification of these large atmospheric events. The review covers many aspects, ranges from understanding the relation between atmosphere and ocean circulation patterns, through to the active exchanges of energy between the two domains. The structure of this chapter is therefore as follow: Section 2.1) Atmosphere and Ocean Circulations; Section 2.2) Definitions and Classification of Tropical Cyclones. Section 2.3) Ocean Stratification and Tropical Cyclone Intensification; and Section 2.4) Tropical Cyclone Induced Oceanic Response.

2.1 Atmosphere and Ocean Circulations

The ocean and atmosphere system is driven by the Sun's radiation [*A E Gill*, 1982]. Winds are produced in the atmosphere as a response to the sun's radiative forcing. These winds transfer momentum to the ocean surface, producing ocean currents and distribution of heat in the

atmosphere and in the ocean [*A E Gill*, 1982]. Owing to the tilt of the Earth (i.e. 23.5˚), there is a seasonal variation of the flux received, so the yearly average flux varies with latitude, being minimum in Polar Regions and maximum in equatorial ones. To maintain the energy balance in the ocean-atmosphere system the ocean transports heat (energy) from low to high latitudes (Figure 2-1).

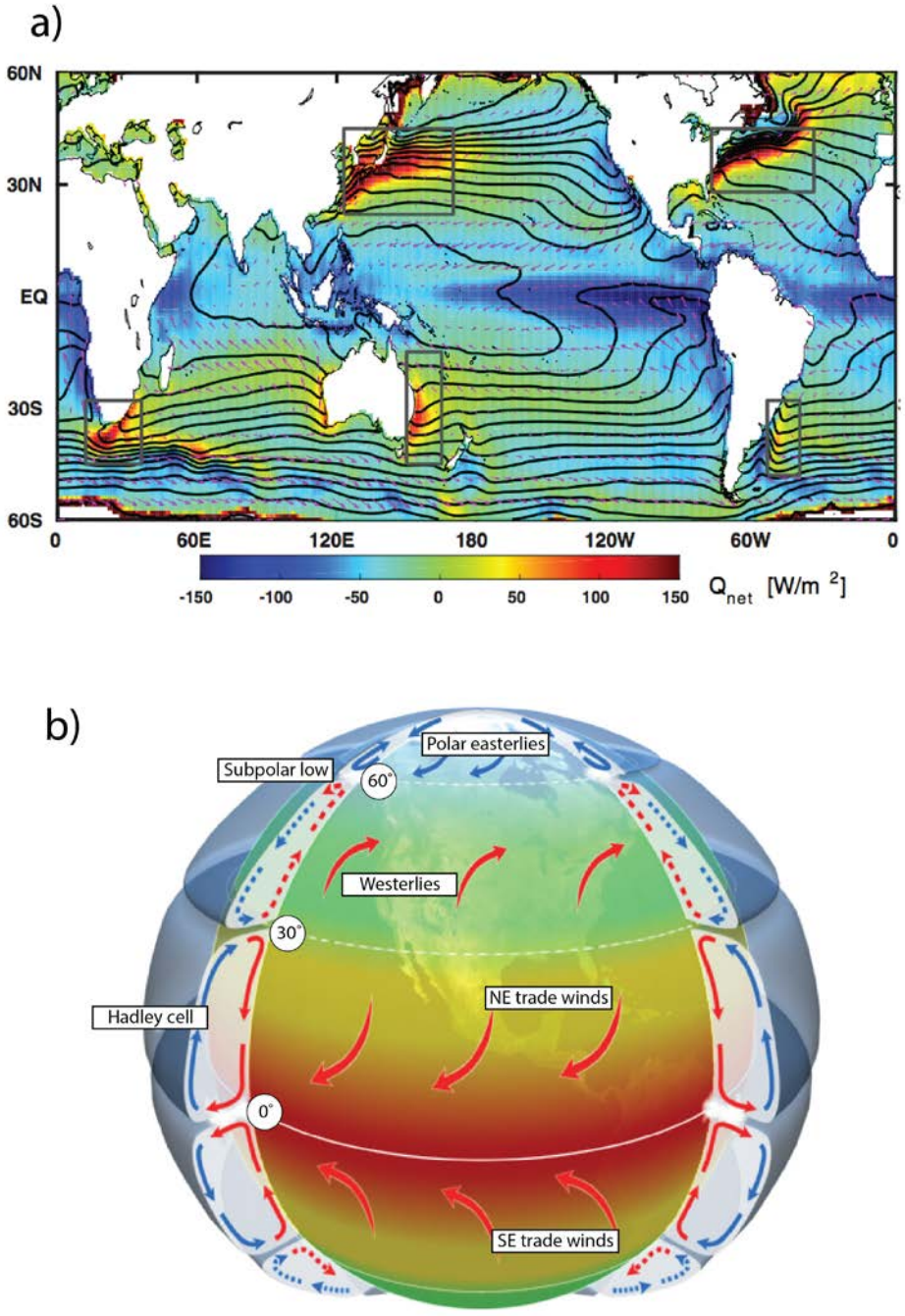

Figure 2-1 (a) Distribution of annual heat flux (Q_{net}, colour scale, positive (red) is heat flux from the ocean to the atmosphere), SST (black contours, in 2K intervals) and near surface ocean wind at 10 m height (pink arrows). Grey squares show the western boundary currents, where ocean currents are stronger and there is high loss of heat to the atmosphere (credit: *Yang et al.* [2016]). (b)

Schematic representation of wind general circulation in the atmosphere (credit The COMET Program).

The general circulation patterns observed in the ocean and in the atmosphere are similar to each other and this is related to fact that the largest energy transfer from the ocean to the atmosphere is by evaporation. Hence, it is possible to observe that the largest oceanic heat losses (i.e. over Kuroshio Current, the Gulf Stream, the North Atlantic and the Norwegian Current) coincide with regions of high wind speeds [*Wells*, 2011]. The predominant atmospheric feature within these regions is very high wind regimes (wind speed ~30 m s^{-1}) in the upper troposphere between 30˚ and 40˚ latitude. Observations in summer show a poleward movement of these jets and a weakening by about 50%. The mean flow is dominated by the eastward (or westerly) winds throughout most of the upper troposphere, but westward (or easterly) winds occur in the near troposphere and near the surface in Polar Regions. The vertical and meridional components of the mean wind circulation (Figure 2-1b) reveal that there are three distinct wind cells (i.e. Hadley Cells 0˚ - 30˚ latitude, Ferrel Cells 30˚ - 60˚ latitude and the Polar Cells 60˚ - 90˚ latitude), which divide the troposphere (i.e. surface 0 m to 10,000 m height) into regions of essentially closed wind circulations.

The air within the atmosphere rises over the equatorial zone, mostly in the Inter Tropical Convergence Zone (ITCZ), where large amounts of latent heat are released by heavy precipitation. This rises to the stratosphere at subtropical latitudes (~30˚) close to where the subtropical jet stream is located. The air then descends, warms by adiabatic compression (i.e. volume changes with no exchange of heat or matter) and its relative humidity decreases. The circuit is completed by a return flow in the low troposphere (i.e. within about 2 km height from the surface) towards the equator. This return flow is seasonally steady and it is known as the trade winds due to its use in the past by the main commercial sailing routes. The subtropical high-pressure systems are the largest within the atmosphere and are generally cloud free regions. The curving of the main wind circulation (i.e. anticyclonic and cyclonic cells) is related to the Earth's rotation. The regions of low level convergence (i.e. around the ITCZ) are areas of upward motion and heavy precipitation.

To the east of the North Atlantic basin (i.e. around the Coast of Cape Verde), there is a typical TC formation region characterized by high Sea Surface Temperature (SST) and favourable Easterly African Trade wind that transport atmospheric disturbances towards the west through the open ocean. Some these disturbances may intensify and become strong TCs on its westward movement towards the US coast.

2.1.1 Spatial and temporal scales in the ocean and in the atmosphere

The main TC regions are dominated by the subtropical gyres (i.e. 15˚- 40˚ latitude), which circulate clockwise in the Northern Hemisphere and anticlockwise in the Southern Hemisphere. Further north (i.e. between about 40˚ and 60˚ N), there are the sub-polar gyres with an anticlockwise circulation in the Northern Hemisphere (opposite direction in the Southern Hemisphere). In the Southern Hemisphere, the sub-polar gyres interact with the Antarctic Circumpolar Current (ACC), which is flowing eastward around the globe unbroken by any land mass. The strength of the surface currents within these oceanic gyres is highest on the western side. For example, the typical surface ocean current is about 0.1 m s^{-1}, whereas in the Gulf Stream (North West Atlantic) and the Kuroshio Current (North West Pacific) there are the highest surface velocities in the world with typical values of 1 - 2 m s^{-1}. The time dependent oceanic motion has a variability ranging from a few days up to a year, which is the typical time scale of mesoscale eddies, over typical spatial horizontal scales of 50 to 500 km [*Wells*, 2011].

Atmospheric systems have a broad range of different spatial and temporal scales, and TC are considered large scale systems (i.e. radius ~200-400 km), with intense wind speeds and heavy precipitation of a duration from days to a few weeks, i.e. there have been records of 30 day TC life span . Whilst the vertical wind flow varies from 1 to 10 m s^{-1}, the horizontal flow ranges from 17 to over 50 m s^{-1}. There are submesoscale atmospheric systems (with radius, r ≤ 100 km) like tornados that also have cyclonic circulation as a result of the parent thunderstorm cloud. However, these storm systems usually have a short duration (i.e. two hours maximum) and the physical processes taking place within them are beyond the scope of the present study.

2.2 Definitions and Classification of Tropical cyclones

2.2.1 Definition of a Tropical cyclone and its evolutionary stages

A TC is a cyclonic, atmospheric system that originates over tropical oceans (more precisely within 30˚ of the Equator) and is driven principally by heat transfer from the ocean to the atmosphere [*K A Emanuel*, 1986; *Schade and Emanuel*, 1999]. The formative stage of a TC, when the wind speed is lowest (wind speed ≤ 17 m s^{-1}), is known as a tropical depression. For 1-minute maximum sustained wind speeds between 18-32 m s^{-1}, they are called tropical storms. It is not until winds speeds exceed 33 m s^{-1} that these atmospheric systems become known as Tropical cyclones. Other terminologies that are equivalent to Tropical cyclones include “hurricanes” in the western North Atlantic and eastern North Pacific, and “typhoons” in the western Pacific [*K Emanuel*, 2003].

TCs usually form over open ocean basins but occasionally can form quickly in coastal seas (e.g. Cuba, Bahamas). This thesis focuses on TCs developing over the open ocean only (i.e. first storm observation was at least 400 km from land) and with 1-min maximum wind speeds above 33 m s^{-1} at any given point during its lifetime. Hence, from now on, unless stated explicitly, the terms Tropical cyclone, TC or simply storm are used interchangeably to refer to this type of phenomena. In addition, not all storms make landfall, and some only reach maximum intensity as they strike coastal areas. Hence, this dissertation only studies the life span of TCs spent over the ocean, up to the point where they make the first landfall (i.e. last TC location at least 400 km from land).

TCs are among the most lethal and costly natural hazards. In the USA during the 2004-2005 season, Atlantic TCs were estimated to have caused $150 billion in damages [*Pielke et al.*, 2005]. Based on the annual number of TCs from 1900 to 2015, there is a worldwide average of eighty seven events per year, but only about nineteen of these develop over the open ocean and reach hurricane category (Figure 2-2). An expected consequence of on-going climate change is the possibility that during this century the number of high intensity TCs will increase, even though it is conceivable that the total number of TCs may decrease [*K Emanuel*, 2005; *Knutson et al.*, 2010]. In light of climate change, it is possible that hazards from TCs together with their socio-economic costs increase within a single human lifetime (AR5, IPCC). The number of storms from 1990 to 2015 (Figure 2-2) shows a clear positive trend (i.e. 10-year running mean) with a larger increase between 1940 and 1960. However, these observed positive trends do not reveal an increase in the number of TCs, but the changes in observation methodologies [*K Emanuel*, 2005]. For example, the technology developments linked to World War 2 and the start of the satellite Earth Observation era.

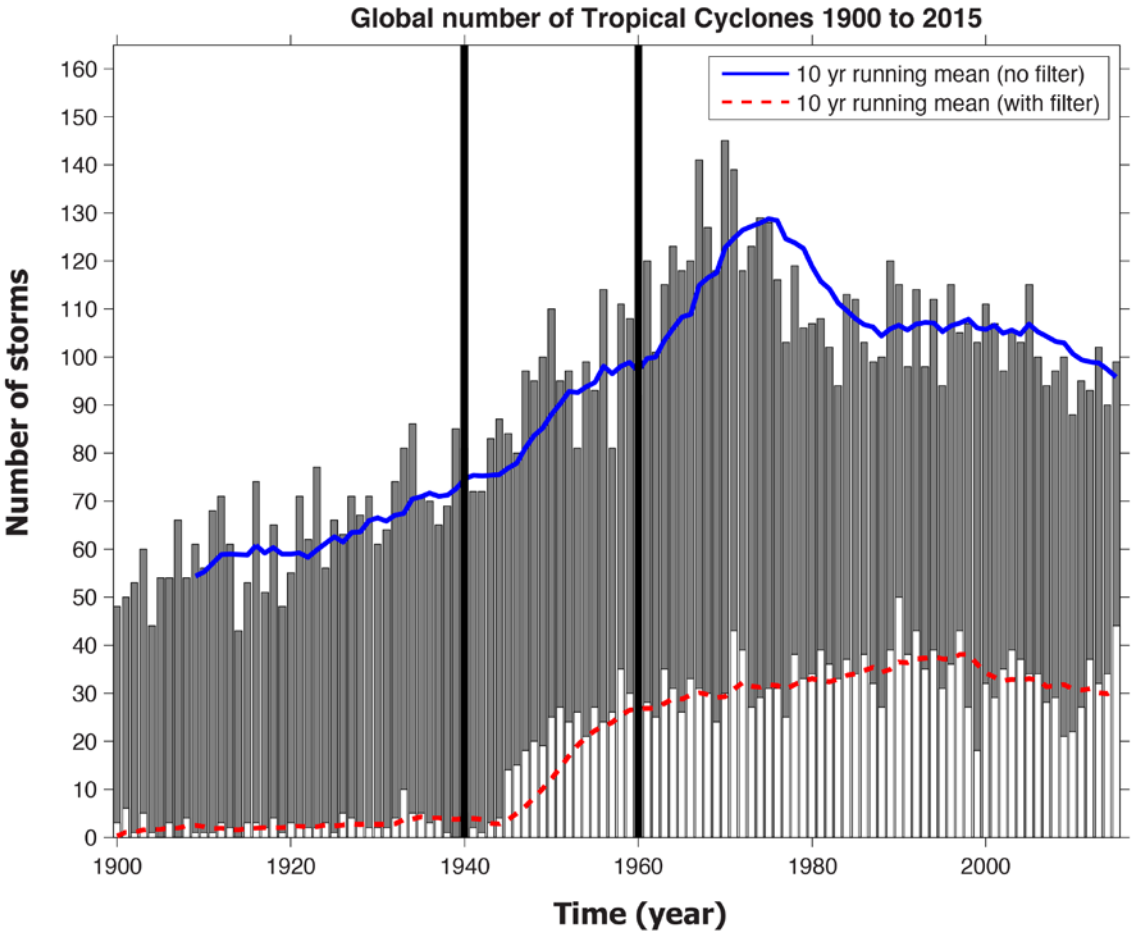

Figure 2-2 Number of Tropical cyclones identified worldwide from 1900 to 2015 (grey bars). For the same time period, number of Tropical cyclones originating over the open ocean and wind speeds reaching 33 m s^{-1} at some stage (white bars). Superposed are the line trends including all the storms in the record (blue-solid line) and including storms of interest only (dashed-red line). Data source IBTrACS (https://www.ncdc.noaa.gov/ibtracs/). The two black bars mark major historical events: complete global Tropical cyclone observations (1940); and start of the satellite era (1960).

2.2.2 Formation and structure of Tropical cyclones

Tropical cyclone genesis, also known as cyclogenesis, is a complex mechanism that spans the formation of a tropical storm (i.e. cold core disturbance) to its development into a fully formed cyclonic system (i.e. warm core storm) moving westward along the trade winds [*Nirupama*, 2013; *Yanai*, 1964]. Not all tropical storms in the easterlies transform into TCs and it seems that these need to be coupled with upper ocean anticyclones. Other necessary *ingredients* for TC formation include weak vertical wind shear, high relative humidity in the mid-troposphere sustaining deep convection, cyclonic absolute vorticity at low levels of the atmosphere, and a warm upper ocean with temperatures of at least 26˚C [*Gray*, 1998].

The typical TC structure consists of a tall cumulonimbus or hot towers extending from the surface to the top of the troposphere (12-15 km; Figure 2-3a) [*McIlween*, 1986]. The physical mechanisms

in the North and South hemispheres mirror each other due to the Coriolis effect [*Dean et al.*, 2009; *I D Lloyd and Vecchi*, 2011]. The Coriolis force is latitudinally dependent (i.e. zero at the equator and maximum at the poles). As the Coriolis forcing is necessary to induce cyclonic wind rotation of TCs, TCs are latitude dependent and commonly originate 5˚ latitude poleward.

TCs are usually described by their characteristic wind circulation and intensity as measured by the maximum sustained wind speed. Hence, the following sections give detailed descriptions of the characterization of the main wind patterns within the storm, storm size and translational speeds.

2.2.2.1 Wind speed and surface pressure

Since the start of satellite observations in about 1960, the most characteristic image of Tropical cyclones is the dense white cyclonic cloud rotating anticlockwise in the Northern Hemisphere. These satellite observations are useful to determine the intensity and the size of a storm approaching land (Figure 2-3b). Furthermore, modern observations like spaceborne microwave sensors (i.e. measuring day and night and through clouds) allow more detailed descriptions of the wind field structure and precipitation patterns within the cyclone as seen from the lower level to the top of the troposphere (Figure 2-3 a and c). The general structure, which is common in all TCs is as follow: (1) boundary layer inflow, (2) eyewall, (3) outflow cloud cirrus shield, (4) rainbands, and (5) upper tropospheric clockwise winds. As a storm intensifies, the eye and eye wall become more pronounced and becomes more evident.

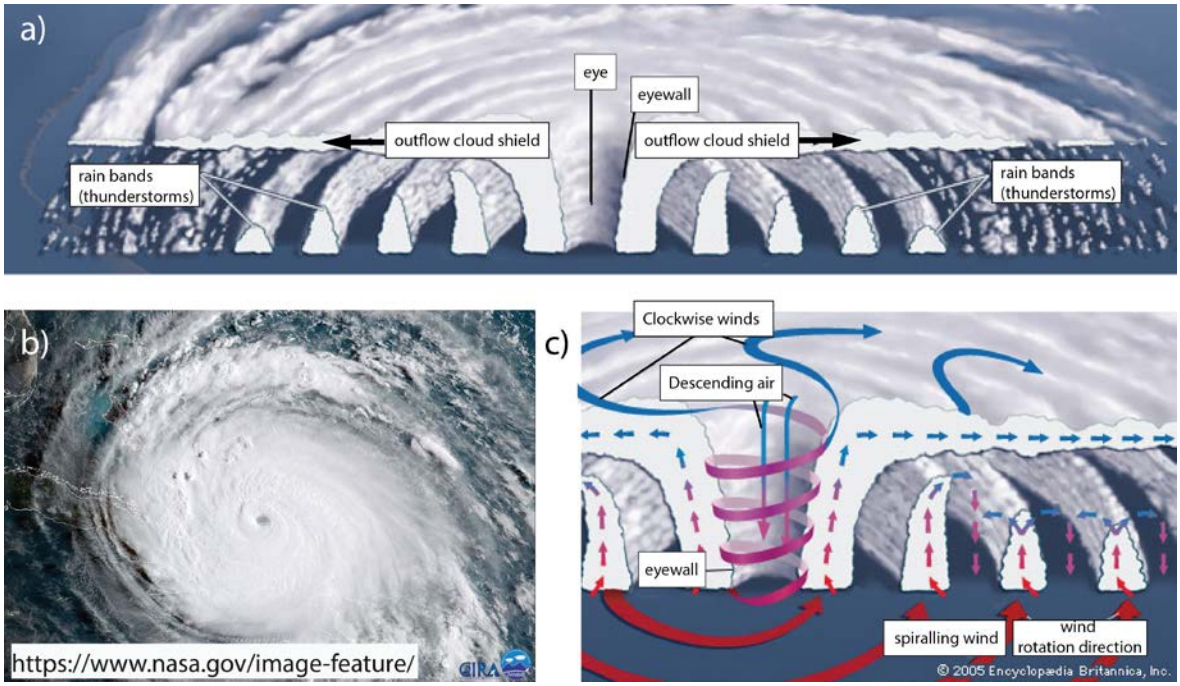

Figure 2-3 (a) cross section of the Tropical cyclone structure showing the eye, eye wall and the concentric rain bands from (credit: https://www.britannica.com); (b) top view satellite image of TC Irma with radial distance of about 500 km (September 2017, North Atlantic) moving over Cuba towards Florida peninsula (credit: https://www.nasa.gov); and (c) Drawing of the cross section of the wind patterns within the storm (credit: https://www.britannica.com).

TCs are classified as synoptic[1] scale low-pressure atmospheric systems, which rotate cyclonically (i.e. anticlockwise in the Northern Hemisphere; and clockwise in the Southern Hemisphere). Winds around the storm are not symmetrical with respect to the axis of motion, as the winds within the right quadrant are typically stronger than the winds within in the left quadrant [*George and Gray*, 1976]. As will be explained later in this thesis, this right-hand bias in TC winds leads to a seemingly biased TC-induced response in the ocean.

Within the storm, the wind flows inward at lower levels, spiralling upwards in the zones of deep convection (i.e. the central eye). From there, the wind spirals outward to the upper atmosphere just below the tropopause (Figure 2-3a). Finally, this wind circulation changes at the very top of the storm, where the wind rotates clockwise [*K Emanuel*, 2003; *Yanai*, 1964].

The parameterization of the wind and pressure profiles within a TC was first introduced by Depperman (1947), who used a simple 2D vortex model to approximate the inner core of solid-body rotation of the storm [*Wood et al.*, 2013]. In this simple model, the wind decreased

1 Synoptic scale is a term used in meteorology to describe horizontal large or cyclonic scale (length scales of 1000 km or more).

proportionally to the distance measured from the centre of the storm. The centre of the storm is commonly known as the eye of the storm and it is a relatively calm region where the wind and surface pressure reach their minimum values. Surrounding the eye is the eyewall, where wind and pressure suddenly increase.

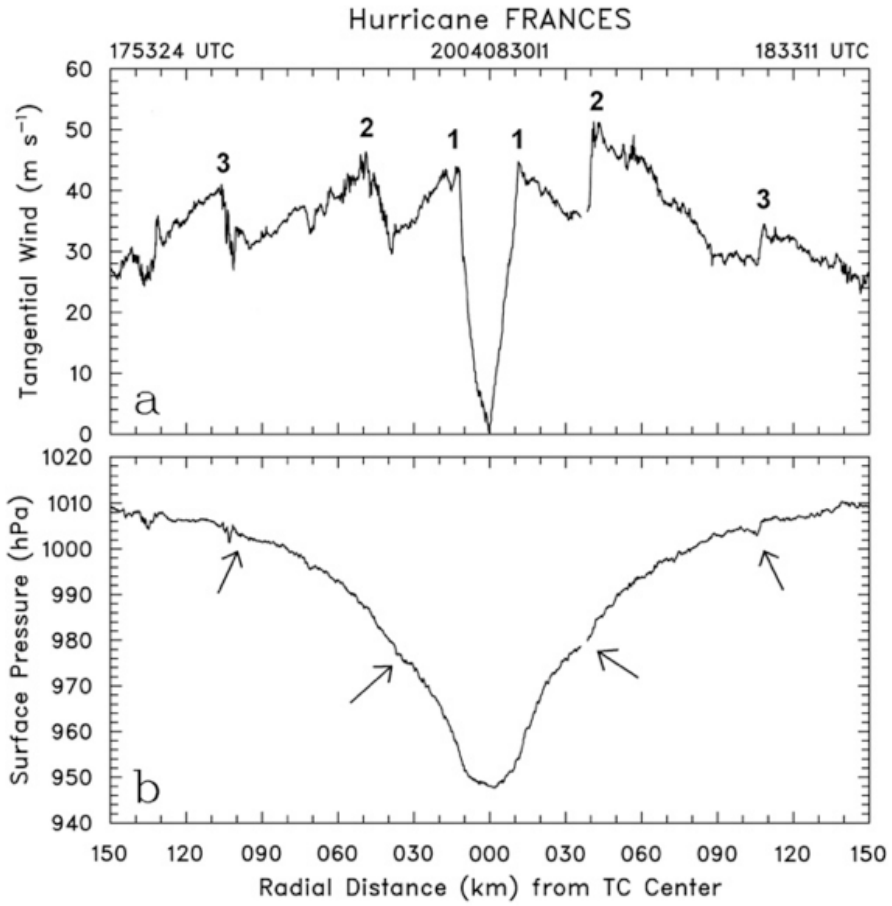

Figure 2-4 Radial profiles of (a) wind speed (m s^{-1}) and (b) pressure (hPa) as measured from flights passes within TC-Frances on 30 August 2004. In (a) there are three peaks in wind speed at each side of the eye (i.e. at radial distance = 0 km) with the potential of various eye replacement cycles (ERC) and with a rightward intensity dominance. The greatest wind speed (i.e. peaks mark with 2) is higher to the right that to the left side of the storm. The arrows in (b) show the location of the two of the three peaks wind speeds on the pressure profiles, which are used to model a partitioned wind speed profile and a total central surface pressure during the ERC [*Wood et al.*, 2013].

There is a Wind-Pressure Relationship (WPR)m which is used by most TC observing centres to derive the intensity of the storm from measures of the mean sea level pressure (MSLP) [*Knaff and Zehr*, 2007

]. Normally, there is only one eyewall, where the maximum wind is strongly anticorrelated with the atmospheric pressure within the storm. However, there are cases where there is an eye replacement cycle (ERC) and there are multiple tangential wind maxima [*Woodruff et al.*, 2012]. Intensity inferred using this relationship is often underestimated for TCs with ERC, which are usually

accompanied by significant fluctuations in maximum wind speed (Figure 2-4a) and central surface pressure (Figure 2-4b). In cases where ERC occurs, the accuracy of TC intensity estimation might be improved using aircraft reconnaissance when available [*Velden et al.*, 2006].

The Dvorak technique is the most widely used WPR to estimate TC intensity based on visible and infrared satellite observations. This technique uses satellite infrared cloud patterns in the inner core of the storm and it relates them to maximum sustained wind speed (MSW; i.e. 1-min average sustained wind). The development of the Dvorak technique allowed estimating TC wind speed and surface pressure in those regions where routine aircraft reconnaissance is not available (i.e. Indian Ocean and South Pacific Ocean). *Velden et al.* [2006] noted that this technique allows inferring wind speeds in knots going from 35 knots (i.e. 17 m s^{-1} or tropical storm intensity) to 170 knots (i.e. 87 m s^{-1} or major Tropical cyclones). Modern adaptations to the Dvorak technique include the analysis of spaceborne microwave radiometer and scatterometer data. These adaptions make it possible to observe wind field and rain band structures that are usually undetectable from infrared and visible satellite imaging [*Velden et al.*, 2006].

2.2.2.2 Size

There is no unique agreed metric to characterise the size of TCs (i.e. area of influence of a TC) and different meteorological agencies currently report the size of storms using different metrics. For example, the US National Hurricane Center (NHC) and the Japanese Joint Typhoon Warning Center (JTWC) – who record TCs in the North Atlantic and North Pacific - determine storm size either as the radius of the maximum wind speed (R_{max}) or the radius of the outermost closed isobar (ROCI). Both measurements are required as it is not always possible to measure R_{max} due to the high turbulence near the eyewall [*Chavas et al.*, 2016]. Furthermore, R_{max} being the shorter of the two distances can only be used in numerical models with high spatial resolution (i.e. less than 4 km) in order to get a credible approximation of R_{max} [*Chavas and Emanuel*, 2014].

Other recent studies used measurements of wind speed within the storm from satellite scatterometers to define a radius of vanishing winds, or outer radius (R_{12}), the latter is based on the azimuthal distance of the 12 m s^{-1} wind speed [*Chavas and Emanuel*, 2010; *Vigh*, 2015]. The measure of R_{12}, as measured with scatterometers, is a good approximation of the radius of R_{max} and gives an optimal threshold to isolate the turbulent circulation near to the eyewall. Lastly, *Y Lin et al.* [2015] estimated storm size as the radius where the precipitation rate equals 0.5 mm h^{-1}, which is also correlated with R_{12}.

Chavas and Lin [2016] produced a global climatology of TC wind speed derived from satellite observations (Figure 2-5) and showed that the global median TC size (R_{12}) is about 300 km. Furthermore, the largest and smallest TC are both found in the Northwest Pacific (i.e. median R_{12} = 352 km) and the Northeast Pacific (i.e. median R_{12} = 215 km) respectively. In the North Atlantic, the average cyclone has a radius of 266 km. These results also suggested that the size of cyclones shows only a small latitudinal dependence, although this dependence depends on the choice of the cyclone size metric i.e. R_{12} has a stronger latitudinal variability than R_0 [*Chavas and Lin*, 2016]. These results agree with the observed dependency of TCs with the temperature of the underlying ocean: whilst warm ocean temperatures are generally prone to TC-intensification, colder oceans generally induce TC weakening [*Balaguru et al.*, 2016; *K Emanuel*, 2005; *K Emanuel and Sobel*, 2013]. This relationship between TC-intensification and ocean temperature, or more specifically Sea Surface Temperature (SST), will be re-examined later.

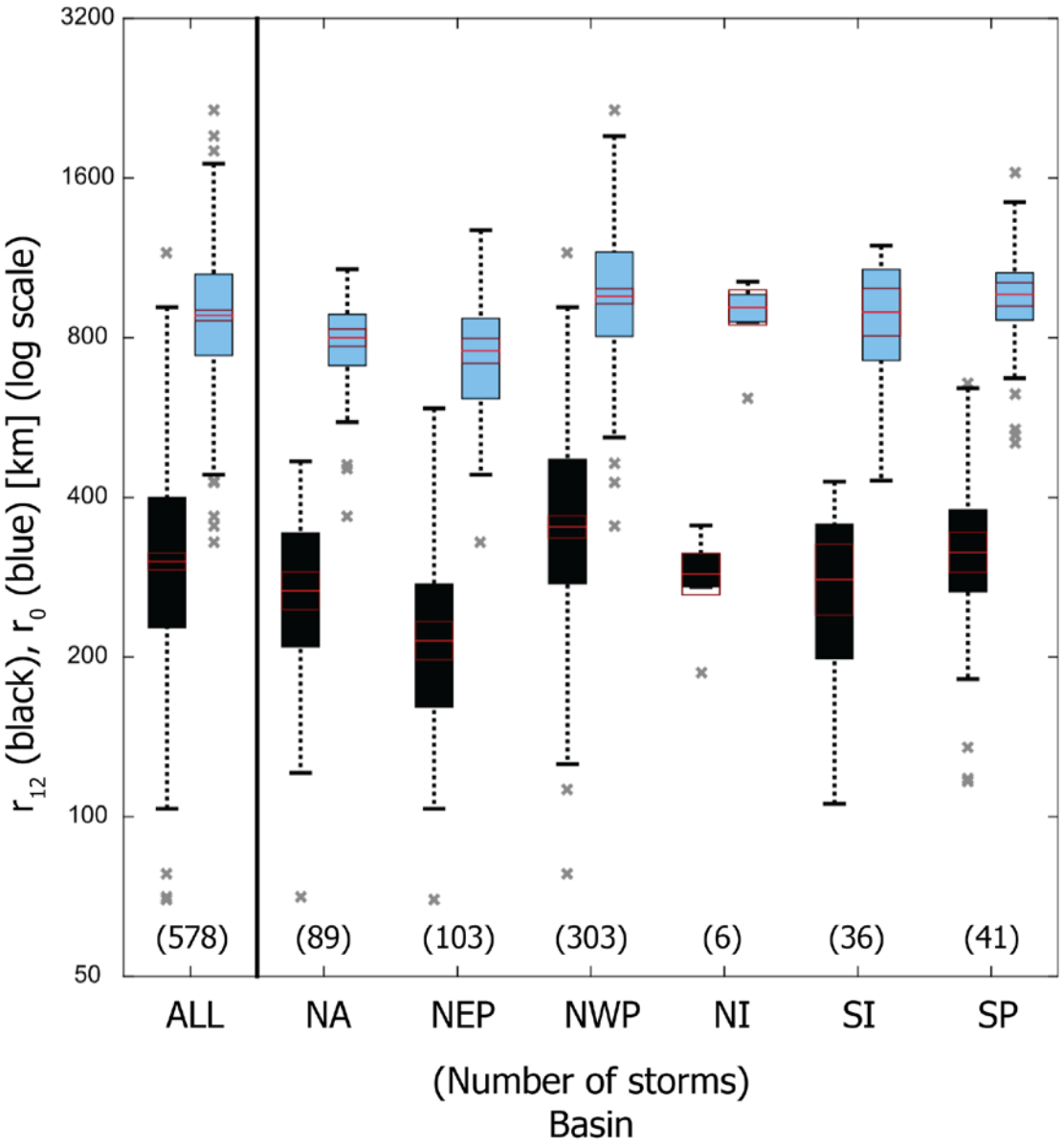

Figure 2-5 Box plot of the distribution of Tropical cyclones sizes in the global ocean (All), North Atlantic (NA), North East and North West Pacific (NEP and NWP), North and South Indian Ocean (NI and SI) and South Pacific (SP). The storm size was measured as the analysed mean radius of the 12 m s^{-1} (R_{12}, black) using global near surface wind vector from satellite scatterometers. Also shown is R_0 (blue) as the size of the cyclones defined as the outer radius of the vanishing wind speed. The box plot displays median (red line), interquartile range [q_1,q_3] (black and blue fill), whiskers (black lines), and outliers as grey crosses; outside the range [q_1-1.5(q_3-q_1), q_3 +1.5(q_3-q_1)] calculated from the logarithm of radius} [*Chavas et al.*, 2016].

Another metric to measure the size of a TC is the outer radius, which relates to the surface area occupied by a given storm at a given time. The outer radius may limit the number of storms that can be generated in a given space and time [*Chavas et al.*, 2016]. Previous studies determined that there is little convection beyond the R_{12} distance [*Dean et al.*, 2009], so TC size might be approximated as R_{12} [*Balaguru et al.*, 2014]. Due to the lack of consensus in the choice of metric to

describe TC size, some studies simply use a fixed radius as measured from the eye of the storm [e.g. *Shay et al.*, 1992]. The work in this thesis uses this simplified approach with different fixed values to determine the TC-induced ocean response, but also discusses the use of variable TC size to represent TC size changes during the life span of a storm.

2.2.2.3 Translational speed

In addition to the rotational wind speed, Tropical cyclones also have a translational speed (U_h) defined as the forward movement of the storm as forced (or steered) by the dominant environmental atmospheric wind [*George and Gray*, 1976; *Mei et al.*, 2012]. Thus, in agreement with the direction of tropical atmospheric circulation of the Hadley cells (Figure 2-1b), TCs move north and westward in the Northern Hemisphere (NH) and south and eastward in the Southern Hemisphere (SH) from their formation regions in the tropics (Figure 2-6).

George and Gray [1976], categorised TCs in three different classes depending on their translational speed as: 1) Slow moving TCs: 0-3 m/s; 2) Moderate moving TCs: 3-7 m/s; and 3) Fast moving TCs: >7 m/s. Since the oceanic response is determined in part by the translational speed of the storm, *I D Lloyd and Vecchi* [2011] suggested that the maximum ocean response occur when $U_H/Lf \approx 1$, where *f* is the *Coriolis frequency* and L is the characteristic length scale or size of the storm. Earlier studies [e.g. *I D Lloyd and Vecchi*, 2011; *Reul et al.*, 2014; *E. M. Vincent et al.*, 2012] used this storm classification to show that slow moving TCs ($U_H \leq 4$ m s^{-1} or $U_H/f < 1$ m s^{-1}) induce a larger oceanic response than fast moving TCs ($U_H > 5$ m s^{-1} or $U_H/f > 1$).

The mean translational speed correlates positively with the maximum wind speed attained by the storm (i.e. category 5 TCs move 1 m s^{-1} faster than tropical storms) and this differs slightly between the two hemispheres [*Chang et al.*, 2016; *Mei et al.*, 2012]. The mean translational speed ranges between 4.6 and 5.3 m/s in the NH and between 4.0 and 4.5 m s^{-1} in SH. On average, storms are faster and stronger in the SH [*Chang et al.*, 2016]. The average wind speed is 11.1 m s^{-1} in NH and 8.3 m s^{-1} in SH. Whilst the highest wind speeds are found in the North-East Pacific (NEP) followed by the North Atlantic (NA), North Indian (NI), North-West Pacific (NWP) and South-West Pacific (SWP) [*Chang et al.*, 2016]. Chapter 7 examines the dependence of TC-induced ocean response on translational speed.

2.2.3 Tropical cyclone climatology

Tropical cyclones generally form over warm tropical ocean where upper ocean temperatures are usually above 26˚C during the summer. The TC-formation regions have absolute vorticity of the

airflow with nonzero values [*K Emanuel*, 2003]. Thus, the common latitudes for cyclogenesis are poleward of 5˚ on either side of the equator [*K Emanuel*, 2003]. TCs tend to dissipate quickly when moving over land or over colder water. The later stage of the storm life can reach subtropical regions, at which point the TCs become known as extratropical storms.

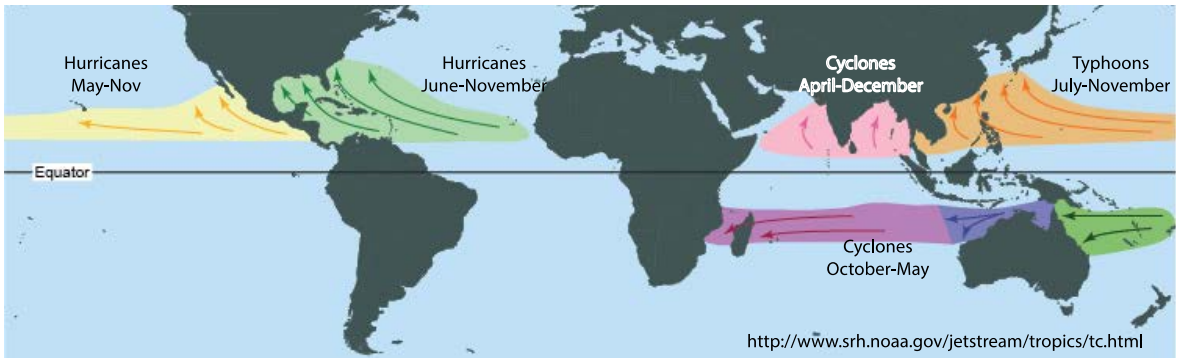

Figure 2-6 Tropical cyclone Global distribution and different naming conventions (i.e. referring to Tropical cyclones with maximum sustained wind speed ≥ 33 m s^{-1}) and the months of each TC-season around the world.

TC seasons are different depending on the oceanic basin but usually are constrained within summer and early autumn months (Figure 2-6). Whilst there is TC activity in four distinct basins in the NH (i.e. North Atlantic, Northwest and Northeast Pacific and North Indian ocean), TC activity is limited to only two basins in the SH (South Indian ocean and Southwest Pacific, including east Australian basin). TCs occur infrequently in the South Atlantic [*K Emanuel*, 2003], so there is no defined TC-season for this basin.

Figure 2-6, shows the official months as described by the US National Hurricane Center (NHC) for TC-activity in each basin, but the number of TC events varies from year to year. *Schreck et al.* [2014] studied TC variability over the period 1981 to 2010. Their results suggested that the North Atlantic (TC-activity from May to December) and the Southwest Pacific (TC-activity from October to May) have the shortest TC seasons, whereas the Northwest Pacific has the longest TC-season in the climatological record (on average all months had at least one event). Furthermore, there are clear differences in the TC intensity that can be achieved within each basin and considering all regions, the Northwest Pacific has the greatest number of Tropical cyclones (with on average 17 storms per year with wind speed ≥ 33 m s^{-1}) followed by the Northeast Pacific, North Atlantic and the Indian Ocean. The number of TCs is lowest in the South Indian and the South Pacific basins (with on average less than 6 events per year). It is worth noticing that historical number of TCs in different basins is strongly related to the technical capability of the meteorological agencies operating in a given region. For example, whilst aircraft recognisance are regular observations in the North

Atlantic and North East Pacific only. In the Indian Ocean TC observations are heavily reliant on ships and more recently on satellite observations [*Knapp et al.*, 2010].

2.3 Ocean Stratification and Tropical cyclone Intensification

Until recently, studies about TC intensification did not pay much attention to the oceanic response that now seems obvious to include. It appears that TC-induced changes in ocean stratification may modulate the amplitude of the TC-induced surface cooling, which in turn may limit TC intensification [e.g. *Vincent et al.*, 2013]. Before going further into explaining TC-ocean interaction mechanisms, this section summarises important concepts about upper ocean structure as a multi-layered water column. Different layers are identified by the Mixed Layer Depth (MLD) and the Barrier Layer (BL). Both MLD and BL are highly variable and the BL is not always present, but when it is present BL is thought to play an important role in TC intensification [e.g. *Balaguru et al.*, 2012; *Price*, 1981; *Stramma et al.*, 1986].

2.3.1 Mixed Layer Depth and Barrier Layer Thickness

The thermal disequilibrium between the ocean and the lower atmosphere is responsible for the large heat fluxes which sustain TC. Understanding TC-induced changes in SST is the starting point to build indices intended to represent TC intensification over the ocean [*Price*, 2009]. The subsurface thermal and haline structures of the water column prior to the passage of a storm modulate TC-induced surface cooling, thus there is the potential to identify oceanic regions where TC-intensification is more likely to take place than others.

The MLD was originally defined as the depth of homogeneous temperature, or the Isothermal Layer Depth (ILD). This was a rather crude view of the subsurface ocean structure and it was useful to overcome data scarcity of temperature and (especially) salinity profiles. However, this representation of upper ocean structure experienced noticeable adjustment, first in 2000, with the inclusion of new algorithms using both temperature and salinity profiles [*Kara et al.*, 2000], and second, since 2005, when the Argo project reached its full global coverage of the ocean [*Montegut et al.*, 2007]. *Montegut et al.* [2007] defined the MLD as the depth ($D_{T\text{-}02}$) at which the temperature has decreased by 0.2˚C compared to the reference temperature measured at depth of 10 m. The 10 m reference depth seeks to avoid thermal diurnal changes in the top few meters. Some regions may have a MLD that is shallower than the reference depth, but these regions correspond to coastal upwelling regions and are not relevant in this thesis. The temperature threshold of 0.2˚C is most widely used in recent research defining the MLD from individual temperature and salinity

profiles [e.g. *D'Ortenzio et al.*, 2005; *de Boyer Montégut*, 2004; *Kumar et al.*, 2014]. MLD computations that use larger temperature thresholds (e.g. ΔT = 0.8˚C) results in a deeper MLD estimates and the differences are particularly significant in polar regions [*Hosoda et al.*, 2010]. Determining the best methodology to compute the MLD is out of the scope of this thesis, which simply uses the same approach as used in previous studies [e.g. *Balaguru et al.*, 2014; *Grodsky et al.*, 2012] based on a thermal threshold of 0.2˚C.

The estimation of the MLD by either of the aforementioned density thresholds make it possible to identify regions with high freshwater inputs where vertical salinity gradients control upper ocean structure. Within these regions, salinity changes in the water column are more important than changes in temperature to determine stability. These regions usually have particular water column arrangements that constrain vertical mixing processes (Figure 2-7), including the cold wake upwelling induced by the passage of a TC. The water between the base of the Mixed Layer and the base of the ILD is known as the BL. A BL is present almost permanently in tropical regions where most of TC activity occurs [*Balaguru et al.*, 2012; *Kara et al.*, 2000; *Montegut et al.*, 2007; *Sprintall and Tomczak*, 1992]. This thesis pays special attention to the observed ocean response to TCs over BL regions.

Following previous works [e.g. *Montegut et al.*, 2007], this thesis defines the pycnocline as the depth D_σ where the potential density (σ_θ) has increased from the reference depth of 10 m by a threshold (Δ_σ) equivalent to the density difference for the same temperature change at constant salinity:

$$\Delta\sigma = \sigma_\theta(T_{10} - \Delta T, S_{10}, P_0) - \sigma_\theta(T_{10}, S_{10}, P_0)$$

Where T_{10} and S_{10} are the temperature and salinity at the reference depth of 10 m. Water structures with BL occur when the pycnocline does not coincide with the thermocline. In those cases where the halocline depth is shallower than the thermocline depth (Figure 2-7a) and the intermediate layer is the BL and its thickness is defined as:

$$BLT = D_{T-02} - D_\sigma$$

where $D_{T\text{-}02}$, is the depth where temperature has decreased by 0.2˚C as compared to the temperature at reference depth of 10 m.

This description of the upper ocean stratification adds more complexity to ocean-atmosphere interactions than using a two-layered ocean structure. In a two-layered water column, above the MLD the water is mixed and the density is homogeneous the isothermal, isohaline and isopycnals are coincident at the same depth level (Figure 2-7b).

The strength of ocean stratification can be measured by the Brunt Väissälä (buoyancy frequency, N^2) expressed in cycles per second (cph). Large values of N^2 are associated with a water column configuration that oppose vertical mixing. Conversely, low values of N^2 indicate water columns that offer low resistance to vertical mixing. Regions with deep BL (i.e. BL > ~20 m) are associated with high values of N^2 (Figure 2-7c), while regions with shallow BL are usually associated with low N^2 values and hence lower resistance to mixing (Figure 2-7d).

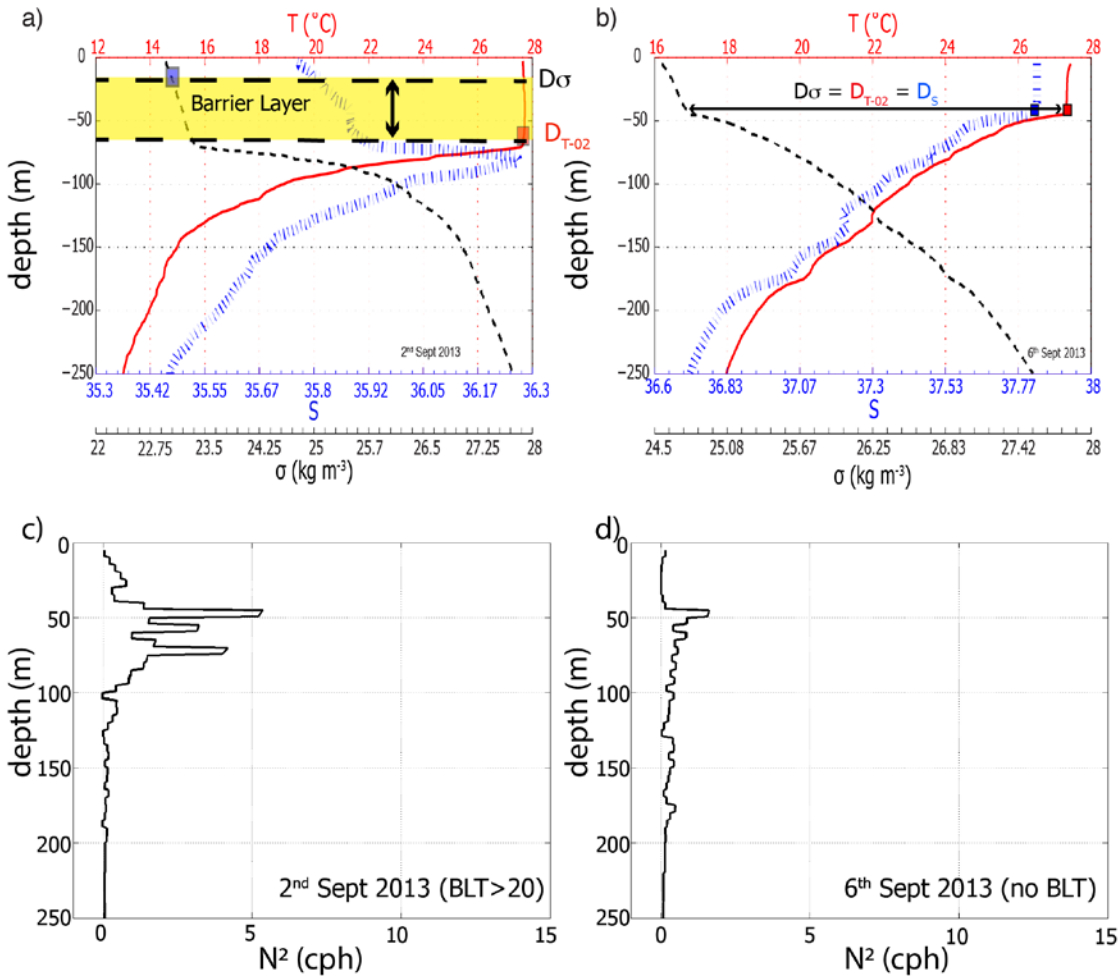

Figure 2-7 Example of two Argo profiles of temperature (red, solid), salinity (blue dotted) and density (black, dashed) in September 2013 in the North Atlantic in a region (5˚N, 24.8˚W) with a thick climatological barrier layer (a) and within the region (25˚ N, 47˚W) with no barrier layer (b). Notice the isopycnocline layer depth (blue square, D_σ) and the isothermal layer depth (red square, D_{T-02}) and see definition in the main text. The Barrier Layer is the defined in the main text as the difference between isopycnocline and the isothermocline. The vertical distribution of the buoyancy frequency (N^2, in cycles per hour) in the same profiles with barrier layer (c) and without (d).

Kara [2003] summarized the MLD seasonal variability in different parts of the global ocean (Figure 2-8). The results showed that the MLD in the North Pacific does not deepen as much as that in the North Atlantic because BL formation is maintained almost year-round by precipitation and weak

upwelling. In the Indian Ocean, the MLD has a strong seasonal variability dominated by changes in surface winds and precipitation linked to the monsoon (June to September: high precipitation; October to November: low precipitation [*Kara*, 2003]). The Antarctic region showed the shallowest and least variable MLD in the global ocean.

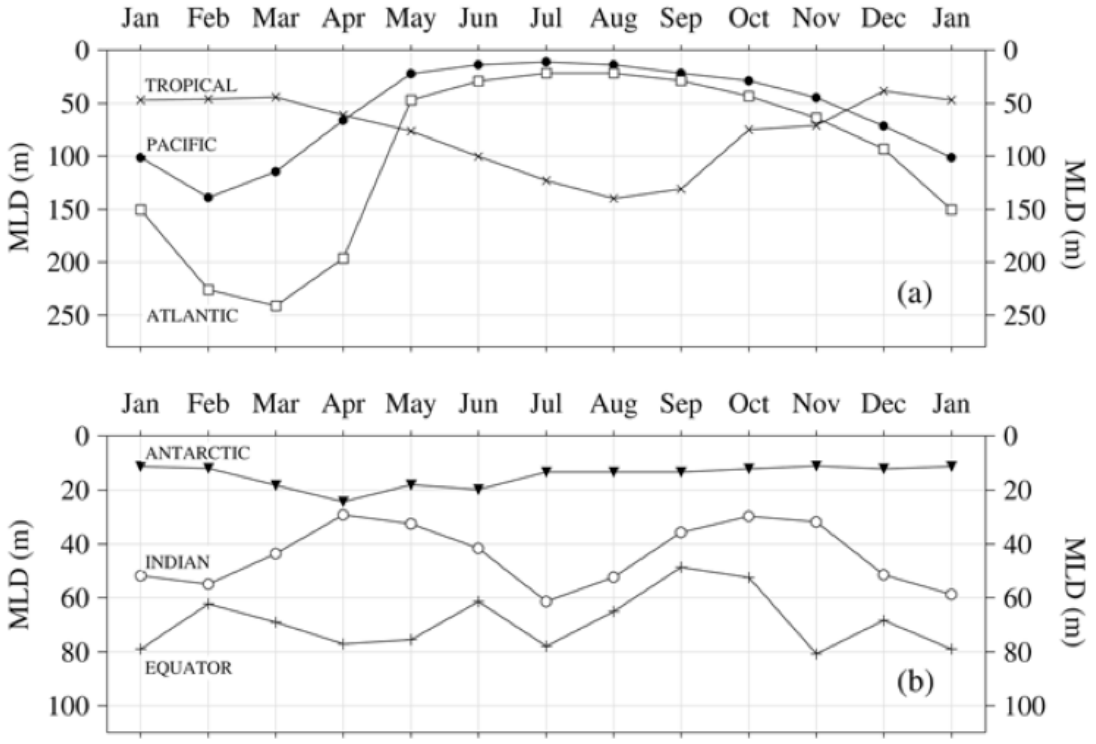

Figure 2-8 Annual changes of the mixed layer depth (MLD) at selected location in the global ocean: (a) Topical Ocean (20˚S, 140˚W), Pacific Ocean (30˚N, 160˚E) and North Atlantic Ocean (40˚N, 30˚W); (b) Antarctic (70˚S, 100˚W), Indian Ocean (10˚N, 55˚E) and Equator (1˚S, 170˚E) (Figure taken from [*Kara*, 2003]). Note different MLD range on top and bottom plot.

2.4 Tropical cyclone Induced Oceanic Response

The ocean response to the passage of a TC is typically evaluated by measuring changes in various ocean parameters, including SST and upper ocean temperature (i.e. usually taking observations from surface down to 100 m), which is related to the ocean heat content (OHC) available to fuel the TC heat engine. All these changes are reflected as variability in the upper ocean structure like the deepening of the mixed layer [*Price*, 2009]. Both in situ observations and numerical studies indicate that it is predominantly heat transfer from the warm ocean to the atmosphere which allows a TC to fully develop and intensify [*Price*, 1983]. In turn, ocean surface cooling induced by upwelling in the wake of the storm interrupts this ocean-to-atmosphere heat transfer and results in a negative feedback and TC weakening [*I I Lin et al.*, 2008; *Schade and Emanuel*, 1999; *Vincent et al.*, 2014].

2.4.1 Tropical Cyclone induced upper ocean mixing

The ocean's response to the passage of TCs includes surface waves higher than 20 m, increased sea surface currents (i.e. horizontal speed ≥ 1 m s^{-1}), and sea surface cooling [*Ginis*, 2002]. *Geisler* [1970] proposed a dynamical ocean response theory. This theory suggested that the TC induced ocean response was a source of near inertial frequency internal waves in the ocean, with a wedge-shaped pattern similar to the one created behind a moving ship. Furthermore, the primary feature of the ocean response to a moving cyclone could be reproduced by using a two-layer model, with an upper layer (H_1) and deeper layer (H_2) of the open ocean ($H_2 >> H_1$) and the density increasing with depth (i.e. $\rho_2 >> \rho_1$) . Geisler's model had two modes known as the barotropic mode (i.e. situations where surface pressure is constant on surfaces of constant densities) and the baroclinic mode (i.e. where surface pressure is not constant on surfaces of constant density). The structure of the modes in the two-layer system (where H_1 and H_2 are depths in m) was as follows [*A Gill*, 1982]:

$$c_e^4 - gH_e c_e^2 + gg'H_1H_2 = 0$$

Where C_e is the equivalent phase speed of one homogeneous fluid layer with an equivalent depth (H_e), g is the gravity acceleration constant (9.8 m s^{-2}) and g' is the reduced gravity acceleration that can be written as follow:

$$c_e^2 = gH_e$$

$$g' = g\frac{\rho_2 - \rho_1}{\rho_2}$$

In the ocean, assuming small differences in density between the two layers, it is possible to approximate $g'/g \approx 0.003$ m s^{-1}, which results in two widely separated roots, C_0 and C_1 corresponding to the barotropic and the baroclinic modes respectively. The simplified equation for each mode is:

$$C_0 = \sqrt{g(H_1 + H_2)}$$

$$C_1 = \sqrt{\frac{g'\,H_1H_2}{H_1 + H_2}}$$

Whilst the velocity of the barotropic mode (C_0) typically is about 200 m s^{-1} in a deep ocean, the speed of the baroclinic mode (C_1) ranges from 2 to 3 m s^{-1} depending on the density contrast between the two layers. Based on the phase speed, each mode is well differentiated and the surface layer (H_1) acts as rigid lid [*Chang et al.*, 2013]. The speed of a given nth mode (C_n) decreases with

the increasing order of the mode [*Ginis*, 2002; *Shay et al.*, 1989]. *Ginis* [2002] modelled numerical responses induced by a storm moving at 5 m s^{-1}. This work suggested that on the one hand, the baroclinic response resulted in a slow-moving oscillating wake behind the storm with a rightward asymmetry, formed by inertial gravity waves. On the other hand, the barotropic response is characterised by a quasi-stationary fast and elongated circulation along the storm track direction with no wake. The storm wake in the open ocean is primarily driven by the strong wind within the storm and the baroclinic response dominates over the barotropic [*Geisler*, 1970; *Ginis and Sutyrin*, 1995; *Price*, 1983]. Owing to the vertical changes associated with the baroclinic response, this is also referred as the first internal mode [*Shay*, 2009].

Additionally, cyclonic surface winds within a storm induce significant turbulent mixing in the ocean, typically within the top 100 m [*Shay et al.*, 1989], which forces an upward movement of cool and salty water between 50 to 100 m depth [*K Emanuel*, 2000; *Ginis*, 2002; *Price*, 1981]. The depth of this uplift can be estimated by the Froude number (F_r), which is a non-dimensional metric used to estimate the expected baroclinic response induced by a moving storm at speed (U_H),

$$F_r = \frac{U_H}{C_1}$$

Slow moving TCs generate inertial gravity waves C_1 that are dominant over U_H and the wind curl induces upper ocean geostrophic transport (i.e. wind induced pressure gradient is compensated by Coriolis force), that drives surface waters away from the centre of storm, which, in turn, forces a cold upwelling [*Ginis*, 2002]. Thus, slow moving TCs might be linked to low Froude Numbers (i.e. $F_r \leq 1$). Whereas for fast moving TCs, where the translational speed is higher than the first baroclinic mode (i.e. $F_r > 1$), the TC induced energy transfer into the ocean is higher but with less induced geostrophic currents. Therefore, slow moving TCs are associated with an ocean baroclinic response, which in turn is associated with upwelling and downwelling [*Ginis*, 2002]. The horizontal scale of the wake is set by the scale of the wind stress curl and the distance of the maximum wind speed [*Ginis and Sutyrin*, 1995; *Price*, 1983]. This theoretical explanation of the TC induced ocean response is further examined in later on this thesis (Chapter 6 and 7) where there is an agreement with the results seen in both in situ and model based studies.

The most noticeable oceanic response to a moving storm is a decrease in SST owed mainly to the before mentioned turbulent mixing forced by the strong winds [*Price*, 1983; *Sanford et al.*, 2011; *Stramma et al.*, 1986]. Thus the cyclonic direction of the wind results in an increased cooling to the right compared to the left of the storm track. The air-sea heat exchange plays only a minor role changing the upper ocean structure [*Price*, 1981; 2009; *Shay*, 2009; *E. M. Vincent et al.*, 2012].

Further, the oceanic response measured as the cooling induced by the storm is limited by the intensity of the storm (i.e. wind speed especially near the eyewall), the translational speed and the initial mixed layer depth prior to the passage of the storm [*Stramma et al.*, 1986]. Latitude and storm size play only a minor role in the oceanic response at a given location [*K Emanuel*, 2000; *Price*, 1981; *Sanford et al.*, 2011; *Shay et al.*, 1997].

2.4.2 Tropical cyclone to ocean negative feedback

Wind Induced Surface Heat Exchange (WISHE) supports the hypothesis that TC intensification depends only on three parameters: the initial storm intensity; the thermodynamic state of the atmosphere; and the heat exchange with the upper layer of the ocean under the core of the TC [*K A Emanuel*, 1986; 1988; 1999]. The latter refers to the ocean-to-atmosphere feedback, which can reduce TC intensity by more than 50% [*Ginis*, 2002; *Schade and Emanuel*, 1999]. This is what is known as negative feedback and reflects that TC intensity is particularly sensitive to the thermodynamic structure of the upper ocean. Therefore, current TC forecasting models account for the SST as a measure of the thermal stratification of the underlaying ocean ahead of the passage of the storm [*Reynolds et al.*, 2007].

Based on the negative feedback principle, it is possible to assume that stronger TCs will induce more mechanical energy into the ocean surface [e.g. *Price*, 1981]. Hence, these TCs will upwell more water to the surface than weaker ones, and will also stimulate stronger negative feedback that in turn will moderate their intensification [*Price*, 1981]. Studies based on historical observations reveal that the amplitude of the cooling increases with cyclone intensity up to category 2 on the Saffir-Simpson scale (wind speed from 43 to 49 m s^{-1}) but that this is not true for TCs of higher intensity [*I D Lloyd and Vecchi*, 2011]. This means that to better understand TC intensification it is important to understand the upwelling induced by vertical turbulent mixing and the forcing from the passage of the TC. Thus, *I D Lloyd and Vecchi* [2011] showed that strong ocean thermal stratification (i.e. as measured by the difference between SST and the temperature below the thermocline) and a shallow MLD (about 20 m or less in the North Atlantic) may favour surface cooling. These conditions often result in reduced Ocean Heat Content (OHC), which is a property of the upper ocean strongly related to TC intensification. Many other TC indices based on temperature have been proposed to represent intensification potential and improve predictability. However, to date, TC indices that include a haline component are seldom used and the potential role of salinity in determining TC intensity is generally neglected. In the following subsections, we review the main TC indices and how they include the thermal ocean component. Towards the end of the thesis, there will be a

discussion of how the haline component could be implemented to improve TC intensification forecasting.

2.5 Tropical cyclone Indices

A number of indices have been proposed to encapsulate the interactions between a TC and the underlying ocean. The following describes the metrics that aim to estimate the importance of the ocean to atmosphere feedback when storm locations (x,y) are known at given time (t).

2.5.1.1 Initial Sea Surface Temperature

This is a measure of the initial Sea Surface Temperature (SST_i) and is the simplest metric to measure the TC induced ocean response. The basis of SST_i relies on the apparent preference of TC formation over oceans with SST ≥ 26˚C [*Miller*, 1958] and the TC's induced thermal changes can be as large as 4˚C to 6˚C [*Price*, 2009].

$$SST_i(x, y) = T_i(x, y, z = 0)$$

However, evidence shows that SST at or above 26˚C is just one necessary condition for TC formation and is not sufficient in itself (Emanuel, 2005). Further, SST is a meteorological predictor that might be considered specific of the present climate [*Camargo et al.*, 2007]. Thus SST_i is only used as an approximation of the ocean conditions before the passage of the storm, but cannot be used to characterise the ocean feedback to the atmosphere.

2.5.1.2 Ocean Heat Content

OHC is also known as hurricane heat potential or Tropical cyclone heat potential. This index is based on the hypothesis that if ocean heat exchange (kJ cm^{-2}) is important to the heat engine of a TC, then oceanic regions with larger heat content are more favourable for storm formation and intensification than regions with lower heat content. This oceanic metric assumes energy conservation from the surface down to the depth of maximum TC-induced mixing. *Leipper and Volgenau* [1972] formulated OHC as the first ocean metric including the effect of the subsurface thermal structure of the ocean and it has been used to generate the NHC TC intensity forecast [*Mainelli et al.*, 2008]. The equation to compute OHC remains the same as the one proposed in 1972:

$$OHC(x, y) = \rho_0 C_p \int_{Z_{26}}^{Z_0} \big(T_i(x, y, z) - T_{ref}\big) dz$$

where ρ_0 is the seawater density (fixed value at 1025 kg m^{-3}), C_p is the heat capacity at constant pressure (4.0 x 10^{-3} J kg^{-1} ˚C^{-1}) and the integral is defined between the surface (Z_0) and the depth of the 26˚C isotherm (Z_{26}). The temperature reference of 26˚C is an estimate of the thermal disequilibrium between the atmosphere and the initial state of the ocean.

The index is based on the hypothesis of conservation of energy within the upper layer (i.e. from Z_0 to Z_{26}), which in TC conditions does not always true due to: 1) Density and heat capacity changes under TC induced mixing conditions; and 2) overestimation of the magnitude of the inferred heat exchange when the TC-induced mixing extents below Z_{26}. Thus, while observations showed that high values in OHC (i.e. ≥ 60 kJ cm^{-2}) favour TC-intensification, low OHC values (i.e. < 60 kJ cm^{-2}) are not directly correlated to the strength of the storm [*Price*, 2009]. Thus, OHC might be a good TC forecasting index only for warm, deep, open ocean conditions.

A modification of the lower temperature limit from 26˚C to 22˚C would indeed respect the principle of conservation of heat and would improve the statistical properties of the current definition of OHC [*Price*, 2009]. Nevertheless there is no guaranty that heat content is the most relevant physical quantity to describe TC-to-ocean interaction [*Price*, 2009].

2.5.1.3 Vertical average of the upper ocean temperature

The vertical average of the upper ocean temperature ($T_{\bar{d}}$) was introduced by *Price* [2009] as an alternative to the OHC. $T_{\bar{d}}$ is the vertical integral from surface down to the estimated mixing depth (d) induced by a passing storm given by

$$T_{\bar{d}}(x,y) = \frac{1}{d}\int_{z=d}^{z=0} T_i(x,y,z)dz$$

where d is the depth of vertical mixing caused by the passage of a TC as represented by the maximum TC induced mixing temperature layer. For simplification, $T_{\bar{d}}$ is computed using d = 100 m (i.e. $T_{\overline{100}}$), the typical observed mixing depth induced by TCs with wind speed ranging from 50 - 70 m s^{-1} (i.e. hurricane category 3 and 4) according to [*D'Asaro et al.*, 2007].

The degree of TC-induced surface cooling is constrained to the upper ocean thermal stratification prior to the storm, i.e. there will be a higher temperature gradient between two consecutive depth levels. Thus the cooling will be small if there is a small vertical temperature difference within the water column (i.e. from surface down to 100 m depth). The innovation of this TC metric is that could be used with a variable TC induced mixing depth by computing the variable mixing depth (d). The computation of d requires: 1) profiles of both temperature and salinity to compute the density profiles ($\rho(z)$); and 2) the bulk Richardson number (Ri), which connects the buoyancy term (i.e.

measured oscillatory frequency given by the Brunt Väissälä number (N^2) and the flow shear term (S^2), i.e. TC induced turbulent mixing in the upper ocean. The parameterization of the Richardson number follows as [*Sanford et al.*, 2011]:

$$Ri = \frac{N^2}{S^2} = \frac{-\frac{g}{\rho_0}\frac{\delta\rho}{\delta z}}{\frac{\delta u^2}{\delta z} + \frac{\delta v^2}{\delta z}}$$

where g is the gravity acceleration (9.8 m s^{-2}), h is the initial mixed layer depth, $\delta\rho$ is the density gradient with depth (dependent of both T and S), ρ_0 is the sea surface density (1025 kg m^{-3}), and the S^2 is the vertical velocity gradient induced by the storm and it is determined by the physical characteristics of the storm and can be determined as [*Price*, 2009],

$$S = \left(\frac{\tau}{h}\frac{4R_H}{U_H}\right)^2$$

where the storm size computed as the radius of the maximum wind speed (R_H, km), horizontal translational speed (U_H, m s^{-1}) and the maximum wind stress (τ, Pa). Thus, regardless of the advantage of including both salinity and thermal stratification, this index has so far not been tested using real observations.

The bulk Richardson numbers ranges from 0.2 to 1 in laboratory conditions [*Jacob et al.*, 2000] with the lowest R_i values found to be in high-shear regimes. In TC conditions, the bulk Richardson number exceeds unity [*Shay et al.*, 1992] and critical Richardson number is found to be 1/4, which is related to the TC induced maximum vertical mixing (i.e. goes below mixed layer depth) [*Sanford et al.*, 2011].

The interpretation of $T_{\bar{d}}$ assuming that a TC induced wake reduces upper ocean temperature, high values of $T_{\bar{d}}$ (i.e. $T_{\bar{d}} \geq 28^{\circ}C$) would indicate that there is a TC favourable upper ocean thermal structure, i.e. TC intensification might happen. Conversely, low values of $T_{\bar{d}}$ (i.e. $T_{\bar{d}} \leq 24^{\circ}C$) would indicate there is a TC-unfavourable upper ocean thermal structure. Further, the difference of the pre-storm SST minus the $T_{\bar{d}}$ (ΔT_d = SST-$T_{\bar{d}}$) is also an estimate of the expected surface temperature after the passage of the storm. Thus in regions with small ΔT_d will experience weaker cooling and will have little effect on the air-sea temperature difference during the passage of the storm [*D'Asaro et al.*, 2014]. In contrast, regions with large ΔT_d TC induced mixing will induce strong ocean cooling with more opportunity enhance of negative feedback between the ocean and storm system.

OHC and $T_{\bar{d}}$ provide very similar results under warm and deep oceanic regions, but differences may arise over freshwater regions (e.g. river plumes and regions with high precipitation regimes) where the saline stratification might dominate over the thermal stratification [*Price*, 2009].

2.5.1.4 Cooling inhibition index and the wind power index

Numerical models represent useful tools when it comes to exploring the simulated ocean response to TC. [*E. M. Vincent et al.*, 2012] used an Ocean General Circulation Model (OGCM) forced by surface fluxes including wind speed from TCs, and estimated the TC induced ocean response using two innovative indices: the wind power index (WPi) and the cooling inhibition index (CI).

As the storm moves over the ocean, a fraction of the Kinetic Energy (E_K) transferred into the ocean is converted into Potential Energy (E_P), whereby light water particles are displaced downward while dense particles are displaced upward [*Z Liu et al.*, 2007]. The WPi is an estimate of the E_K transferred from the cyclone into the ocean, which induces upper ocean mixing. WPi integrates several atmospheric parameters of the storm, including its translational speed, size and intensity. The CI is an estimate of the E_P needed to induce a surface cooling in a given ocean region with determined water structure. CI is a measure of the resistance of the ocean to TC-induced mixing and surface cooling. CI integrates two important upper ocean parameters: the mixed layer depth and the stratification below it. As the CI index considers both thermal and haline stratification, the CI in the Bay of Bengal is higher than in the Arabian Sea [*Neetu et al.*, 2012] owing to the high precipitation and river run-off in this region. *E. M. Vincent et al.* [2012] suggested that the spatial and temporal coverage of Argo is not sufficient to correctly represent all pre-cyclone oceanic conditions. Therefore, and as seen previously with T_b, the application of CI has been limited to numerical models only.

I D Lloyd and Vecchi [2011] used the depth of the mixed layer temperature isotherm minus 2˚C (h_2) to estimate the surface cooling induced by the passage of the storm. This index measures the same information as CI, which are the depth of the mixed layer and the importance of the thermal stratification at the base of the mixed layer [*E. M. Vincent et al.*, 2012]. The main difference of these two indices is that h_2 accounts for thermal stratification only, and the salinity stratification is ignored. As it was noted before for the T_d, salinity dominated stratification can be important in some oceanic regions.

Chapter 3

Datasets and data sources

This chapter introduces the sources, accuracies and processing steps applied to the data used in this thesis. The main datasets used in this work include: Tropical cyclone database from the International Best Track Archive for Climate Stewardship (IBTrACS; Section 3.1); Climatology datasets for temperature, salinity, Mixed Layer Depth and Barrier Layer (Section 3.2); satellite measurements of sea surface temperature (Section 3.3) and sea surface salinity (Section 3.4); Argo temperature and salinity observations (Section 3.5); and output from the Forecasting Ocean Assimilation Model (FOAM) data-assimilating model system (Section 3.6).

3.1 International Best Track Archive for Climate Stewardship (IBTrACS)

Tropical cyclone track data used in this dissertation are taken from the International Best Track Archive for Climate Stewardship (IBTrACS) version code v03r08 (https://www.ncdc.noaa.gov/ibtracs) and includes data from several meteorological agencies [*Knapp et al.*, 2010]. There are discrepancies in the information reported by different agencies in each basin (Levinson et al., 2010). However, IBTrACS includes the original maximum wind speeds (as reported by each agency), thus it is possible to choose the information from the meteorological agency most relevant to the ocean basin where the observations were required. Instead of trying to homogenise the IBTrACS dataset, this thesis only used information of all those agencies included in the World Meteorological Organization (WMO) and some of the agencies included within the

Regional Specialized Meteorological Centre (RSMC). A key source of disagreement amongst the data from these agencies is the definition of the maximum winds speed (MWS). Whilst for the agencies within the WMO the maximum wind speed is defined as the maximum 10-minute sustained wind within a storm at 10 m over a smooth surface, the RSMC agencies use the 1-minute sustained wind speed. In order to count storms by their category on the Saffir-Simpson hurricane scale, the 10-minute winds were divided by 0.88 to roughly covert to 1-minute values using the method given in [*Knapp et al.*, 2010].

At the moment there is no global consensus for reporting storm sizes (see Chapter 2), so IBTrACS does not include this information in the database. Following [*I D Lloyd and Vecchi*, 2011], this thesis uses a fixed radius (e.g. maximum distance from storm centre of 400 km) to determine the maximum horizontal extension of the TC forcing over the ocean surface.

The IBTrACS database provides information about all TCs globally from 1981 to 2015 [*Schreck et al.*, 2014]. This thesis uses a study period of eleven years from 2005 to 2015 inclusive. The choice of the study period was based upon keeping the time period approximately in line with other datasets (i.e. see below Argo time period). TC locations of active storms is reported every six hours i.e. at 0, 6, 12 and 18 hours GMT. This work generally used observations at 12 pm GMT to compare with ocean conditions (e.g. temperature and salinity from Argo and FOAM system).

3.2 Climatology datasets

3.2.1 World Ocean Atlas

The information on the ocean background variability in temperature and salinity was obtained from the monthly climatology included in the World Ocean Atlas 2013 (WOA13). WOA13 contains an equal climatological mean of six decades from 1955 to 2012 [*T. P. Boyer et al.*, 2014]. The climatological mean fields of temperature and salinity are given on a regular grid with a spatial resolution of one quarter of a degree (1/4 degree, about 25 km). For the purpose of this thesis, the analyses focused on the first 33 out of 102 standard depth levels (i.e. 0-400 m depth).

Both temperature and salinity analyses were computed by objective analysis of all scientifically quality controlled historical temperature and salinity [*Locarnini et al.*, 2013; *Zweng et al.*, 2013]. [*T. P. Boyer et al.*, 2014] described the data sources included in WOA13 and *Johnson et al.* [2013] described the quality control of the data included in the analyses. Data analysis of this climatology dataset includes flagging of the data rather than elimination [*Locarnini et al.*, 2013], hence it is possible to study different scales of spatial variability (i.e. from large to mesoscale), as well as

interannual and interdecadal variability of the water mass properties. To ensure inclusion of all the real information with the minimum data contamination, the WOA13 analyses apply different statistical checks, which include averaging and taking the standard deviation of all data within five-degree horizontal distance. These analyses flag data at five and three standard deviations distances from the mean at depth above and below 50 m depths respectively.

3.2.2 Mixed Layer Depth

This thesis used the Mixed Layer Depth dataset distributed by the Asia-Pacific Data-Research Center (APDRC). Information and documentation of this dataset were downloaded from the host website (http://apdrc.soest.hawaii.edu/projects/Argo/index.php). This product uses Argo profiles only, covering the period 1st January 2005 to date, with a monthly temporal resolution. Data have been interpolated to a 1-degree spatial resolution grid using a variational interpolation algorithm. This ensures that interpolated data are as close as possible in both space and time from the original observation. The gridded fields in the dataset include:

(1) Mixed Layer Depth (MLD) - computed as the depth where density increases from the reference depth of 10 m by the value equivalent to a temperature drop of 0.2˚C [*de Boyer Montégut*, 2004];

(2) Isothermal Layer Depth (ILD) - the depth where temperature differs from its 10 m value by 0.2˚C;

(3) Top of the Thermocline (TTD) - the depth at which temperature decreases by a given amount from its 10 m value. TTD may differ from ILD if there is a temperature inversion below 10 m depth.

(4) Barrier Layer Thickness (BLT, or simply BL) - the difference between TTD and MLD (TTD minus MLD).

For the purpose of this work, this thesis did not consider cases of compensated BLT (i.e. regions where MLD > TTD), which is an ocean stratification state that occasionally occurs in Polar Regions [*de Boyer Montégut*, 2004].

In the same way as WOA13 provides long-term salinity and temperature climatologies, the APDRC also distributes monthly climatology of MLD using the averages in a month to produce long-term averages over 2005 - 2017.

3.3 Sea Surface Temperature

Sea surface temperature (SST) analyses were used to study the natural variability of the SST during the TC seasons in each ocean basin. The SST analyses were taken from the Group of the High Resolution SST (GHRSST) and corresponds to the dataset known as AVHRR-only, which is a useful analysis dataset for climate studies [*Reynolds and Chelton*, 2010]. The GHRSST SST analysis is produced daily on a 0.25˚ grid at the National Oceanic and Atmospheric Administration (NOAA) National Climatic Data Center. This product uses Optimal Interpolation (OI), using data from the 4 km Advanced Very High Resolution Radiometer (AVHRR) Pathfinder Version 5 time series (when available, otherwise operational NOAA AVHRR data are used), in situ ship and buoy observations. Ship SSTs are corrected relative to the buoy SSTs by subtracting 0.14˚C from all ship observations before they are used to bias correct the satellite data [*Reynolds and Chelton*, 2010]. Therefore, all observations are corrected to buoy SST (and not, as recommended by Donlon (2007) to foundation temperature, which is the temperature of the water column free of diurnal temperature variability). The OI analysis is a daily average SST that is bias adjusted using a spatially smoothed 7-day in situ SST average and is thus tuned to a water depth of about 0.3 meter [*Reynolds et al.*, 2007]. Day and night satellite fields are independently bias adjusted. These SST data are available from 1981 to present. SST analyses data were downloaded from JPL GHRSST data server on 1st June 2014 (http://ghrsst.jpl.nasa.gov).

3.4 Sea Surface Salinity

This thesis used SSS products from the European Space Agency (ESA) Soil Moisture and Ocean Salinity mission (SMOS). The products consist of the Ifremer Level 4a SSS thematic research products, which are available from CNES-IFREMER Centre Aval de Traitement des Données SMOS (CATDS) at IFREMER, Plouzané (France) [*Guimbard et al.*, 2017]. These products are 7-day composites of SSS Level 3 gridded products. These products have ¼˚ spatial resolution and have been corrected with a large-scale bias correction based on Argo monthly climatology temperature and salinity. The temporal coverage of the SMOS CATDS data covers from May 2010 to March 2017. In particular, this thesis focused on the data during the storm seasons 2011 and 2014 to track the temporal evolution of the Amazon plume in those years (Chapter 5). The data were downloaded via FTP server at https://www.catds.fr/Products/, where further information is available about the construction of this dataset. In addition, the site also provides details about the accuracy of the products (typically 0.1-0.5 psu at large scales) and remaining technical challenges linked to SSS retrieval, particularly at high winds (where there is no consensus on the retrieval strategy).

3.5 Argo

The Argo program provides in situ profiles of temperature and salinity over the ocean, as well as observations of an increasing number of other ocean variables. Argo consists of almost 4000 profiling floats distributed globally over the open ocean. Since 2005, Argo provides regular measurements of temperature and salinity with a typical sampling cycle every ten days of profiles from near the surface (typically 5 to 10 m depth) down to 2000 m. The spatial resolution is about 3 degrees, roughly corresponding to a profile every 300 km [*Ninove et al.*, 2016; *Roemmich et al.*, 2009]. Compared to other in situ observations (i.e. ship based measurements, gliders, moorings), Argo provides broader spatial and temporal resolution.

The accuracies of the temperature, salinity and pressure sensors mounted on Argo platforms are reported as ±0.005˚C, ±0.01 psu and ±2.4 dbar respectively (Argo Quality Control Manual, 2011). Each sensor is subject to different quality control checks. These checks considered all Argo floats available worldwide from 2005 to 2015. The data were subject to real-time and delayed-mode quality control checks to ensure that all the data were classified as 'good' (i.e. QC = 1, see Argo Quality Control Manual, 2011). The process of quality control of the delayed mode can take up to eighteen months from the moment when the profile was recorded. This processing time depends on the Global Data Assembly Centres (GDACs) and ensures the best quality of the data for analysis after any sensor drift adjustment needed have been applied (Wong, et al 2011). Furthermore, following the recommendations in the Argo User Manual, floats were checked against the so-called 'grey list' (downloaded on 19th February 2016) [*Carval et al.*, 2015]. Floats included in this list were not included in the analysis, as they have been reported to have problems in one of the sensors during the real time quality checks (e.g. drift). Argo data is freely available at the GDAC Ifremer (GDAC; ftp://ftp.ifremer.fr/ifremer/argo/). Data were downloaded from GDAC on 23th December 2015.

Table 1 Quality control checks for all the Argo floats included in this study. The parameters of interest are Temperature, Salinity and Pressure.

Terms	**Criteria**
QC flag	QC = 1; keep 'good' data only
Argo Grey list	Platforms ID number were not in the grey list (download 19th February 2016)
Profiles	Both temperature and salinity
Missing value at a given level	Exclude all parameters at the same level
Negative pressure value	Exclude all parameters at the same level

In addition to standard quality control checks, the Argo data used in this thesis had to pass an additional control check to make sure that all data were 'OK', meaning that all the platforms were providing information on the three parameters with equal quality (Table 2). Some floats provided no information for one of the three sensors (e.g. temperature and pressure data available but missing salinity). Other floats (i.e. APEX) showed negative values in pressure sensors, which can be related to a micro leak fault in the pressure pump (see Argo data management 2011). Following Feistel (2010), for each profile passing the quality control checks, the potential density was calculated at each level using the Thermodynamic Equation Of Seawater 2010 (TEOS10). The resulting Argo profiles dataset was gridded to a homogeneous ½˚ horizontal grid and the depths were approximated to standard depth levels from surface down to 400 m in 5 m depth intervals.

In addition to these QC checks, this thesis applied additional threshold checks to identify *suspicious bad* floats as follow:

- Temperature and salinity differences at a given depth between two consecutive profiles of the same float were not larger than 10˚C and 2 psu respectively.
- Distance between two consecutive profiles of the same float was not larger than 20 km.

Those platforms labelled as *suspicious bad* floats were not immediately rejected, but instead were inspected manually (i.e. plots of T and S, contrasting results against Argo visual website JCOMM). In some cases, floats failed to pass the quality control checks not because of a technical fault, but because the float was operating over regions of very rapid ocean variability, e.g. river outflows and extreme wind induced upwellings, in which case the data were retained.

3.6 Forecast Ocean Assimilation Model data output (FOAM)

3.6.1 System description

The Forecast Ocean Assimilation Model (FOAM) system version 12 is an operational ocean analysis and forecast system run daily at the United Kingdom Meteorological Office (UK Met Office or UKMO), which produces analyses and forecasts of ocean state, ocean currents and tracers *(Storkey et al.*, 2010). This model is sometimes known as FOAM-NEMO because, since 2008, the hydrodynamic model component of FOAM is the Nucleus for European Modelling of the Ocean (NEMO) primitive equation ocean model [*Madec and Imbard*, 1996; *M. J. Martin et al.*, 2007]. The system also includes coupling to the sea ice model, LIM2 *(Blockley et al.*, 2012).

The FOAM configuration used here is based on ORCA025. This has a latitude-longitude grid with a spatial resolution of ¼˚ or ~28 km near the equator, reducing to ~6 km at high latitudes. This configuration has 50 vertical levels with 1 m resolution near the surface (i.e. depth from 0-10 m) and becomes increasingly coarser at deeper levels. The vertical mixing uses the turbulent kinetic energy (TKE), which is already embedded in NEMO [*Blanke and Delecluse*, 1993]. There is a prognostic equation for TKE and a diagnostic equation for the turbulent mixing length based on the local stability profile. Convection is parameterised using an enhanced vertical diffusion. The model is forced at the surface by 6-hourly mean fluxes from the Met Office Numerical Weather Predication (NWP) model [*Storkey et al.*, 2010].

3.6.2 Data assimilation description

The data assimilation component of FOAM v12 is NEMOVAR. NEMOVAR is a multivariate, incremental 3D-Var, first guess at appropriate time (FGAT) data assimilation scheme that has been developed specifically for NEMO [*Blockley et al.*, 2014]. The horizontal background error correlation for temperature and salinity are based on the Rossby radius (Cummings, 2005). The vertical background error correlations are flow dependent and parameterised based on the mixed layer depth [*Waters et al.*, 2013].

FOAM is run daily, and produces 5-day forecasts of the ocean state, including 3D fields of temperature, salinity, pressure, and currents. The NEMOVAR system includes bias correction schemes for SST. This removes biases in SST data due to errors in the non-constant atmospheric constituents used in the retrieval algorithms by correcting data to a reference data set of assume

unbiased SST observations [*Donlon et al.*, 2012; *M. J. Martin et al.*, 2007; *Waters et al.*, 2013]. There are known systematic errors in the wind forcing near the Equator, which are counteracted by the addition of a correcting term to the subsurface pressure gradients in the tropics to improve the retention of temperature and salinity increments by the model [*Bell and Chelliah*, 2006].

3.6.3 Observations assimilated in FOAM

FOAM assimilates a large range of observations, including temperature and salinity profiles from Argo floats, ship-based conductivity-temperature-depth (CTD) sections and expendable bathythermograph (XBT) casts [*Matthew J. Martin*, 2016]. FOAM uses OSTIA SST analyses based on satellite data from the GHRSST project (see Section 2.3) [*Donlon et al.*, 2012].

All available observations in near real time (i.e. data with no post processing corrections) are assimilated using a 24-hour window. The subsurface temperature and salinity profiles are obtained from GTS (Global Telecommunications System) and include measurements taken by Argo floats, underwater gliders, moored buoys and marine mammals as well as manual profiling methods such as XBT and CTD. FOAM assimilates other ocean observations from satellites (e.g. sea surface height and sea ice thickness). Due to the sparseness of surface salinity data, the surface salinity forecast in FOAM is relaxed towards climatological estimates from EN3 monthly climatology [*Matthew J. Martin*, 2016]. For a full description of the data assimilation in FOAM, see for example [*Blockley et al.*, 2014; *M. J. Martin et al.*, 2007] and for a description of the EN3 climatology dataset see also the Met Office online resources (http://www.metoffice.gov.uk/hadobs/en3/).

FOAM is forced at the surface by analyses and forecasts of momentum, freshwater and heat from the Met Office NWP system. Surface fluxes are taken from the Met Office Numerical Weather Prediction global model (See Davies 2005). Freshwater inputs from rivers are modelled as surface freshwater fluxes, as described in [*Blockley et al.*, 2014]. Boundary conditions are also described in [*Blockley et al.*, 2014] and are not detailed here.

3.6.4 Mixed Layer Depth in FOAM system

The FOAM system provides a number of derived parameters, which are variables that are computed using other variables. One of these is the Mixed Layer Depth (MLD). The computation of the FOAM MLD is based on a threshold method of *Kara et al.* [2000], which uses thermal and density thresholds of 0.8˚C and 0.03 kg m^{-3} respectively. This thermal threshold is considerably larger than the 0.2˚C used in this thesis. The lower thermal threshold used in this thesis seems to better capture

MLD in regions where there is a salinity compensation effect, e.g. River outflow regions [*Hosoda et al.*, 2010].

Chapter 4

Composite Tropical Cyclone Footprint Method

This chapter introduces the Composite Tropical Cyclone Footprint (CTCFP), which is a new methodology to create a global representation of the TC induced changes in both temperature and salinity. The development of this methodology relates to the first objective (or research question) of this thesis (Chapter 1), which was to design a method to increase the number of observations of TC-induced ocean response using either in situ observations or model data. The CTCFP is based on the Lagrangian TC-induced SST response proposed by [*I D Lloyd and Vecchi*, 2011]. Furthermore, the method builds on [*Park et al.*, 2011], which was the first attempt of using Argo data in an objective and systematic method including all the available floats operating within a TC distance range. The original script to compute the CTCFP was written using MATLAB and the reader might find it at the end of this thesis (Appendix A). Additionally, working scripts will be available online upon the acceptance and publication of this thesis.

The layout of this chapter is as follow: Section 4.1 is an explanation of the need to design the CTCFP; Section 4.2 provides a summary of the pairing sampling process to compute the average the TC-induced ocean response; Section 4.3 introduces the concepts of ocean conditions before, during and after the TC passage; and finally Section 4.4 is a summary of using CTCFP.

4.1 Foundations of the CTCFP

The rationale for creating the CTCFP is the need to objectively quantify changes in the upper ocean induced by an extreme and rapidly moving TC, despite generally poor data availability, either due to sampling issues or concerns over representativeness or accuracy. A new composite method should provide the means to collate information from single or multiple events, independently of the nature of the data (i.e. satellite, in situ or model data). Ideally, the method should ultimately allow results from different data sources to be combined (e.g. combine Argo, mooring and satellite observations), however, this aspect is beyond the scope of this thesis.

Argo temperature (T) and salinity (S) profiles have been used in a number of past studies to examine TC-induced ocean changes in T and S [*Grodsky et al.*, 2012; *Reul et al.*, 2014]. In some cases, other in situ observations such as glider surveys [*Domingues et al.*, 2015; *Mrvaljevic et al.*, 2013] or mooring arrays [*Han Zhang et al.*, 2016] have also been used, when those were available near the track of a passing storm. However, the scope of these past studies tended to be limited: 1) by focussing on a very small number of observations; 2) by considering only a small number of storms, or even more typically, just part of the track of one storm; and/or 3) by sampling a limited range of upper ocean stratification conditions. The new CTCFP method should provide the means to address these concerns.

In contrast, numerical model simulations provide extended, uniform and gap-free datasets, which have been used extensively to study the TC induced ocean response, also providing the main insight into the spatial characteristics of the TC impact along and across TC tracks [*Jullien et al.*, 2012; *Emmanuel M. Vincent et al.*, 2012]. However, one has to bear in mind that numerical models are only a representation of the understanding of the mechanisms and processes taking place in nature, which in turn is largely limited by the capacity of observing these events and their impacts. Thus, observations and model-based studies are inter-related, even though sometimes progress does not happen in parallel [*Schade and Emanuel*, 1999]. For example, the ocean surface cooling in the wake of a storm was first observed in 1950 using mooring arrays, and then later using satellite data [*Stramma et al.*, 1986]. But it took more than 15 years to recognise that the ocean surface cooling negatively related to the intensity of the storm, and only then did these physical processes start to get represented in numerical models, resulting in significant improvement in storm intensity forecasting [*Schade and Emanuel*, 1999]. This is why this thesis developed the CTCFP to be used on both in situ and satellite observations and output from the FOAM system, and to allow us to examine differences between TC induced ocean response observed from in situ data and model simulations.

I D Lloyd and Vecchi [2011] proposed a method to estimate the composite TC-induced ocean response by using SST data retrieved around the paths of different TCs events in the North Atlantic between 1998 to 2007. One known limitation of that method was that it considered only SST, and did not account for the subsurface components of temperature and salinity changes, which are known to be closely related to the TC-intensification. To date, there is no published method by which the TC-induced ocean response can be systematically assessed. The CTCFP method presented in this chapter builds on the method presented in *I D Lloyd and Vecchi* [2011] to develop an objective means to quantify ocean changes around the passage of TCs. The CTCFP method is tailored to the specific sampling characteristics of Argo data, before being used later in this thesis to study the ocean response observed with in situ data for specific TCs in the North Atlantic (Chapter 6), then in different oceanic basins (Chapter 7) and then applied to FOAM numerical data only (Chapter 8). Identified limitations of the method and recommendations for potential improvements are summarised in the final section of this chapter and in Chapter 9.

4.2 Pairing observations before and after TC

To properly observe TC induced changes at a given location in the ocean would require *Eulerian* observations (i.e. fixed *point*) to allow us to witness TC induced changes at a specific location over time. Given the complex and highly variable TC pathways and speeds throughout the sub-tropical ocean, it is not generally possible to obtain observations that cover the spatial likelihood of TC occurrences. The work in this thesis uses Argo floats as an alternative to other in situ observations available at all times even during TC conditions. Argo floats provide Lagrangian in situ observations, as they drift freely with the horizontal ocean circulation (see Chapter 3, Section 3.5). Argo floats provide a worldwide view of the upper ocean structure (top 2000 m) of the open ocean that is generally independent of the local weather conditions. The CTCFP is designed to assemble Lagrangian observations of Argo to provide Eulerian viewpoints at various locations of TCs. Argo data are selected according to the Quality Control (QC) method described in Chapter 3.

The TC induced ocean response is computed from the difference in the ocean conditions *after* minus *before* the passage of the TC. Notice that the term “ocean conditions” refers to the profiles of temperature (T) and salinity (S) obtained at each float sampling cycle. The pairing criteria used in this thesis were as follow:

1. Pairing profiles (i.e. measurements before and after) were from the same float (based on the identification platform number i.e. unique ID platform).

2. Profiles were separated by a distance of no more than 20 km (~0.2˚) from each other. This maximum distance threshold is selected as the maximum travelled distance between two Argo sampling cycles assuming high current transport as encountered in western boundary currents or within mesoscale eddies [*Cheng et al.*, 2015; *Shay*, 2009]. Ideally this distance would be as close to zero as possible, but this is not possible due to the drifting nature of Argo floats.

3. For ease of reference, time (t) was referenced against the time, t_0, of the passage of the storm at that point, with t_0 = 0 days. Thus, time before TC is negative (t < 0) and time after TC is positive (t > 0).

4. The pre-storm (or pre-TC) ocean conditions were defined as the average conditions calculated over $t_{BEF'}$ = [-13:-3] days. The choice of the upper temporal limit (t = -3 days) accounts for the fact that an ocean location can start to respond to the storm 2 to 3 days before the passage of the storm [*I D Lloyd and Vecchi*, 2011; *E. M. Vincent et al.*, 2012]. The lower temporal limit (t = -13) relates to the temporal resolution of the Argo cycling (i.e. 10 day cycle).

5. Data were checked for any TC activity in the days preceding the t_{BEF} period of interest, to exclude Argo observations that may have been affected by any previous TCs. There are a number of historical cases where successive TCs followed similar pathways within a few weeks of each other. It is estimated also that TC induced changes in SST can continue for up to 20 days after the passage of a TC [*I D Lloyd and Vecchi*, 2011]. Thus, the method in this thesis established that pre-storm ocean conditions were not affected by any TC during the previous 30 days.

6. The post-storm oceanic conditions were computed for each profile from day 0 to day 30 after the passage of the storm. Although TC-induced surface cooling may last more than 50 days, it takes on average between 20 to 30 days for the ocean to return to pre-storm values [*I D Lloyd and Vecchi*, 2011]. Using a longer time window would risk producing a weaker TC-induced signal that becomes increasingly difficult to separate from background ocean variability (e.g. mesoscale eddies, high variability boundary currents).

7. Pre- and post-storm conditions were estimated based on all profiles operating within a given search radius from the TC-location. The typical value used in this thesis is R_{max} = 400 km, a choice made on the basis of results from model simulations showing that TC-induced surface cooling occurs over a swath 200 to 400 km wide.

4.2.1 Choice of search radius, Rmax

The choice of R_{max} around the TC is important and the value cannot be simply boundless to just maximise the number of in situ observations at each TC-location. Thus, in cases where the search radius is larger than the storm size, the method would include ocean observations that are not impacted by the passage of the storm. This would diminish the average oceanic response observed for small TCs. On the other hand, if the search radius is smaller than the storm size, this would omit observations from the outer regions of the storm. Also, as expected, the larger the search radius the higher the number of TC frequencies per grid cell. Figure 4–1 shows how the western and eastern Pacific present TC frequencies between 1 and 1.5 storms when using a 200 km radius, but 10 to 15 storms for 400 km radius in the same oceanic regions. In this thesis, a fixed search radius of 400 km is used, corresponding to a length scale that encompasses the most characteristic TC sizes [*Chavas et al.*, 2016; *I D Lloyd and Vecchi*, 2011] and the horizontal spatial resolution of the Argo network (1 profile per 300 km on average).

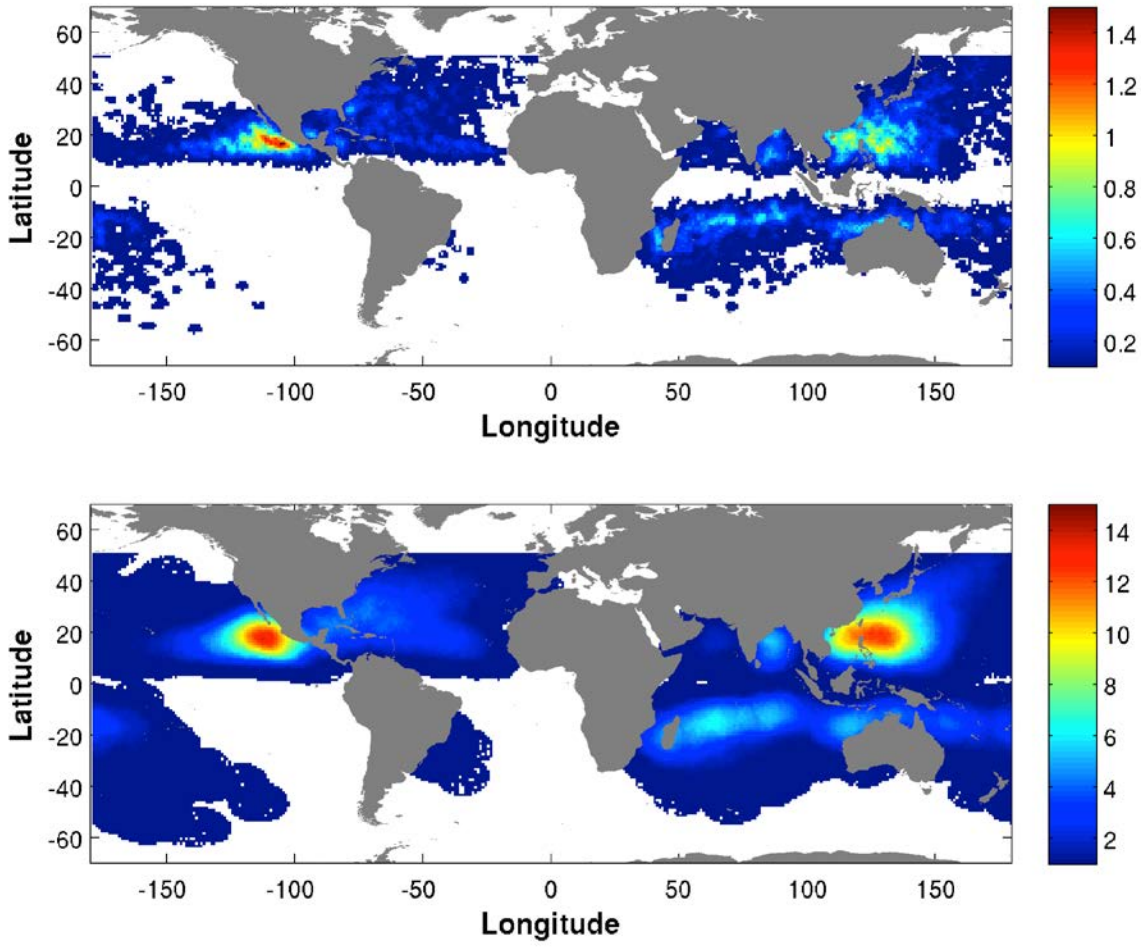

Figure 4-1 Number of TC reported during the period 2005 to 2014, at noon GMT that overlap with a search radius of 200 km (top) and 400 km (bottom) per 1˚x1˚ between 50˚N and 50˚S. Colour scale is average number of TC per year.

4.2.2 Composite ocean response

The CTCFP method systematically selects and pairs Argo profiles of temperature (T) and salinity (S) from the surface down to 400 m. The method then computes the TC-induced ocean response for each pair as the post- minus pre-storm difference at a particular location. The TC-induced changes of T and S in the water column are designated as dT and dS.

dT and dS can be calculated at any location along the track of any given storm (TC-loc_n, identified by TC-name, time, longitude and latitude) and depend mainly on the choice of search radius, R_{max}, measured from the centre of the storm on the track. Finally, if a given location features N_{obs} observations (pairs of Argo profiles), the composite CTCFP ocean anomaly A (for T or S) is computed as:

$$A_T = \sum_{n=1}^{n=N_{obs}} \frac{dT}{n} \text{ and } A_S = \sum_{n=1}^{n=N_{obs}} \frac{dS}{n}$$

The CTCFP makes it possible to compute the composite ocean response also across different TC-locations, for example to identify dependencies of the ocean response on various characteristics of the TC (e.g. wind speed, translational speed, size) and the pre-storm upper ocean structure (i.e. MLD and BLT).

4.2.3 Spatial representation of CTCFP Argo pairing at a given TC-location

To illustrate the method, Figure 4–2 shows the locations of Argo profiles along the track of TC-Katia in September 2011 in the North Atlantic (Figure 4–2 a). At a given TC-location (e.g. TC-loc_5 at 12-noon GMT on 1st September 2011), there were 23 Argo profiles with 400km of the TC centre on the track (Figure 4–2 b). The locations of the Argo profiles relative to the TC centre can be standardized by converting them into a common TC-centric reference grid (Figure 4–2 c) along across- and along-track distances D_x and D_y. These distances were computed using the heading (translational direction) of the storm and serve to position the Argo profiles in four quadrants relative to the TC reference frame. Thus, counting anti-clockwise from the front-right quadrant, Q1, we have Q2, Q3 and Q4 corresponding to front-left, back-left and back-right relative to the centre of the TC. To test the TCFP method, this thesis focussed on studying the TC induced changes across-track under the assumption of the TC induced thermal rightward changes [*Price*, 1981]. Across-track changes in the following chapters, were computed as the averages of all profiles along the x-axis (Figure 4-3 a, blue lines) at each depth level. This average TC induced ocean response provides information to the right and to left of the storm. The along track averages (Figure 4-3 a, red lines) would give information to the front and to rear quadrant of the storm.

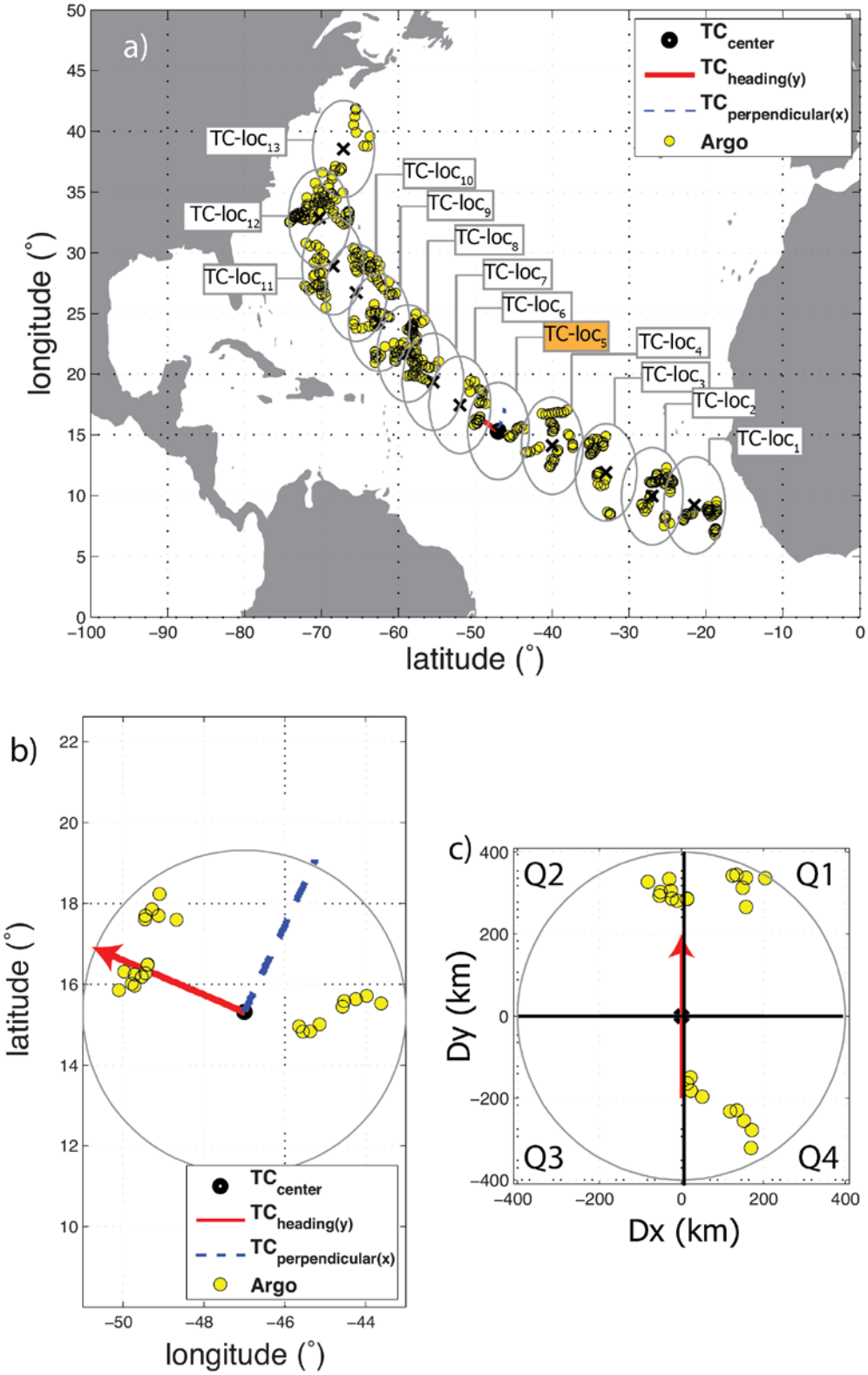

Figure 4-2 Argo profiles within 400 km of the TC centre at 13 locations (TC-loc$_1$ to TC-loc$_{13}$) along the path of TC-Katia in September 2011 in the North Atlantic; b) Detail of Argo data available at TC-loc$_5$ (12-noon GMT on 1st September 2011); and c) same as in b) but shown in a TC-centric cartesian reference frame. The red arrow indicates the TC heading (and direction perpendicular to the heading as blue broken line).

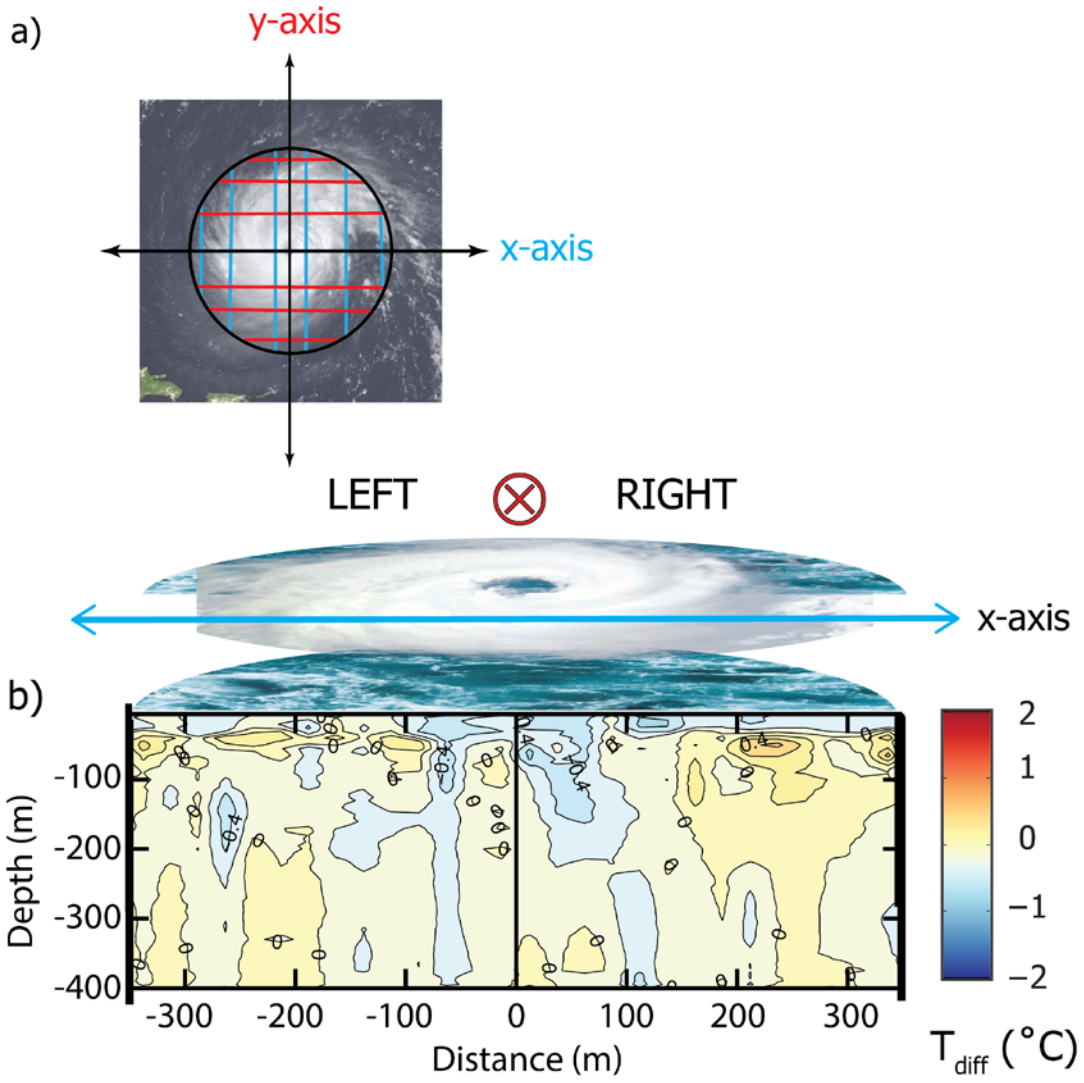

Figure 4-3 (a) View from the top of a TC with the x (blue) and y (red) axis centred at the eye of the storm; (b) Cartoon representation of a TC over a cross section ocean thermal structure computed as averaging all temperature profiles underneath the storm. Notice that the TC forward direction goes into the plane of the drawing (circle with an inscribed X) and divides the plane to the right (x > 0 km) and to the left (x < 0 km) section of the storm.

4.3 Detecting TC-induced ocean response against the ocean background variability

As for the conversion of Argo positions into a TC-centric spatial reference system, the time of Argo profiles was similarly converted to be referenced relative to the time (t_0) of the passage of the storm over a given TC-location. The time when a TC is considered to directly impact a given location is taken to be 3 days, from about 2 days before to at least 1 day after the passage of the eye, i.e. t_0 = [-2, +1] days.

As discussed previously, analyses only proceed for locations where no TC activity was reported within a time period (t_{BEF}) of 30 days before the TC, so that:

$$t_{BEF} = [-35:-3] \text{ days}$$

The reference time (t_{ref}) used to estimate average pre-storm oceanic conditions corresponds to a fixed period of ten days just before the first signs of the storm:

$$t_{ref} = [-13:-3]$$

Similarly, the time period used to estimate average post-storm oceanic conditions is:

$$t_{AFT} = [+2:+60]$$

The pre-storm ocean conditions (A_{ref}) were computed using all the T and S profiles available within spatial (R_{max}) and temporal period (t_{ref}) at each TC-location. Similarly, the post-storm conditions (A_{AFT}) are computed using all the T and S profiles available within spatial (R_{max}) and temporal period (t_{AFT}). The TC-induced ocean changes (A_{diff}) are then computed as:

$$A_{diff} = A_{AFT} - A_{ref}$$

We note that the TC induced changes, $A_{diff,}$, are not exactly equivalent to the anomalies from the climatological mean, ΔA. Therefore, in general, $A_{diff} \neq \Delta A$. In following chapters, we refer to these quantities as A_{diff} and ΔA respectively.

The chosen values of R_{max}, t_{ref} and t_{AFT} contain implicit assumptions about the spatial and temporal scales of the ocean natural variability. It is assumed that the TC-induced ocean responses computed in this manner will be sufficiently strong to stand out against the natural variability of the ocean. Optimising these values is difficult as our knowledge of the ocean variability at these temporal (10-day or less) and spatial (3˚ by 3˚ or less) scales in different regions remains limited. It is possible that the natural ocean variability will mask the signature of all but the strongest TC-induced ocean

responses. Sensitivity tests for different values of R_{max}, t_{ref} and t_{AFT} could be carried out, but this was not possible within the limits of this thesis.

4.3.1 Estimating TC-induced ocean response against ocean background variability

The magnitude of the TC induced oceanic response varies regionally within the same basin. This is owing to factors affecting the ocean response, which are related to the background oceanic and atmospheric conditions. Whilst the locations of the observations (i.e. Argo profiles) pre-storm and post-storm are within the fixed search radius and within a maximum travelling distance, the Argo observations may also reflect some local ocean background variability that is unrelated to the TC, and which may ultimately mask the TC-induced ocean response. In this thesis, the background variability was removed from Argo profiles by subtracting the monthly climatological average in both T and S profiles, as obtained from the World Ocean Atlas 2013 (WOA13) dataset (see section 3.2). However, even though removing the climatological signal from the original profiles will mitigate some of the background variability, it is likely that some background variability will remain (i.e. there will be intraseasonal variability), and this should be taken it into account in the conclusions of this thesis. Furthermore it is worthwhile to note that removal of the climatology did not change significantly the final results. This is because this thesis is looking at TC induced changes between before after the passage of the storm.

In the following chapters, the background ocean variability is considered in greater detail, using also SST and SSS observations from satellites (Chapter 3, section 3.3 and section 3.4) that provide details of the ocean variability at greater spatial and temporal resolution (i.e. daily observations at 0.25˚ by 0.25˚) than is possible with the Argo *in situ* observations. Following on from the example shown in Figure 4–2, Figure 4–3 shows the maps of daily SST anomalies (ΔSST) in the North Atlantic for the example case of TC-Katia in September 2011. The figure shows a warm surface temperature anomaly (ΔSST ≥ 2˚C) in day d1 (28 August 2011) at location TC-loc_5, some 5 days before the passage of TC-Katia over that location. On the day when TC-Katia reached that same location (TC-loc_5 on 1st September 2011) the SST shows no anomaly at this location i.e. ΔSST ≈ 0˚C. Depending on the timing of the Argo profiles, the background ocean variability seen by the satellites may not be picked up by Argo.

As discussed, one way forward is to remove the local background variability from the Argo data before the computation of CTCFP. The monthly temperature and salinity climatology from WOA13 is one of the most comprehensive and reliable dataset available to remove some of the background variability in the Argo profiles. Figure 4–4 shows an example of removing the temperature

climatology from Argo temperature profiles. This method assumes that, after the monthly climatology is removed, the TC-induced changes are the biggest signal in the remaining variability. This might be one of the main limitations of the method as it is known that other important oceanic (e.g. eddies, ocean fronts, etc.) and atmospheric (e.g. thunderstorms, weather fronts, sea breezes, etc.) events can take place over periods shorter than a month , and may be masking TC-induced signals.

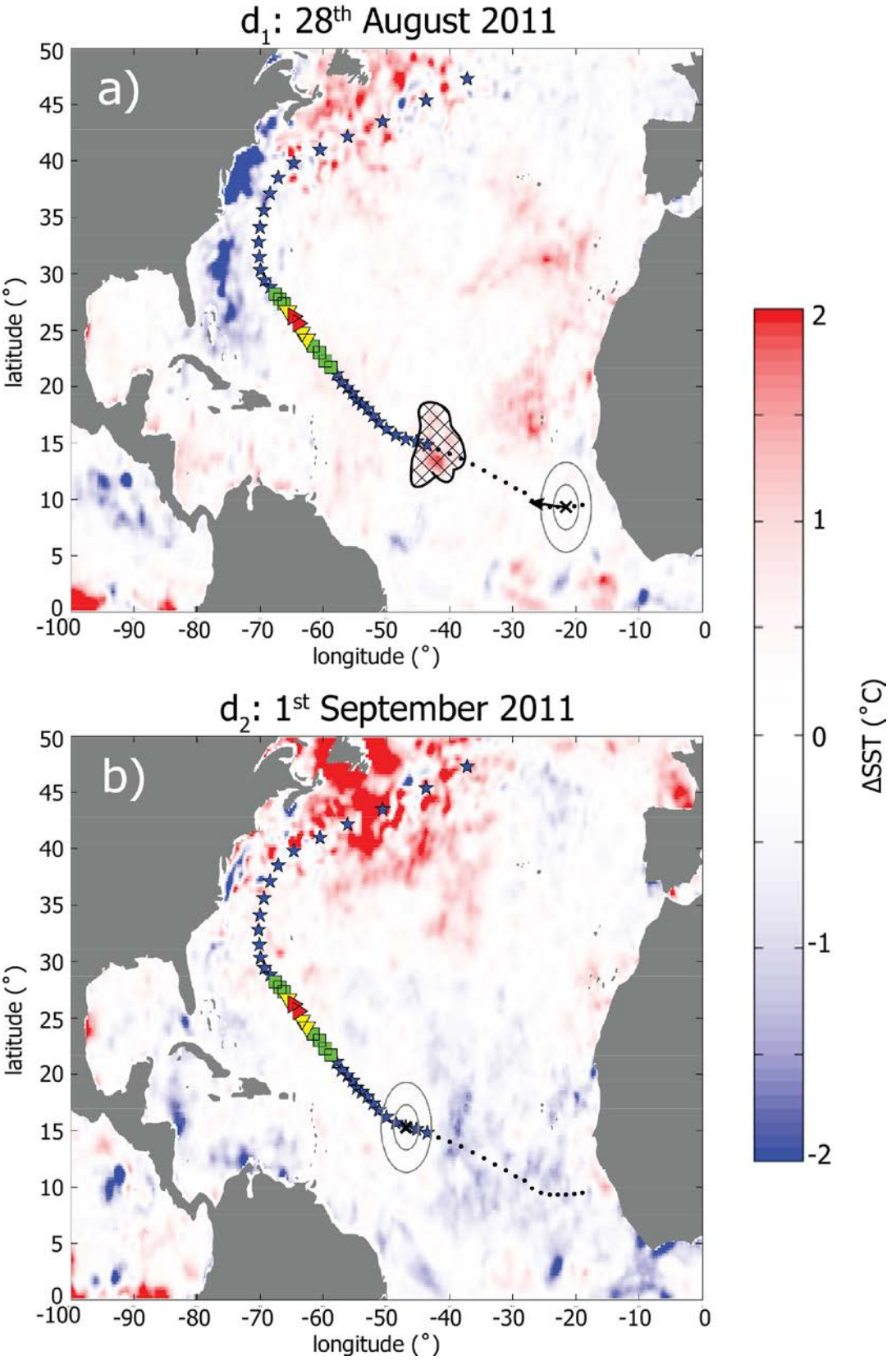

Figure 4-4 Daily ΔSST in the North Atlantic on a) 28th August 2011 (d_1) when TC-Katia was at TC-location TC-loc_1 (black circles) and b) 1st September 2011 (d_2) when TC-Katia reaches TC-loc_5 (black circles). On d1, a warm ΔSST is seen over TC-loc_5 (hatched area). Symbols along the track indicate storm intensity from tropical storm (dots) to TC-category 1 (blue stars), TC-category 2 (green squares), TC-category 3 (yellow inverted triangles) and TC-category 4 (red upright triangle).

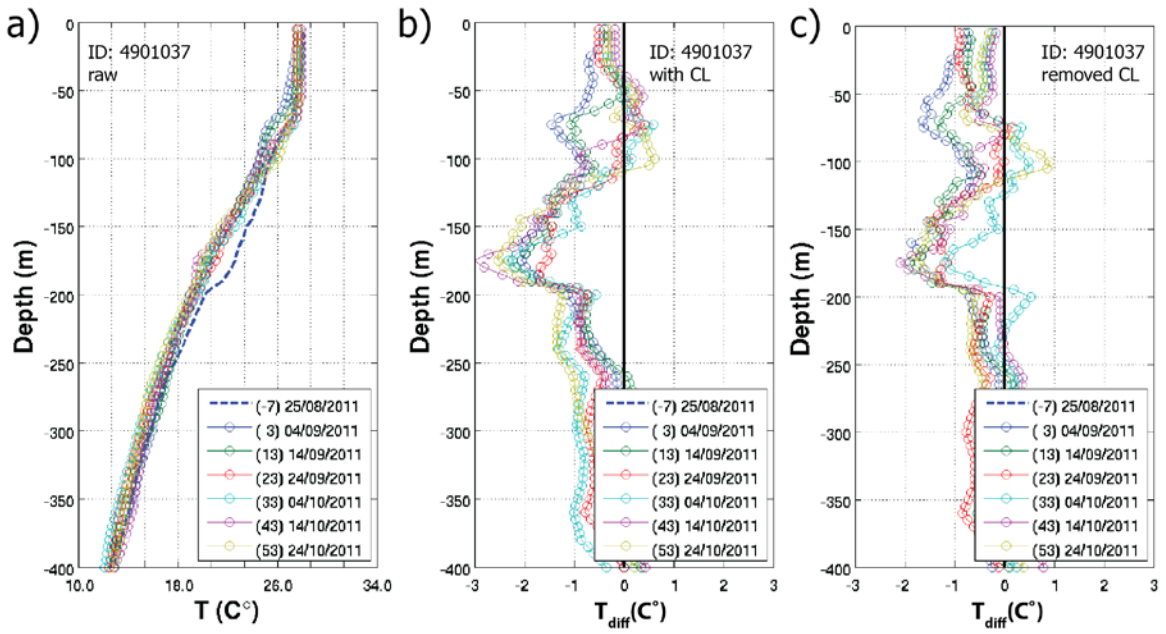

Figure 4-5 Example of background variability mitigation by removing climatology from Argo temperature profiles (0 to 400 m): a) Argo temperature profile raw; b) CTCFP response (Tdiff = TBEF-TAFT); and c) CTCFP response with climatology removed. All lines are from the same Argo platform (ID: 4901037) on different days before (-7 days, broken line) and after (circle-lines) Katia crosses over TC-loc5. The legend refers to Argo sampling time relative to t0 and the Argo sampling date.

4.4 Summary and limitations of the CTCFP method

This chapter introduced the rationale and development of the CTCFP method, a new approach which rests on the concept of objectively and systematically accumulating observations of the TC-induced ocean response for single or multiple TC events in TC-centric spatial and temporal reference frames. The method is designed to evaluate the ocean response for different TC events and locations, to determine the influence of different oceanic (i.e. temperature and salinity) and atmospheric conditions (i.e. TC wind speed and TC-size). This chapter also provided details about practical aspects related to pairing observations before and after the passage of the storm.

The work so far identified some limitations of the method and possible improvements, most notably relating to background ocean variability, which are described in more detail here.

4.4.1 Achieving better sampling with float to float measurement differences

The CTCFP method relies on pairing only measurements from the same Argo platform IDs as there might be differences between measurements from different floats (i.e. different instrumental errors or calibration). In this work, the pre- and post-storm temperature and salinity profiles were taken from the same Argo float. This criterion results in fewer observations than if all combinations of floats had been included. Multi-float pairing could significantly improve sampling but would

require extra care to ensure float-to-float consistency. This development should be investigated and implemented in any future working versions of the method.

4.4.2 Mitigating high-frequency ocean variability within days of the TC

Figure 4–3 showed that removing the WOA13 monthly climatology profiles from the Argo data can mitigate some of the natural variability that may otherwise mask the TC-induced ocean response. However, some natural variability will remain and will not be removed by averaging over the t_{ref} reference period (taken here as 10 days before the passage of the storm). As more and more data become available (e.g. from in situ sensors and satellites), it might become possible to develop and use daily climatologies. An attempt was made in this thesis to build daily in situ T and S climatology at various TC-locations, but due to lack of observations, this TC-climatology was not fully implemented. Further investigations would be needed to optimise the time window, but this should be revisited in future to implement more robust versions of the CTCFP.

Chapter 5

Ocean Natural Variability

5.1 Introduction

Quantifying TC induced changes is a complex activity due to variations in the background state of both T and S. As discussed in the previous chapter, these variations might be caused by processes such as the seasonal cycle, meso- and large-scale spatial variability. This chapter summarizes the natural variability in terms of SST, SSS, MLD and BLT in the North Atlantic, which is then used in Chapter 6 for the computation of the anomalies (ΔA, as seen in Chapter 4) in the same basin. Further in this thesis (Chapter 7), the CTCFP analysis is extended to other basins (i.e. North-East and North-West Pacific and North Indian Ocean), so the natural variability and the anomalies were computed as it is described in this chapter (i.e. plots not included).

The layout of this chapter comprises of two sections, which are: 5.2) North Atlantic Oceanic Natural Variability; and 5.3) North Atlantic Anomalies in 2011 and 2014

5.2 North Atlantic Oceanic Natural Variability

5.2.1 Sea Surface Temperature Natural Variability

The annual mean SST is determined by ocean to atmosphere heat exchanges, which are strongly governed by insolation heat input (i.e. solar energy), meridional currents and coastal upwelling

(Chapter 2). At the sea surface of the WOA13 dataset (depth ≈ 0 m), during the Summer/Autumn months in the North Hemisphere (June-October; Figure 5-1 a-d) there is a zonal climatological temperature variability, where the western side of the North Atlantic basin is warmer than the eastern side. The maximum seasonal temperature change occurs in a region centred in the Gulf of Mexico (25˚N, 90˚W) where seasonal SST increases gradually from 24.8˚C in June to 28.9˚C in August (Figure 5-1b). In October, surface temperatures start to cool down, which coincide with the decay of TC activity in this basin (Figure 5-1c). Monthly variability, measured as the standard deviation in temperature (T_{std}) is about 1˚C across the whole summer (Figure 5-2). The seasonal temperature variability peaks ($T_{std} \geq 2$˚C) northward from about 30˚N and in the northwest of the basin coincident with the western boundary current (i.e. Gulf Stream).

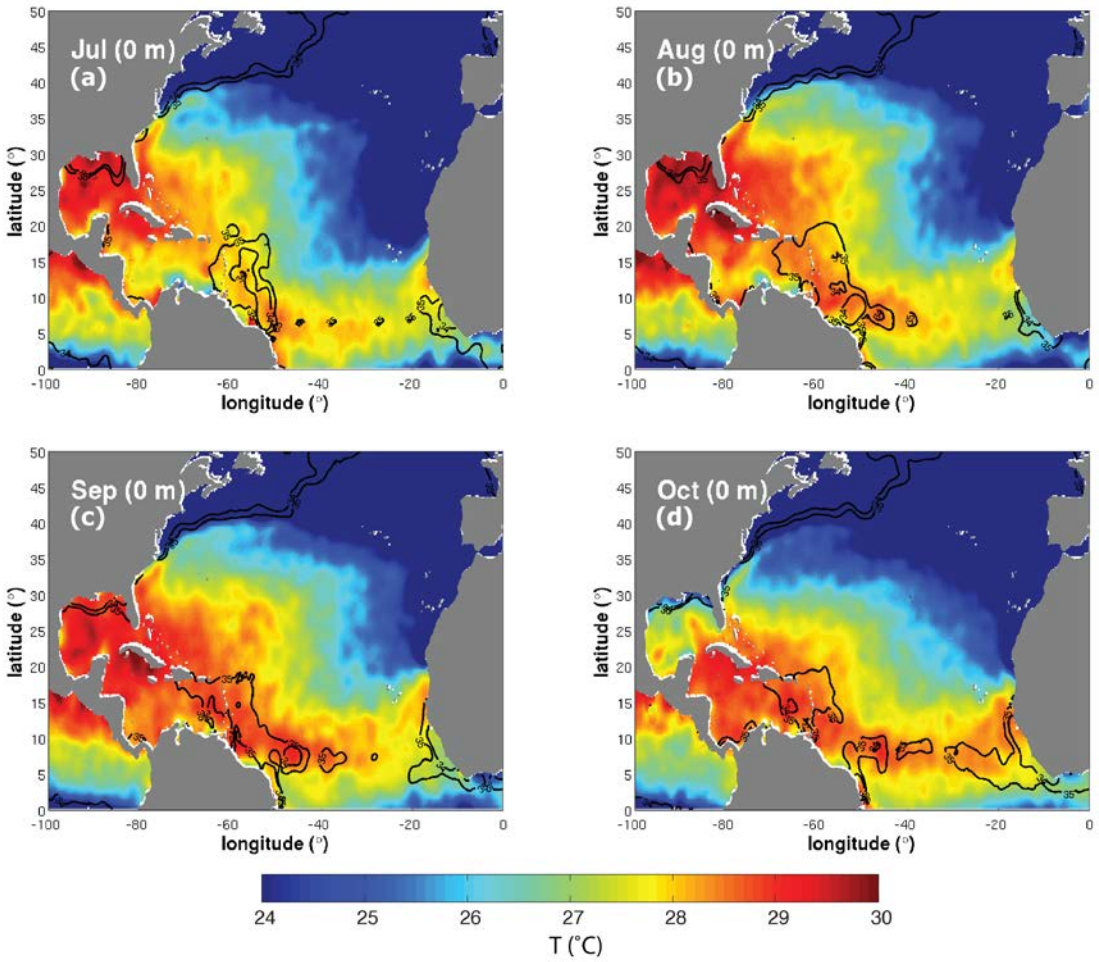

Figure 5-1 Historical (1955-2012) monthly temperature at the surface (0-1.5 m depth) during TC months (i.e. July to October). The seasonal extension of the Amazon-Orinoco plume can be seen as the black contour line in the southern half of the maps (line is the 35 psu boundary). Data source: WOA13v2 (https://www.nodc.noaa.gov/OC5/woa13/)

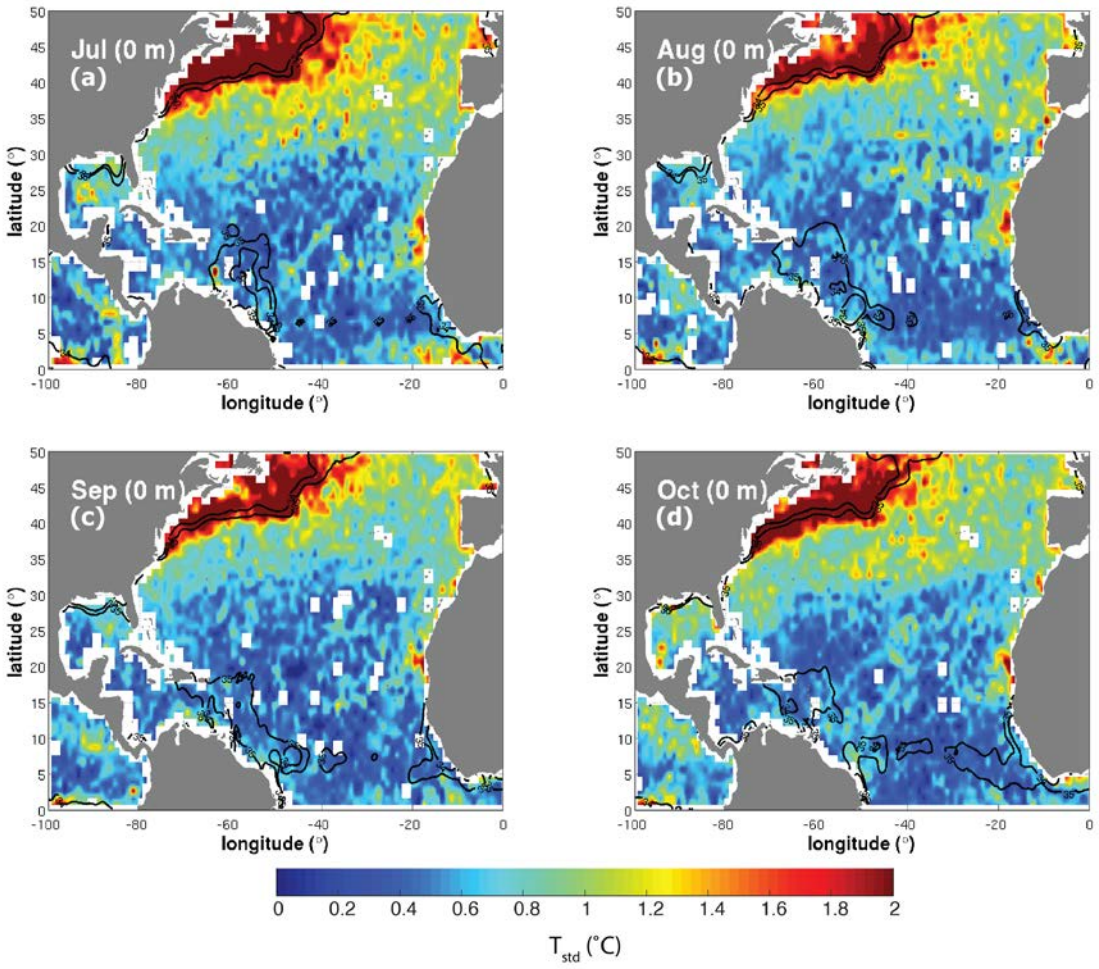

Figure 5-2 Historical (1955-2012) monthly temperature standard deviation at the surface (0-1.5 m depth) during TC months (i.e. July to October). The seasonal extension of the Amazon-Orinoco plume can be seen as the black contour line in the southern half of the maps (line is the 35 psu boundary). Data source: WOA13v2 (https://www.nodc.noaa.gov/OC5/woa13/). White squares are missing data within WOA13 dataset

5.2.2 Sea Surface Salinity Natural Variability

The seasonal natural variability in salinity within the study region (i.e. latitudes from 5˚ N to about 50˚N) is determined mainly by freshwater exchanges between the atmosphere and the ocean and river discharge. Sea Surface Salinity WOA13 (SSS-WOA13) data show (Figure 5-2), a persistent high salinity region ($S_{max} \geq 38$ psu) centred on the North Atlantic sub-tropical gyre (at ~25˚N, ~36˚W) which is associated with high evaporation rates and low precipitation [*J. Boutin et al.*, 2016; *Tim P. Boyer and Levitus*, 2002]. There are lower salinity regions ($S \leq 36$ psu) associated with persistent westerly winds northward of the salinity high (latitude ≥ 30˚N) and with the high rainfall in the Intertropical convergence zone (ITCZ) at ~5˚N. In addition, there is high river runoff from the Amazon and the Orinoco rivers, which develop a fresh surface tongue ($S \leq 35$ psu) that extends

from west towards the east of the basin between latitudes 5˚ to 20˚ N (Figure 5-2). The extension of the plume has latitudinal and zonal variabilities that appear to be of importance for determining the strength of the stability of the water column on the western side of the basin [*Balaguru et al.*, 2012; *Grodsky et al.*, 2012; *Reul et al.*, 2014]. The seasonal latitudinal extension of the plume oscillates between 15˚N in July (Figure 5-2) and 20˚N in August (Figure 5-2 b). The zonal extension of the plume is minimum in July (Figure 5-2 a), when is mostly confined to the western side of the basin, and it reaches it is maximum in October (Figure 5-2 c), when it crosses the whole basin and joins the Orinoco fresh water plume. The monthly variability (Figure 5-4) measured as the standard deviation in salinity (S_{std}) is maximum within the region enclosed by the Amazon-Orinoco region where $S_{std} \approx 1$ psu. Excluding the latitudes north of 35˚N, the rest of the basin outside the boundaries of the Amazon-Orinoco plume surface salinity variability ranges between 0.05 psu and 0.1 psu.

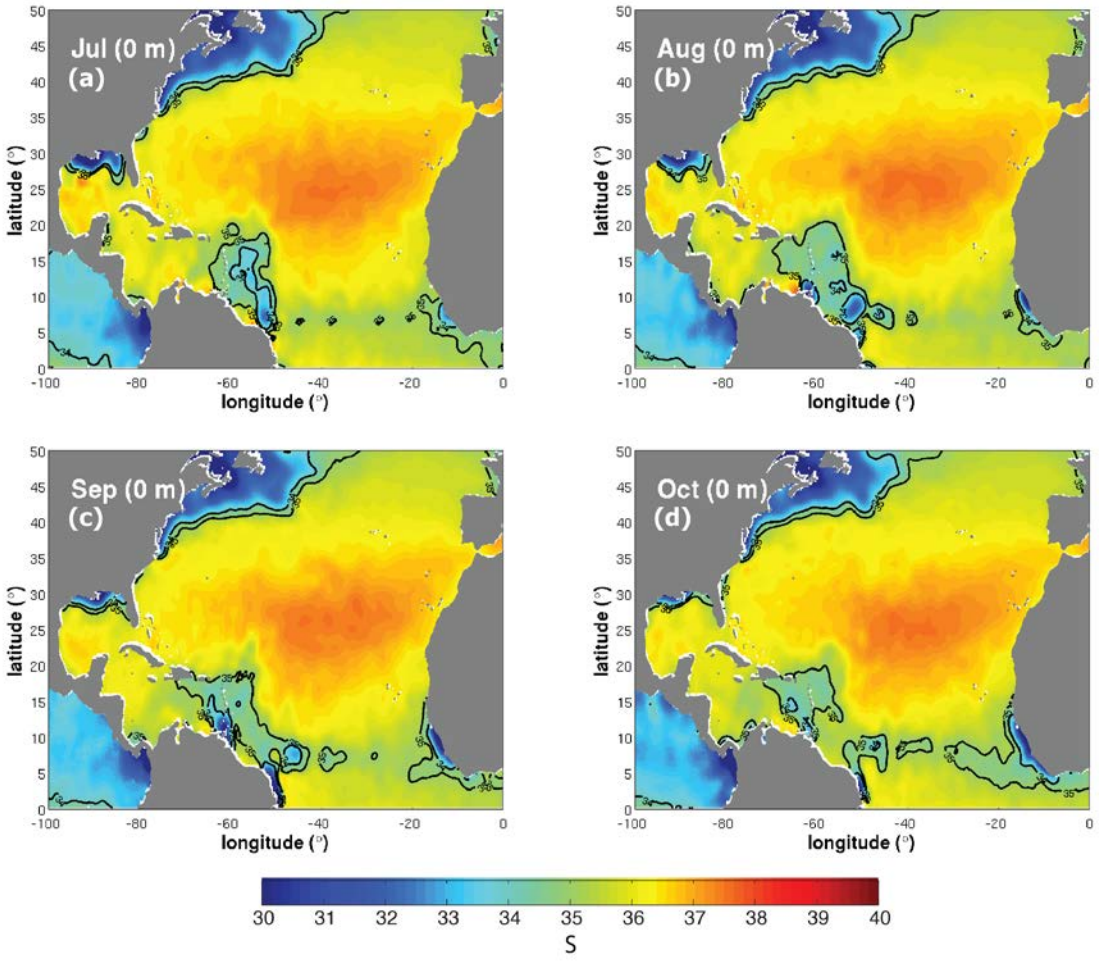

Figure 5-3 Historical (1955 – 2012) Salinity seasonal variability at the sea surface (0-1.5 m depth) during TC months (i.e. July to October). The seasonal extension of the Amazon-Orinoco plume (black 35 psu contour line). Data source: WOA13v2 (https://www.nodc.noaa.gov/OC5/woa13/).

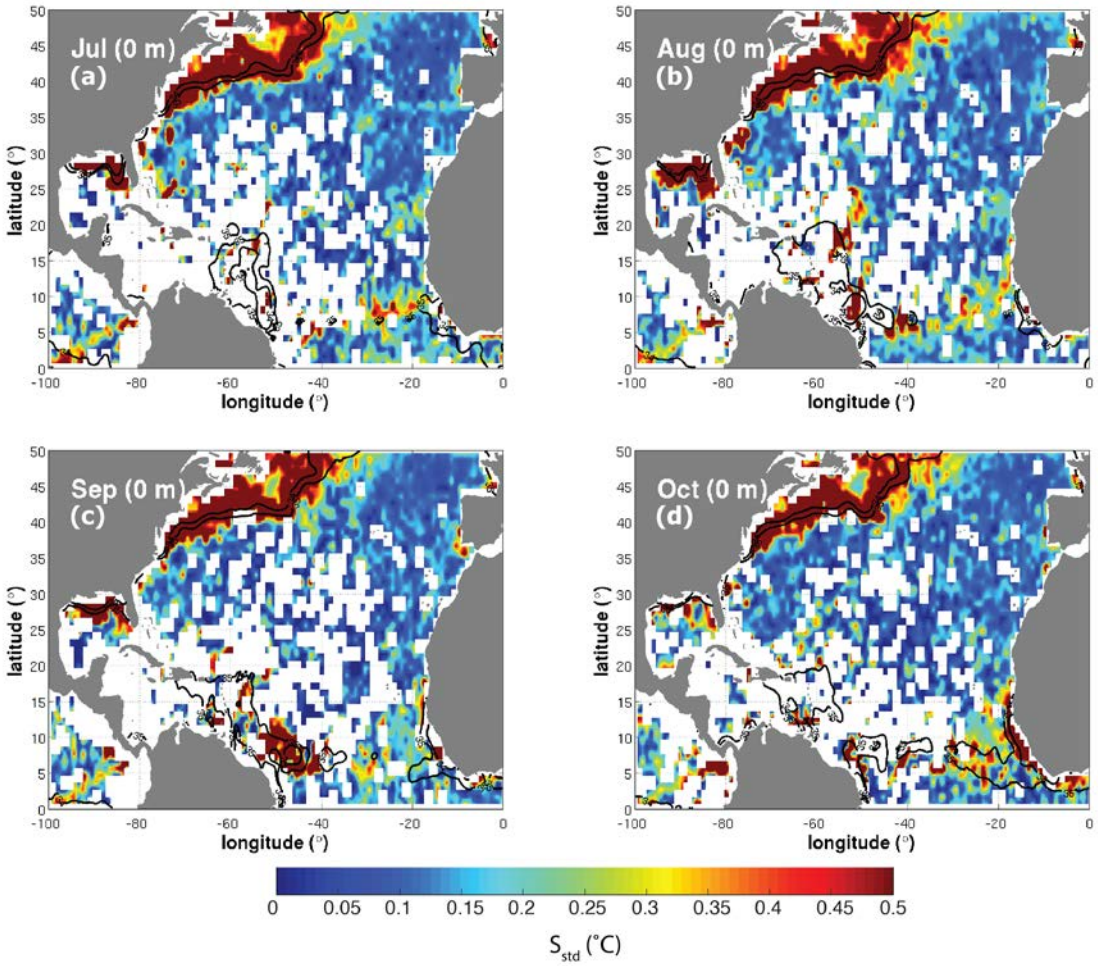

Figure 5-4 Historical (1955 – 2012) Salinity standard deviation seasonal variability at the sea surface (0-1.5 m depth) during TC months (i.e. July to October). The seasonal extension of the Amazon-Orinoco plume (black 35 psu contour line). Data source: WOA13v2 (https://www.nodc.noaa.gov/OC5/woa13/). White squares are missing data within WOA13 dataset.

5.2.3 Mixed Layer Depth and the Barrier Layer

During winter months (not shown) the predominant heat flux is from the ocean to the atmosphere due to atmospheric storm processes (i.e. rain and wind) inducing mixing and cooling of the ocean surface, which results in a weaker stratification and a deeper MLD. During summer months as the heat flux reverses and the ocean warms at the surface, stratification increases and MLD shallows (Figure 5-3). There is a large spread in both spatial and temporal natural variability of the MLD [*Tim P. Boyer and Levitus*, 2002; *Kara*, 2003]. The MLD ranges from about 20 m pole-ward of 30˚N at the beginning of the TC season in June to more than 60 m at the end of the season for the same latitudes. There are two climatological MLD maximum values at the beginning of the season (Figure 5-3a). One of these climatological maxima (MLD_{max1}), extend basin-wide from 0˚ to about 5˚ N and is present during the whole TC season. The other MLD climatological maximum (MLD_{max2}) is located in the middle of the basin (15˚ - 25˚N; 50˚ - 30˚ E) and it has a large temporal variability, with an intermittent presence during the TC season. Thus MLD_{max2} is high ($MLD_{max2} > 35$ m) at the start and at the end of the TC season (June and October) and MLD_{max2} is low ($MLD_{max2} < 30$ m) during August-September. The temporal MLD variability is linked to surface processes (i.e. atmospheric induced surface forcing, lateral advection, internal waves), thus it ranges from diurnal to interannual variability (i.e. both seasonal and intra-seasonal variability).

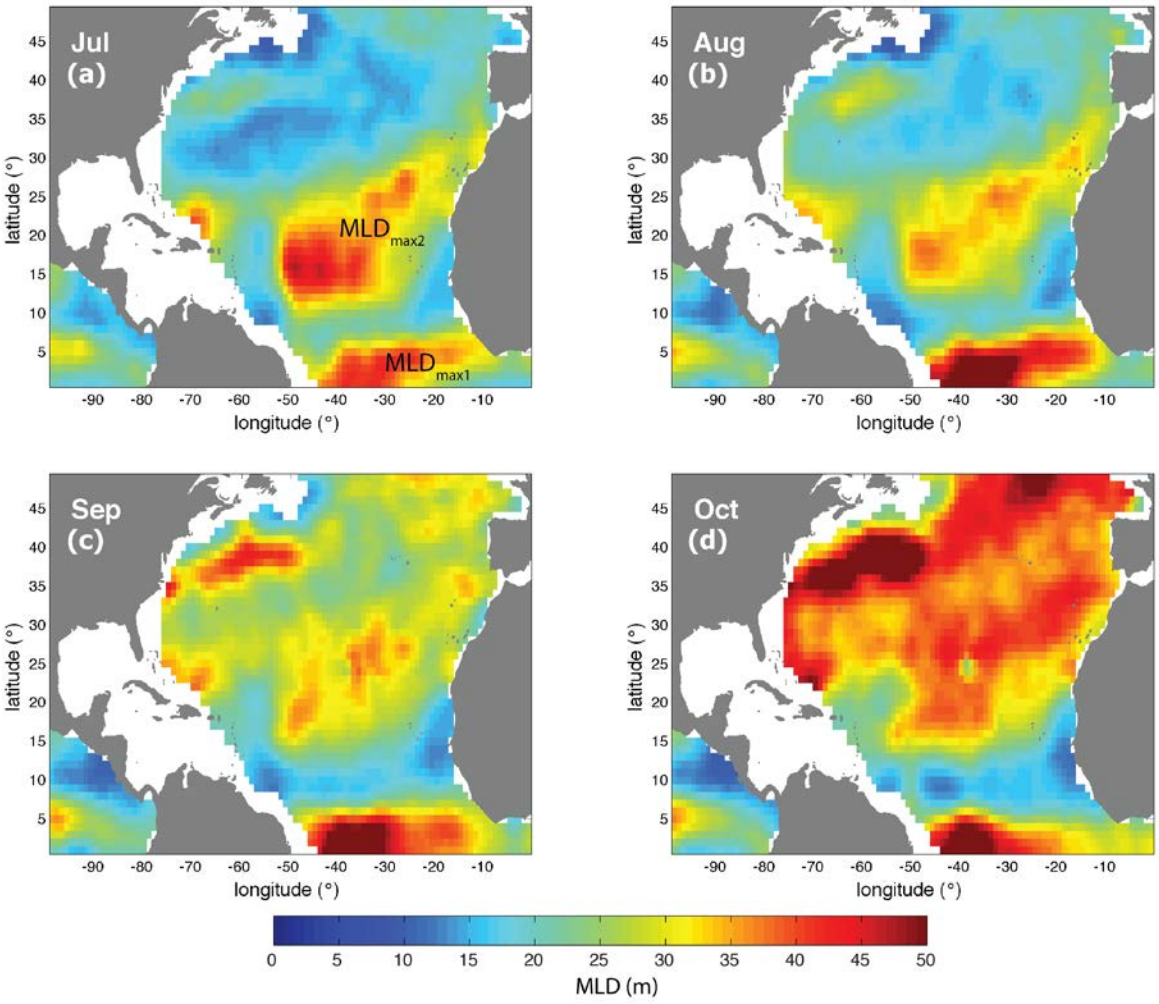

Figure 5-5 Mixed Layer Depth (MLD; m) monthly climatology in the North Atlantic as computed using Argo temperature and salinity profiles from 2005 to 2017 for a) July, b) August, c) September and d) October. As described in the main text, MLDmax1 and MLDmax2 in July are the two MLD climatological maximums. Missing data (white) in regions near the East coast of the American continent with no interpolation information (i.e. Argo profiles). Data source: http://apdrc.soest.hawaii.edu

The natural variability of the MLD is primarily controlled by the thermal structure of the ocean. In fact, 63% of the MLD natural variability is accounted for by changes in the isothermal depth compared with only 14% by isohaline depth changes [*Helber et al.*, 2012]. The remaining 23% of the MLD variability is from the combined contribution of the thermal and haline water column structure. For regions where there are high heat fluxes and low precipitation rates, temperature structure seems to dominate over haline configuration of the water column [*Helber et al.*, 2012; *Montegut et al.*, 2007]. Conversely, in regions with high precipitation rates and low heat fluxes, salinity changes within the water column, especially at the surface, and hence salinity is the dominant factor determining the configuration of the water column [*Helber et al.*, 2012]. In these

regions, the MLD is shallower than the isothermal layer depth (ILD) and the space between the two is known as the Barrier Layer Thickness or simply Barrier Layer (BLT or BL).

In the tropics there is a thick BL due to heavy precipitation, oceanic circulation, wind seasonality and river runoff. In the North Atlantic basin, there is a thick BL (BL ≥ 20 m) in the west linked to temperature inversions induced by the Amazon and the Orinoco River runoffs [*Mignot et al.*, 2007]. There is evidence of a link between the presence of BL and climate mechanism at different atmospheric scales [*Christophe Maes and O'Kane*, 2014; *Wyrtki*, 1981]. [*de Boyer Montégut*, 2004] used individual Argo profiles to build a global climatology of the MLD and BLT. The resulting MLD and BLT from individual profiles resulted in thicker structures than previous methodologies like [*Sprintall and Tomczak*, 1992] , which used gridded data. The Equatorial Current retroflection carries the Amazon fresh water across the basin at ~6˚N following currents of equal temperatures [*Pailler et al.*, 1999]. This would explain (Figure 5-4) the thicker BL at this latitude during the summer and autumn (July-August-September, JAS).

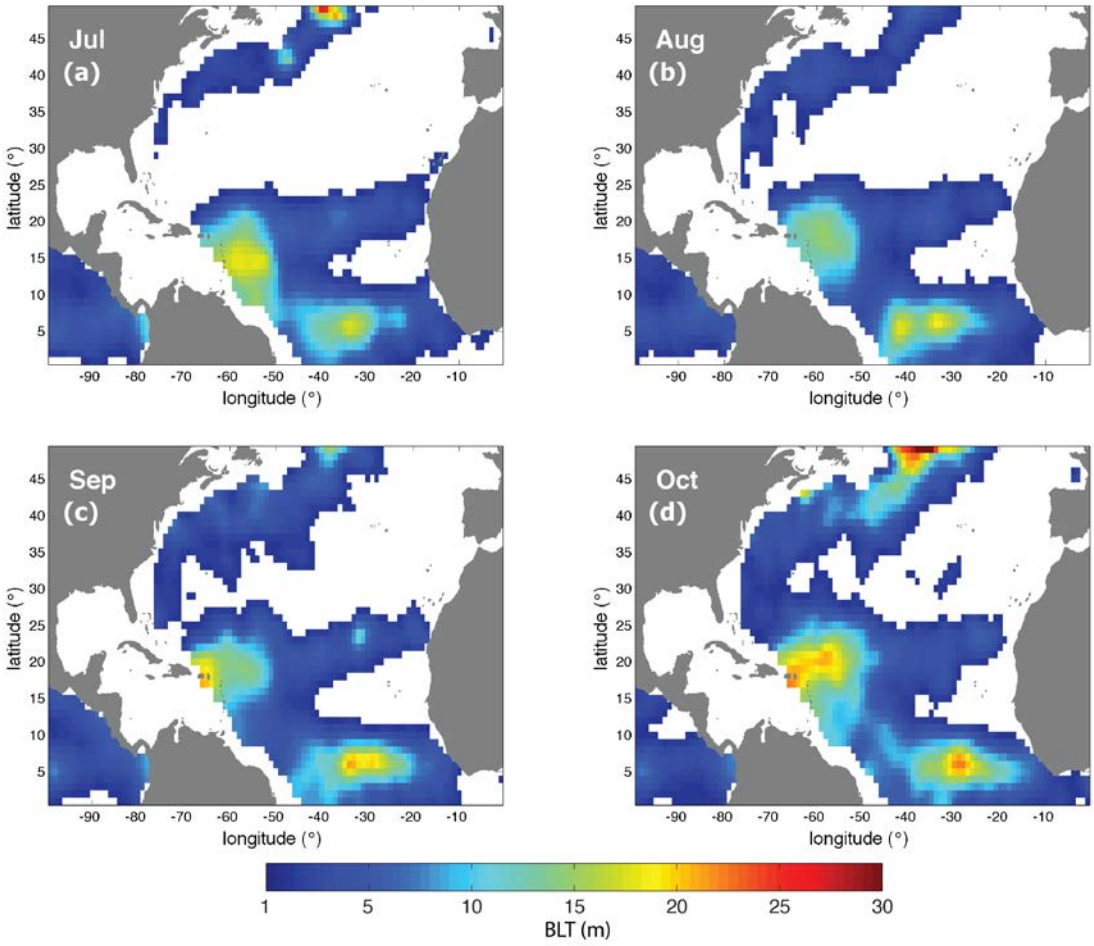

Figure 5-6 Barrier Layer Thickness (BLT, m) monthly climatology (TC season months) in the North Atlantic as computed using Argo temperature and salinity profiles from 2005 to 2017. Missing data (white) in regions near the East coast of the American continent with no interpolation information (i.e. Argo profiles). Data source http://apdrc.soest.hawaii.edu

5.3 North Atlantic Anomalies in 2011 and 2014

5.3.1 Sea Surface Temperature

The anomalies in SST (ΔSST) were computed by removing the WOA13 monthly climatology from the monthly averages of the daily SST for each year. The 2011 anomaly maps (Figure 5-5 left column) showed some cooling features (i.e. ΔSST < 0˚C) that were not seen in the 2014 anomaly maps (Figure 5-5 right column).

At the start of the storm season in July-August 2011 (Figure 5-5 a and c), the region of the Amazon-Orinoco plume region and its surroundings was over 1.5˚C warmer than the seasonal climatology. At the same time, on the northeast side of the basin there was a cold region feature centred at

29.4˚N, 27.4˚W with ΔSST < -1˚C, with an apparent v-shaped feature (Figure 5-5c). In September 2011 (Figure 5-5 e),there two cold features (ΔSST ≈ -1.8 ˚C) at both sides of the basin, outside of the boundaries of the Amazon-Orinoco plume region and the cold shaped feature at the north east of the basin disappeared.

The beginning of the 2014 season (Figure 5-5 b and d) saw a different geographical distribution of the relatively warm temperature described earlier for the 2011 season. Anomalies in SST were about zero (ΔSST ≈ 0˚C) within the Amazon-Orinoco plume region and its surroundings. In the northwest side of the basin there was a positive anomaly (ΔSST ≥ 2˚C) extending northeast from 25˚N (Figure 5-5).

5.3.2 Sea Surface Salinity

Figure 5-6 shows SSS anomalies (ΔSSS), which were computed as the average SSS in a month minus the climatological monthly salinity average (WOA13 salinity at the surface). Fresh salinity anomalies (ΔSSS < 0 psu) were confined within the Amazon-Orinoco plume region. The monthly latitudinal extent is similar between the two years analysed here. However, the zonal distribution showed some differences. In 2011, the Amazon-Orinoco plume region reached a basin wide extension from August to October (Figure 5-6 c, e and g), in the same months for 2014 (Figure 5-6 d, f and h) the fresh water tongue extent was not as well defined as it was in 2011 and only traversed the basin at the end of the season. This zonal distribution of the fresh water tongue in 2011 as seen from the monthly averages from SMOS-L4 data (Figure 5-6 , broken-magenta contour line) was different from the seasonal distribution measured using WOA13 salinity data (Figure 5-6 , bold-black contour line).

5.3.3 Mixed Layer Depth and Barrier Layer Thickness

Following the methodology to obtain ΔSST and ΔSSS in 2011 and 2014, this section presents the Mixed Layer Depth anomalies (ΔMLD) and barrier layer thickness anomalies (ΔBLT) for the same years (see Figure 5-7 and Figure 5-8 respectively). The start of the 2011-season (Figure 5-7 a) saw a MLD (ΔMLD ≈ -10 m) and a thicker BLT (ΔBLT ≈ 15 m) within the Amazon-Orinoco region. Conversely, for the 2014 season whilst the MLD was deeper than climatology (ΔSST ≈ +5 m), the BLT was notably thinner (ΔBLT ≈ -15 m).

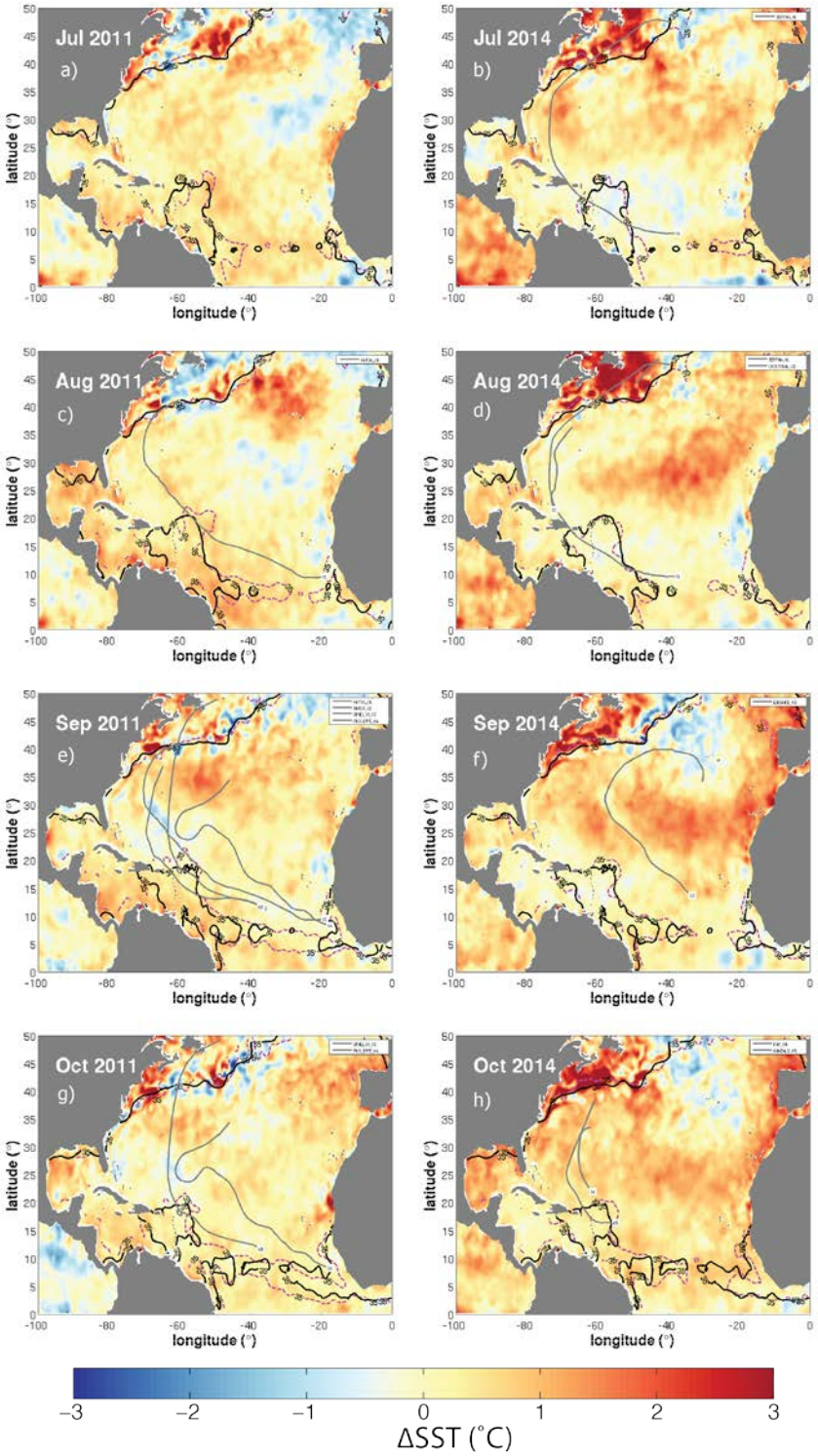

Figure 5-7 Sea Surface Temperature anomalies (ΔSST, in ˚C) during the TC-season months (July-October) in 2011 and in 2014. ΔSST as computed by taking the average SST in a month minus the surface temperature in WOA13 (0-1.5 m). The contour of 35 psu as seen in WOA13 (bold-black contour line) and in SMOS (broken-magenta contour line). TC activity within each month (bold-grey lines). Data source: GHRSST, http://www.ghrsst-pp.org and SMOS-L4 (CATDS, http://www.catds.fr)

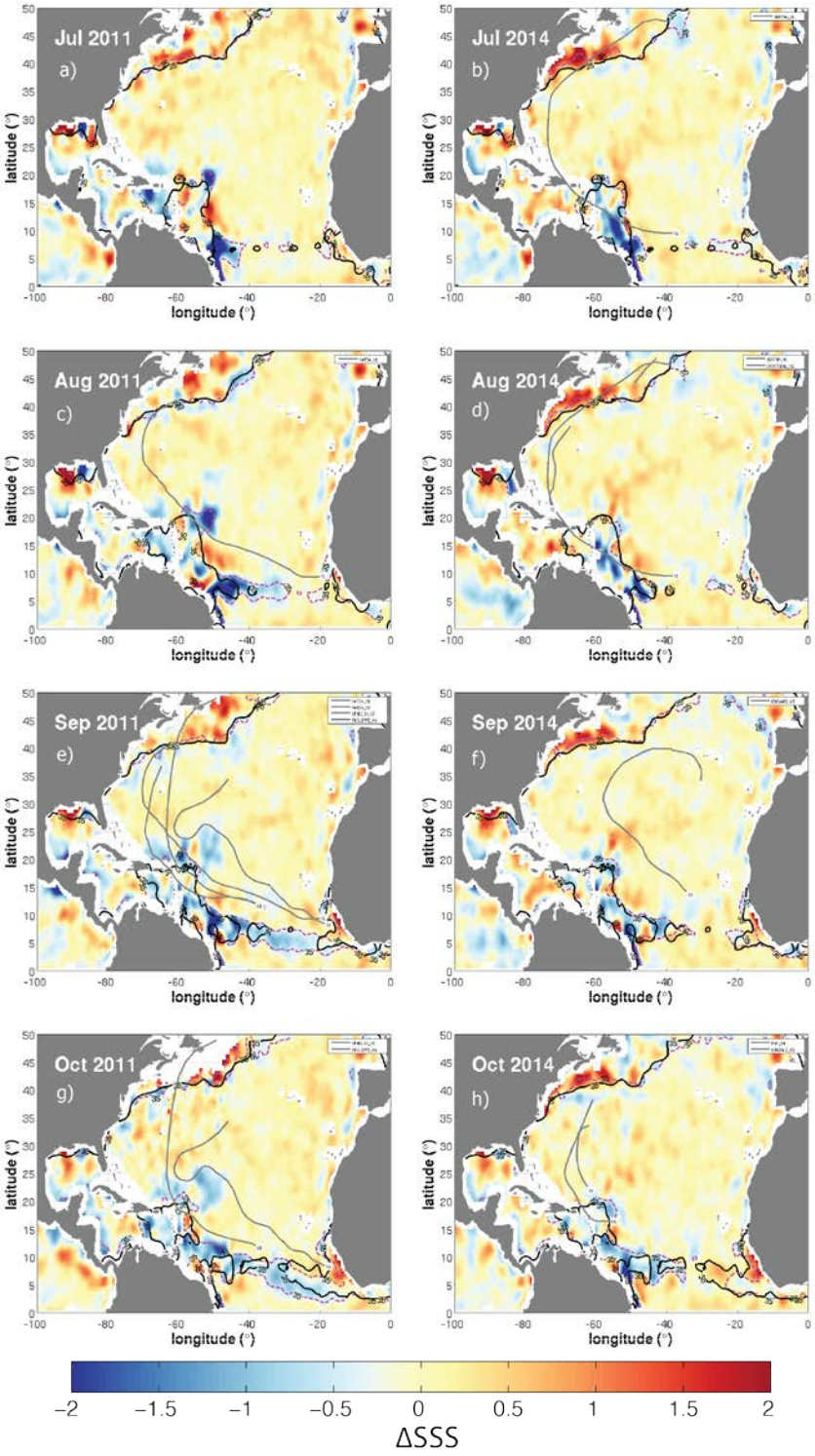

Figure 5-8 Sea surface salinity anomalies (ΔSSS, unitless) during the TC-season months (June-October) in 2011 and in 2014. Anomalies were as computed using the averages SSS in a month minus the surface salinity in WOA13 (0-1.5 m). The contour of 35 psu as seen in WOA13 (bold-black contour line) and in SMOS (broken-magenta contour line). TC activity within each month (bold-grey lines). Data source: SMOS-L4 (CATDS, http://www.catds.fr)

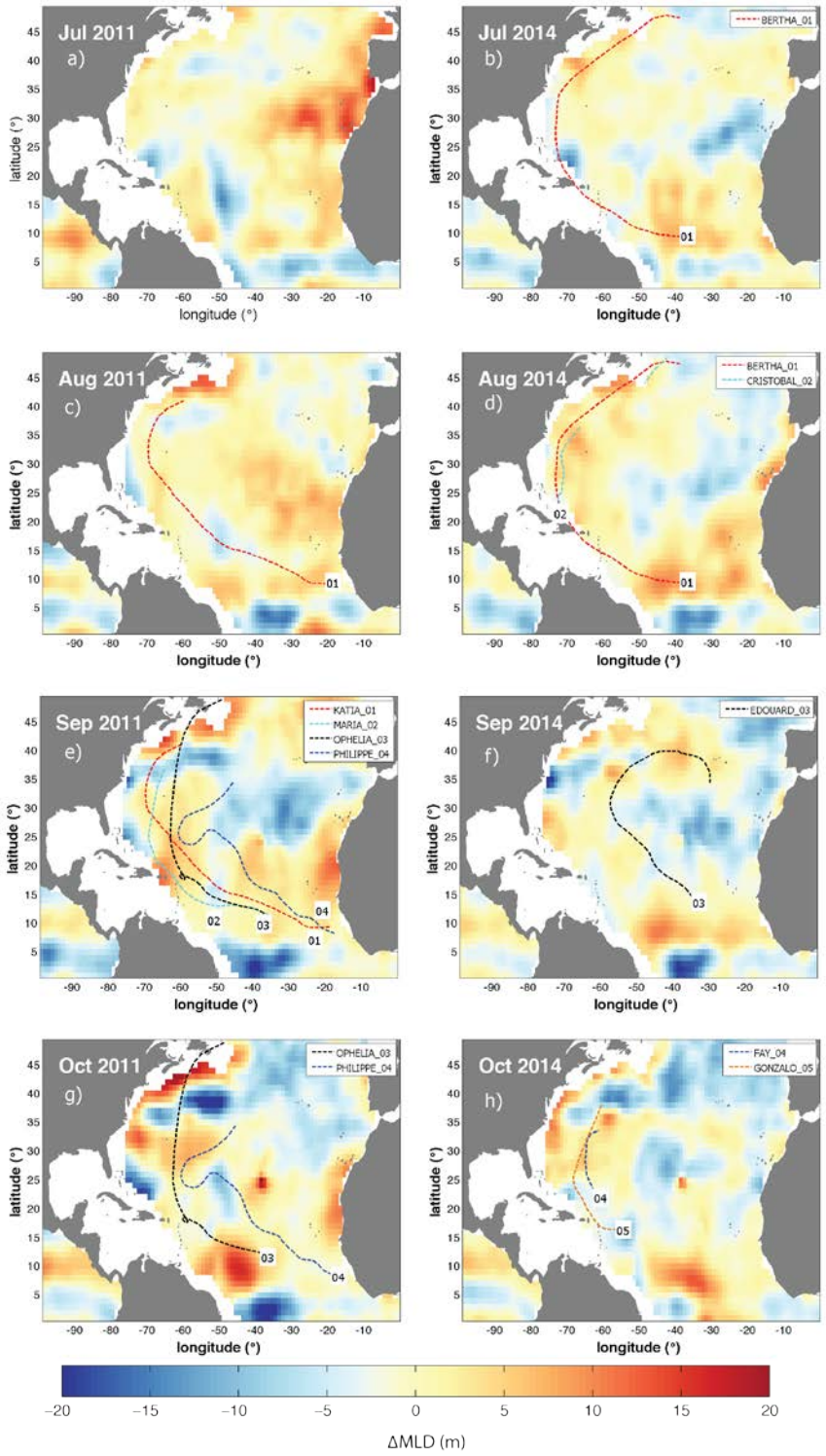

Figure 5-9 Mixed layer depth anomalies in the North Atlantic during August, September and October of the years 2011 and 2014. Anomalies were computed by subtracting the monthly climatology to the average of a given month. For reference only, notice the TC-tracks (dashed lines) of the monthly TC-activity for each of the years

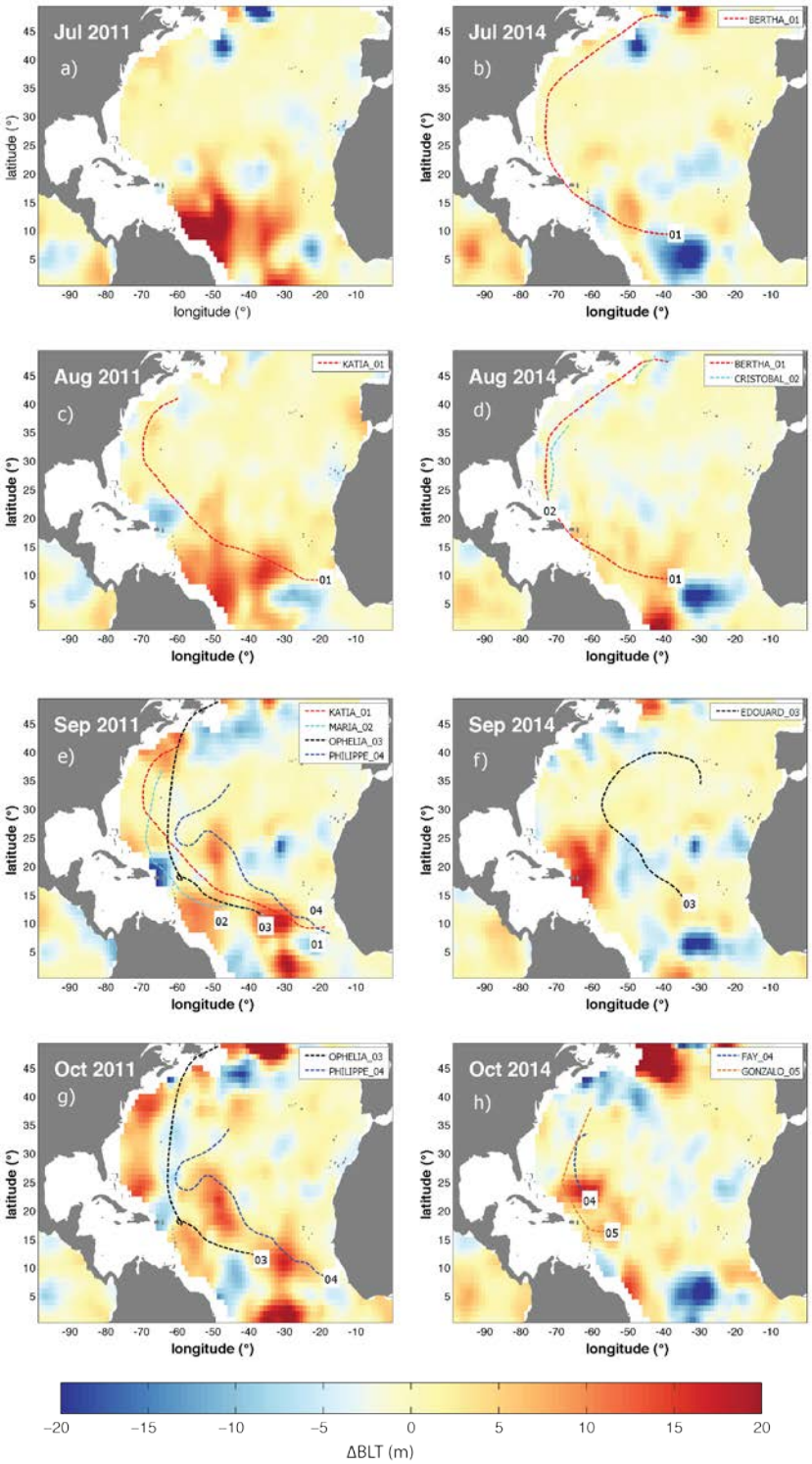

Figure 5-10 Barrier Layer Thickness anomalies (ΔBLT, m) in the North Atlantic during TC-season (June-October) in 2011 and 2014. Anomalies were computed by subtracting the monthly climatology to the average of a given month. For reference only, notice the TC-tracks (dashed lines) of the monthly TC-activity for each of the years.

Chapter 6

Case studies using the CTCFP method

6.1 Introduction

This chapter, applies the CTCFP (presented in Chapter 4) to two case studies in 2011 and 2014, which have been previously studied using different methods, i.e. comparing both satellite (SST and SSS) and Argo in situ observations (profiles of T and S from surface to 400 m depth) in one location before and after the passage of a storm [e.g. *Grodsky et al.*, 2012; *Reul et al.*, 2014]. The aim of this chapter is twofold. Firstly, it aims to answer one of the research questions of this thesis namely whether it is possible to observe a change in both in situ Argo T and S observations from profiles taken near to the passage of storm, and hence, assess the oceanic conditions when there is an oceanic response. Secondly, it aims to validate the CTCFP method by applying it to two case studies and compare the results to those reported in the literature. In addition, the justification of case studies also exemplifies the advantage of using CTCFP method in conditions where there are TC-overlapping events, which were ignored in previous studies.

The layout of this chapter is as follow: firstly Section 6.2 presents a North Atlantic Tropical cyclone climatology and the justification of the study cases. Next sections present the results of using CTCFP with satellite (Section 6.3) and in situ Argo datasets (Section 6.4); finally Section 6.5) present the main conclusion of using the CTCFP in the case studies.

6.2 North Atlantic Tropical cyclone Climatology

Based on the historical record from 1900 to 2014 in the IBTrACS dataset (Figure 6-1a), there were about 12 TCs each year with only about 3 events per year developing over the open ocean (i.e. first TC observation distance ≥ 300 km from land) and reached wind speed equal or above 33 m s^{-1}, i.e. TCs known as Hurricanes in the North Atlantic (Chapter 2). Owing to the well-defined boundaries of the North Atlantic basin, it is possible to test hypotheses and new methods to understand the formation and the evolution of these storms, which then can be applied to other basins [*Balaguru et al.*, 2012]. Thus this chapter focusses on TC seasons 2011 and 2014 to study TC induced changes into the North Atlantic using the CTCFP method (Chapter 4).

From all TC seasons within the study period, 2010 and 2011 (Figure 6-1b) were two of the most active seasons and this was reflected in the Accumulated Cyclone Energy (ACE) in each season (ACE_{2010} = 174 x 10^4 $knots^2$ and ACE_{2011} = 134 x 10^4 $knots^2$), which was higher than the computed average from the period (ACE_{2005_2014} = 123 x 10^4 $knots^2$). Furthermore, both 2010 and 2011 seasons also resulted in a high number of TC overlapping events, which adds complexity to CTCFP analysis, especially in defining the ocean conditions with no TC-activity (Section 4.2). However, TCs in 2010 occurred all too close in space and time to test the advantages of using the new CTCFP method to sample the ocean response of a given storm. On the other hand, in 2011 (Figure 6-2a) there were four TC formations, with only one TC-overlapping event, which occurred between TC-Katia and TC-Maria. Furthermore, there were more Argo observations within TC locations in 2011 than in 2014 (i.e. due to sampling criteria established with the CTCFP).

The criteria to choose the second case study was mainly that there were no TC-overlapping events and that there were similar number of storms. Thus this chapter used TCs in 2014 as the other case study to demonstrate CTCFP response with no overlapping events.

The ACE computed using strong TCs only (Figure 6-1b), was 75 x 10^4 $knots^2$ and 58 x 10^4 $knots^2$ in 2011 and in 2014 respectively. Despite the differences in terms of ACE, both seasons had similar number of storms (i.e. 4 and 5 storms each year), which are further describe in next section 6.2.1.

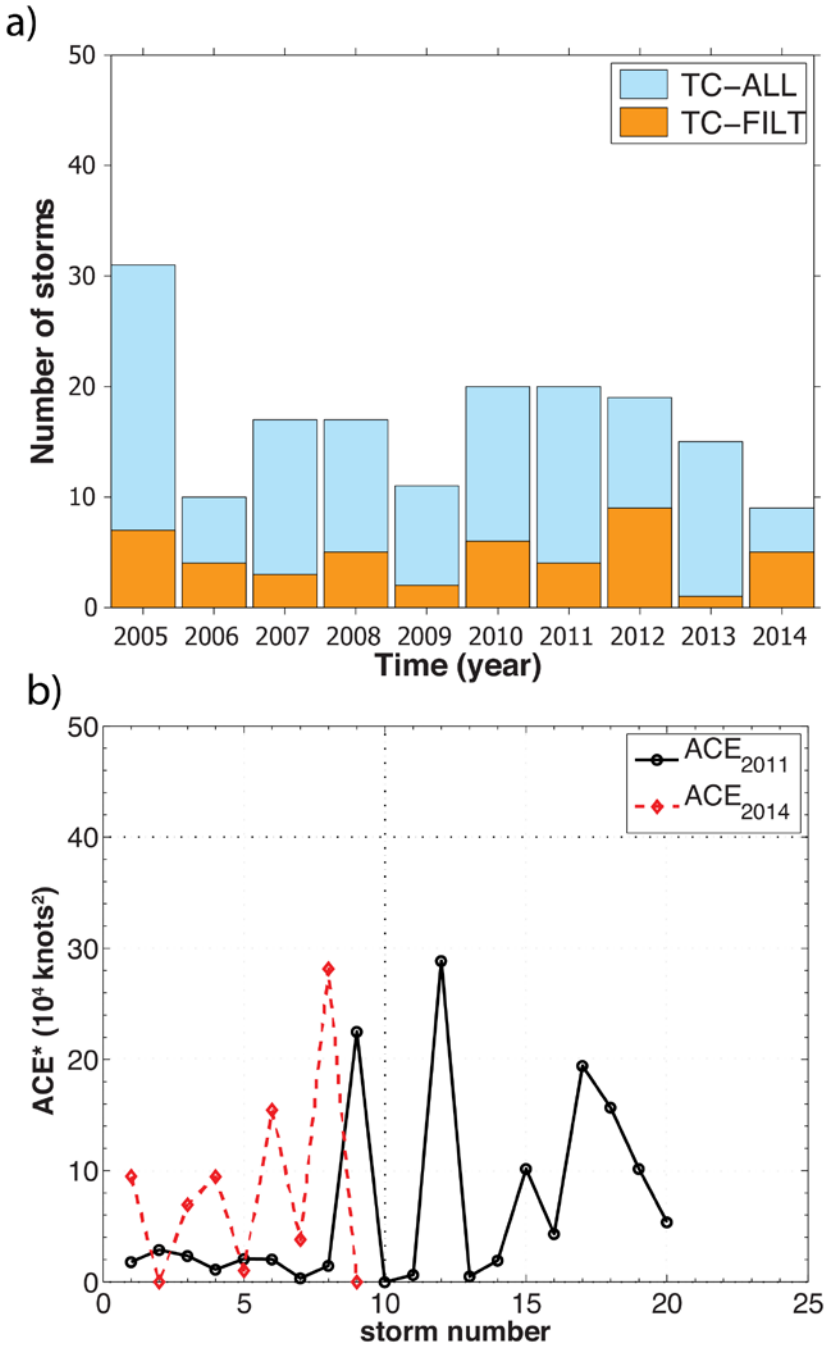

Figure 6-1 (a) Number of Tropical cyclones in the North Atlantic from 2005 to 2014, before (TC-ALL) and after (TC-FILT) applying a filter to select strong Tropical cyclones (wind speed ≥ 33 m s^{-1}) and developing over the open ocean (first TC observation ≥ 300 km). (b) Accumulated Cyclone Energy (ACE*, 10^4 $knots^2$) for each filtered storm (x-axis) occurring in the North Atlantic during seasons in 2011 (black-solid) and 2014 (broken-red), which resulted in annual ACE of 134 x 10^4 $knots^2$ and 74 x 10^4 $knots^2$ respectively. Notice the names (see main text) of the strong storms (i.e. wind ≥ 33 m s^{-1}), which contributed the most to the annual ACE each year. ACE* computation used wind speed (in knots) as sourced from IBTrACS, version Data source: IBTrACS, version 9 (https://www.ncdc.noaa.gov/ibtracs/).

6.2.1 Hurricanes in 2011 and 2014

This section summarizes the main physical characteristics as reported in IBTrACS of all filtered TCs occurring in 2011 and 2014 (Figure 6-2 and Table 6-1). The time of each TC-location is in the form of date and also as the day of the year, which for simplification this thesis referred to it as jday. The use of the jday facilitated the spatial and temporal comparison of TC activity within the same season or between two different years (Figure 6-2).

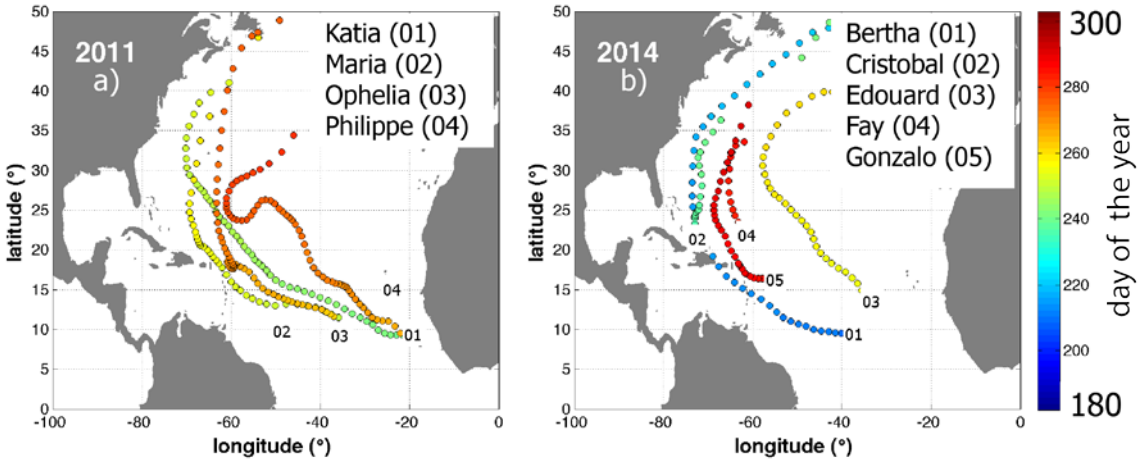

Figure 6-2 Spatial and temporal location of Tropical cyclones in the North Atlantic in 2011 (a) and 2014 (b) TC-seasons. Marker colour represents the day of year at which TC crossed a given location. Temporal upper and lower limits are 1st July and 30th October respectively.

In 2011 (Figure 6-2a), there was one TC-overlapping event where TC-Katia (240 - 253 jday) was closely followed by TC-Maria (249-259 jday) and then later in the season TC-Ophelia (263 - 276 jday). TC-Katia and TC-Ophelia provided the greatest contribution to the overall ACE in that year (Figure 6-1b, solid-black). Both TC-Katia and TC-Ophelia originated at the eastern side of the basin (near Cape Verde) and moved westward crossing through the freshwater plume extension (4˚ S - 35˚ N; 80˚ W - 20˚ W) of the Amazon and the Orinoco river outflows.

In 2014 (Figure 6-2b), the largest contributions to the overall ACE were provided by TC-Edouard, which spanned from 253 jday to 265 jday and moved northward with little westward component. Towards the end of the season TC-Gonzalo (from 284 to 291 jday), which like Katia and Ophelia in 2011, originated on the eastern side of the basin.

Table 6-1 Filtered tropical cyclones in the North Atlantic during 2011 (green) and 2014 (blue) storm seasons. TC number refers to the storm's chronological occurrence in each year. The other physical parameters are described in the IBTrACS dataset (Chapter 4).

TC number	Name	Wind max ($m\ s^{-1}$)	Start date (day year)	End date (day year)
01	Katia	61.7	28/08/2011 (240)	10/09/2011 (253)
02	Maria	36	06/09/2011 (249)	16/09/2011 (259)
03	Ophelia	61.7	20/09/2011 (263)	03/10/2011 (276)
04	Philippe	41.2	23/09/2011 (266)	08/10/2011 (281)
01	Bertha	36	29/07/2014 (210)	08/08/2014 (220)
02	Cristobal	36	23/08/2014 (235)	30/08/2014 (242)
03	Edouard	54	10/09/2014 (253)	22/09/2014 (265)
04	Fay	36	10/10/2014 (283)	12/10/2014 (285)
05	Gonzalo	64.2	11/10/2014 (284)	18/10/2014 (291)

As seen earlier in this thesis (Section 2.2), propagation direction of TC is dependent on the dominant wind direction at that latitude, which in the case of the North Atlantic are the Easterly winds [*K Emanuel*, 2005]. Therefore, TCs described here followed a common mechanism in NA where there is a formation phase near Cape Verde, followed by a westward TC intensification phase with a westward translational movement pushed by Easterly winds.

6.2.2 Wind Speed and Translational Speed

TC intensity tends to increase with latitude. Thus both 2011 (TC-Katia in Figure 6-3 a) and 2014 (TC-Edouard in Figure 6-3 b) seasons saw a rapid TC intensification between latitudes 15˚ and 25˚ N where wind speed rapidly rose from about 25 $m\ s^{-1}$ to over 30 $m\ s^{-1}$. The different intensification rates observed for each storm are partially related to different upper ocean structures [*Androulidakis et al.*, 2016; *Balaguru et al.*, 2012] but are mainly controlled by the dominant

atmospheric conditions including large-scale atmospheric circulation. Accordingly, Figure 6-4 shows the evolution over time of the wind speed and the U_H for each storm included in this study.

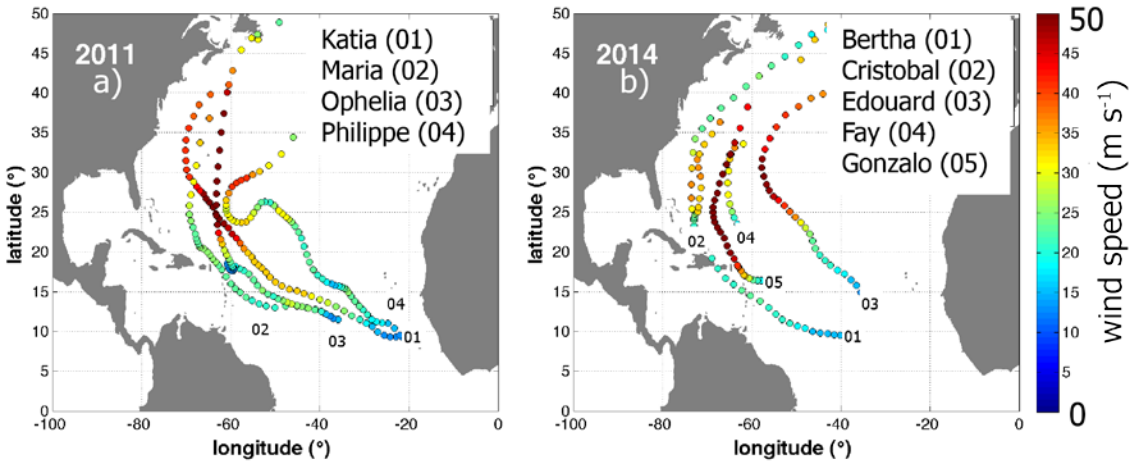

Figure 6-3 Wind speed at each location for Tropical cyclones in the North Atlantic used in this study in 2011 (a) and 2014 (b). Colour of markers shows the wind speed (ms^{-1}) from IBTrACS.

Previous studies [e.g. *Grodsky et al.*, 2012; *Reul et al.*, 2014] looked at the potential relationship between TC-intensification and the BL over the Amazon plume using TC-Katia. TC-Katia was the first TC of that season originating on 28th August (240 jday) and developing over the open ocean. As reported by previous works [*Androulidakis et al.*, 2016; *Grodsky et al.*, 2012], by 2nd September (246 jday), TC-Katia was in the vicinity of the Amazon-Orinoco plume. Whilst its intensity increased rapidly (Figure 6-4 a) from tropical storm category (wind ≈ 20 m s^{-1}) to category 4 Hurricane (wind > 60 m s^{-1}), its translational speed (Figure 6-4 c) dropped from 9 m s^{-1} to about 4 m s^{-1}. Shortly after, TC-Maria originated following a similar path, however, it did not intensify as much as Katia and it remained a tropical storm throughout its passage over the Amazon-Orinoco region with a low translational speed (U_H < 2 m s^{-1}). Maria's lack of intensification seems linked to the cold wake left by TC-Katia a few day earlier [*Balaguru et al.*, 2014]. Further, on 20th September (263 jday), TC-Ophelia started moving fast (U_H ≈ 8 m s^{-1}) towards the Amazon-Orinoco region where it slowed to a translational speed below 2 m s^{-1}, but its wind speed rose from 20 m s^{-1} to more than 60 m s^{-1}.

In 2014 there were TCs crossing over the Amazon plume region too. There was TC-Bertha, 27th July to 8th August (210 – 220 jday) and TC-Gonzalo, 11th October to 18th October (284 – 291 jday) that crossed the Amazon-Orinoco region with U_H of 8 m s^{-1} and 5 m s^{-1} respectively. Whilst Bertha reached wind speeds of 33 m s^{-1}, TC-Gonzalo became the strongest storm of the season (wind > 60 m s^{-1}).

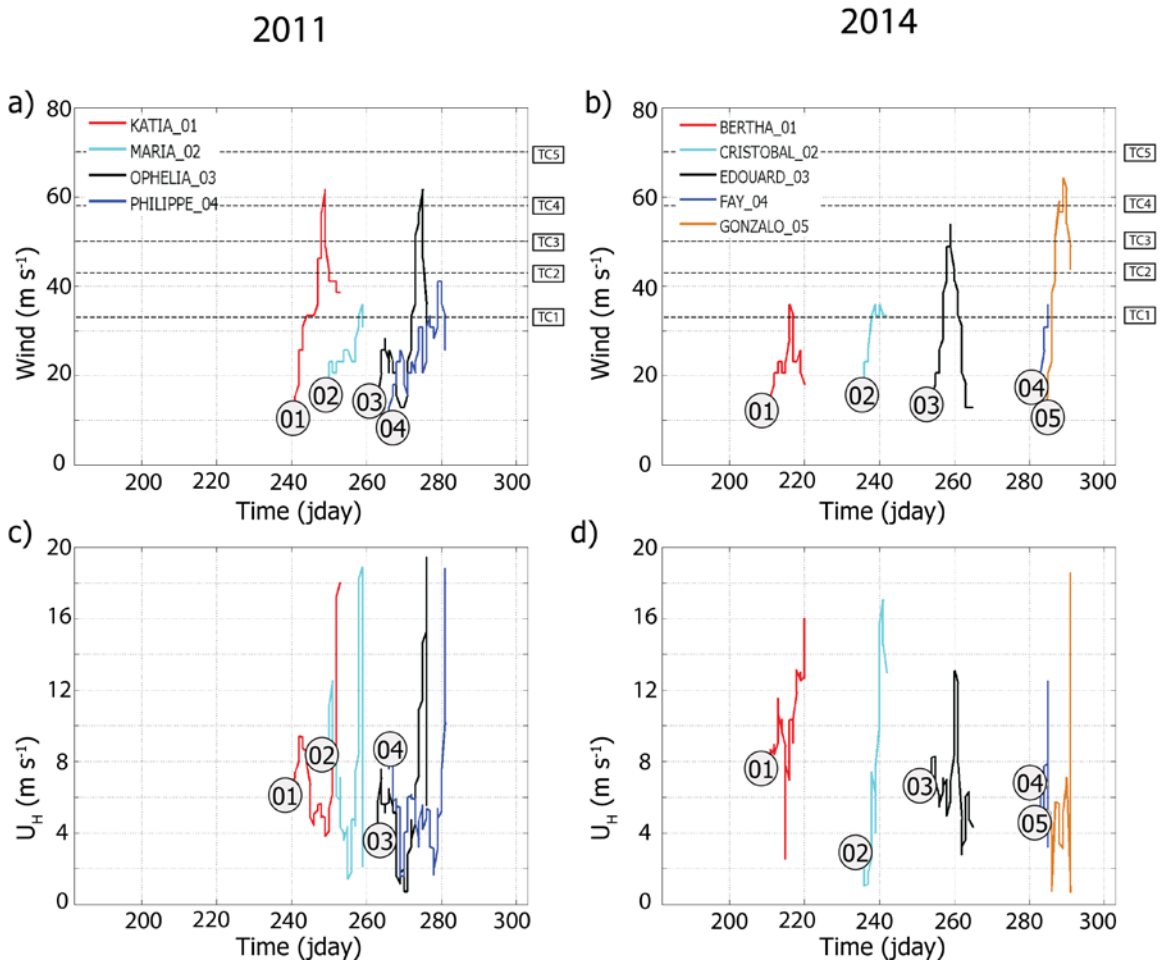

Figure 6-4 Evolution over time of the intensity measured as the maximum wind speed at each TC-location (a-b) and the translational speed (c-d) of each Tropical cyclone in the North Atlantic during storm seasons in 2011 (left) and 2014 (right). Notice wind speed category (broken line) as using the Saffir-Simpson scale classification.

6.3 TC-induced response as seen from satellite observations

This chapter used the CTCFP method to compute the TC induced changes in SST (SST_{diff}) at each TC location as the daily (days 1 to 60 after TC's passage) difference in SST from a SST reference (SST_{ref}), where SST_{ref} was taken as the 10-day SST average before TC's passage (Chapter 4). Notice that Figure 6-5 shows the resulting 2011 SST_{diff} time series (Figure 6-5 , left column) and at each TC location (Figure 6-5 , right column). Furthermore, Figure 6-5 may be used to identify the largest cooling (Figure 6-5 , red star) in both time and space. For example, in 2011, TC-Katia was responsible for the largest reduction in SST ($SST_{diff} < -2$ ˚C) on 7th September (250 jday) (Figure 6-5 a). TC location (Figure 6-5 e) was in proximity to the western boundary current, the Gulf Stream, where the MLD and BLT anomalies were minimum (Figure 5-7e and Figure 5-8e). At this time the storm was travelling at is minimum translational speed ($U_H \approx 5$ m s^{-1}) and then as it moved to northern latitudes, the translational speed progressively increased to above 10 m s^{-1}. Previous works

reported the surface cooling of TC-Katia [*Androulidakis et al.*, 2016; *Grodsky et al.*, 2012; *Hernandez et al.*, 2016].

TC-Katia crossed 2nd to 4th September (245 to 247 jday) over the tip of the Amazon-Orinoco plume region. Katia's induced cooling over the Amazon-Orinoco plume region was only about 0.5˚C. At this time, whilst the translational speed decreased from 8 to 4 m s^{-1}, the wind speed increased from below the TC threshold of 33 m s^{-1} to more than 40 m s-1 (Figure 6-4). However, couple of days after (249 jday) TC-Maria crossed over the same region and it remained a rather weak storm with a maximum wind speed barely reaching 33 m s^{-1}. Based on the TC-overlapping concept [*Balaguru et al.*, 2012], TC-Maria found cooled surface water left by TC-Katia induced upwelling. Finally, this season saw TC-Philippe, which also induced an important surface cooling at about 30˚N (i.e. outside the Amazon-Orinoco plume region) on the 8th October (280 jday) and it coincided with a TC intensity reduction. TC-Philippe was not a very strong storm (CAT1 hurricane, wind < 40 m s^{-1}), however it induced a surface cooling (SST_{diff} ≈ - 1.8 ˚C) comparable to TC-Katia.

In 2014 (Figure 6-6), all the storms induced a clear surface cooling (SST_{diff} ≤ -2 ˚C). The greatest surface cooling occurred in the tracks of TC-Edouard and TC-Fay where the cooling almost reached -2.5˚C. These cooling events occurred in sub-tropical latitudes (25˚ to 30 ˚N) and towards the end of the storm life of both TCs. In the case of TC-Edouard, the storm moved mainly in the middle of the basin, thus its cooling was constrained between 55˚ W to 60˚W. In the case of TC-Fay, and similarly to TC-Katia, the maximum cooling occurred towards the western boundary. Hence the largest averaged TC induced cooling occurred under TC-Katia in 2011 (Figure 6-7 a) and under TC-Fay in 2014 (Figure 6-7 b).

Regarding the SSS variability at each TC-location, L4a SSS SMOS data were plotted at each TC-location (Figure 6-8). The temporal resolution of the data (i.e. 10 day average) does not allow drawing any conclusions about TC-induced changes at each TC-location. The resulting signal was significant with salinity differences of more than 1 psu in both directions to increasing and decreasing salinity. Nevertheless, high variability seen in the SSS data, TC-locations with significant TC-induced saltines increments (i.e. within the 20-day post storm period) were coincident within regions where SST cooling was weak. Furthermore, these regions where confined within the proximity of the Amazon plume region, which would confirm that BL region within the freshwater plume oppose resistance to the TC-induced turbulent mixing [*Androulidakis et al.*, 2016; *Balaguru et al.*, 2012; *Reul et al.*, 2014].

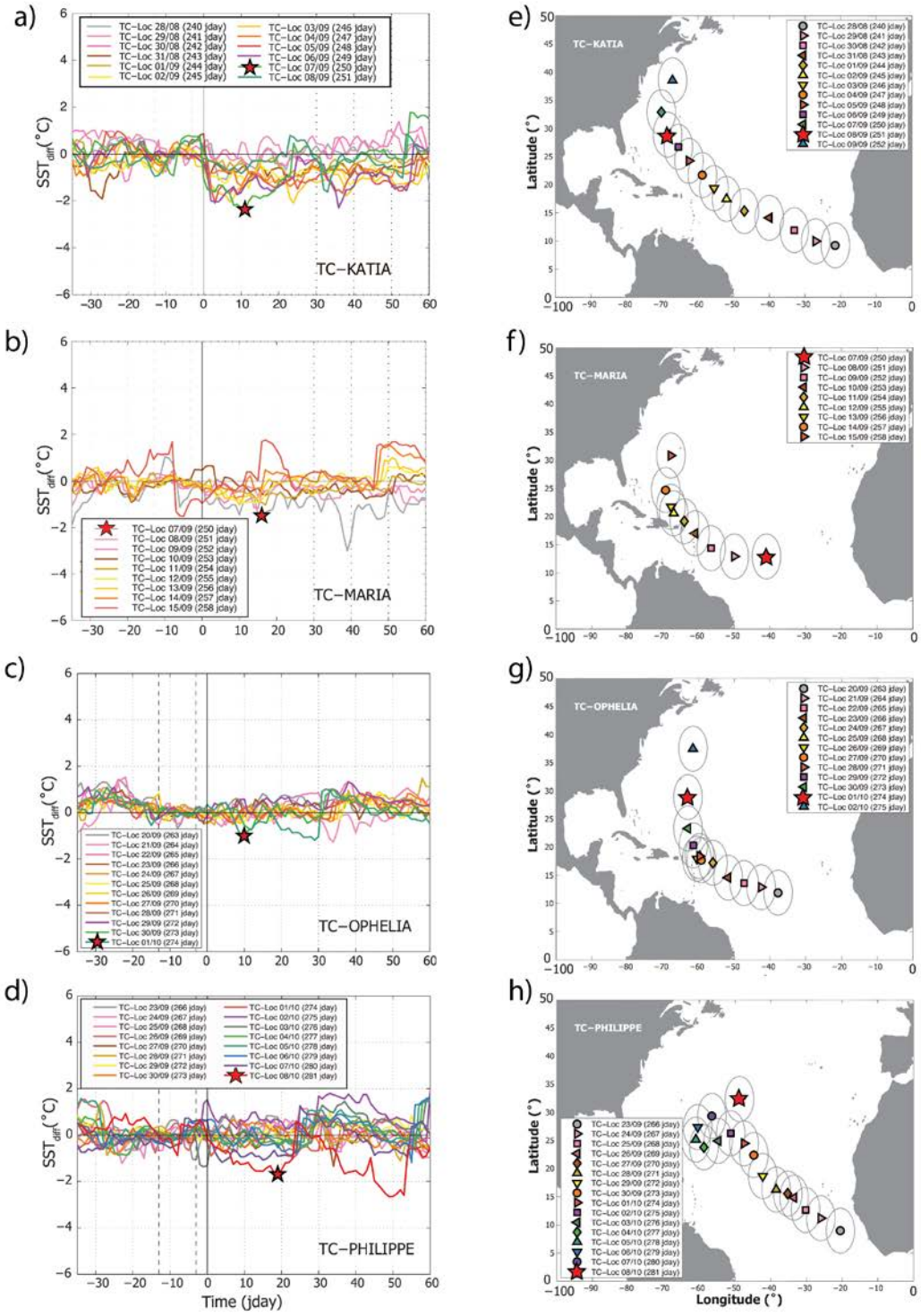

Figure 6-5 GHRSST data to compute (left) Time series of the TC induced changes on Sea Surface Temperature (SST_{diff}, ˚C) at each TC-location (right) of storms during 2011 in the North Atlantic. The maximum cooling (red star) induced by each TC within the first 20 days after the storm's passage.

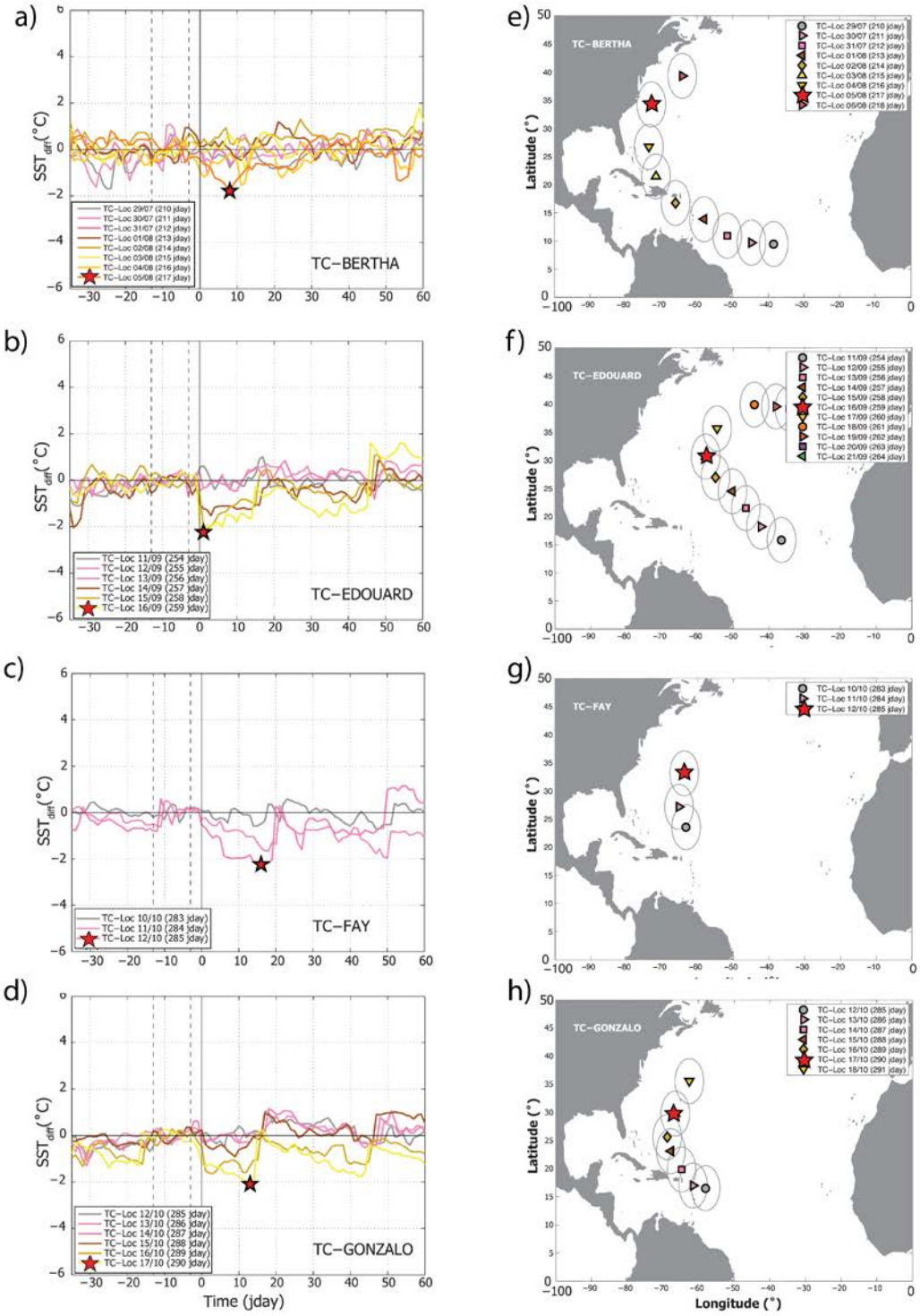

Figure 6-6 GHRSST data to compute (left) time series of the of the TC induced changes on Sea Surface Temperature (SST_{diff}, ˚C) at each TC-location (right) of storms during 2014 in the North Atlantic. The maximum cooling (red star) induced by each TC within the first 20 days after the storm's passage.

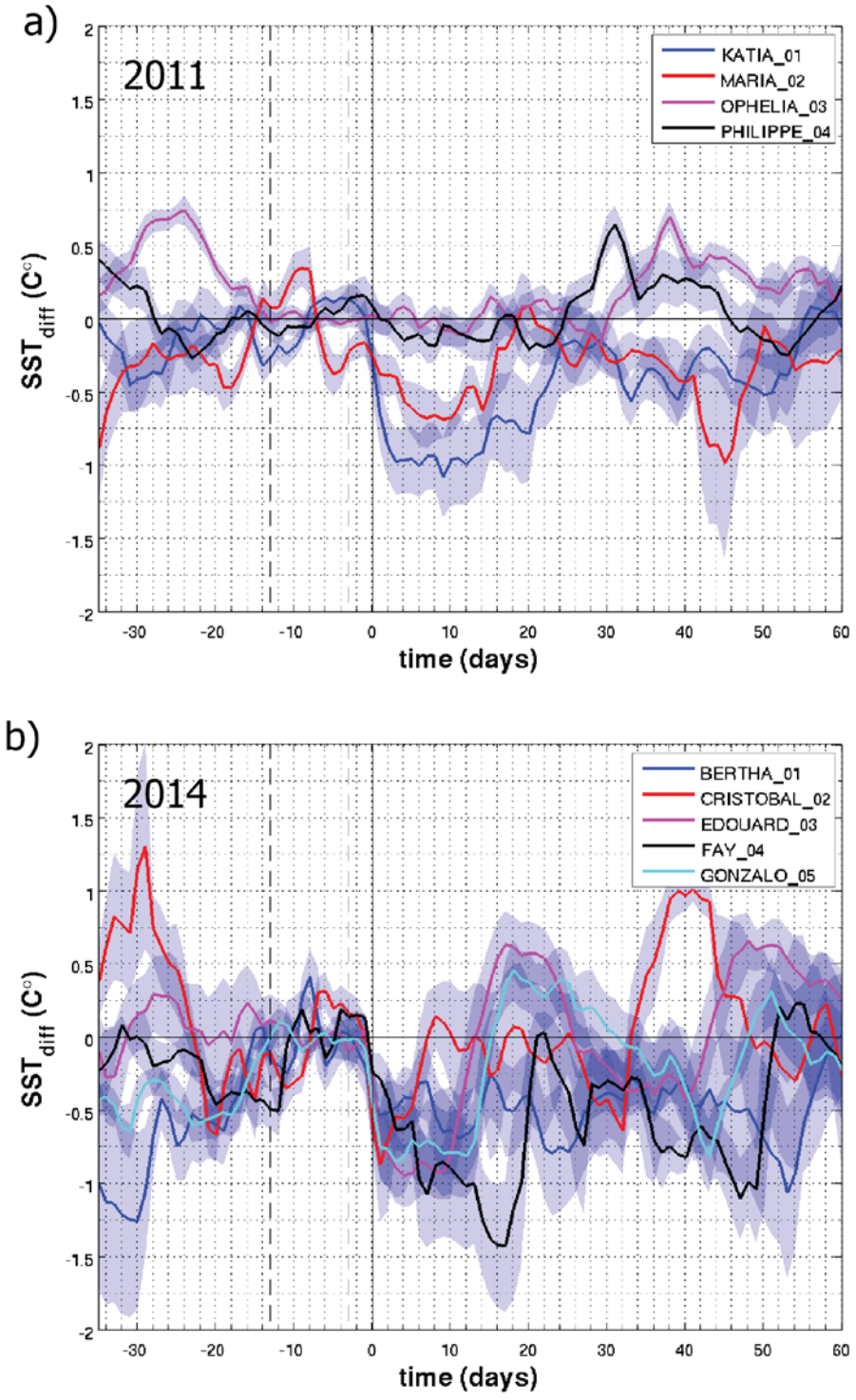

Figure 6-7 Time series of the of the average TC induced changes on Sea Surface Temperature (SST_{diff}, ˚C) of each TC occurring (a) 2011 and (b) 2014 in the North Atlantic. The shaded area around the lines is the Standard Deviation of the Mean (SEM)

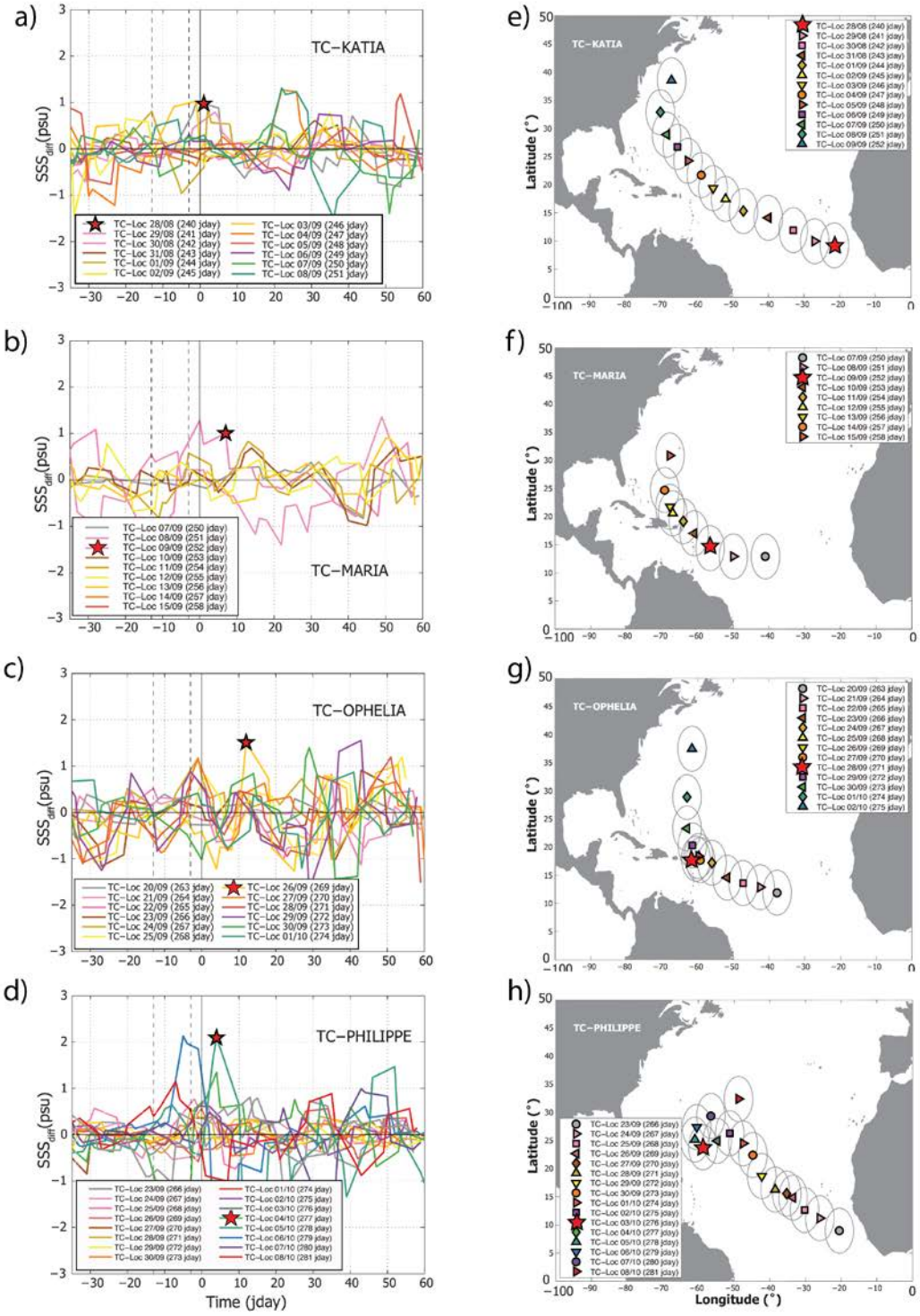

Figure 6-8 SMOS-L4a (left) time series of the TC induced changes on Sea Surface Salinity (SSS_{diff}, psu) at each TC-location (right) during storm season in 2011 in the North Atlantic. The maximum salinity increase (red star) induced by each TC within the first 20 days after the storm's passage.

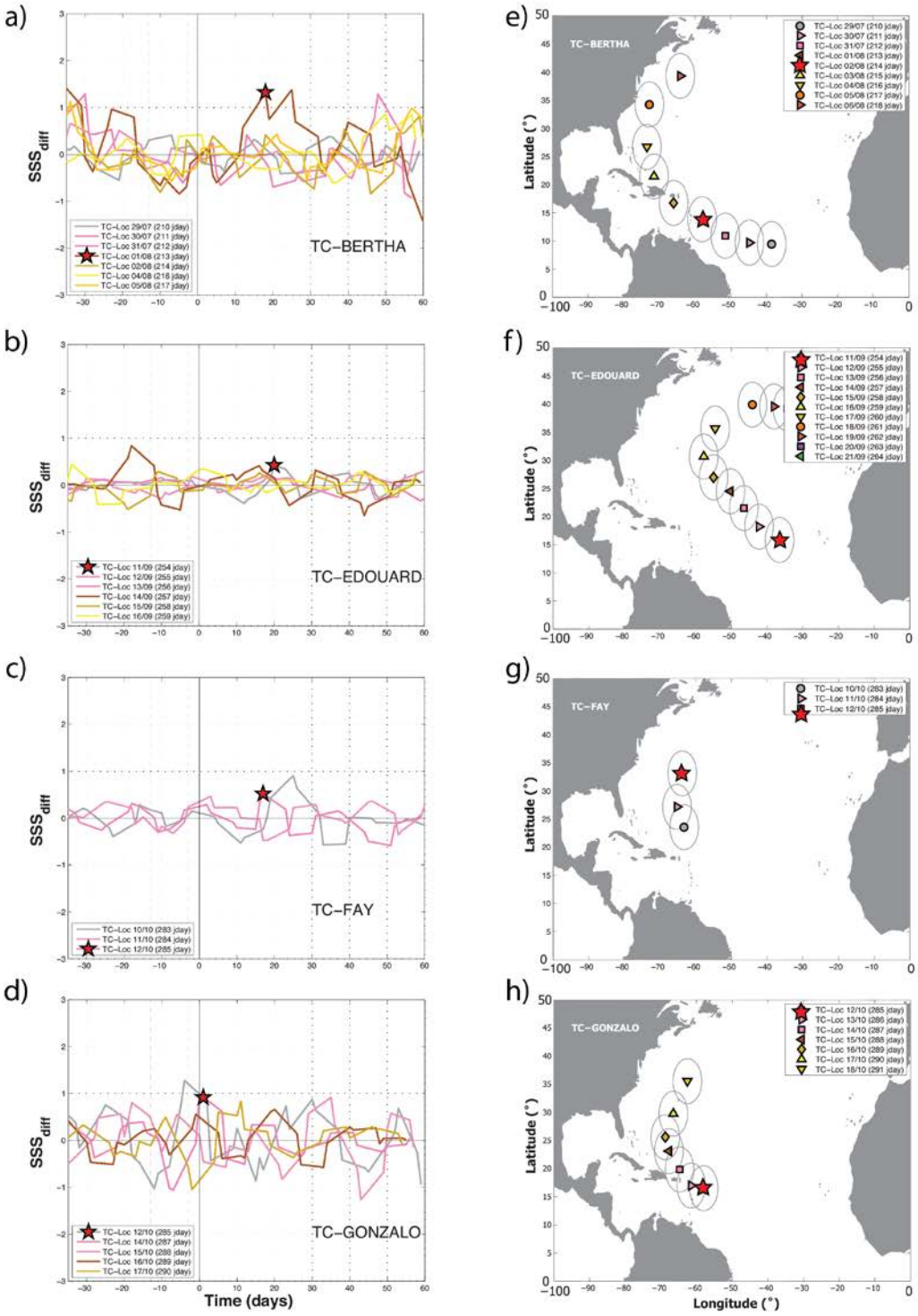

Figure 6-9 SMOS-L4a (left) time series of the TC induced changes on Sea Surface Salinity (SSS_{diff}, psu) at each TC-location (right) during storm season in 2014 in the North Atlantic. The maximum salinity increase (red star) induced by each TC within the first 20 days after the storm's passage.

6.4 TC-induced ocean response as measured in Argo

6.4.1.1 Number of profiles within the TC searching radius

The CTCFP method using Argo, resulted in the analysis of 992 and 906 profiles around TC-locations in 2011 and 2014 respectively. The number of observations included in this study is much higher than in any of previous work, i.e. bearing in mind earlier studies used only 2 Argo profiles at a single TC-location [*Grodsky et al.*, 2012; *Reul et al.*, 2014]. Argo floats are not homogeneously distributed within the basin and drift with the predominant ocean currents. Hence, in the North Atlantic the accumulation of observations is higher towards the northwestern side of the basin (i.e. with the dominance of the Gulf Stream Current) than to the eastern side. This could explain that as storms move towards the northwest the number of Argo observations increases. The number of profiles around the passage of a given TC-location is dependent on the TC-activity of the season (i.e. high activity seasons may see more TC-overlapping events than low activity ones), the chronological order of storms within the season and the life span of the storm. The sampling criteria of the ocean before the storm's passage (i.e. 20-day with no TC-activity within a 400 km radius) may well promote sampling disparity between storms occurring within the same season. Thus the number of observations before-TC in 2011 was noticeably higher for TC-Katia (N = 48 obs) than for the subsequent TC-Maria (N = 9 obs) and TC-Ophelia (N = 2 obs) with similar paths (Figure 6-10 a). Finally TC-Philippe developed last in the season and followed a different path with respect to the previous storms, which comparatively with other storms in the same season, TC-Phillipe had a higher number of observations (N = 55 obs).

As expected the lower number of TC-overlapping events in 2014 yield to a more uniform number of observations between different TCs than the 2011 season (Figure 6-10 b). The relatively low number of observations around TC-Cristobal and TC-Fay, might be linked to their predominantly northward movement and a short storm lifespan. Nevertheless, the number of observations around TC-Fay (N = 20 obs) was comparable to the number of observations around TC-Maria, which had a longer lifetime but under the influence of TC-overlapping track with TC-Katia.

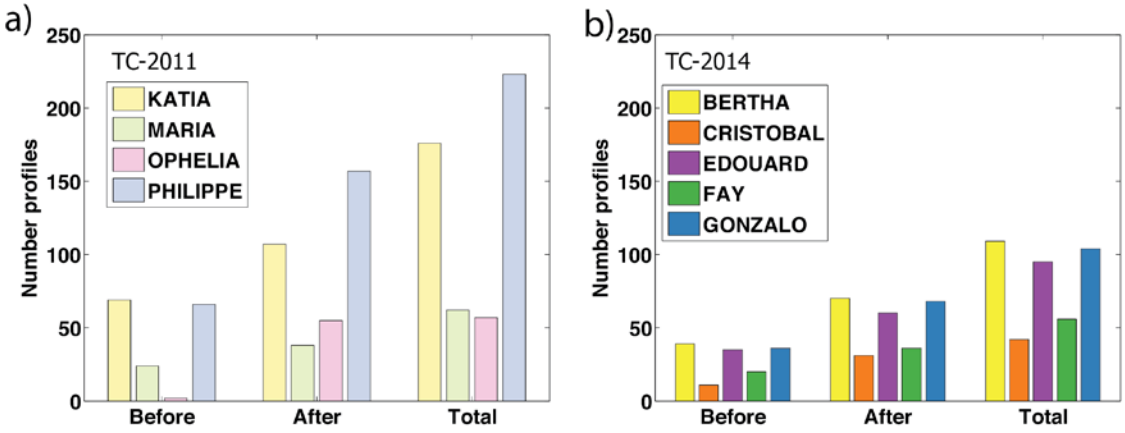

Figure 6-10 Total number of Argo profiles Before, after and within a TC searching radius (i.e. r = 400 km) during TC-season (a) 2011 and (b) 2014.

This chapter used Argo observations at the surface (depth ≤ 10 m depth), as it would be the closest surface observation that would be comparable to both satellite SST and SSS measurements. In order to explore the potential of CTCFP method using Argo and comparing the results using SST, this section looks at those TC-locations with the highest TC-induced SST cooling (Figure 6-5 and Figure 6-6). Some of these TC-locations were also included in previous case studies so this allowed the comparison of results.

6.4.1.2 TC induced changes in T and S profiles

At the surface (i.e. 10 m depth), most of the Argo paired profiles (~ 60%) around TC-location in 2011 and 2014 captured a decrease in temperature of 1˚C or more (Figure 6-11) and about a 30% of the pairs captured an increase in temperature of about 1˚C. Furthermore, observations in 2014 capture a higher averaged TC-induced cooling (T_{diff} ≤ 2.0˚C) than in 2011. The interpretation of the TC-induced warming seen under some TC-locations, was not observed in the previous SST analysis neither was mentioned in the literature. Even though these TC induced warming events are the minority, they might be further investigated in the future work of this thesis (Chapter 8).

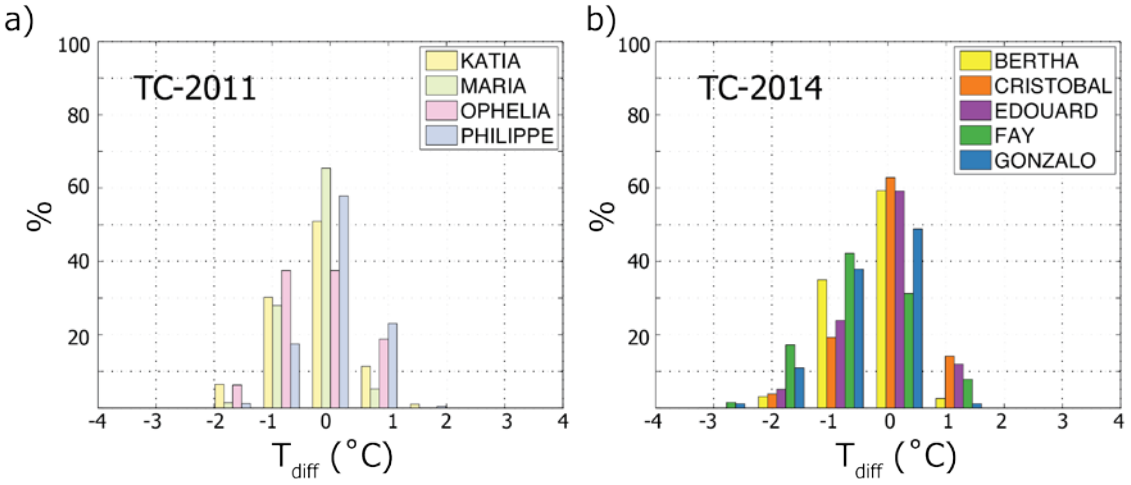

Figure 6-11 Number of observations (in percentage) of the TC-induced temperature changes at 10 m (T_{diff}) in the North Atlantic during (a) 2011 and (b) 2014 TC-seasons. Argo thermal differences were computed as the difference in Argo profiles after-TC minus before-TC. Hence TC induced temperature increase ($T_{diff} > 0$) or decrease ($T_{diff} < 0$).

Not all the paired Argo profiles show a clear TC induced change in salinity. Thus about 40% of the observations captured a significant absolute salinity change ($S_{diff} \geq |0.2|$ psu) (Figure 6-12). However, on the contrary to what it was seen with the temperature profiles, TC-induced changes in salinity at 10 m were evenly distributed as TC-induced both an increase and a decrease in salinity. For example, all TCs in 2011 (Figure 6-12a) induced a freshening of 1 psu or more, but as well there was a salinity decrease of the same magnitude. TC-Katia induced the greatest increase in salinity from all storms in that season, which was captured by only three paired profiles.

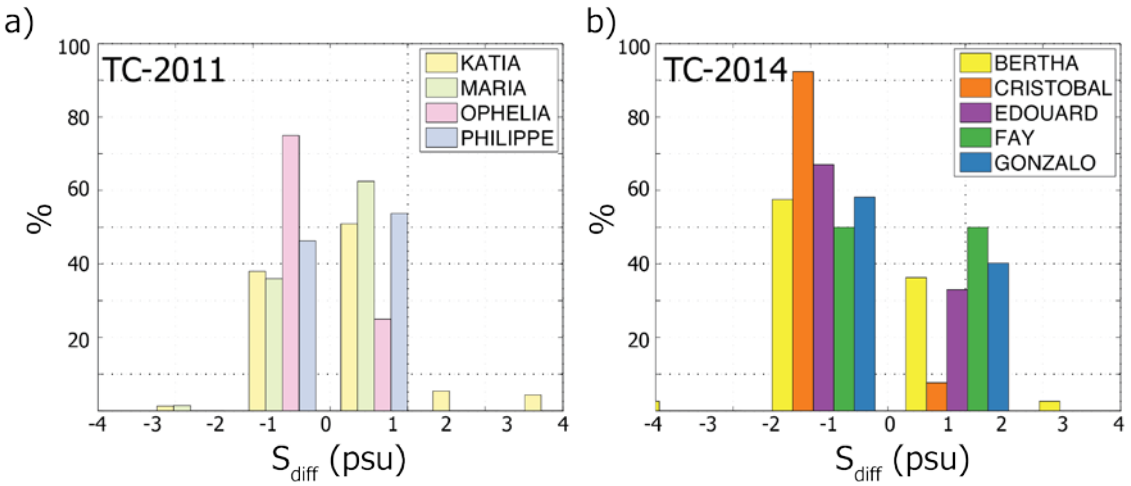

Figure 6-12 Number of observations (in percentage) of the TC-induced changes in salinity at 10 m (S_{diff}) in the North Atlantic during (a) 2011 and (b) 2014 TC-seasons. Argo haline differences were computed as the difference in Argo profiles after-TC minus before-TC. Hence TC induced salinity increase ($S_{diff} > 0$) or decrease ($S_{diff} < 0$).

6.4.1.3 TC induced changes in T and S and the ocean conditions before the passage of a TC

This section explores TC induced increase/decrease in both Argo temperature (i.e. $T_{diff} \geq 1$ or $T_{diff} < 1$) and salinity (i.e. $S_{diff} \geq 0.2$ and $S_{diff} < 0.2$) at 10 m and if changes are statistically related to each other or to other variables. Thus it was possible to perform a multiple Pearson correlation test between two given variables and it resulted in two correlation matrices with correlation (R_{Peason}) and statistical significance ($P_{Pearson}$) values for each year (Figure 6-13). These matrices summarize the level of association between TC-induced changes and the different variables relating to: 1) TC physical characteristics (i.e. U_H, wind, lat and lon); and 2) the ocean conditions before the arrival of the storm (i.e. MLD, BLT) and the TC induced changes measured as T_{diff} and S_{diff} at 10 m. Even though some correlations were significant (pval ≤ 0.05, 95% significance level), correlation values were moderate (-0.3 ≥ R ≥ +0.3) in most of the combinations between two variables. Nevertheless, in most cases seen in both years there was no agreement between the two correlation matrices. For example, whist in 2011 TC-induced cooling ($T_{diff} < 1$) resulted to be statistically significantly negatively correlated ($R_{Pearson} \approx -0.2$, P_{Peason}) with an increase in salinity, in 2014 the correlation was near zero and it was not statistically significant at the same level of significance.

TC induced decrease in temperature seemed to be positively correlated in both years with a decrease in salinity. These results were statistically significant in both years and it would suggest that TC induced cooling may be linked to a TC induced salinity decrease. Further, TC induced cooling resulted being negatively correlated with MLD in 2014 only. This result would agree with the mechanism described earlier in this thesis, where TC induced cooling regions might be link to shallow MLD. In 2011, correlation between the two was positive, but the statistical significance was very low ($P_{Pearson} = 0.8$).

TC induced salinity increase was negatively correlated with MLD in both years with $P_{Pearson}$ values of 0 and 0.04 for 2011 and 2014 respectively. TC induced salinity increase was positively correlated with BLT, but only in 2011 the correlation was statistically significant. Nevertheless, these correlation tests would confirm that TCs tend to increase surface salinity over regions with a shallow MLD and deep BLT.

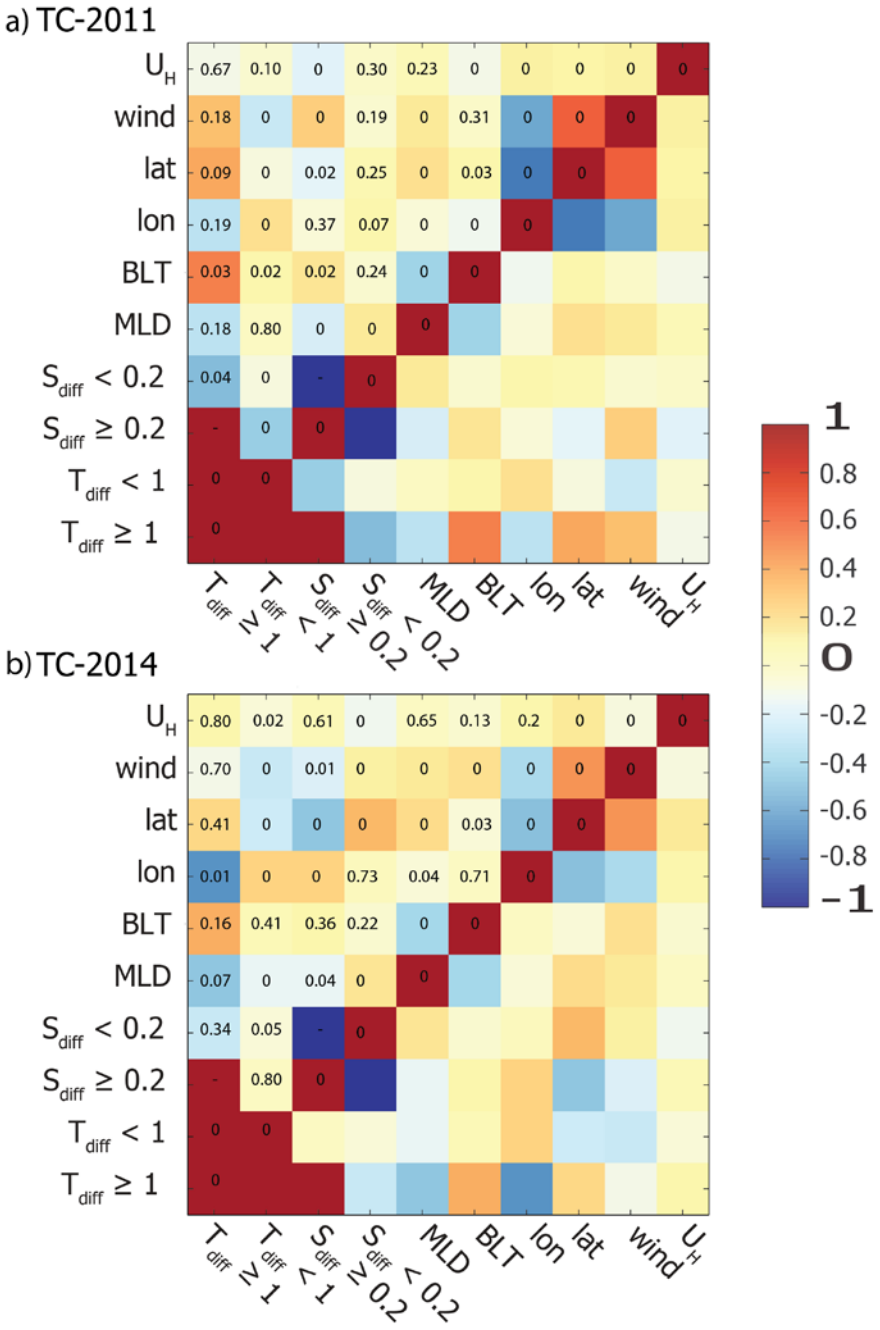

Figure 6-13 Correlation matrix computed at each paired Argo observation around Tropical cyclones in 2011 (a) and in 2014 (b). The p-values (numbers in black) indicate that there was some level of correlation (p-value below 0.05). However correlation testing (and p-values) were not consistent between the two years. The correlation matrix included the following variables: translational speed (U_H), wind speed (wind), latitude and longitude (lat and lon), Barrier Layer Thickness (BLT), Mixed Layer Thickness (BLT, m), TC-induced salinity difference lower than 0.2 psu ($S_{diff} < 0.2$), TC-induced salinity difference higher or equal to 0.2 psu ($S_{diff} \geq 0.2$), TC-induced temperature difference lower than 1˚C ($T_{diff} < 1$) and TC-induced temperature difference higher or equal to 1˚C ($T_{diff} \geq 1$). Colormap relates to the correlation value (R) between to variables. The diagonal elements of the matrix show the correlation of a variable with itself. Notice that values of the upper and lower side of the matrix mirror each other. Hence p-values are noted on one side of the matrix only. Empty p-values (-), mark correlation between two variables there were not enough cases to perform a significance test.

6.4.1.4 TC induced changes in a given TC-location

In this section, the average TC-induced ocean response were computed as the average change in T and S profiles within a given TC-location. This methodology is similar to what it was used in the literature [e.g. *Grodsky et al.*, 2012; *Reul et al.*, 2014]. Hence the average TC-induced response in 2011 showed that TC-Katia induced the greatest average cooling ($T_{diff} \approx -2^{\circ}C$) at the TC-location on 7th September (250 jday) (Figure 6-15), which was coincident with the cooling observed in the SST satellite data. The second greatest average cooling (not shown) captured in Argo was in the tail of TC-Philippe ($T_{diff} \leq 1.5^{\circ}C$). The average ocean thermal response in Argo and in GHRSST was coincident in the same TC-location, even though the satellite data saw larger cooling values (~0.5˚C) than the floats (Table 6-2). In the case of TC-Maria Argo did not capture a change thermal change because the ocean surface layer was already cooled by the passage of Katia. Both satellite and Argo showed that all the storms in 2014 induced thermal changes of at least 1.8˚C.

Table 6-2 Date of largest cooling in SST (GHRSST) and in Argo floats operating within the searching radius (r ≤ 400 m). Notice that SST and Argo measurements are values at about 10 mm and 10 m depth respectively.

		GHRSST		Argo	
TC-name	**Year**	**cooling date (jday)**	**SST (˚C)**	**cooling date (jday)**	**T10 (˚C)**
Katia	2011	07/09 (250)	2.4	07/09 (250)	1.8
Maria	2011	07/09 (250)	1.8	07/09 (250)	0
Ophelia	2011	01/10 (274)	1.5	01/10 (274)	0.8
Philippe	2011	08/10 (281)	1.8	08/10 (281)	2
Bertha	2014	05/08 (217)	1.8	04/08 (216)	1.8
Edouard	2014	16/09 (259)	2.1	16/09 (259)	1.8
Fay	2014	12/10 (285)	2.3	11/10 (284)	2
Gonzalo	2014	17/10 (290)	2.3	17/10 (290)	2

The average TC-induced ocean response in Argo salinity profiles was computed in the same way as for temperature. The resulting average haline change showed that TC-Katia induced the largest response in salinity on the 3rd September 2011 (246 jday) on its passage over the Amazon plume (Figure 6-14). Argo salinity measurements were not compared against SSS satellite based observations because it was not possible to differentiate TC response in the SSS satellite time series.

The ocean response induced by the passage of TC-Katia was a particular case in 2011 where there was a clear signal of both temperature and salinity. Therefore, *Grodsky et al.* [2012] suggested that when TCs are crossing over the Amazon region, there might be a TC induced mechanism, that upwells salty water from below to the surface. This was also confirmed by 2014 TC-induced changes, particularly TC-induced changes by TC-Bertha and TC-Gonzalo that crossed the Amazon region on 31st July (212 jday) and 12th October (285). This would explain the fact that in light of such a TC-induced salty upwelling there is a near zero thermal response. The Amazon plume region is characterized by a near permanent BL, where salinity at depth is higher than at the surface. On the other hand, profiles operating outside of the Amazon plume region (i.e. also region where TCs tend to induce largest surface cooling) showed an almost zero TC-induced change in salinity.

TC-induced changes in salinity, especially in the Amazon plume region, might be related to the stability of the water column (i.e. presence of BL, or not). Thus this section, studied the stability of the water column as computed by the buoyancy frequency in cycles per hour (N, cph) using T and S at each profile. Results of the computed N-Values showed that there was a difference of the water column stability between profiles inside and outside of the plume region. Hence at the crossing over the Amazon region TC-Katia N-values > 4 cph from surface to just about the MLD at 15 m depth (Figure 6-16). As suggested by *Grodsky et al.* [2012], these high N-Values could be related to the increased water column stability promoted by the presence of the BL. Conversely floats within the cooling region registered low N-Values ($N \leq 4$ cph) and the maximum buoyancy frequency was below the MLD, which was about 25 m. Following the same reasoning as before, these results would suggest the stability of the water column within the cooling region was lower, so TCs may induce turbulent mixing on its passage.

In the case of TC-Bertha and TC-Gonzalo over the Amazon region N-values did not show such a clear pattern of behaviour as described earlier in TC-Katia. Whilst in the case of TC-Bertha only one float (B4) had a really large N-value ($N > 6$ cph) (Figure 6-17). The buoyancy frequency computed in the nearby floats resulted to be lower as 2 cph. In the case of TC-Gonzalo maximum N-values were below the MLD ($N \approx 4$ cph).

The buoyancy frequency in the cooling regions (Figure 6-18) was just about 2 cph for both TC-Bertha and TC-Gonzalo. Furthermore the maximum N-values were coincident with the MLD, which were 25 m and 48 m for each storm. There was one exception with one float around TC-Bertha (Figure 6-18 c), which had its maximum N-values above the MLD. The distance of the floats around TC-Bertha were mostly within the radius of 200 km, with only B8 at about 400 km from the closest point to the storm track.

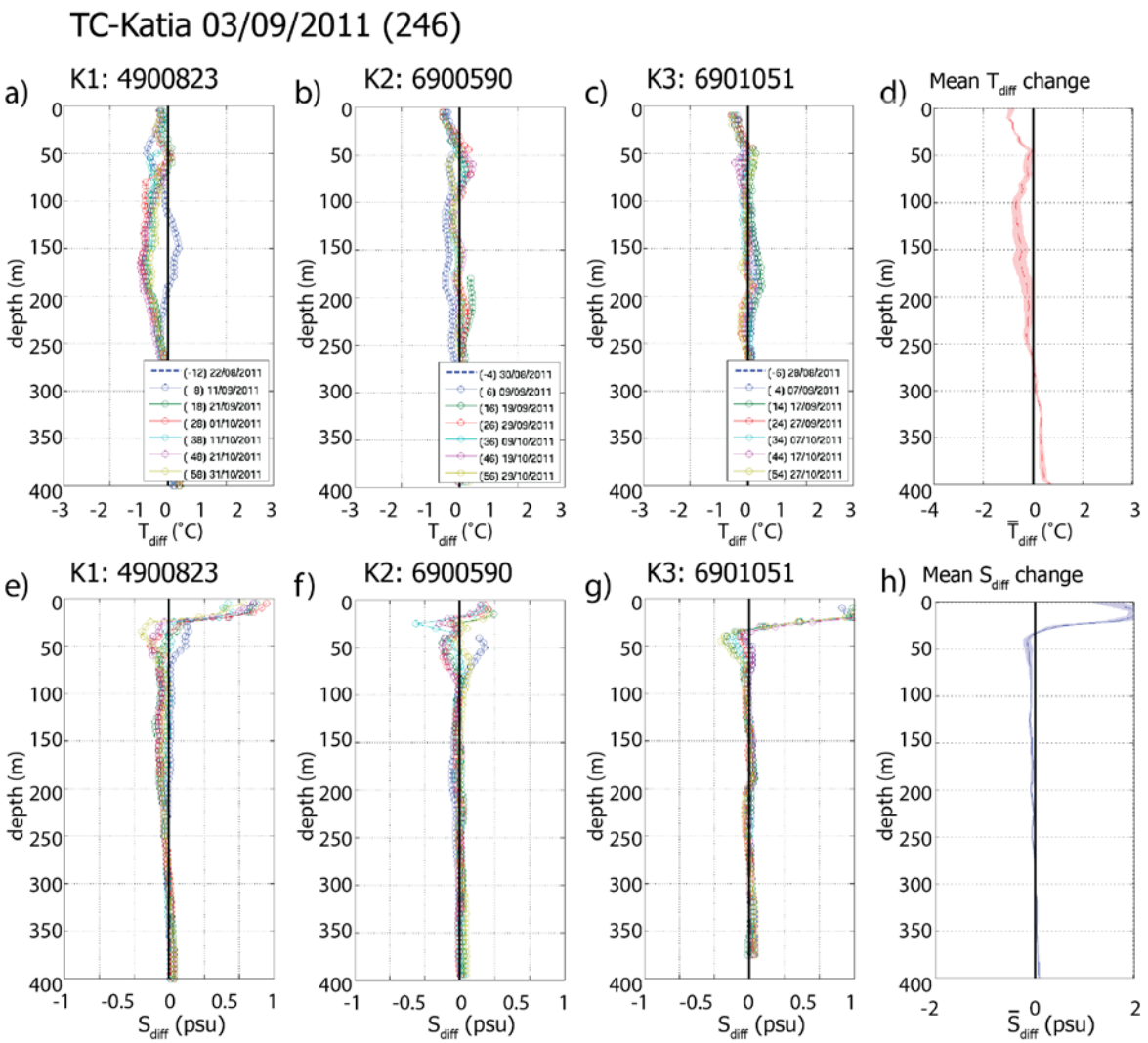

Figure 6-14 TC-induced the largest response in Argo salinity on the 3rd September 2011 (246). There were 3 Argo floats (K1: 4900823, K2: 6900590 and K3: 6901051) TC-induced changes in Argo temperature (a-c) and salinity (e-g) profiles. The average ocean response in temperature (d, $\bar{T}$) and salinity (h,$\bar{S}$) was computed as the average of the profiles from the four floats. The shaded area around the averaged profile is the standard error of the mean (SEM).

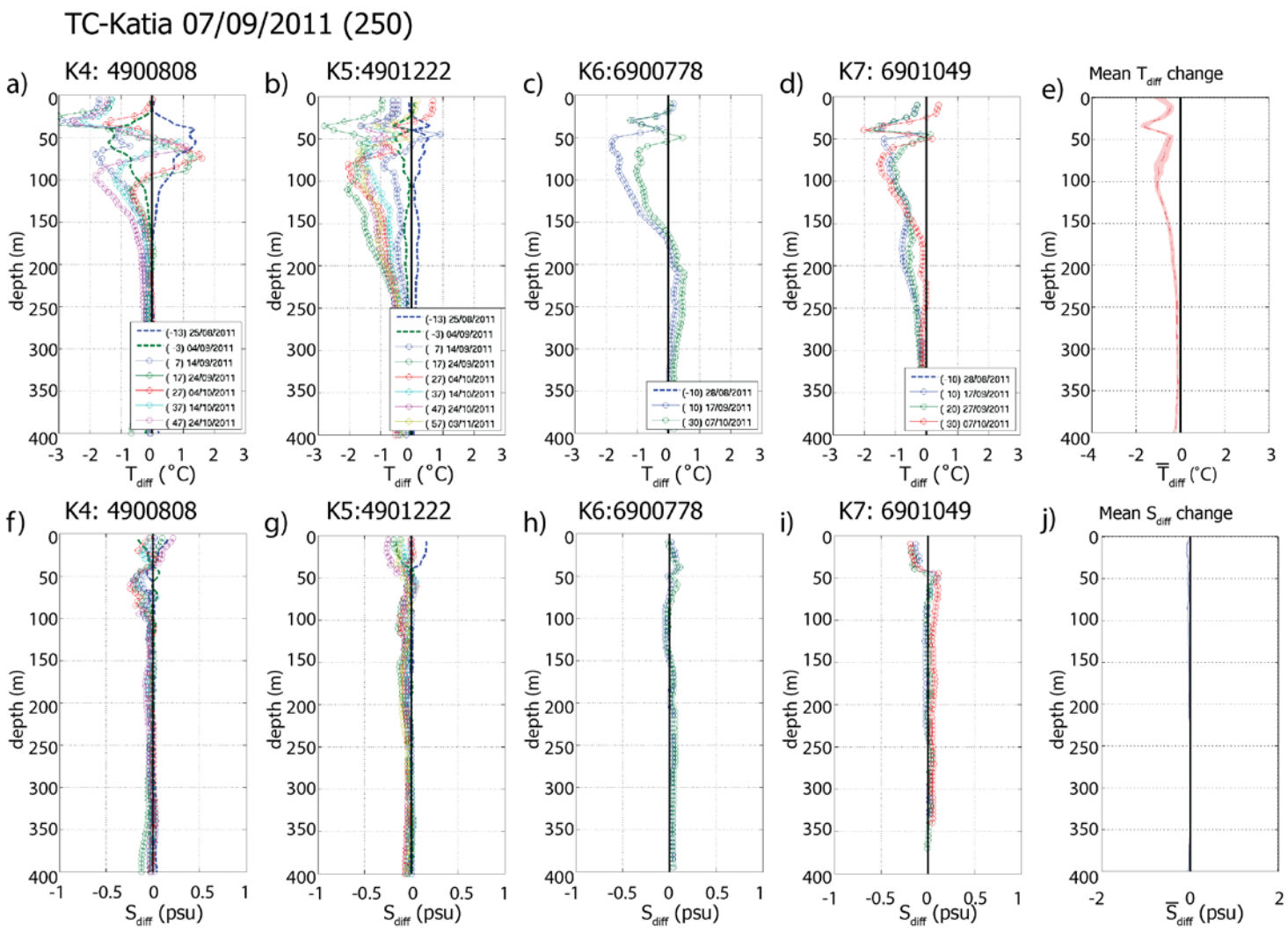

Figure 6-15 Largest TC-induced thermal response on the 7th September 2011 (250). There were 4 Argo floats (K14: 4900808, K5: 4901222, K6: 6900778 and K7: 6901049) TC-induced changes in Argo temperature (a-d) and salinity (f-i) profiles. The average ocean response in temperature (e, $\bar{T}$) and salinity (j,$\bar{S}$) was computed as the average of the profiles from the four floats. The shaded area around the averaged profile is the standard error of the mean (SEM).

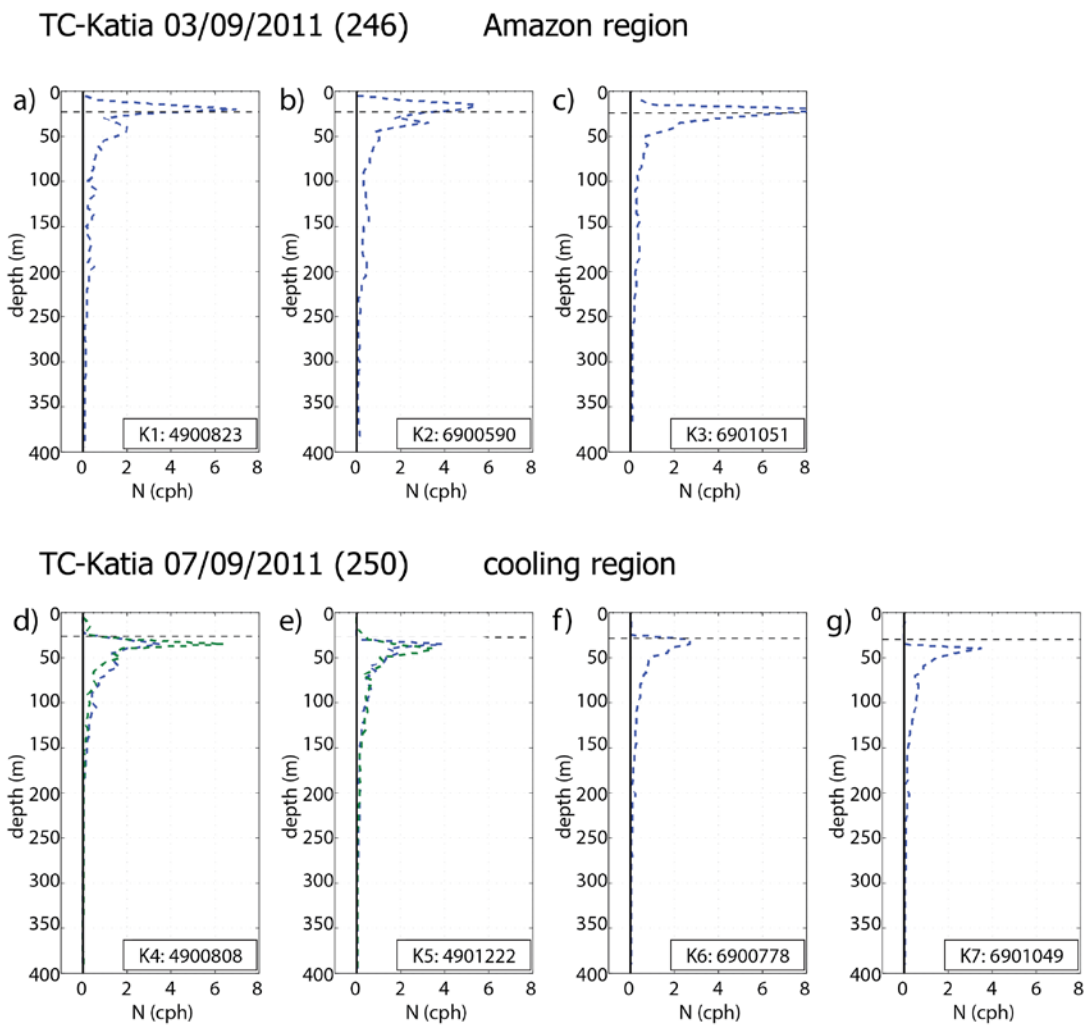

Figure 6-16 Buoyancy frequency (N, cph) as computed at each Argo float around TC-Katia as it passes over the Amazon region (a-b) and through the TC-location where TC-induced the highest surface cooling (e-h). Floats are numbered chronologically as the encounter Katia's path (K1 to K7) and there included the platform identification number. The Mixed Layer Depth (MLD, black-broken line).

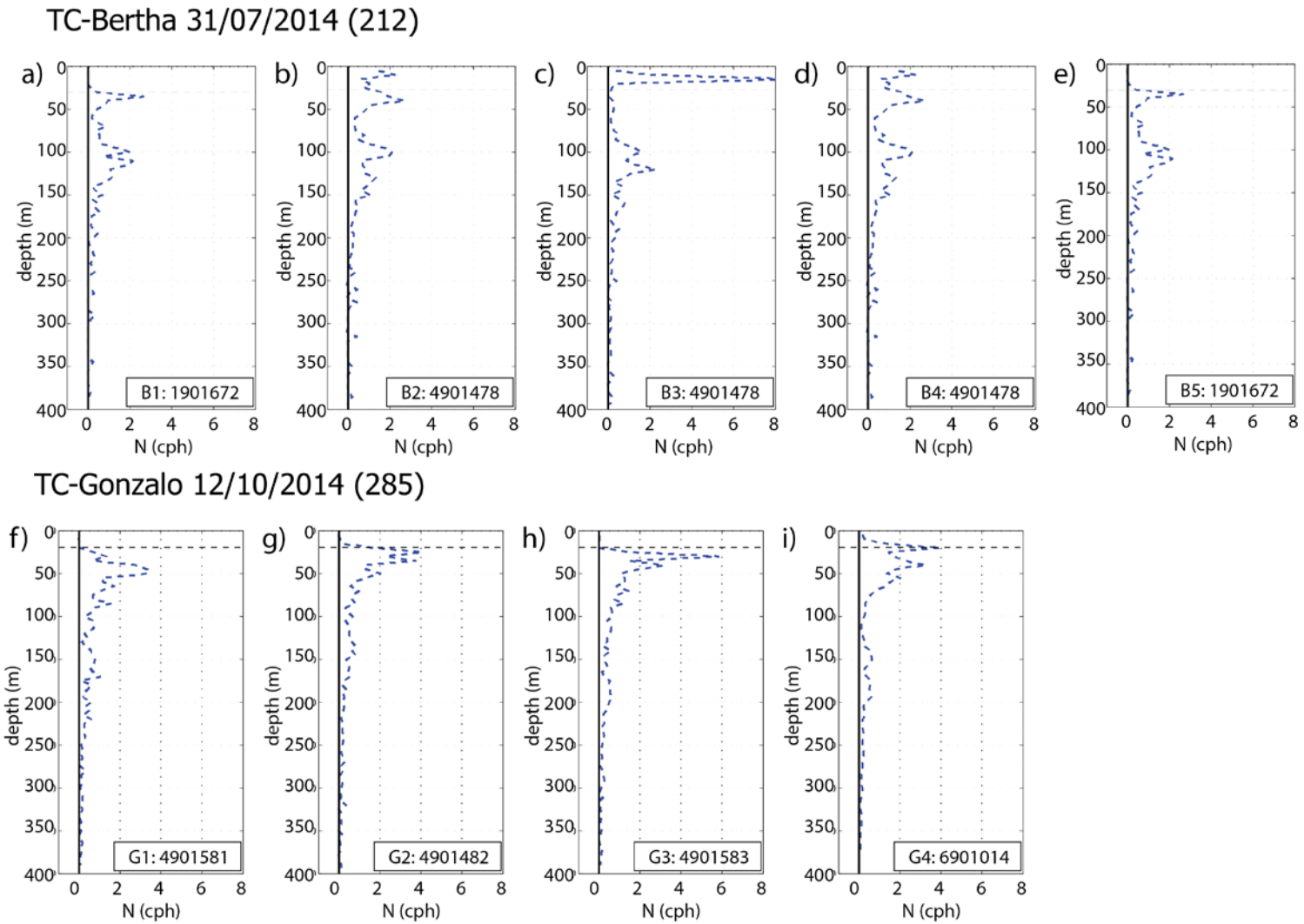

Figure 6-17 Buoyancy frequency (N, cph) as computed at each Argo float around TC-Bertha (a-e) and TC-Gonzalo (f-i) as these cross over the Amazon. Floats are numbered chronologically as these encounter storm's path preceded of the first letter of the TC-name (B: Bertha, G: Gonzalo). There is the platform identification number. The Mixed Layer Depth (MLD, black-broken line).

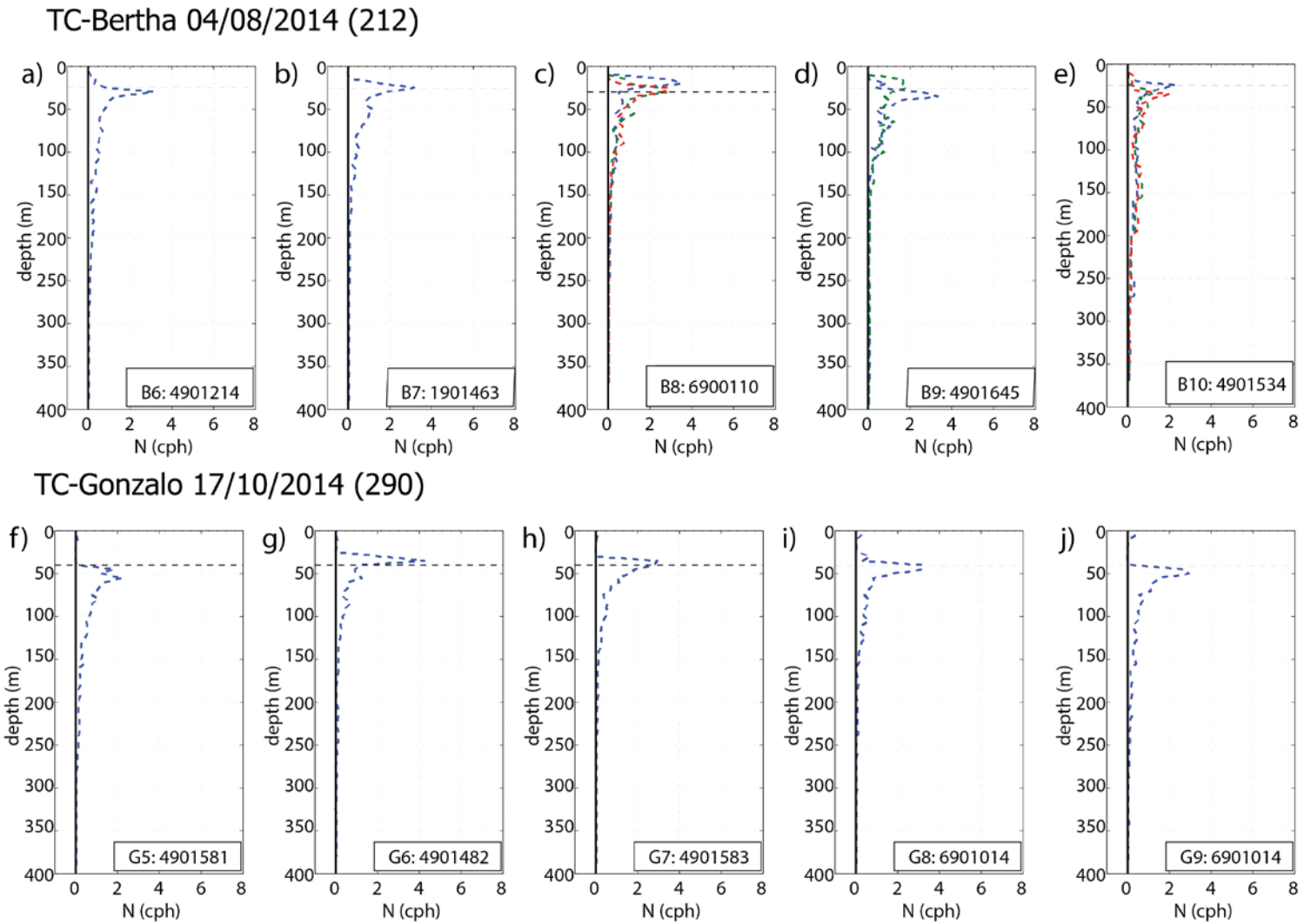

Figure 6-18 Buoyancy frequency (N, cph) as computed at each Argo float around TC-Bertha (a-e) and TC-Gonzalo (f-i) as these cross over their regions of maximum TC-induced cooling. Floats are numbered chronologically as these encounter storm's path preceded of the first letter of the TC-name (B: Bertha, G: Gonzalo). There is the platform identification number. The Mixed Layer Depth (MLD, black-broken line).

6.5 Conclusions

The North Atlantic basin has been the subject of many studies aiming to understand the oceanic response to the passage of TCs [*Androulidakis et al.*, 2016; *Hernandez et al.*, 2014; *L L Liu and Wang*, 2015; *L Y Liu et al.*, 2015; *Reul et al.*, 2014; *Rumyantseva et al.*, 2015]. Most of these storms (80% of all TCs in the North Atlantic) originate as a tropical disturbance from the African easterly winds, near Cape Verde coast and whilst moving westward increase their intensity with the potential of hitting the North and Central American coasts with devastating economic and social consequences [*Pielke et al.*, 2005]. Therefore there is scientific and societal interest in understanding the potential factors modulating TC-intensification.

This chapter presented two case studies using the CTCFP method to study the TC-induced ocean response in 2011 (Figure 6-5) and 2014 (Figure 6-6) over the Open Ocean, where there were cases of TC-overlapping during the first case study but not during the second. There was a similar number of TC occurrences (4 TCs of similar characteristics) during each case study all TCs induced a clear reduction in the SST in the most northern TC-locations. This latitudinal distribution of the TC-induced cooling coincide with the distribution of the natural variability in the basin of MLD and BLT (Figure 5 3 and Figure 5 4), i.e. largest cooling events linked to shallow MLD and attenuated BLT. The difference between the two years was that in 2011 only one TC (i.e. TC-Katia) produced a reduction in SST of more than 2˚C. This results would suggest that cases where TC overlapping occur, the earlier TC would upwell cold water to the surface and deepen the mixed layer depth, so the later TCs would encounter the surface cooling left by the previous TC so it might be not possible to promote a decrease in temperature. Furthermore, based on Figure 6-5 and Figure 6-6 , TC-induced surface cooling may last for about 20 days or more. This result coincided with previous works using model output dataset [*Balaguru et al.*, 2014; *I D Lloyd and Vecchi*, 2011]. Therefore there is enough evidence to suggest that that 20-days is the minimum time lapse between two storms to ensure observations with no TC-activity.

To this date it is already understood that the mechanism by which TC-induced turbulent mixing and upwelling of colder water from below the thermocline is negatively related with TC-intensity [*Price*, 1981]. However, this chapter seeks to study whether there are TC-induced changes in salinity and how these might be related to the already observed TC-induced thermal changes. Such changes have been less reported than thermal changes. Recently though, with the advent of new satellite missions (e.g. SMOS and Aquarius), measuring SSS [*Grodsky et al.*, 2012] and other studies showed that TC-Katia induced an increase in salinity of more than 2 psu on its passage over the Amazon plume. Their work also showed good agreement with some Argo floats, which were operating in the same region. This chapter used the SMOS-L4a data to track salinity changes at the surface and the monthly anomalies in September 2011 showed a salinity increase to the right of TC-Katia. This

pattern was not seen in any other TC included in this study. This new satellite data was a useful information to get the basin wide variability in salinity within a month (Figure 5-6). However, SMOS-SSS time series (Figure 6-8 and Figure 6-9) at each TC-location resulted in a very noisy signal and with limited potential to draw further interpretation from it. However this might change with the new Climate Change Initiative (CCI), which aims to improve the existing SSS data by merging all existing L-band missions. The expectation is that the new dataset will have a better spatial resolution (from current 100 km^2 to 25 km^2) and temporal resolution (from current repeated passes of 10-day to 7 or even 3 repeated passes) [*J. Boutin et al.*, 2018]. So, for future research it would be desirable to use the CCI SSS dataset and test its potential to further study the TC-induced response in SSS.

Next, this chapter used Argo data implementing a CTCFP sampling methodology (see Chapter 4) to observe TC-induced ocean response. This method resulted in a high number of observations both in each TC-location and covering a broad range of ocean conditions. Thus this is a more systematic Argo pairing sampling method than earlier works [e.g.*Grodsky et al.*, 2012].

Both satellite SST and Argo surface temperature observations along TC-track showed there were TC-locations where there was a clear surface cooling. Thus these regions might be flagged as *cooling regions or* areas (latitudes between 20˚ to 35˚ N) where TC induced cooling may commonly occur. Within these cooling regions there was a low water column stability (N ≈ 2 cph), which would support the idea that TC-induced cooling may happen within the *cooling regions*.

Finally, TC-induced changes in Argo salinity were both positive and negative. This chapter found that in 2011 TC-Katia induced the greatest change in salinity, and that is consistent with previous works [*Androulidakis et al.*, 2016; *Grodsky et al.*, 2012; *Reul et al.*, 2014]. In 2014, TC-Gonzalo induced a similar ocean response over the Amazon region where salinity increased more than 1 psu and temperature did not change. This result supports similar findings by [*Domingues et al.*, 2015], who used glider observations in a nearby location. The N-values around TC-Katia were high around the storm on its passage over the Amazon plume (Figure 6-16). However, this was not the case for TCs in 2014 TC-Bertha and TC-Gonzalo, where floats showed no discernible pattern over the Amazon region (Figure 6-17). Therefore, it was not possible to find a pattern that would satisfactorily describe TC-induced changes in salinity and the N-values around the TC-locations.

The presence of fresh water at the surface that creates water column configuration of high stability (i.e. high N-values) is the barrier layer [*Balaguru et al.*, 2012]. Thus the presence of BL may reduce TC-induced cooling, which in turn may promote the TC-intensification. However, the results obtained from Argo showed a TC-induced salinity response, which suggests a complex ocean to storm relationship. Based on the result of this chapter it is not possible to find such a relationship

using *in situ* Argo observations in one location only. Therefore, the next chapter explores the potential of building a composite TC-induced response including all the Argo observations from 2005 to 2015.

Chapter 7

Observational Evidence for an Oceanic Response to Tropical cyclones

7.1 Introduction

As seen in the earlier in Chapter 5 with individual case studies, several North Atlantic storms induced changes seen in situ Argo observations. Although the number of profiles found around the individual storms was higher than previous studies, results were not consistent across similar ocean regions or amongst different case studies. Therefore, this chapter aims to answer the following questions: (1) is there a TC-induced ocean response in terms of salinity?; (2) are salinity and temperature changes related?; and (3) How do changes in salinity relate to TC-intensity?

This chapter used in situ observations from Argo floats operating nearby all storm locations for a 10-year period (2005-2015) in the North Atlantic (NA). To further generalise the observed TC-induced ocean response the analysis was extended to the North East and West Pacific (NEP and NWP) as well as the North Indian Ocean (NI). Whilst the influence of the storm's physical components to the resulting TC-induced response was explored by categorising TCs according to wind speed (i.e. using SSHWS classification) and translation speed (U_H). The limitation of observations might be overcome by using the CTCFP method (Chapter 4) for different TC-locations with similar TC-conditions (e.g. wind and U_H) and with similar ocean conditions (i.e. MLD and BLT).

The layout of the rest of this chapter follows with Section 7.2 which outlines the observational data and method used. Section 7.3 presents the results of applying the CTCFP method to different TC wind and U_H categories and Section 7.4 provide the conclusions.

7.2 Data and Method

Earlier in this thesis (Chapter 3) there was a detailed description of each dataset and the CTCFP method (Chapter 4) used here. TC-locations were obtained from the IBTrACS database. The analysis was initially conducted at latitudes from 5˚ to 45˚ N in the North Atlantic, which included both the formation region (i.e. about 5˚-10˚ N) of most TCs close to the Cape Verde islands and the TC-induced cooling regions on the north west side of the basin. Additionally, this chapter repeated the analyses for the other basins in the Northern Hemisphere within the same latitudinal range where most TCs originate during the summer months (Chapter 2). Within the TC formation latitudes in all basins, during the summer, the seasonal surface temperature routinely exceeds 28 ˚C for much of the lower latitudes of study regions (Figure 7–1). However, the seasonal surface salinity configuration is different in each basin. The North Atlantic is the highest (S > 36 psu), followed by West and East Pacific and the lowest salinity in the Indian Ocean.

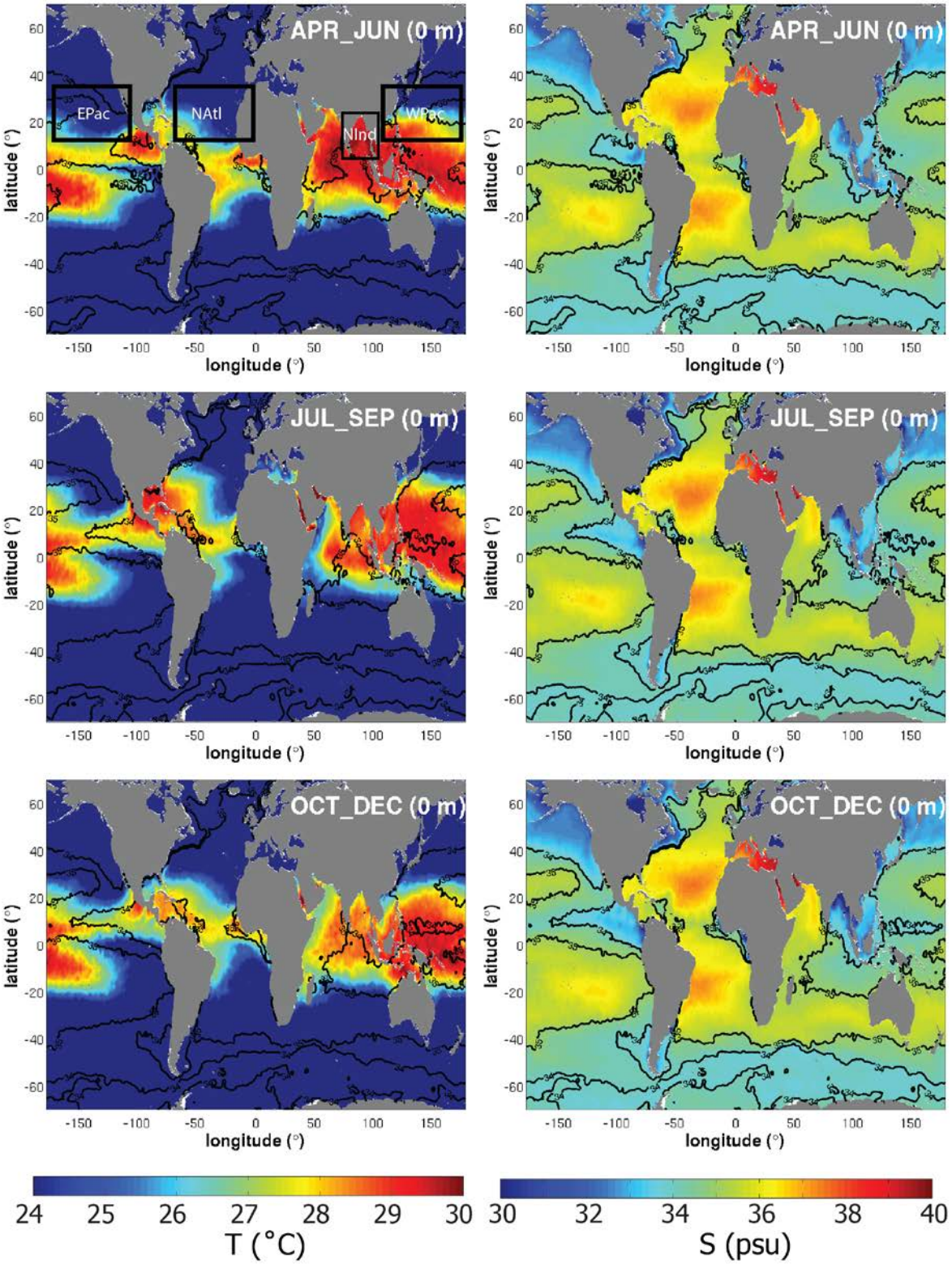

Figure 7–1 Global World Ocean Atlas 2013 (WOA13) seasonal mean surface (1 m depth) temperature (left) and salinity (right). Black boxes in (a) show the study regions, which were: North Atlantic (NA), West Pacific (NWP) and East Pacific (NEP) and the North Indian Ocean (NI).

The latitudinal range of this study included both the tropics and part of the subtropical region. This excluded latitudes where extratropical cyclones form as they are not within the scope of this study.

This chapter applied a storm selection to the IBTrACS database, so it only retains TCs reaching the hurricane category (i.e. TCs of hurricane category SSHWS, wind ≥ 33 m s^{-1}) and generating over the Open Ocean (i.e. first TC location at ≥ 300 km from land). More detail description of this TC selection was given earlier in this thesis (Chapter 6, Section 6.2). Based on the literature review [e.g.: *I D Lloyd and Vecchi*, 2011; *Mei et al.*, 2012], this chapter differentiated fast and slow moving storms as storms moving at translational speed of U_H > 4 m s^{-1} and U_H ≤ 4 m s^{-1} respectively. Earlier research suggests that slow moving storms induce a higher surface cooling than faster moving storms [*I D Lloyd and Vecchi*, 2011]. Thus, slow moving storms are more likely to weaken through the negative feedback system. This suggests that there is translational speed threshold, below which a given storm may be more likely to weaken [*I I Lin et al.*, 2009]. In the Tropics, translational speed is correlated to wind speed (e.g. a category 4 storm will only increase to category 5 if its translational speed is greater than 3.9 m s^{-1})[*Mei et al.*, 2012].

This chapter used Argo temperature and salinity profiles (0 to 400 m depth) in ocean regions within a radial distance of 400 km of an IBTrACS location for a TC (Chapter 4). Floats were paired using the CTCFP method described earlier in this thesis (Chapter 4). This method systematically paired Argo profiles from the same float (i.e. float identification number) operating before and after the passage of the storm at a given TC-location.

The data were first pre-processed by removing the climatological seasonal cycle of temperature and salinity using World Ocean Atlas 2013 (WOA13, see Chapter 3). For each profile location, the wind speed and translational speed were those reported by the IBTrACS dataset at the centre of the TC-location. Furthermore, this chapter used monthly data for the MLD and the BLT (see Section 3.2.2 as described in *de Boyer Montégut* [2004]. Thus, each Argo location was interpolated with the nearest MLD and BLT information and this information was taken as the pre-storm ocean conditions included later in this chapter. MLD and BLT were also computed at each profile, but this information was used for quality check of monthly products of MLD and BLT.

7.3 Results and discussion

7.3.1 Tropical cyclone selection

This chapter presents the results of applying the CTCFP during the storm season (July-October) in the Northern Hemisphere basins from 2005 to 2015. In terms of North Atlantic TC-activity, whilst

August and September were the most active months (Figure 7–2), May and November were the least active months (not shown). These periods of activity agree with the TC-climatology described in Chapter 2. During this period, using the filtering storm criteria explained above, 49 out of 181 TCs were selected as developing over the open ocean with the required high wind speeds. This TC-selection resulted in the analysis of 506 TC-locations distributed in the North Atlantic, which were daily noon (GMT) TC-locations in the IBTrACS dataset.

Following previous studies [*I D Lloyd and Vecchi*, 2011; *Neetu et al.*, 2012; *Price*, 1981; *Emmanuel M. Vincent et al.*, 2012], this thesis used a fixed radius of 400 km as the area affected by the passage of the storm in the North Atlantic (Figure 7–2). As seen in Chapter 4 (Figure 4–1), the analysis of the global TC frequency is dependent in the choice of the searching radius at a given TC location. Thus the choice of 400 km resulted in a larger region affected by the passage of a storm compared to a 200 km radius. Furthermore, this radius is a good choice to ensure there were Argo observations within each TC location (Chapter 4) and to reduce the uncertainty relating to the background variability.

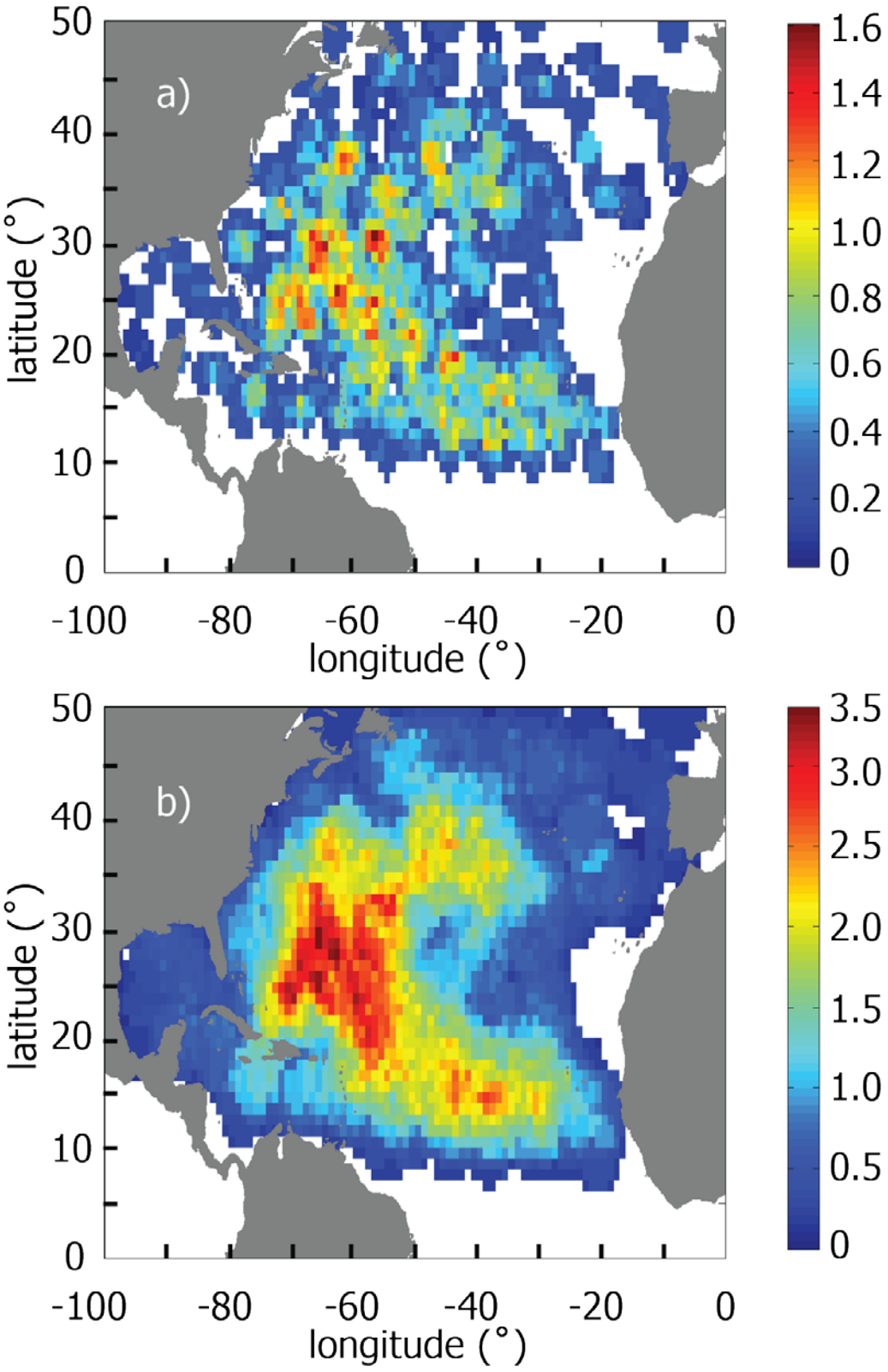

Figure 7–2 Frequencies of yearly TC events in the North Atlantic from 2005 to 2015 affecting 1˚ by 1˚ bin boxes when TC affected regions is assumed to be a radial distance of **(a)** 200 km or **(b)** 400 km from the centre of the storm. Frequencies were computed as the number of the storms in each bin box divided by the total number of years. Notice colour scale are different rage, so changes in each plot are visible. This figure supports the conclusions (Section 4.2) of choosing a general fixed searching radius.

As seen in Figure 7–3, when all the storms in IBTrACS are included, the translational speed shows a clear latitudinal dependency (Figure 7–3a, no-filter). This latitudinal dependency is less clear when the storms are filtered. These results are in agreement with previous studies that investigated the translational speed variability globally [*Mei et al.*, 2012]. The meridional variability of the translational speed also showed a reduced amplitude in the signal when filtering storms (Figure 7–3 b). Furthermore, there was a clear latitudinal variation of the wind speed (Figure 7–3c). TCs tend to intensify with latitude reaching a maximum at about 22˚ N (Figure 7–3c), poleward of this, TC intensification stops increasing with some evidence of a slight decrease towards the pole. The meridional TC-intensity variability including all storms (Figure 7–3d no-filter) showed a westward intensification from the areas where TCs form. This meridional intensification levelled off by looking at the selected storms only (Figure 7–3d, filtering), which might be a result of removing the storm intensification at the moment approaching coastal regions. TCs moving eastward tend to have a wind speed less than critical threshold (i.e. 33 m s^{-1}) and so are excluded from this analysis.

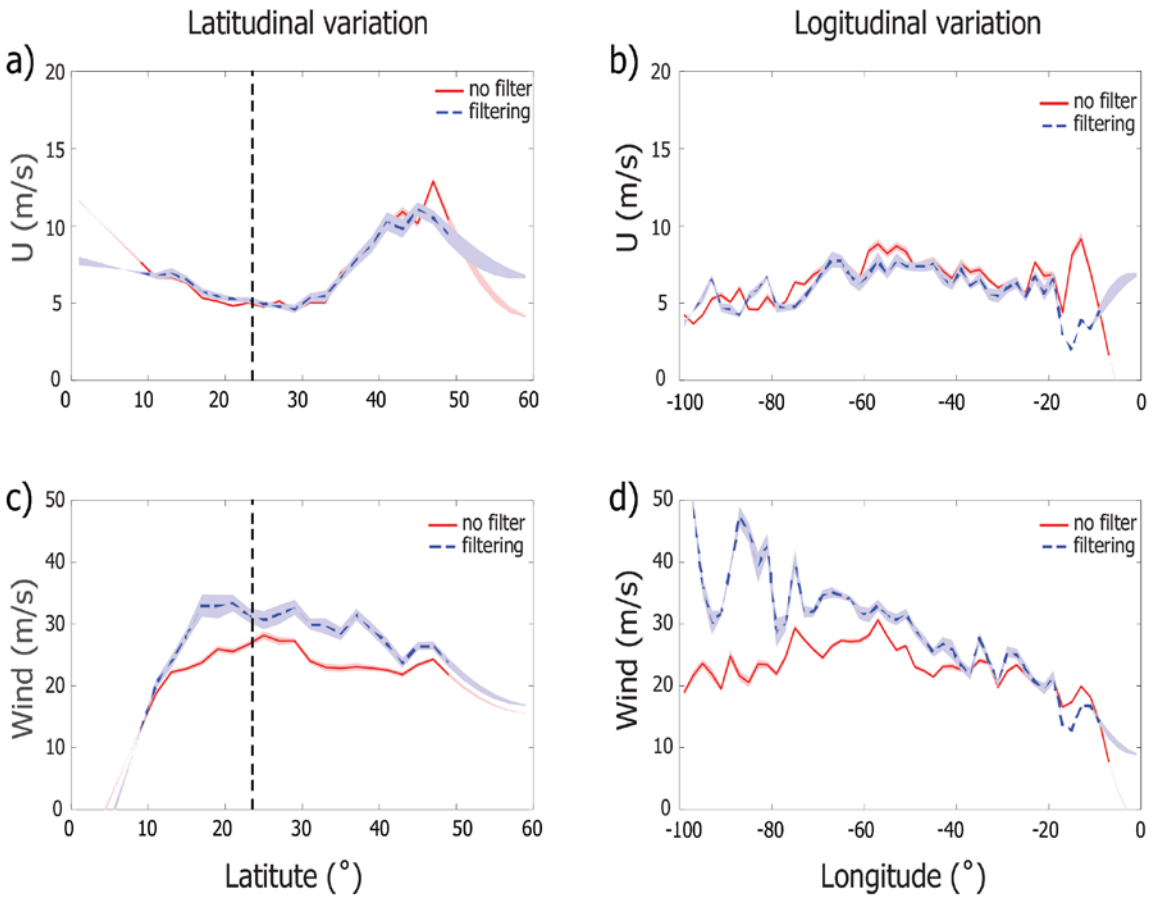

Figure 7–3 North Atlantic (2005 – 2015) Tropical cyclones translational speed (a-b) and the wind speed (c-d) variability along latitudes (left) and longitude (left). Both translational speed (U) and wind speed (wind) were in meters per second. The application of the filter (blue) removed storms not reaching hurricane category within the open ocean (i.e. at least 200 km from land). The 22˚ N (vertical broken line) marks the latitudes south of which most TC-intensification occurs. The other basins showed similar latitudinal and longitudinal variation patterns.

7.3.2 Translational speed and Oceanic TC-Response in Argo

Within the period 2005-2015 in the North Atlantic, the composite TC-response included 1282 pairs of Argo profiles across all wind and translational speeds (Figure 7–4a). The number of observations was not homogeneous across categories (Table 7-1), but there were limited observations around slow moving storms ($U_H \leq 4$ m s^{-1}) of category 2 or above (Table 7-1). Fast moving storms ($U_H > 4$ m s^{-1}) had more observations up to category 4. In general the higher the category the fewer observations, which might be related to the fact that open ocean North Atlantic TCs reached a maximum of category 4 intensity within the study region. However, there might be more storms intensifying above category 4, but close to land at the western boundary or where the storms are north of 40˚ N, which in either case were excluded. Furthermore, whilst TC-locations up to category 1 were distributed across all latitudes (Figure 7–4 a), TC-locations of category 2 and 3 were concentrated within the middle section of the basin between 15˚ to 25˚ N and 60˚ to 25˚ W. Most of the study region within the basin had at least 5 paired profiles within the first 20 days after the passage of the storm (Figure 7–4 b).

Table 7-1 Argo paired observations around Tropical cyclones in the North Atlantic, North East and West Pacific and in the Indian Ocean. Observations were divided by intensity on the Saffir-Simpson Hurricane scale and by the translational speed of the storm (slow: $U_H \leq 4 m\ s^{-1}$; and fast $U_H > 4\ m\ s^{-1}$). Storm locations at 12:00 GMT were extracted from IBTrACS dataset during the period 2005-2015.

Ocean basin	North Atlantic		North East Pacific		North West Pacific		North Indian	
	SLOW	FAST	SLOW	FAST	SLOW	FAST	SLOW	FAST
CATEGORY								
0	525	1004	811	1176	3385	4451	842	118
1	109	474	173	268	1650	1786	270	45
2	20	142	60	86	1297	1120	66	0
3	8	92	40	45	716	640	131	4
4	38	61	39	65	324	586	61	0
5	0	2	0	6	0	36	0	0
Subtotal	525	1004	811	1176	3385	4451	842	118
TOTAL	2475		2769		15991		1537	

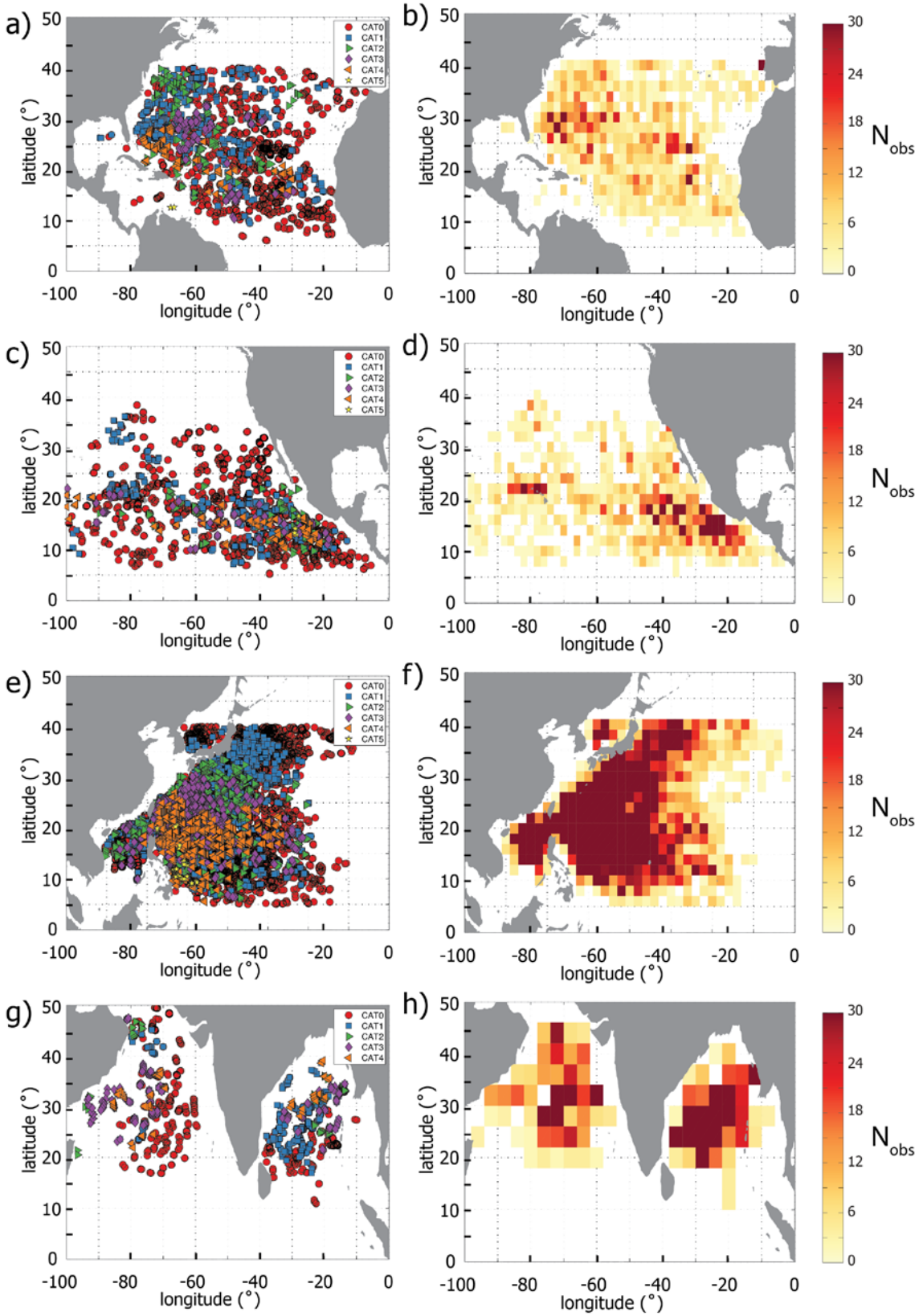

Figure 7–4 Argo paired locations (2005-2015) captured within ±20 days from the passage of the storm and distributed according to the wind category on Saffir Simpson wind speed scale (left) in the (a) North Atlantic, (c) North East Pacific, (e) North West Pacific and (g) North Indian Ocean. (b, d, f and h) For same regions the number of Argo paired profiles in bins 2˚ by 2˚ in the same basins (right).

Although recently some Argo floats have been deployed with the capability of profiling at depths as shallow as 1 m, this chapter used a depth of 10 m as the shallowest depth, which in many cases can be compared to satellite observations (both SST and SSS) [*Jacqueline Boutin et al.*, 2012]. Furthermore, the interaction between the ocean and a storm is at the surface and more specifically near the eye, which is the region where thermal changes are most important in the negative feedback system [*Price*, 1983]. Temperature changes (T_{diff}) in the North Atlantic (Figure 7–5) at 10 m depth show that, on average, the cooling peaked when storms travelled at 4 m s^{-1}. This matches the threshold between fast and slow moving systems described above.

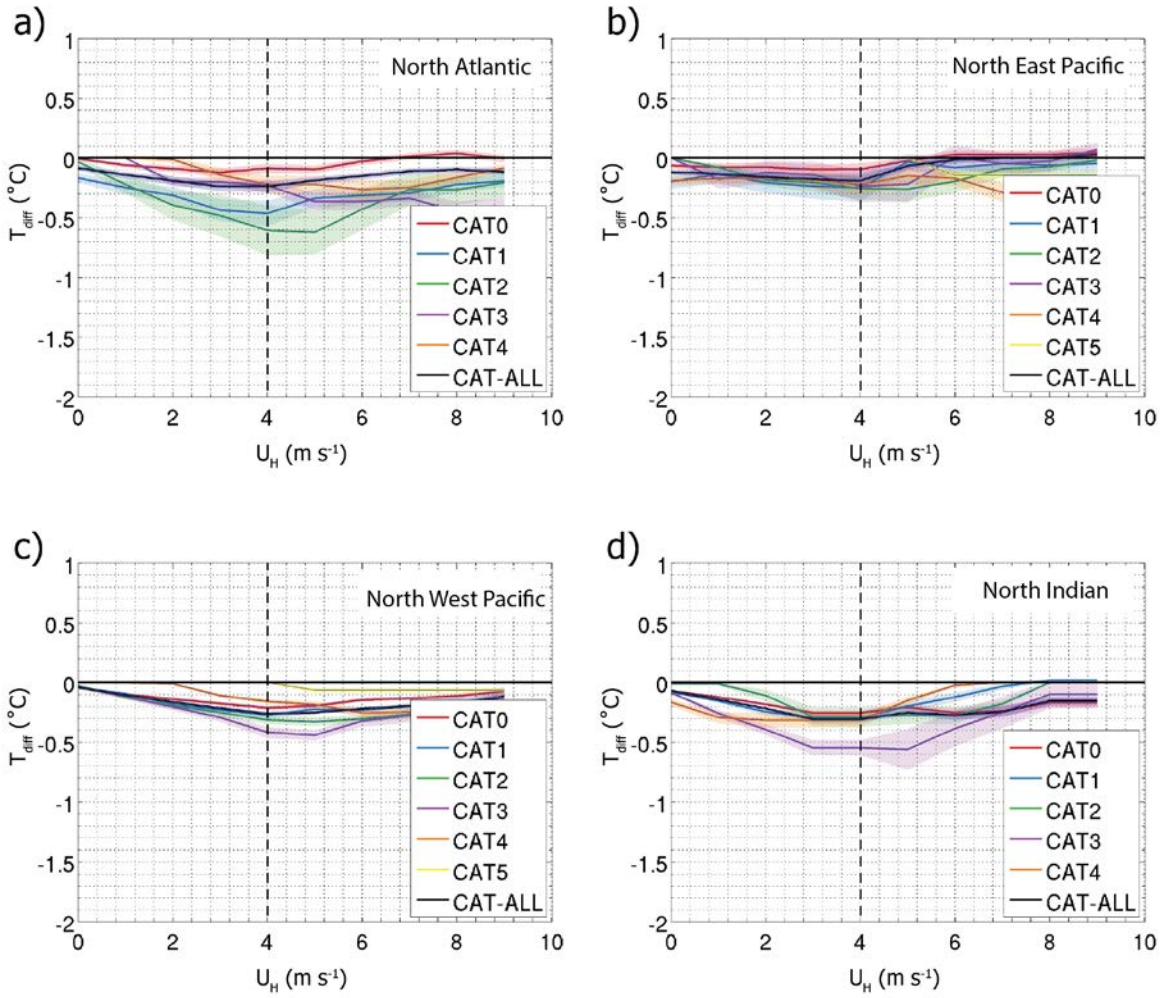

Figure 7–5 Tropical cyclone induced changes in Argo temperature (T_{diff}) at 10 m against the translational speed (U_H, m s^{-1}) in the (a) North Atlantic, (b) North East Pacific, (c) North West Pacific and in (d) North Indian. The dashed line indicates the division used in this study between slow-moving ($U_H \leq 4$ m s^{-1}) and fast-moving storms ($U_H > 4$ m s^{-1}). The lines of this plot were smoothed using a moving window of 5 units along the x-axis. The standard error of the mean (SEM; shaded area) was computed as the standard deviation divided by the square root of the number of observations.

There was no such clear dependency of TC-induced changes in Argo salinity (S_{diff}) at 10 m and the translational speed (Figure 7–6 a). For example, in the North Atlantic, storms induced an average salinity increase of about 0.1 psu for storms of category 1 and 2 moving at about 4 m s^{-1} or more. The average salinity response in the North East Pacific (Figure 7–6 b) showed an increase at translational speeds as low as 1 m s^{-1}. In the North West Pacific (Figure 7–6 c) salinity changes peaked at about 0.05 psu at 5 m s^{-1}. Finally, TCs in the North Indian Ocean (Figure 7–6 d) did not show a clear change in salinity at translational speeds between 3 and 4 m s^{-1}. Furthermore, in the North Indian basin only, whilst most of the storm categories show a salinity increase of up to 0.1 psu, category 3 storms show decrease in salinity. These results suggest that the threshold translational speed used may not be equal across different basins.

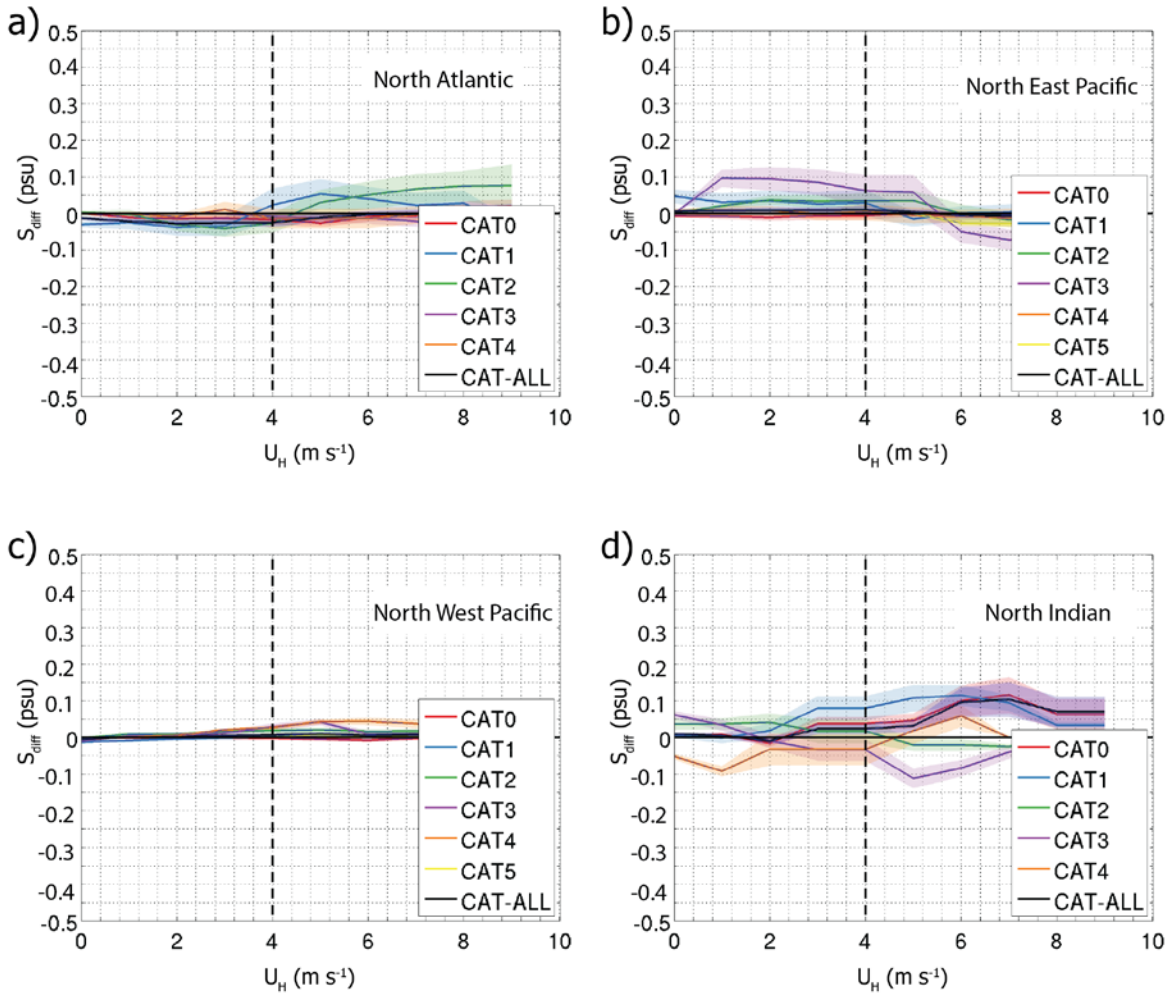

Figure 7–6 Tropical cyclone induced changes in Argo salinity (S_{diff}) at 10 m against the translational speed (U_H, m s^{-1}) in the (a) North Atlantic, (b) North East Pacific, (c) North West Pacific and in (d) North Indian. The dashed line indicates the division used in this study between slow-moving ($U_H \leq 4$ m s^{-1}) and fast-moving storms ($U_H > 4$ m s^{-1}). The lines of this plot were smoothed using a moving average with a moving window of 5 units along the x-axis. The standard error of the mean or SEM (shaded area) was computed as the standard deviation divided by the square root of the number of observations.

TC induced temperature changes did not recover to the pre-storm values. The term recovery time was used as when observations (T or S) returned to about 0.5 units (~0.2 units for salinity) from the maximum TC induced change. In the North Atlantic, TC-induced changes in temperature (Figure 7–7 a-b) at 10 m depth showed that, excluding category 3 storms, the overall recovery time was about 20-25 days after the passage of the storm. The TC-induced thermal response averaged across all storms (i.e. no distinction of wind and translational speed) resulted in a surface cooling of about 0.5 ˚C. However, the TC-induced thermal response was considerably larger at slow speeds than at fast translational speeds. The scarcity of observations of storms of higher categories (i.e. Category 4 and Category 5) limits the knowledge of the TC-induced response with higher wind speeds. The thermal TC-induced response was monotonically increasing with wind speed for slow moving storms (Figure 7–8 b). However, this is not same for fast moving storms (Figure 7–8 a), where category 2 storms show a larger cooling than category 3 storms. These results of the TC-induced changes at the surface obtained using the composite method are consistent with previous satellite SST observations [*I D Lloyd and Vecchi*, 2011; *Mei et al.*, 2012].

The North Atlantic composite TC-response in salinity at 10 m depth shown in Figure 7–8 a-b within the first 20 days after the passage of the storm reflect those results from TC-induced ocean thermal response in many aspects. The greatest S_{diff} was linked to storms of category 2 and this was higher still with storms of higher intensity. However, contrary to that described in the TC-induced thermal changes, in the North Atlantic fast moving storms demonstrate a larger salinity increase compared to slow moving storms. Thus category 2, fast moving storms resulted in an average salinity increase of about 0.4 psu (10 to 15 days after TC) and whereas for the same category for slow moving storms the change was a 0.2 psu increase within the first week. Furthermore, the salinity induced response under category 3 storms varied between ±0.2 psu. These results agreed with the salinity changes described in the previous chapter that TC-induced changes in salinity can be either positive or negative.

The timings of the thermal and salinity response were not coincident (Figure 7–7 and Figure 7–8), for either slow or fast moving storms. Thus for slow moving TC category 2 storms, the largest TC-induced cooling occurred within 15-20 days after the passage of the storm. On the other hand, under the same storm conditions, the largest S_{diff} occurred 6-8 days after the passage of the storm. Furthermore, fast moving TC category 2 storms induced the largest surface cooing (T_{diff} = 1.5˚C) and the largest salinity change (S_{diff} = 0.2 psu) at about 3 and 10 days after the passage of the storm respectively.

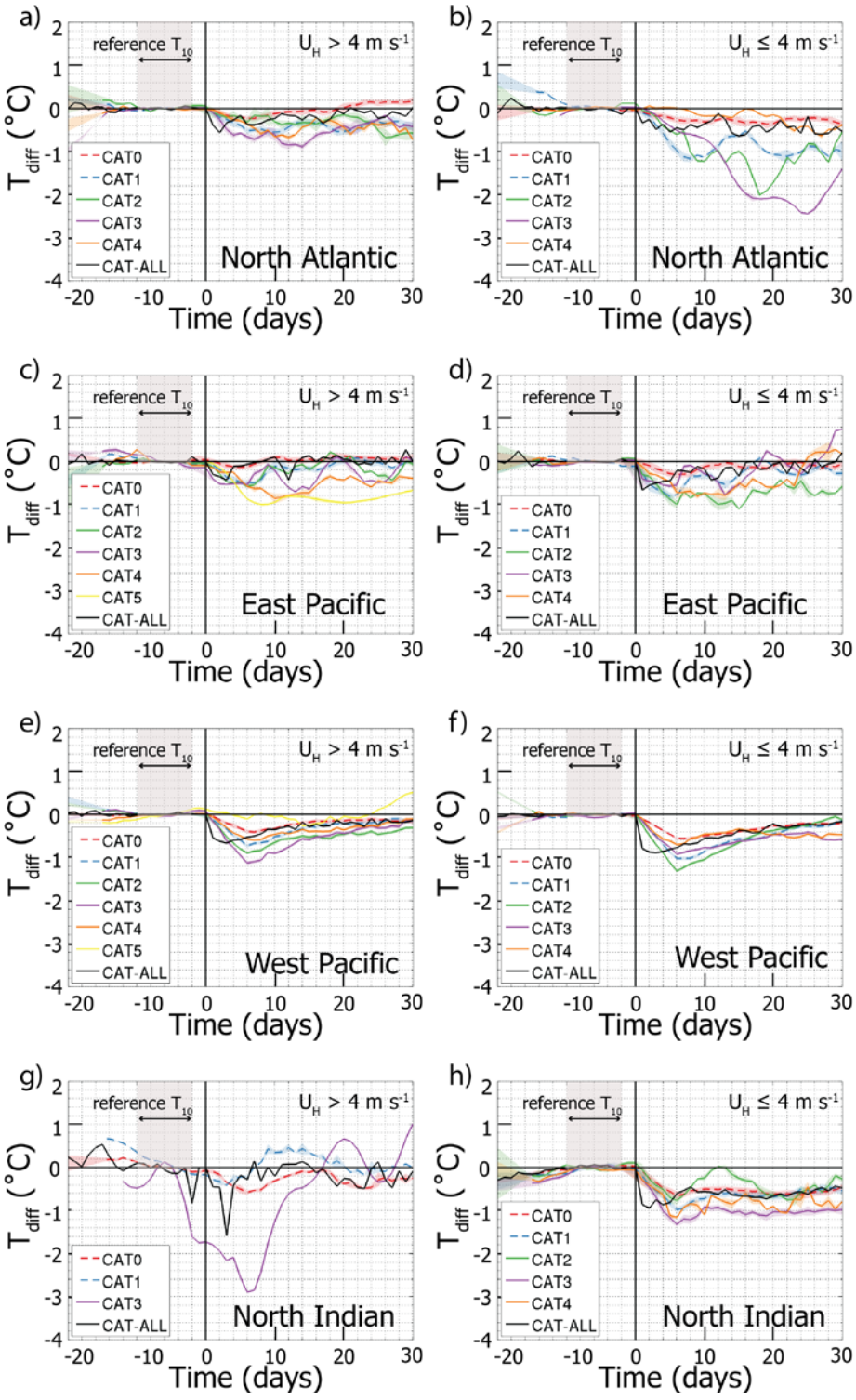

Figure 7–7 2005-2015 CTCFP ocean response in Argo (depth = 10 m) salinity (S_{diff}) for slow (right) and fast (left) moving storms for each wind category in SSHWS. Salinity reference (grey area) was the average over days -13 to -3 at each TC-location in the North Atlantic, East Pacific, West Pacific and North Indian Oceans. The shaded area around the lines is the standard error of the mean (SEM).

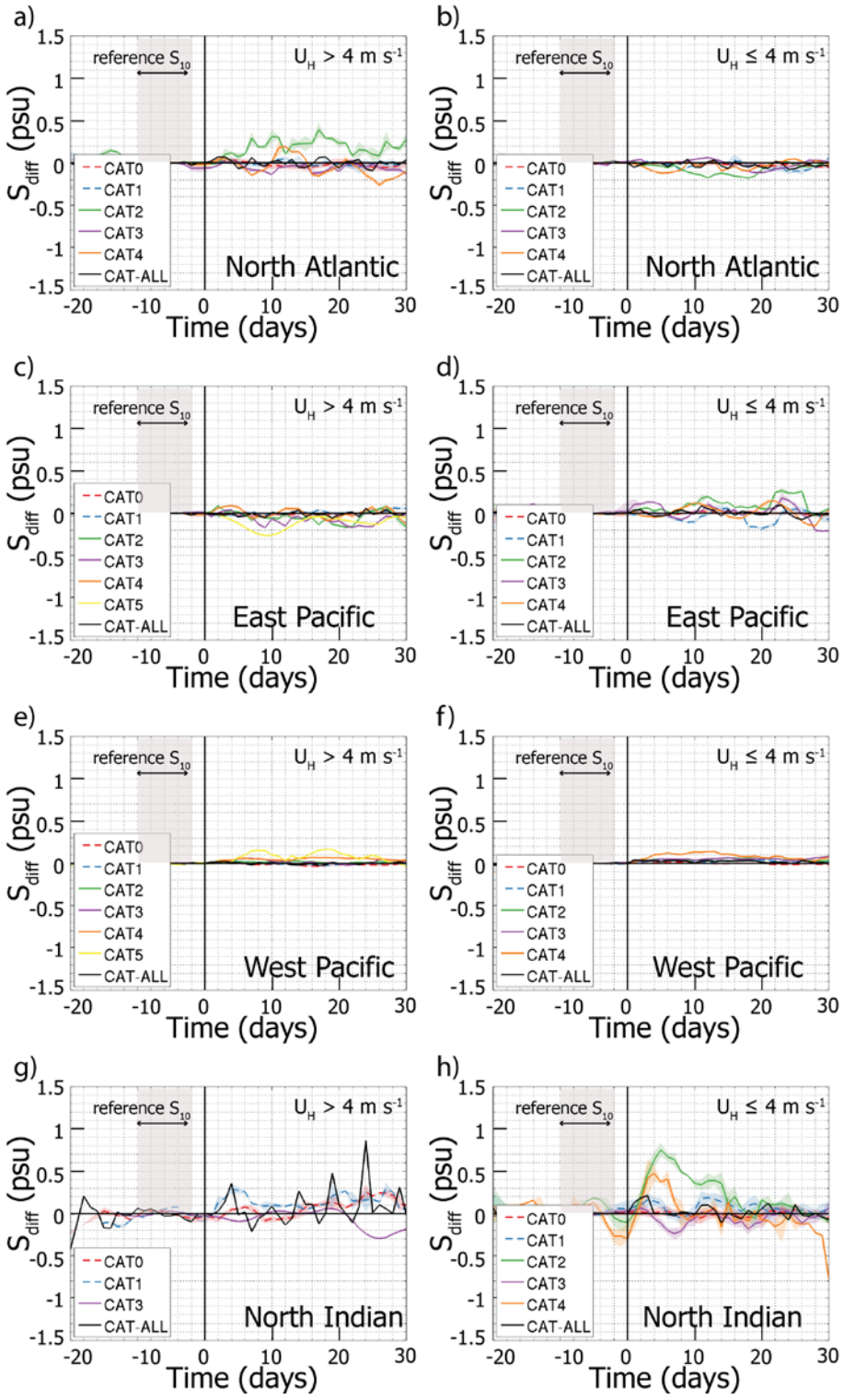

Figure 7–8 2005-2015 CTCFP ocean response in Argo (depth = 10 m) salinity (S_{diff}) for slow (right) and fast (left) moving storms for each wind category in SSHWS. Salinity reference (grey area) was the average over days -13 to -3 at each TC-location in the North Atlantic, East Pacific, West Pacific and North Indian Oceans. As discussed in the main text and in Table 7-1, there is a big disparity between different TC categories. This should be tacken into account in the interpretation of the observed TC induced increased salinity under slow TCs CAT2 in the North Indian Ocean. The shaded area around the lines is the standard error of the mean (SEM).

7.3.3 Global Temperature and Salinity Response

The overall thermal composite response was mostly negative across all basins (notice the North Indian had a limited number of observations, which will be discussed later), suggesting that in general the passage of the storm induced a surface cooling. Storms in the North Atlantic induced the largest cooling followed by West and East Pacific and then North Indian Ocean (Figure 7–7). On average for all basins slow moving storms resulted in a greater temperature change than resulting from fast moving storms. This supports the hypothesis that slow moving storms potentially have more of an impact due to the longer exposure time of a given ocean location to the storm [*I D Lloyd and Vecchi*, 2011]. Furthermore, there is a non-monotonic dependence of the temperature change and the intensity of the storm, which can be related to the fact that TC-induced cooling leads to a reduction in the TC-intensification system [*Ginis*, 2002; *I D Lloyd and Vecchi*, 2011; *Schade and Emanuel*, 1999].

The global composite response in salinity (Figure 7–8) showed very different patterns of change and there was no predominant type of change. Whilst thermal changes somehow related to the TC-intensity and translational speed, salinity changes were not. However, there were some distinctive changes, where the absolute average change was higher than 0.1 psu, which is much greater than the instrumental accuracy in Argo floats (±0.01 psu). These changes were positive in the North Indian and in the North Atlantic Ocean and were induced by category 2 storms. Nevertheless in both these basins, TC-induced haline changes resulted from category 2 storms, in the North Indian these were slow moving and in the North Atlantic were fast moving. The number of observations in the Indian Ocean (N_{obs} = 118) was low compared to the North Atlantic (N_{obs} = 1004) (Table 7-1). This thesis did not further investigate how these results might vary upon a change in the number of observations. However, the study in the Indian Ocean is limited by the number of observations.

In the North East Pacific, category 2, slow moving storms induced a cooling ($T_{diff} \approx -1\,^{\circ}C$) and a salinity decrease or freshening ($S_{diff} \approx -0.4$ psu). This is different to the ocean response described in the North Atlantic, where storms of the same strength induced a cooling ($T_{diff} \leq -2\,^{\circ}C$) and a salinity increase ($S_{diff} \approx 0.5$ psu). Furthermore, results of the haline composite response in the North West Pacific were near zero across all categories. Finally, the North West Pacific saw the higher number of observation (Table 7-1) around the strongest storms (i.e. TC category 5), which were TC locations approaching Pacific islands of Papua Guinea, Indonesia and Philippines (Figure 7–4). These results suggest that TC-induced changes are only partly related to the wind and translational speeds alone and there might be other factors controlling the TC-induced changes in both temperature and especially salinity.

7.3.4 Extent of TC Ocean Response in the North Atlantic

To study the vertical extent across track, the vertical profiles within the search radius from the storm centre were averaged along the X-axis (as referenced from storm's track). As most of the thermal and haline TC-induced responses occurred within the first 20 days after the passage of the storm, the vertical cross section composite included the average profiles from day 1 to day 20.

The resulting TC-induced response including all storms resulted in the average TC-induced ocean response shown in Figure 7–9. There was an average cooling of about -0.4˚C that extended about 100 km from the centre of the storm on both sides of the storm from the surface down to 400 m (Figure 7–9 a). The average thermal response was spatially right biased, as the surface cooling on the right side of the storm was larger than that to the left. Whilst the TC-induced cooling extended from 0 km to more than 300 km to the right, it only extended to 100 km to left (Figure 7–9 a). These results are in agreement with the righthand side bias seen in satellite observations and supported by theory [*Monaldo et al.*, 1997; *Price et al.*, 2008; *Stramma et al.*, 1986]. In addition to the surface cooling, there is a clear subsurface warming core at about 220 km to the right of the storm, where storms induced an increase of almost 1 ˚C to the waters at ~50 m depth. There is another warming core at the same depth to the left (100 km from the centre), where there was an average temperature increase of almost 0.5 ˚C. These results agree with model simulations showing the maximum TC-induced anomaly to be located about 60 km to the right of the storm [*Price*, 1981].

The average TC-induced response included an increase in salinity (positive S_{diff}, up to ~0.2 psu) to the right (0 to 75 km) of the storm and on average a decrease in salinity to the left (0 to -100 km) of about -0.04 psu (Figure 7–9b). Although the positive salinity anomaly to the right had a similar extension to the surface cooling, there was a saltier patch at about 50 km to the right where the average salinity change peaked above 0.2 psu. To the left of the storm track there was a clear decrease in near-surface salinity, where the average salinity dropped to -0.1 psu from the centre to about 150 km and within the top 50 m of the water column. It is possible to distinguish a freshening 100 km to the right of the storm at about the same depth. These results show as an asymmetry of the haline ocean response to the passage of the storm, which depends on two storm related mechanisms. Whilst the salinity increase to the right might be related to the dominant rightward wind induced turbulent mixing [*Price*, 2009], the surface freshening to the left might be related to the leftward rainfall bias noticed from passive microwave satellite observations [*Cecil and Wingo*, 2009].

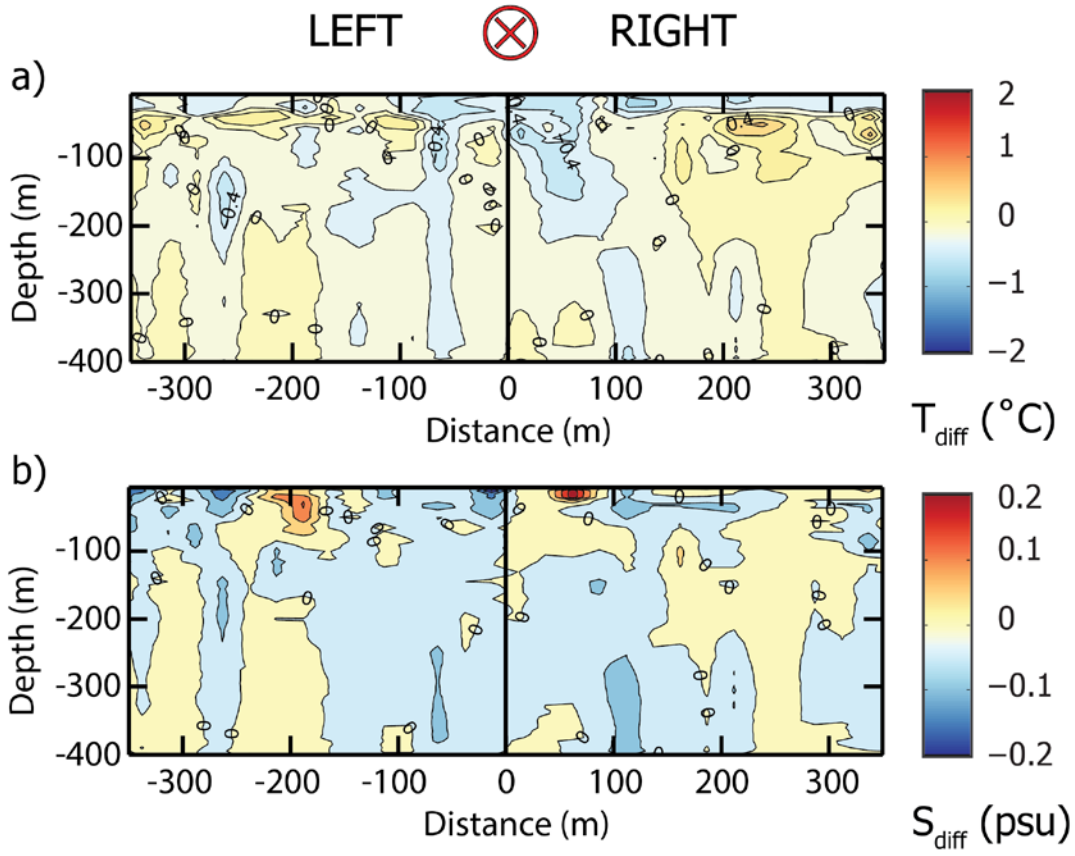

Figure 7–9 Cross track section (X-axis) of the average (from 1 to 20 days after storm's passage) composite TC-induced differences in temperatuere (a) and in salinity (b) in the North Atlantic. Notice that the TC forward direction goes into the plane of the drawing (circle with an inscribed X) and divides the plane to the right (x > 0 km) and to the left (x < 0 km) section of the storm.

Additionally, TC-induced responses in salinity and in temperature were different from each other. This data did not show any correlation (R ≈0) between T_{diff} and S_{diff}. As it was stated before, the sign of the TC-induced changes might be linked to the rainfall within the storm. However, there was also no correlation between S_{diff} and T_{diff} at different distances from the centre of the storm.

7.3.5 North Atlantic Ocean Response to Atmospheric Factors

This thesis characterized the atmospheric component of the storm by its wind and translational speeds and also by its size (i.e. fixed radius of 400 km). To discern the composite ocean response, sensitivity to each of these features (excluding storm size), both thermal (Figure 7–10) and haline (Figure 7–11) responses were computed for each of these features separately. Storms were grouped as weak (categories 0 to 2) and strong (categories 3 to 5). The resulting thermal composites for weak and strong storms (Figure 7–10 a-b) showed similar patterns than for the average thermal response (Figure 7–9 a). Further salinity composites for different TC-intensity showed basic salinity changes to the ones observed in the average salinity composite (Figure 7–9b and Figure 7–10 c-d).

There were significant differences in the magnitudes of the observed changes between different TC-intensities. Whilst weak storms induced an average cooling of 0.4 ˚C, strong TCs induced an average cooling of over 1.5 ˚C. Furthermore weak storms induced changes from the surface down to a maximum depth of 200 m to the right of the storm and down to 400 m to the left of the storm.

The thermal composite response was different between slow and fast moving storms. Whilst slow moving storms induced a clear surface cooling (Figure 7–10 c), fast moving storms resulted in a reduced cooling to the left of the storm (Figure 7–10 d). These results support the hypothesis that the maximum TC-induced ocean response links to slow and strong storms. Additionally, under fast moving storms cooling was concentrated between ± 100 km from the centre of the storm and was concentrated in the upper 250 m of the water column. The thermal positive changes in temperature could indicate warming due to wind-induced downwelling [*Price*, 1981]. These warming vertical structures were clearer under slow and especially strong storms, where there was a TC-induced positive thermal change of up 1.2˚C to the right of the storm. These observations also confirm the rightward bias in the surface cooling and also are the most visible under strong storms and to some extent under fast moving storms. Thus, under strong storms, cooling to the right of the storm had a larger spatial (cooling extension ≈ 250 km to the right) extension than to the left side (cooling extension ≈ 100 km to the left). The cooling depth under these storms also was deeper on the right (cooling depth ≈ 400 m) compared to the left side (cooling depth ≈ 250 m).

The saline composite response in the North Atlantic peaked under strong storms (Figure 7–11 b). Salinity changes reached 0.15 psu on average and extended from the surface down to a maximum depth of 100 m. Below this depth, salinity changes inverted its sign, thus a TC-induced salinity increase resulted at the surface and a freshening at greater depths. Furthermore, strong storms showed a rightward bias in the salinity changes both positive and negative. This supports the hypothesis that the rightward bias is driven by the strong surface winds [*Price*, 1981]. Furthermore, these results suggest that the salinity increase is mainly related to high intensity storms and with lower magnitude of change to fast moving storm (Figure 7–11 b and d). Slow moving storms increased the salinity just below the core of the storm between ±50 km from the centre of the storm (Figure 7–11 c). Additionally, to the left (at about 180 km and 250 km) of the slow moving storms there were two strong freshening patches (S_{diff} ≈ -0.2 psu), which extended from surface to about 200 m depth.

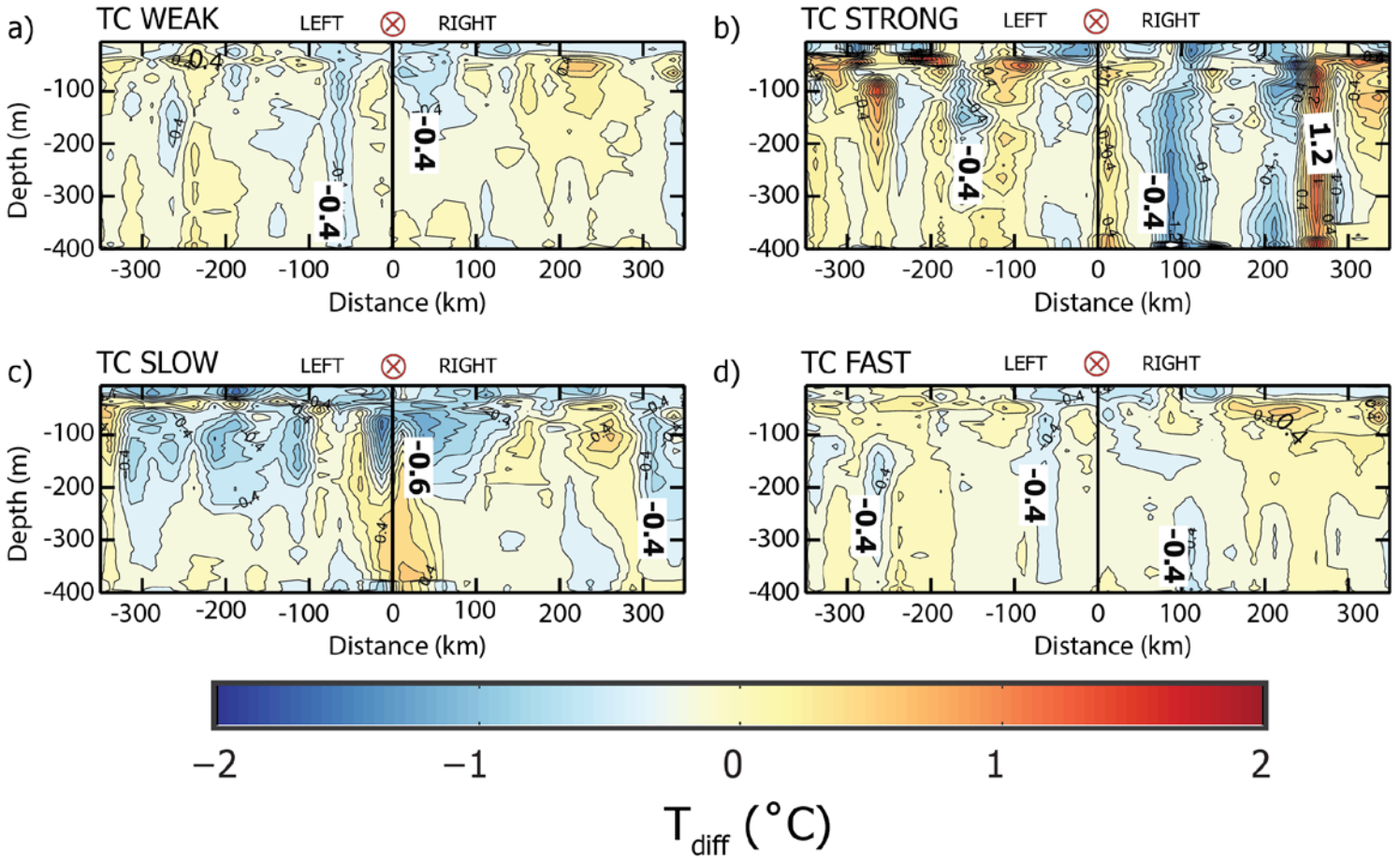

Figure 7–10 North Atlantic TC-induced temperature composite response cross track structure (i.e. perpendicular to storm direction) for storm locations with (a) weak (CAT0, CAT1 and CAT2) and (b) strong (CAT3) wind speed; (c) slow ($U_H \leq 4$ m s^{-1}) and (d) fast ($U_H > 4$ m s^{-1}) translational speed in the North Atlantic. Notice that the TC forward direction goes into the plane of the drawing (circle with an inscribed X) and divides the plane to the right ($x > 0$ km) and to the left ($x < 0$ km) section of the storm.

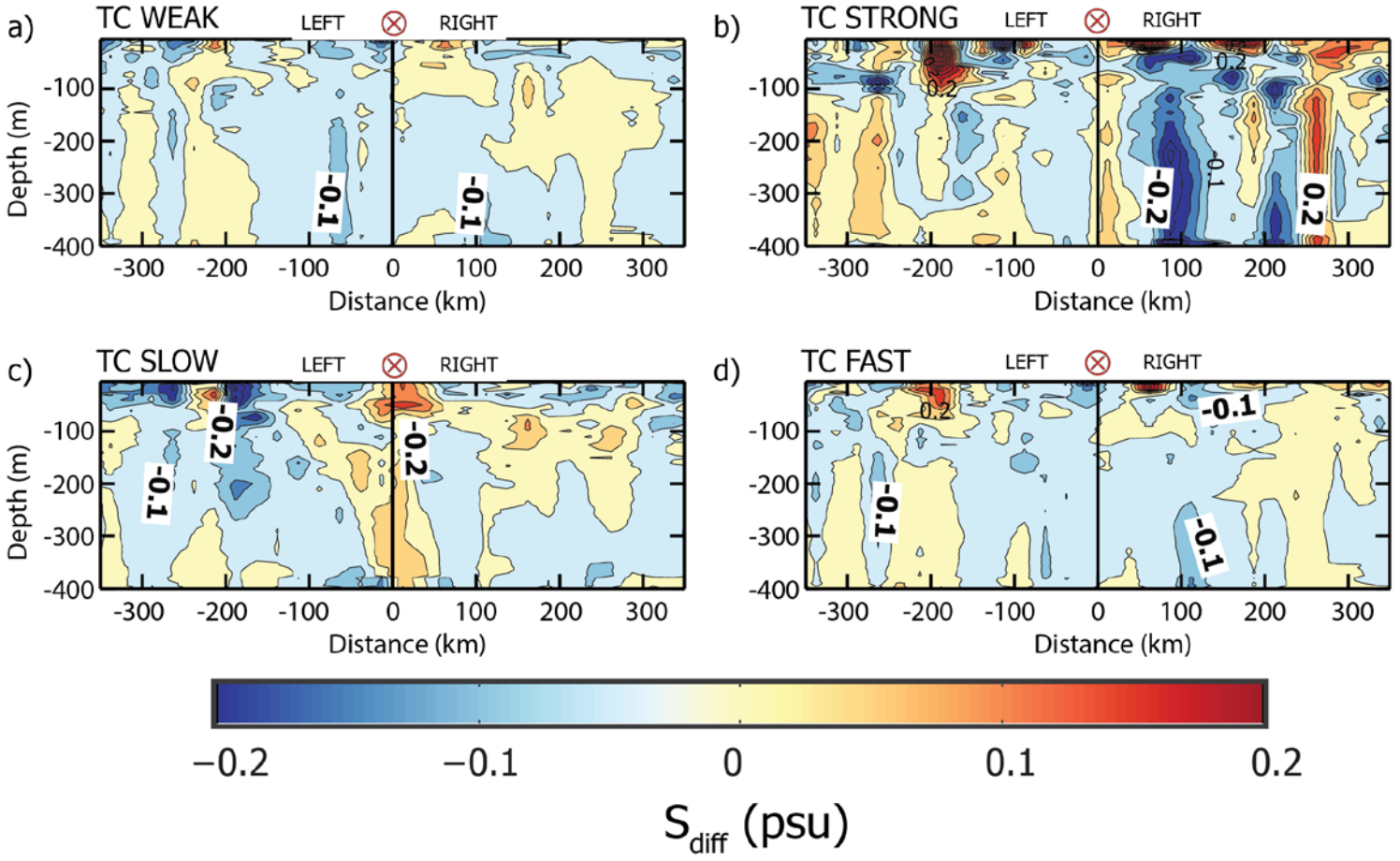

Figure 7–11 North Atlantic TC-induced salinity composite response cross track structure (i.e. perpendicular to storm direction) for storm locations with (a) weak (CAT0, CAT1 and CAT2) and (b) strong (CAT3 and CAT4) wind speed; (c) slow ($U_H \leq 4$ m s^{-1}) and (d) fast ($U_H > 4$ m s^{-1}) translational speed. Notice that the TC forward direction goes into the plane of the drawing (circle with an inscribed X) and divides the plane to the right (x > 0 km) and to the left (x < 0 km) section of the storm.

7.3.6 North Atlantic composite ocean response sensitivity to oceanic component

The pre-storm ocean configuration as given by both temperature and salinity profiles may determine the ocean response. Thus, the evolution of thermal and saline structure defines the ocean component of this interactive system, which this thesis defined as the pre-storm Mixed Layer Depth (MLD) and the Barrier Layer (BL). On the one hand the MLD determines the magnitude of TC-induced change in temperature within the upper layer of the ocean. Thus there might be a reduced thermal ocean response over regions with deep MLD [*Neetu et al.*, 2012; *E. M. Vincent et al.*, 2012]. On the other hand BL opposes to the TC-induced turbulent mixing, consequently there might be a reduced TC-induced surface cooling [*Balaguru et al.*, 2012; *K Emanuel and Sobel*, 2013]. Furthermore, together with this reduced TC-induced surface cooling, regions with wide BL might be linked to the TC-intensification due to a low negative feedback interaction between the ocean and the atmosphere [*Wang et al.*, 2011]. The stabilizing effect of the salinity is related to the depth were the buoyancy frequency (N^2) is maximum [*C Maes*, 2008]. As expected in the North Atlantic basin, BL and N^2 computed between 1 and 20 days before the passage of the storm (Figure 7–12), showed high values in the proximities of the Amazon Plume, and there was a significant correlation ($R = 0.25$) between the two. Furthermore there was a higher negative correlation ($R = -0.57$) between N^2 and the MLD. Thus in the North Atlantic the buoyancy number decreases as the MLD increases. Furthermore, Figure 7-13, shows that the North East Pacific has the largest N^2, but its BL is similar to the one seen in the North Atlantic. This might suggest that BL only does not explain water column stability as measure with N^2. Therefore, the in the following, this section focusses on the North Atlantic region to study the pre storm ocean component modulating the TC response.

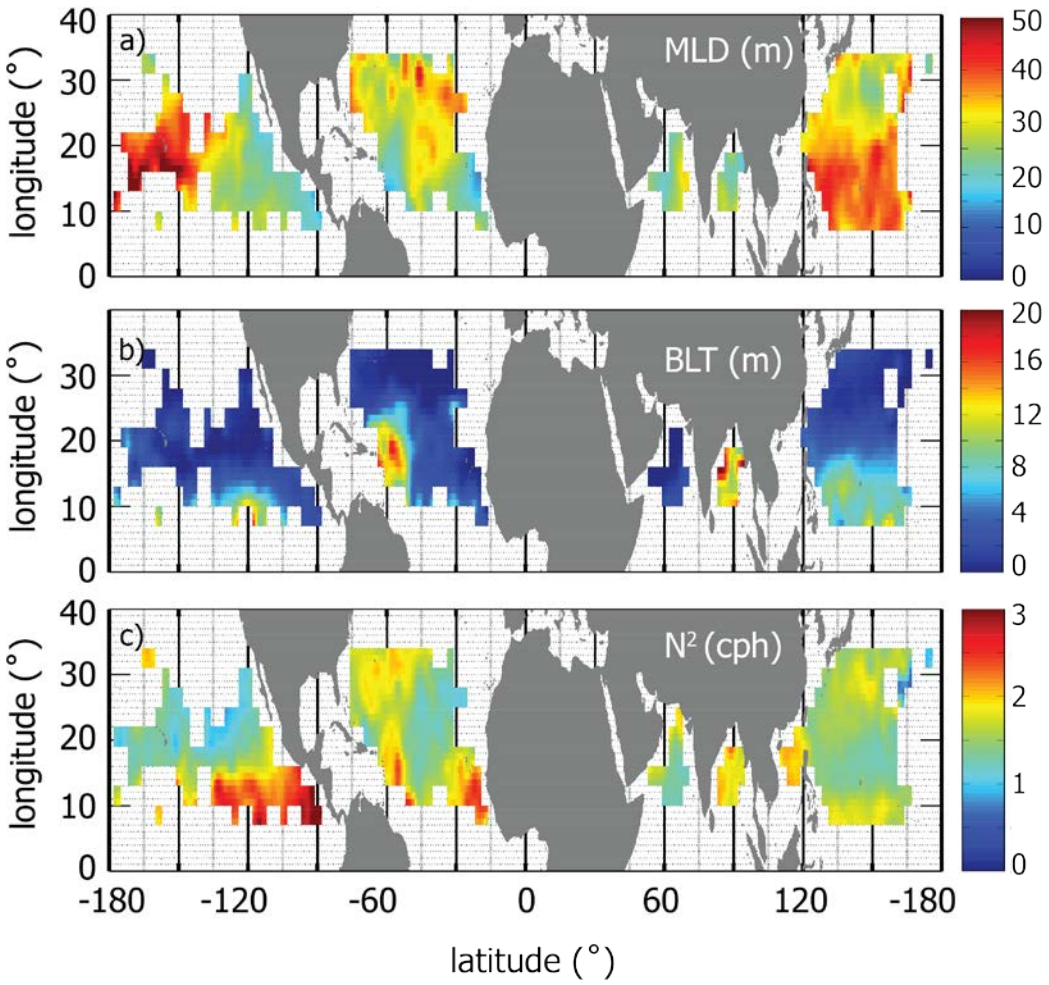

Figure 7–12 Global (a) Mixed Layer Depth (MLD, m); (b) Barrier Layer Thickness (BLT, m) and (c) Buoyancy number (N^2, cph) at each Argo location from -1 to -20 days before the passage of a Tropical cyclone. Notice that the units for the MLD and BLT are meters (m) and the buoyancy frequency (N^2) is in cycles per hour (cph).

In the North Hemisphere, the North West Pacific presented the largest MLD with median of 30 m with outliers as wide as 90 m (Figure 7–13). However, for the other basins in this study, including the North Atlantic, the median MLD was below 30 m. Thus this chapter used a value of 20 m, to study the sensitivity of the ocean response with shallow MLD (pre-storm MLD ≤ 20 m) and deep MLD (pre-storm MLD > 20 m) (Figure 7–14 a and Figure 7–15 b). Similarly (Figure 7–14 c and Figure 7–15 d), this chapter examined the TC-induce response over shallow BLT (BLT ≤ 10 m) and over deep BLT (BLT > 10 m). The choice of these thresholds intended to maximise the number of observations within each basin and in the global study. In the case of the MLD, the threshold was close to the lowest 1st quartile, which was in the Indian Ocean (Figure 7–13). In the case of the BLT, there was a lower spread of the sample the upper quartile in most of the basin was below 10 m.

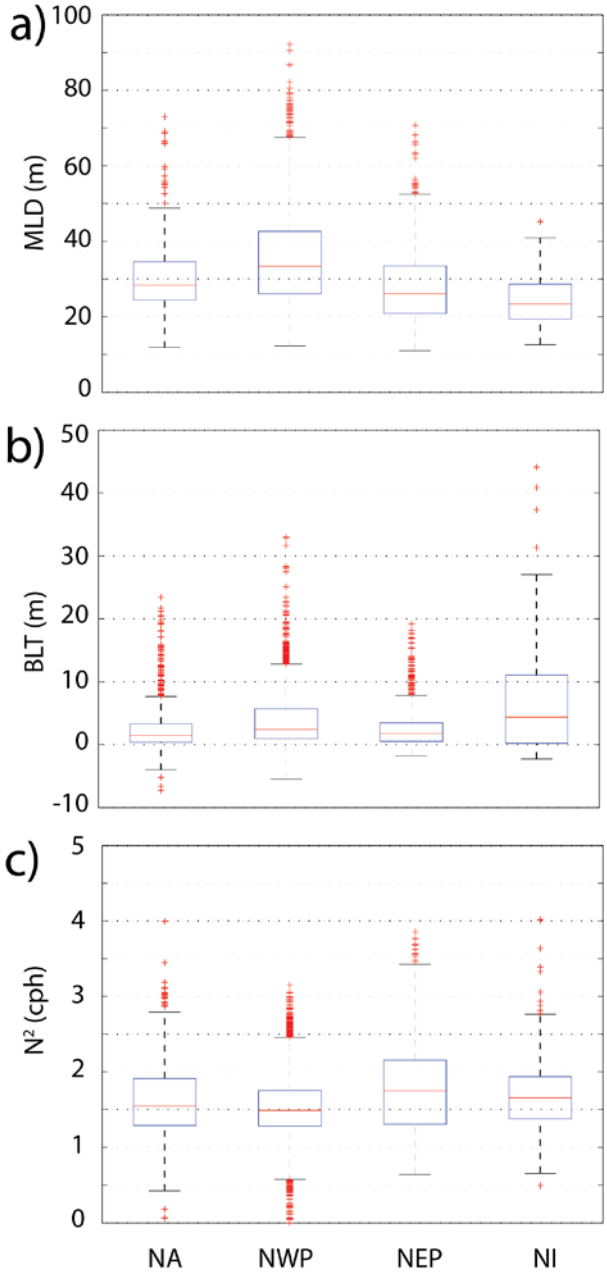

Figure 7–13 Boxplot of the (a) MLD, (b) BLT and (c) N2 in the North Atlantic (NA), North West Pacific (NWP), North East Pacific (NEP) and in the North Indian (NI) oceans. Values were computed at each Argo location within each TC-location and within -1 to -20 days from the passage of the storm. For each box, data is characterized as the median (red line), the bottom and upper limits of the box (i.e. Inter Quartile range) are the 25th and 75th percentile respectively. The bottom and upper whiskers (black) are the minimum and maximum values. The outliers (red) are values outside of the minimum and maximum limits.

In the North Atlantic, the thermal composite response (Figure 7–14a) with a shallow MLD showed that TCs induced a wide spatial spread warming (positive) response, $T_{diff} \geq 1.5^{\circ}C$ from the surface down to about 80 m (to the right) and about 50 m (to the left). These results showed that there was a rightward bias in the TC-induced warming response. Furthermore, there was only a small average cooling at the surface (0 – 50 m) of about 0.5˚C between 150 km and 200 km to the right of the

storm. At both sides of the storm, there were other TC-induced cooling patches ($T_{diff} \leq -0.4^{\circ}C$), but these were mostly deep (Depth ≥ 100 m) cooling patches. In most cases one can assume assume that temperature remains constant from the surface down to the base of the MLD [*Hosoda et al.*, 2010; *Emmanuel M. Vincent et al.*, 2012]. Hence it is not possible to observe the warming of the water column related to the TC-induced downwelling.

The thermal composite response was markedly different over the different regimes of BLT (Figure 7–14 c-d). On the one hand storms travelling over shallow BLT induced an average cooling of 0.4 ˚C with a clear rightward bias and encompassed to the 50 m. On the other hand, storms moving over thick BLT also induced a surface cooling of similar magnitude but this was clearer within the subsurface than over at the top surface. This could be due to the fact that the BLT inhibits the turbulent TC-induced mixing [*Balaguru et al.*, 2012], so the remaining observed cooling could be due to other TC-induced mechanisms like upwelling of cold water from below the thermocline [*H. Zhang et al.*, 2016]. Furthermore, whereas storms moving over shallow BLT showed a clear rightward bias, there was not such a clear signature across section difference around storm moving over deep BLT. These results were against the initials expectations from other works using model simulations that showed a clear reduction of the TC-induced surface cooling [*Androulidakis et al.*, 2016; *Li et al.*, 2017]. However, from these results it is possible to conclude that in the North Atlantic, a deep BLT does not reduce completely TC-induced surface cooling but it does change the patterns of the observed thermal changes. Thus over shallow BLT TC-induced thermal changes are limited to the top 50 m and over deep BLT TC-induced thermal changes are scattered all over the water column. These observed changes in the T_{diff} changes suggest that TC-induced mechanisms are different depending on the BLT.

Whilst there were TC-induced changes in salinity under storms travelling over shallow MLD, there were only small salinity changes over deep MLD (Figure 7–15 a-b). Over shallow MLD, TC-induced salinity changes were mostly positive ($S_{diff} \approx 0.2$ psu) and were mainly at the top of the water column reaching about 150 m and about 50 m to the right and to the left side of the storm respectively. There was a rightward bias in the horizontal TC-induced change in salinity. Whilst TC-induced salinity changes extended from the centre of the storm to about 150 km to the right, it only reached to about 50 km to the left. There were noticed negative TC-induced changes at both sides of the storm. These were located between 150 to 250 km at the right and between 50 to 80 km to the left of the storm, which extended from the surface down to 400 m depth. Furthermore, at depths greater than 50 m TC-induced changes in salinity were mostly negative to the left of the storm and these were mostly positive to the right. These results would agree with those works suggesting that

TC-induced salinity increased might be more visible to the right of the storm were it is expected to be most of the TC-induced upwelling.

The largest TC-induced changes in salinity (S_{diff} ≈ -0.2 psu) were related to those storms travelling over regions with deep BL (Figure 7–15d). As others already point out [*Androulidakis et al.*, 2016; *Grodsky et al.*, 2017; *Grodsky et al.*, 2012; *Hernandez et al.*, 2014], these TC-locations were located mainly in the vicinity of the Amazon plume, where the surface freshwater from the river outflow produce a thick and stable BL Furthermore, the sign of these changes were both strongly positive and negative. There were two-core concentrations of positive changes (S_{diff} ≈0.2 psu). One from 50 km to 100 km to the right of the storm and getting as deep as 150 m and the other one covering space from 180 km to more than 250 km to the left of the storm and reaching similar depths as the previous one. TC-induced salinity changes were small (S_{diff}≈ 0 psu) for those storms travelling over shallow BL (Figure 7–15c).

The positive salinity changes (red, salinity increase) showed dominance to the right of the storm, from about 100 km to about 300 km, and from the surface down to 400 m (Figure 7–15). At the surface (0 to 50 m) salinity changes were negative (blue, salinity decrease). These changes could be interpreted as TC-induced salinity decrease (or freshening) of the water column. Furthermore storms travelling over shallow MLD showed a clear left ward freshening bias that would agree with previous works [*Y C Lin and Oey*, 2016] showing higher stratification to the left of the storm due to predominance of rainfall.

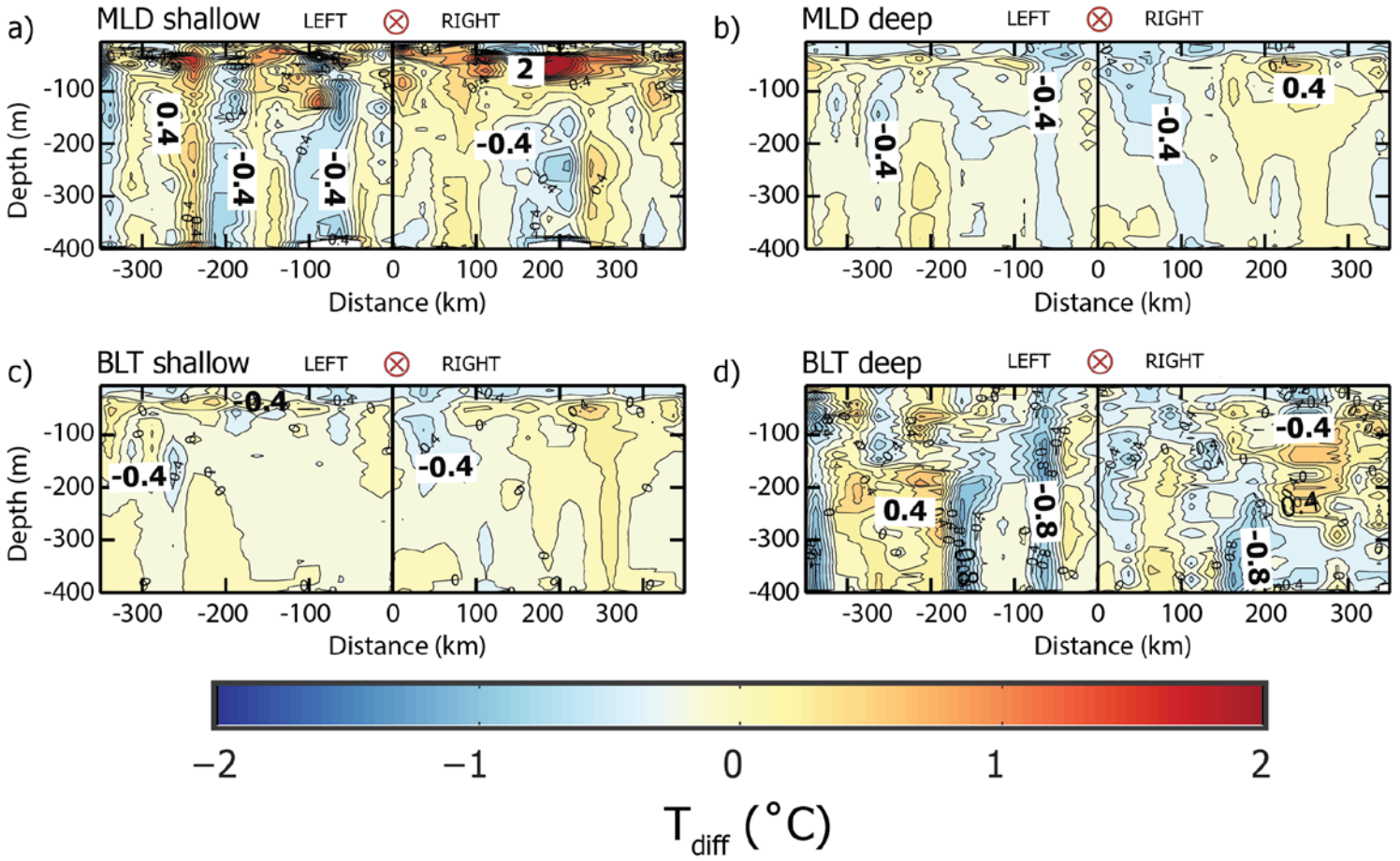

Figure 7–14 North Atlantic TC-induced temperature composite response cross track structure (i.e. perpendicular to storm direction) for storm locations with (a) shallow MLD (MLD ≤ 20 m) and (b) deep MLD (MLD > 20 m); (c) shallow BLT (BLT < 10 m) and (d) deep BLT (BLT > 10 m). Notice that the TC forward direction goes into the plane of the drawing (circle with an inscribed X) and divides the plane to the right (x > 0 km) and to the left (x < 0 km) section of the storm.

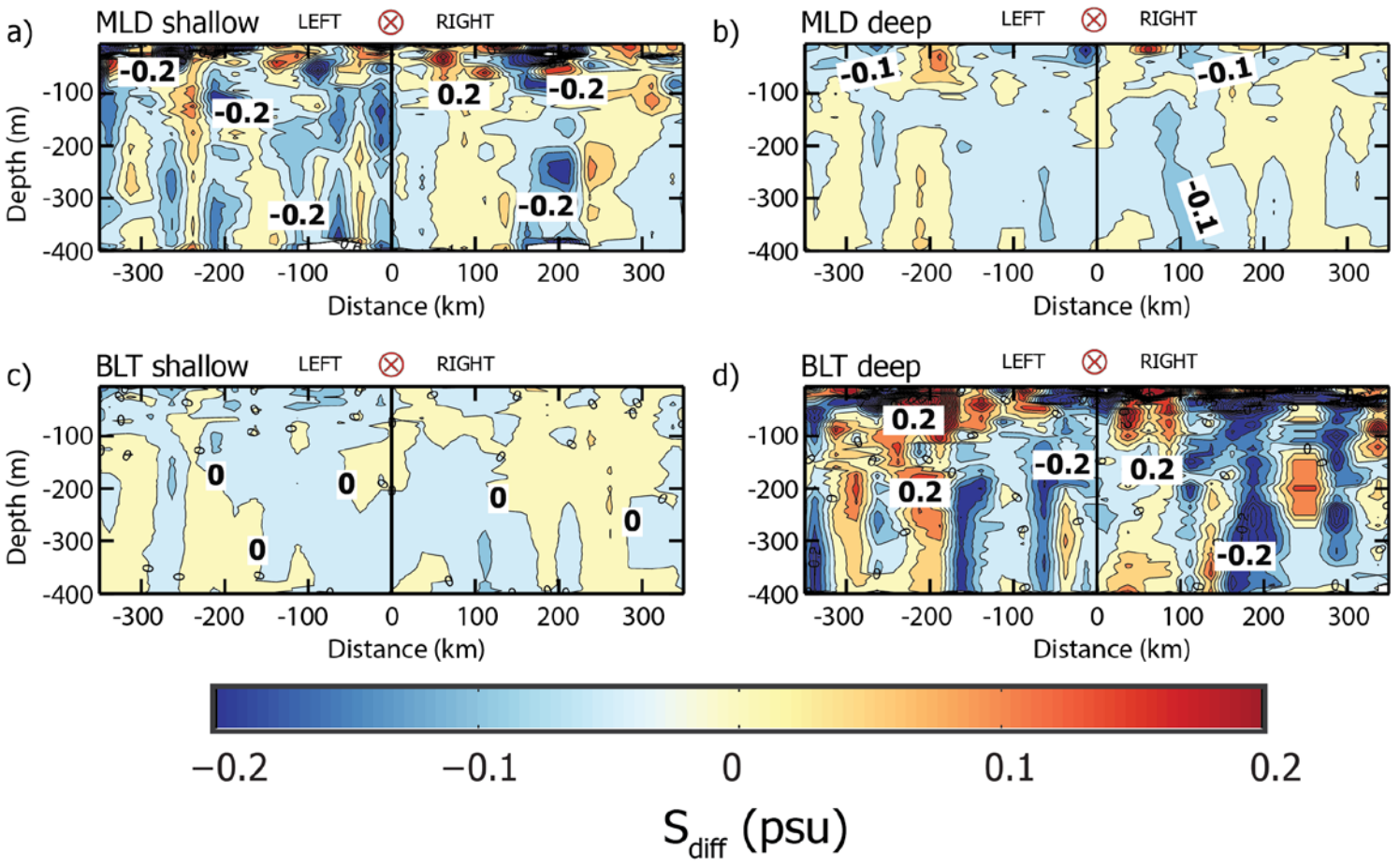

Figure 7–15 North Atlantic TC-induced salinity composite response cross track structure (i.e. perpendicular to storm direction) for storm locations with (a) shallow MLD (MLD ≤ 20m) and (b) deep MLD (MLD > 20 m); (c) shallow BLT (BLT < 10 m) and (d) deep BLT (BLT > 10 m). Notice that the TC forward direction goes into the plane of the drawing (circle with an inscribed X) and divides the plane to the right (x > 0 km) and to the left (x < 0 km) section of the storm.

7.4 Conclusions

This chapter used the composite TC-induced composite response method (see Chapter 4) to observe the ocean response to the passage of TCs from 2005 to 2015. The concept of the composite ocean response to the passage of storms using in situ observations was developed by extending earlier works using satellite observations of TC-induced SST cooling of a set of storms chosen according to their physical characteristics, i.e. adding impartiality to the TC selection [*I D Lloyd and Vecchi*, 2011]. Argo observations were used as these have proven to be very valuable in observing TC-induced changes in temperature and salinity not only at the surface but throughout the water column to a typical depth of 200 m [*Z H Liu et al.*, 2014; *Reul et al.*, 2014; *Vissa et al.*, 2012]. However, those works and Chapter 5 in this thesis, focussed on rather specific case studies, where conclusions were limited to the description of those particular events. With this in mind the results presented in this chapter were already based on a large number of Argo temperature and salinity profiles around different TCs. Hence, this is the first work to date objectively showing TC-induced responses in both temperature and salinity profiles from the surface down to a depth of 400 m. The study was initially designed to study storms in the North Atlantic, but was later extended to other basins in the Northern Hemisphere.

The analysis of different time series of TC-induced changes in temperature (Figure 7–5) and salinity (Figure 7–6) through time have been presented. The resulting time series were firstly categorized according to two criteria, which were: 1) wind speed as described in the Saffir Simpson scale and 2) translational speed as slow ($U_H \leq 4$ m s^{-1}) and fast ($U_h > 4$ m s^{-1}) moving storms. The interpretation of these time series is that the thermal and saline responses to the passage of storm were linked to different TC-induced mechanisms. Furthermore, temperature and salinity changes were not related to each other, so the occurrence of TC-induced cooling did not imply a TC-induced response in salinity of either sign. The thermal ocean response at the surface was generally negative (cooling) and it showed a monotonic dependence with TC-intensity up to category 2 in all basins included in this study. On the other hand, the ocean surface response in salinity showed no dependence with the translational speed nor with TC-intensity. Therefore, the saline ocean response might be dependent on the pre-storm ocean conditions (MLD and BLT) and/or on the rainfall associated with the storm. Whilst this chapter used information of the MLD and BLT at each Argo location to investigate effect of the pre-storm modulating the TC-induced ocean response, the effect of the rainfall was not further investigated.

In most of the basins except the Indian Ocean, TC-induced changes in temperature were generally larger under slow moving storms than under the fast moving ones (Figure 7–7). Assuming that the

surface cooling is due mainly (80 %) to the TC-induced turbulent mixing [*J Lloyd et al.*, 2011; *Price*, 1976; *Sanford et al.*, 1987; *Stramma et al.*, 1986], it might be possible that TC-induced cooling is related to the time a storm spends at a given location. Observations presented in this chapter show that slow moving storms spend more time over the same TC-location, thus inducing higher mixing into the water column, which it results in a larger cooling (Figure 7–7) below the surface. The cooling observed in the North Atlantic was comparable to that observed in other basins. This chapter noted an irregular number of TC observations (i.e. especially numbers of TC CAT 2) in the North Indian Ocean (Table 7-1). Therefore conclusions relating to this basin need to be revisited using an improved TC database for this basin.

The comparison of TC-induced changes in salinity showed a more complex response than the thermal induced response. This is because salinity and temperature show different responses to the TC-inducing mechanisms. Therefore, in the North Atlantic, since salinity at the base of the MLD is higher than at the surface, TC-induced mixing and upwelling may increase surface salinity (i.e. positive salinity change, $S_{diff} > 0$ psu). However, an increase in salinity might be reduced by rainfall (i.e. colder and fresher than the ocean) that will tend to freshen and cool the surface and the subsurface depending on the level of stratification [*Zhao et al.*, 2017]. By looking at both temperature and salinity Argo profiles, it may be possible to infer a relationship between rainfall and TC-induced changes in salinity, which in turn might be related to the translational speed of the storm. The potential effect of the rainfall on the resulting ocean response would be that rainfall and TC-induced mixing will contribute to the observed SST cooling. Therefore rainfall and TC induced mixing would contribute to the negative feedback. On the other hand, the rainfall contribution to the TC-induced change in salinity may be counteracted by the TC-induced mixing. Thus, assuming that TC induced mixing would increase salinity, rainfall would oppose this salinity increase. Furthermore, slow moving storms would have the potential of providing more freshwater into a given location than fast moving storms [*Y C Lin and Oey*, 2016; *Zhao et al.*, 2017]. Therefore, the overall TC-ocean system depends not only on the wind induced vertical mixing and the total volume of water, but is also related to the translational speed of the storm.

The results presented in this chapter were comparable to previous works [e.g. *I D Lloyd and Vecchi*, 2011], the global thermal composite response measured at 10 m depth by Argo in the North Atlantic was evident for slow moving TCs. As seen in Figure 7–7, in the North Atlantic slow moving category 2 storms induced the largest cooling followed by slow moving category 2 storms in the West and East Pacific and finally North Indian Ocean. The global composite response in Argo salinity at 10 m depth did not show such a clear pattern of haline TC-induced change (Figure 7–8). Whilst category 2 fast moving storms induced the largest salinity increase across basins (excluding the North Indian

Ocean), category 2 fast moving storms in the East Pacific induced a positive salinity change (i.e. freshening or salinity decreasing) instead.

North East Pacific and North Indian Ocean show similar pre-storm ocean conditions in terms of MLD and BLT to those seen in the North Atlantic. However, salinity changes in the North Eastern Pacific and North Indian Ocean did not show a clear TC-induced salinity increase over regions with a deep BLT. On the contrary, the study of composite response in those basins showed a freshening of the top surface (0 – 100 m). From these results, this chapter suggests that the mechanism described by [*Grodsky et al.*, 2012] is specific for the North Atlantic. Therefore, it is not possible to conclude that TCs induce a salinity increase over deep BLT regions. Furthermore, in the North West Pacific TC-induced changes in salinity were near zero for all the cases studied. These differences between basins suggest that the study of the TC-induced response might depend on the pre-storm ocean conditions, which are characteristic for each basin. Thus, this chapter suggests that as there was both a thermal and saline TC-induced response, it is necessary to further investigate this relationship in each individual basin. Further, the implementation of the composite TC-induced response using additional sources of data such as rain data [*Y C Lin and Oey*, 2016] might be a further step to improve atmosphere-ocean interaction in a more generic analysis. Finally, this chapter concluded that studying both temperature and salinity TC-induced changes appeared to be useful to describe the physical conditions in which storms affect the ocean. TC-induced salinity changes were both positive and negative in sign and appeared to be related to the translational speed of the storm. Therefore these results supported that salinity changes may be linked to the rainfall and translational speed of the storm.

Chapter 8

Tropical cyclone induced changes over the Amazon plume in the FOAM system

8.1 Introduction

This chapter aims to bring light to this argument between observational and model based studies by applying the CTCFP method to output from the FOAM-NEMO assimilation system [*Matthew J. Martin*, 2016]. Thus, this chapter investigated the thermal and saline ocean response to the passage of storms as seen in a FOAM-NEMO dataset spanning 2011 to 2015 in the North Atlantic. In Chapter 6, the TC-Katia (2011) and TC-Gonzalo (2014) case studies provided two exceptional examples of ocean response, where both storms crossed the Amazon plume (Figure 8-1) and generated surface cooling and salinity increase. This chapter studies the composite TC-induced response in FOAM-NEMO for the same two events, but including also analyses of the ocean response in FOAM-NEMO generated by the storms over and away from the plume.

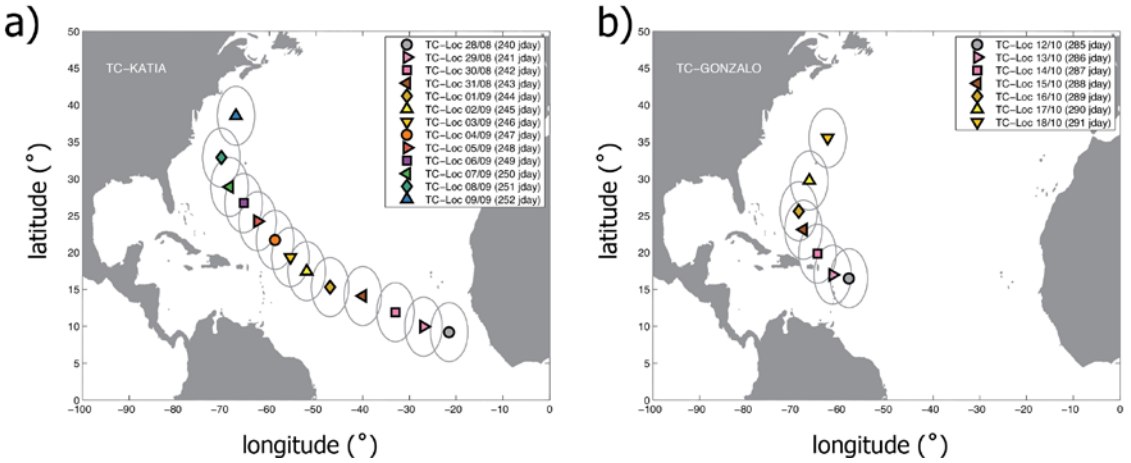

Figure 8-1 North Atlantic daily TC-locations (12-noon) along the track of (a) TC-Katia 2011 and (b) TC-Gonzalo 2014.

8.2 Data and method

Chapter 4 provided detailed information about the FOAM-NEMO assimilation system (hereafter referred as FOAM). This chapter used profiles of temperature (T_F) and salinity (S_F) from FOAM at each grid cell (grid spacing = 25 km) as if these were individual Argo profiles. Analyses focused on profiles from the shallowest depth level in FOAM (depth ≈ 0.5 m) to 400 m depth. FOAM Sea Surface Temperature (SST_F) and Sea Surface Salinity (SSS_F) were taken as the value of each parameter at the shallowest depth level. This work used a five-year subset for the years 2011 – 2015 in the North Atlantic obtained from the operational FOAM system.

The climatological references for temperature and salinity were taken from WOA13 (see Chapter 3) and used to compute the FOAM monthly mean anomaly for temperature (Figure 8-2) and salinity (Figure 8-3) for the two years of interest (2011 and 2014) and for the whole time period (not shown).

These analyses used the MLD and BL products distributed by APDRC Data Centre (see Chapter 3), to make it possible to compare results with those obtained earlier for in situ observations only (Chapter 5 and 6). MLD and BL were interpolated to the nearest time and grid spacing in FOAM. The description of the spatial distribution of the MLD and BL is provided in Chapter 5. The MLD products provided by APDRC correspond to MLD_{02} after *Hosoda et al.* [2010] based on a temperature difference threshold ΔT = 0.2˚C. The MLD provided in the FOAM dataset is defined as the depth where temperature difference reaches 0.8˚C (MLD_{08}), which is generally deeper. Thus, the FOAM MLD was not used in the following analyses.

To study the potential influence of the Amazon freshwater plume on the TC-induced ocean response, this chapter considers separately the TC-response over the plume and the TC-response outside of the plume (or 'Open Ocean'). The 'plume region' was delimited by the 35 psu surface isohaline [*Reul et al.*, 2013] for latitudes below 30˚N (black and magenta lines in Figure 8-2 and Figure 8-3).

8.3 FOAM SST and SSS anomaly in 2011 and 2014 TC-seasons in the North Atlantic

The FOAM monthly climatology was computed by taking monthly averages over five years. This short FOAM climatology showed a significant correlation with the long term WOA13 climatology. For the summer months (Jul-Oct), the climatological values for both surface temperature and salinity (depth ≈ 0 m) showed correlation coefficients over 0.9 with WOA13, thus indicating a close linear relation between the two climatologies. Since FOAM assimilates in situ observations that are also included in WOA13, it was expected there would be a good fit between the two climatologies.

The root mean square (RMS) difference for surface temperature between the FOAM climatology and WOA13 was usually less than 0.5 ˚C at low latitudes, but can reach more than 2 ˚C near the western boundary current. The surface salinity RMS differences were less than 0.15 psu over most of the basin, but reached over 0.5 psu in the Amazon plume region (this region has the least number of salinity observations according to [*Matthew J. Martin*, 2015]. The annual monthly averages of FOAM SST_F and FOAM SSS_F showed high correlations against similar monthly products from GHRSST and SMOS SSS respectively (not shown).

The monthly SST anomaly maps (Figure 8-2) for the TC season in 2011 and 2014 show FOAM minus WOA13 temperature differences usually below 1 ˚C, with the exception of the western boundary current region where WOA13 temperature can be over 2˚C warmer than in FOAM, particularly in 2014. Monthly SSS anomaly maps derived from FOAM and WOA13 (Figure 8-3) show largest discrepancies around the Amazon River plume and great variability in the location of the anomalies between months and between years. Thus, during the TC-season in both years, the SSS_F was 2 psu greater than WOA13. This could be related to a number of factors including the fact that FOAM uses a climatological river input, incorrect propagation of the low salinity river outflow waters in the model [*Matthew J. Martin*, 2016] and the large salinity gradients reported in this region [*Jacqueline Boutin et al.*, 2012; *J. Boutin et al.*, 2014]. Note however that despite the anomalies between FOAM and WOA13, the location of the Amazon plume (indicated by the 35 psu isohaline)

is similar in both datasets. The SST and SSS anomaly maps compare well with those produced with in situ observations in Chapter 5).

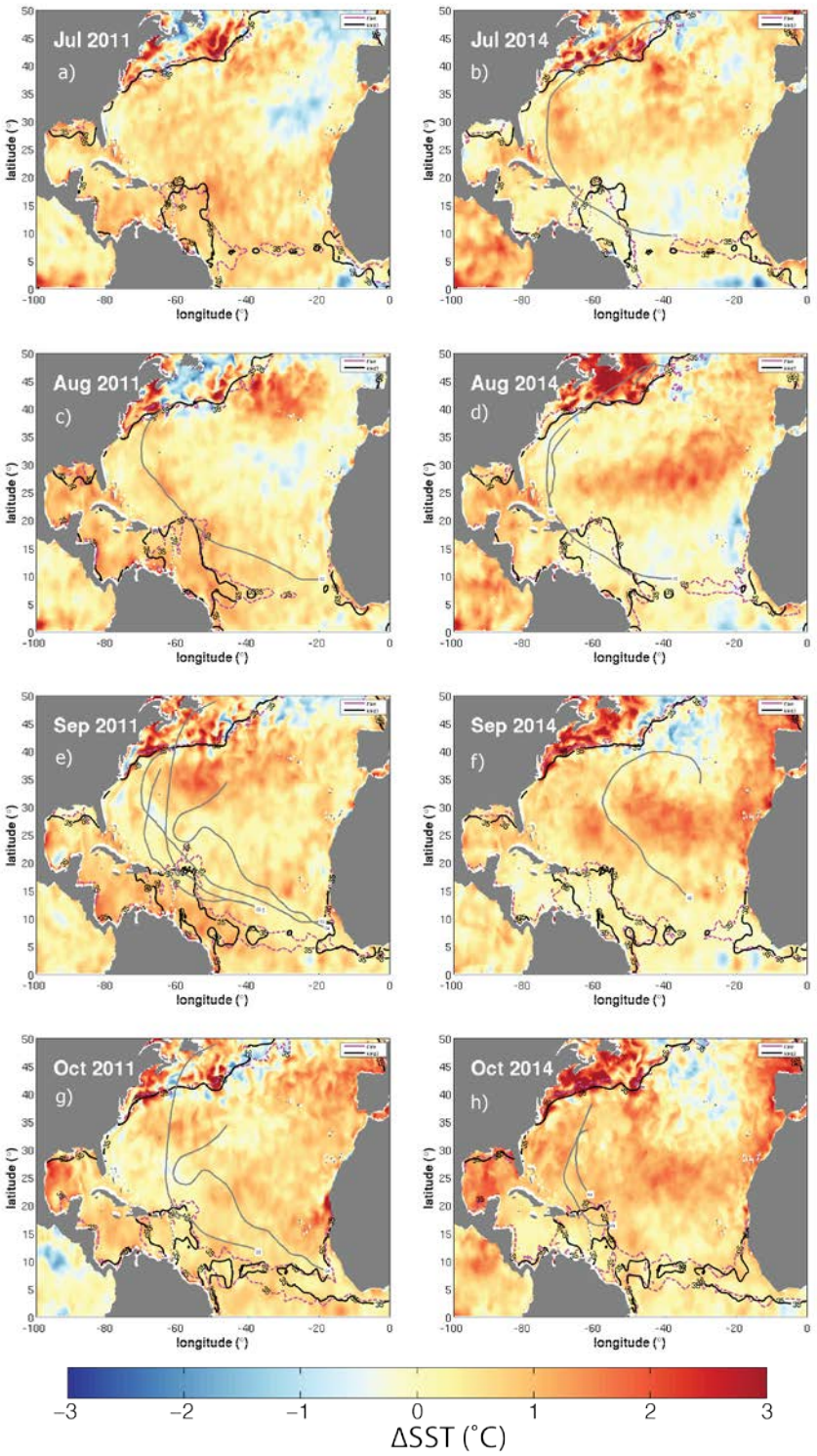

Figure 8-2 FOAM Sea Surface Temperature anomalies (ΔSST) during the Jul-Oct TC-season in 2011 and 2014 in the North Atlantic. The anomalies were computed against the long-term SST climatology from WOA13. The Amazon freshwater plume is identified by the 35 psu isohaline as depicted by FOAM (broken magenta) and WOA13 (solid black). Note the basin wide extension of the 35 psu surface isohaline across the Atlantic, which is related to the freshwater contributions from the Amazon and Orinoco rivers (South America) and the Niger and Congo rivers (West Africa).

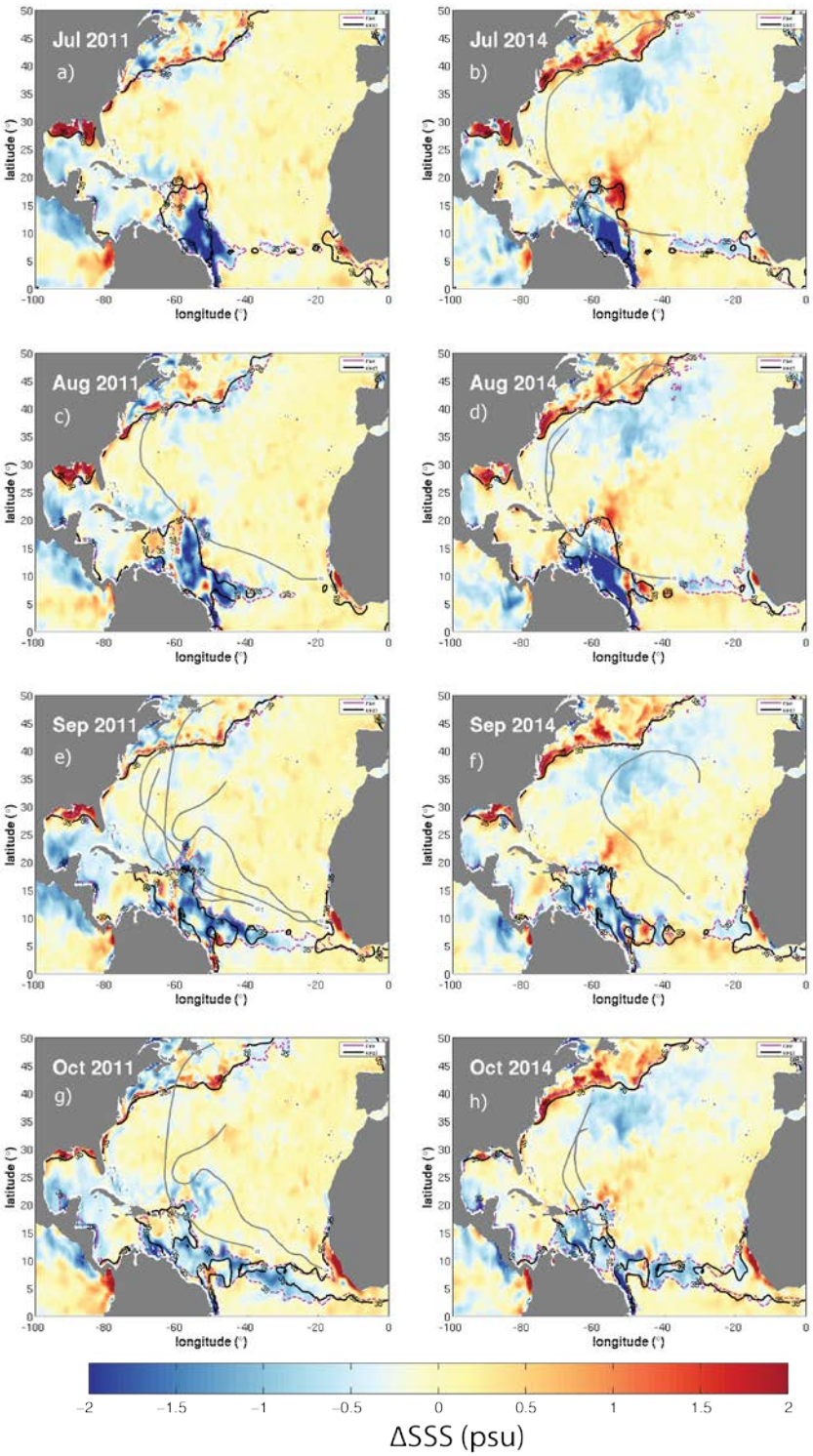

Figure 8-3 FOAM Sea Surface Salinity anomalies (ΔSSS) during the Jul-Oct TC-season in 2011 and 2014 in the North Atlantic. The anomalies were computed against the long term SST climatology from WOA13. The Amazon freshwater plume is identified by the 35 psu isohaline as depicted by FOAM (broken magenta) and WOA13 (solid black). Note the basin wide extension of the 35 psu surface isohaline across the Atlantic, which is related to the freshwater contributions from the Amazon and Orinoco rivers (South America) and the Niger and Congo rivers (West Africa).

8.4 TC-induced ocean response in FOAM

The characterization of the TC-induced ocean response in FOAM was computed following the CTCFP approach introduced in Chapter 4. Although the maximum cooling is reported to occur on average within a 200 km radius from the centre of the storm (Vince, 2012), this work uses a fixed search radius of 400 km as was done previously for observation-only analyses, to make these model results more easily comparable with those reported in earlier chapters. Following the same reasoning, the composite ocean response was evaluated for profiles from the surface down to 400 m depth. Temperature and salinity values at the shallowest FOAM level (depth ≈ 0 m) are taken to represent sea surface temperature (SST_F) and sea surface salinity (SSS_F) respectively.

The successive steps to compute the composite thermal and haline ocean response at each depth level in FOAM were as follows: 1) Remove the climatology (i.e. WOA13) from the respective temperature and salinity profiles; 2) Compute the pre-storm unperturbed ocean temperature and salinity at the surface (SST_0 and SSS_0) and subsurface (T_0 and S_0) as the average in the 10-day before the arrival of the TC (from day -13 to day -3 relative to the passage of the storm) at each grid point within the searching radius; 3) compute the ocean response at each depth as the daily difference between the temperature (T_x) and salinity (S_x) at a given day and the unperturbed ocean conditions:

$$\Delta T = T_x - T_0$$
$$\Delta S = S_x - S_0$$

ΔT and ΔS are profiles of the changes in temperature and salinity respectively at each FOAM depth level from the surface to 400 m. Thus, as before, negative temperature changes (ΔT < 0˚C) represent cooling induced by the storm, and positive changes (ΔT > 0˚C) represent warming.

8.4.1 FOAM ocean response to TC-Katia and TC-Gonzalo over the Amazon plume

Temperature and salinity profiles from FOAM were used to analyse the TC-induced ocean response of TC-Katia (2011) and TC-Gonzalo (2014) over the Amazon plume. In Chapter 5, CTCFP analyses of in situ data confirmed that both storms showed a temperature decreased (cooling) and salinity increase in the wake of the storms. As noted above, monthly mean FOAM data showed lower salinity values at the surface than climatology within the region of the Amazon plume. Similar results were reported also by studies comparing the FOAM system against satellite data [*Matthew J. Martin*, 2016]. However, analyses of NEMO model output without assimilation reported that the Amazon plume did not have appropriate northward extension [*Hernandez et al.*, 2016]. Thus, although the SSS signature of the Amazon is anomalously strong in FOAM is compared to

climatology, the assimilation of in situ and satellite observations in FOAM leads to a more accurate positioning of the Amazon plume.

Figure 8-4a and Figure 8-4b show TC-induced reductions in SST_F of about 1.5˚C and about 1.8˚C within the first 10 days after the passage of TC-Katia and TC-Gonzalo respectively. In both cases, the largest cooling occurred in TC-locations at higher latitudes and away from the Amazon plume region. On the other hand, both storms induced a salinity increase of about 0.3 psu in TC-locations near the Amazon plume (Figure 8-4 c-d). The temporal representation of the ocean response in Figure 8-4 shows that the maximum TC-induced cooling occurred about 10 days after the passage of the storm, while the salinity increase reached its maximum around day 15 and day 18 after the passage of TC-Katia and TC-Gonzalo respectively. Note that neither cases returned to pre-storm salinity levels.

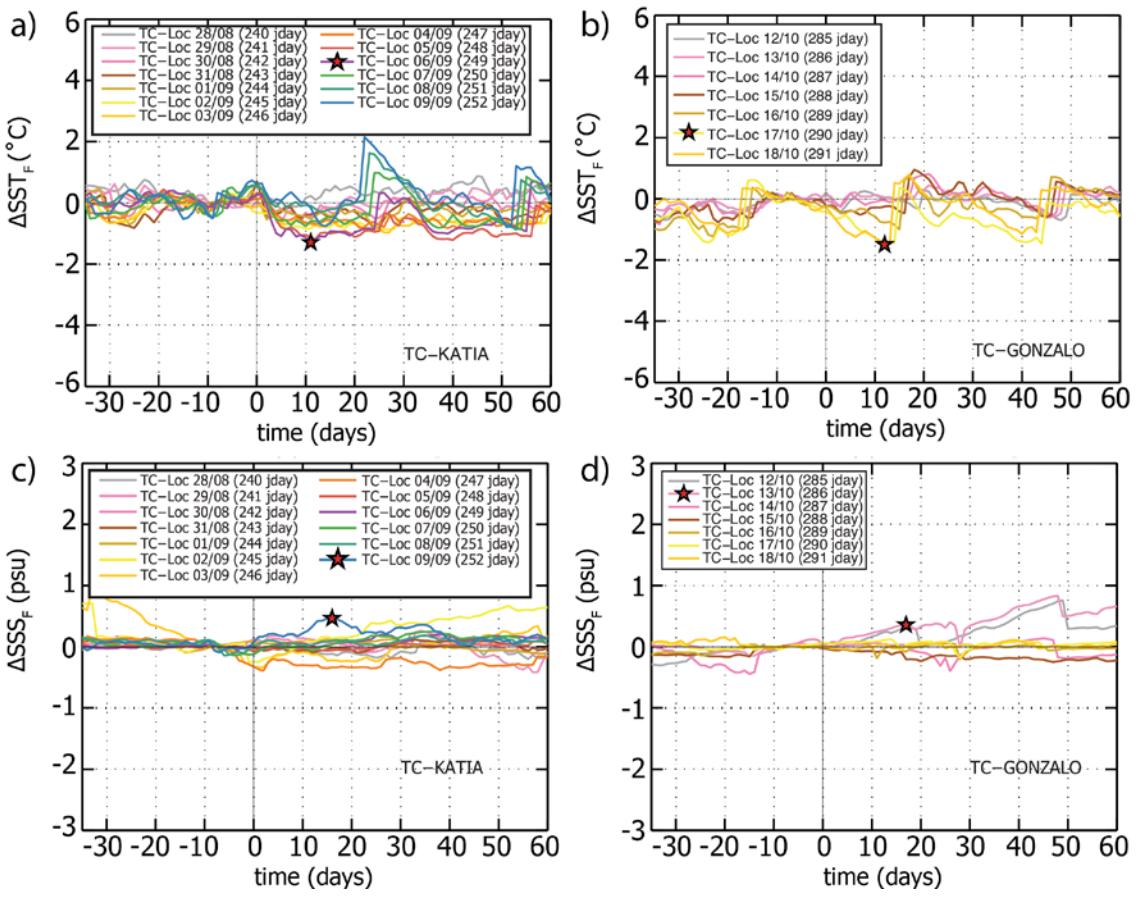

Figure 8-4 Temporal representation of TC-induced changes in FOAM at each TC-Location for (left) TC-Katia (2011) and (right) TC-Gonzalo (2014) in (top) Sea Surface Temperature (ΔSST_F) and (bottom) Sea Surface Salinity (ΔSSS_F). Note the different TC-location of the largest cooling and largest salinity increase (red star) for each storm. TC-locations and dates are as referenced in Figure 8-1.

In order to visualise the spatial distribution of the TC-induced changes in SST_F and SSS_F, Figure 8-5 presents the TC-induced changes in the ocean 10 days after the passage of the storm. These results are representative of the horizontal distributions of TC-induced changes at other post-storm times (i.e. from 10 to 20 days after the storm) and averaged over different post-storm time windows.

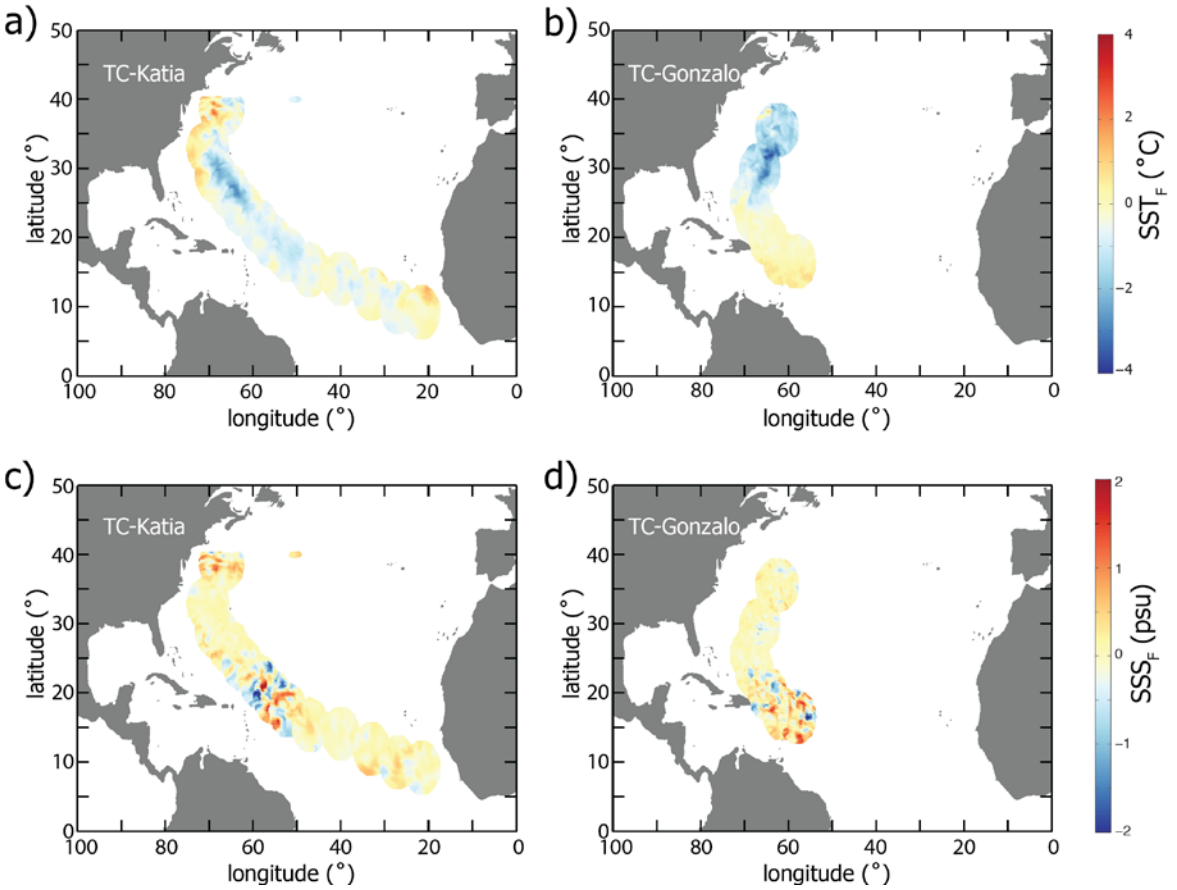

Figure 8-5 TC-induced changes in (a-b) FOAM Sea Surface Temperature (SST_F) and (c-d) Sea Surface Salinity (SSS_F) 10 days after the passage of (left) TC-Katia and (right) TC-Gonzalo (right) in 2011 and 2014 respectively.

The surface temperature change for TC-Katia was close to zero before the storm reached the location of the Amazon plume (15˚ N, -50˚W). After the storm crossed the freshwater plume, the cooling reaches up to 2˚C at about 30˚N (Figure 8-5 a). This cooling distribution is in good agreement with satellite observations (Chapter 6). In the case of TC-Gonzalo, the surface cooling also occurred when the storm have moved away from the Amazon plume (Figure 8-5 b) and again the surface temperature decreases by more than 2˚C towards 30˚N. The changes in SSS_F for both TC-Katia (Figure 8-5c) and TC-Gonzalo (Figure 8-5d) were around zero at most of the TC-Locations, but both storms induced positive salinity changes around the Amazon plume, showing as anomalies scattered on both sides of the storm track.

Within the region of the Amazon plume, the TC-induced ocean salinity response showed both positive (salinity increase) and negative (salinity decrease) values, with salinity changes of ± 2 psu on either side of the track (Figure 8-5 c). These results concur with those presented in Chapter 6 using satellite and in situ observations. Furthermore, the patches of salinity increase are spread nearly across the full TC track (i.e. left and right of the storm). Previous works [*Grodsky et al.*, 2012; *Reul et al.*, 2014] suggested that the salinity increase was concentrated to the right of the storm. The horizontal distribution of TC-induced change in salinity (Figure 8-5 c-d) suggest that salinity changes are scattered across the storm track with no clear rightward bias. The distribution of FOAM SSS changes for TC-Gonzalo look very similar to those seen for TC-Katia (Figure 8-5 d).

From the study of these two TC case studies, it is possible to see that both TC-Katia and TC-Gonzalo induced a broad cool wake at locations away from the Amazon plume, but that the TC-induced response in FOAM SSS seems less coherent and more complex than seen in Chapter 6 using in situ observations. In the next section, the composite TC-induced ocean response of FOAM is obtained for all TC events in the 2011-2015 period of the FOAM data considered.

8.4.2 FOAM ocean response to 2011-2015 Tropical cyclones in the North Atlantic

The CTCFP method introduced in Chapter 4 was found to offer a good method to overcome the scarcity of in situ observations around the TC tracks. The FOAM system provides regular gap-free daily data, and in this section, the FOAM temperature and salinity data for 2011-2015 is examined to derive the composite ocean response under different storm and ocean conditions.

During this period, it was possible to identify a total of 131,125 TC-locations across the whole North Atlantic basin where a TC-induced ocean response might occur. Following the methodology used in Chapter 7, the TC-locations were classed by intensity (i.e. weak and strong) and by translation speed (i.e. slow and fast) of the storms as they passed that location. “Weak” storms consisted of TC Categories 0 to 2, and “strong” storms relate to Category 3 and above. Storms were considered “slow” when their translation speeds was 4 m s^{-1} or less, and “fast” when moving at speeds above 4 m s^{-1}.

Similarly, TC-locations were classed according to MLD and BL conditions, into regions where MLD is “deep” (MLD > 20 m) or “shallow” (MLD ≤ 20 m). The BL was present mainly at low tropical latitudes southward of 30˚ N. Again, BL was classed as “shallow” (BL ≤ 10 m) and “deep” (BL > 10 m).

8.4.2.1 Composite FOAM ocean response in different storm conditions

The composite TC-induced ocean response in FOAM temperature is shown in Figure 8-6 where the temperature response is found to be greatest under strong and under slow storms. The FOAM temperature profiles show a surface cooling of up to 0.6 ˚C which extends from the surface to a maximum depth of 100 m for strong storms, and to almost 200 m for slow storms (Figure 8-6 b-c). Furthermore, whilst cooling tended to occur on the right relative to the track under strong storms, the effect was centred under the eye for slow storms. These differences in the location of the cooling relative to the TC track were also seen using in situ observations, and are thought to be associated with two different TC-induced cooling mechanisms: whilst strong storms are associated with very intense turbulent mixing and heat fluxes as the main drivers of temperature change, slow moving storms are associated with wind induced upwelling close to the eye wall [*Cheng et al.*, 2015]. Note that, although these results are similar to those found using Argo temperature data (Chapter 7), data from the FOAM assimilation system do not show the warm downwelling structures, which were visible in individual Argo profiles.

At depths greater than 150 m, the composite thermal response was near zero for the ocean conditions included in this study. These results contrast with the expectation of upwelling and downwelling described in the previous chapter and in previous works using Argo observations [*Cheng et al.*, 2015].

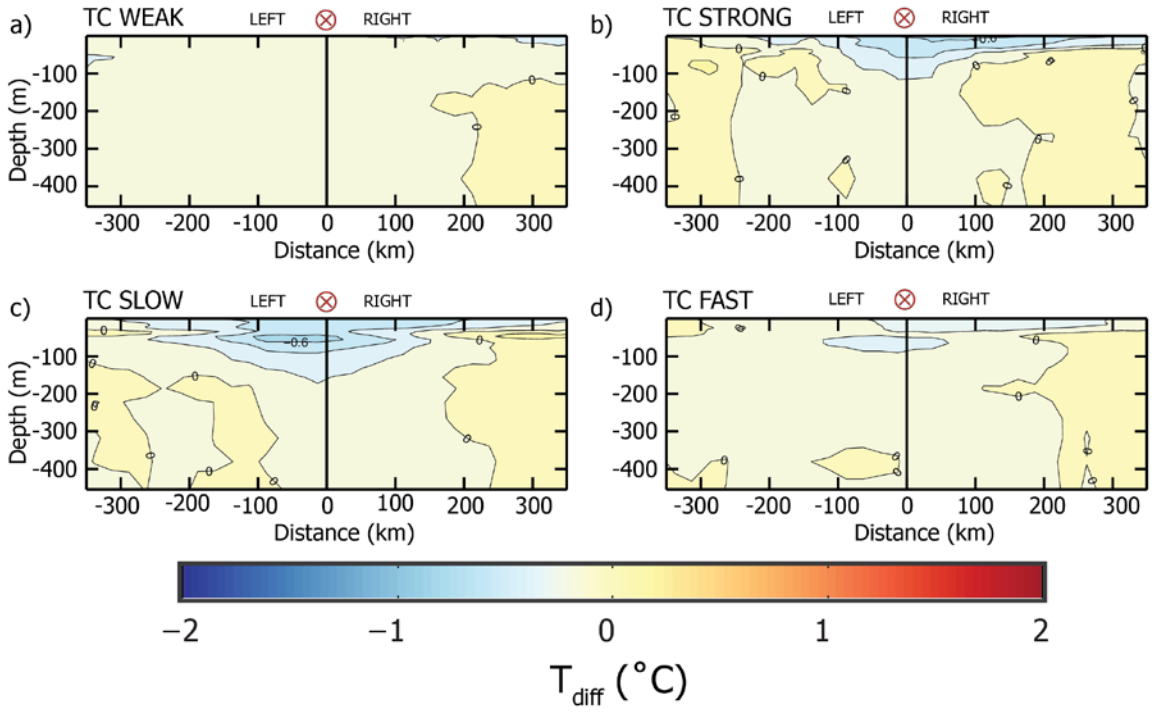

Figure 8-6 FOAM composite TC-induced temperature response for a) weak (CAT0 to CAT2), b) strong (CAT3 and CAT4), c) slow (UH ≤ 4 m s-1) and d) fast (UH > 4 m s-1) TCs in 2011-2015 in the North Atlantic. Contour lines join points of equal temperature every 1˚C in the FOAM data.

The composite TC-induced response in FOAM salinity, shown in Figure 8-7, indicates that salinity changes are below 0.1 psu in magnitude for all storm categories and speeds. These results contrast with the composite TC-response for salinity obtained using Argo profiles in Chapter 7 (Figure 7–11) and suggest that the TC-induced changes in salinity seen with Argo are not present in FOAM. However, inspection of individual FOAM profiles showed some degree of salinity change associated with the passage of storms, although the signals were highly variable and generally low in magnitude, and were smoothed out in the final composite TC-response.

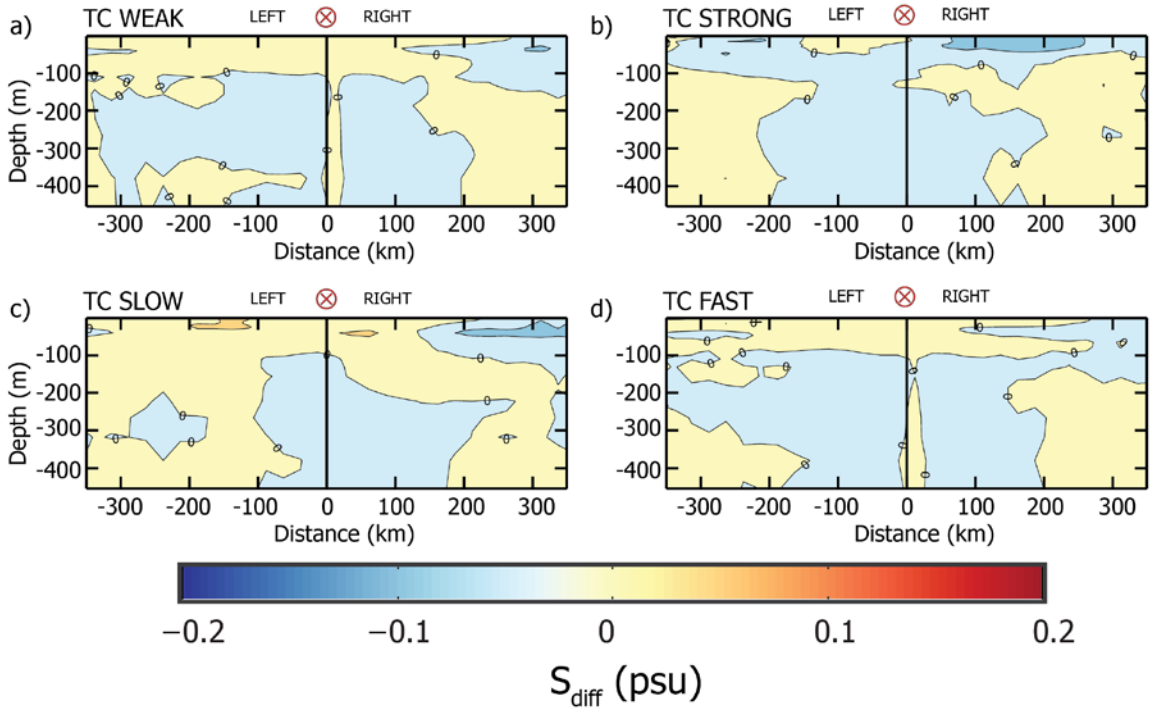

Figure 8-7 FOAM composite TC-induced salinity response for a) weak (CAT0 to CAT2), b) strong (CAT3 and CAT4), c) slow ($U_H \leq 4$ m s^{-1}) and fast ($U_H > 4$ m s^{-1}) TCs in 2011-2015 in the North Atlantic. Contour lines join points of equal salinity every 0.1 psu in the FOAM data.

8.4.2.2 Composite FOAM ocean response in different ocean stratification conditions

The composite TC-induced temperature response in FOAM, shown in Figure 8-8 for different ocean stratification classes, indicates that TC induced temperature change is near zero in all cases even though there is a slight cooling associated with deep MLD and low BL. This results contrasted to the results seen in previous chapter, where the TC-induced response seen with Argo (Chapter 7, Figure 7–14) showed cells of TC-induced warming and cooling throughout the water column, from the surface down to 400 m. Besides the difference in magnitude between the results seen in FOAM and Argo, the TC-induced thermal response in FOAM consists only of cooling and is limited to the top 100 m depth.

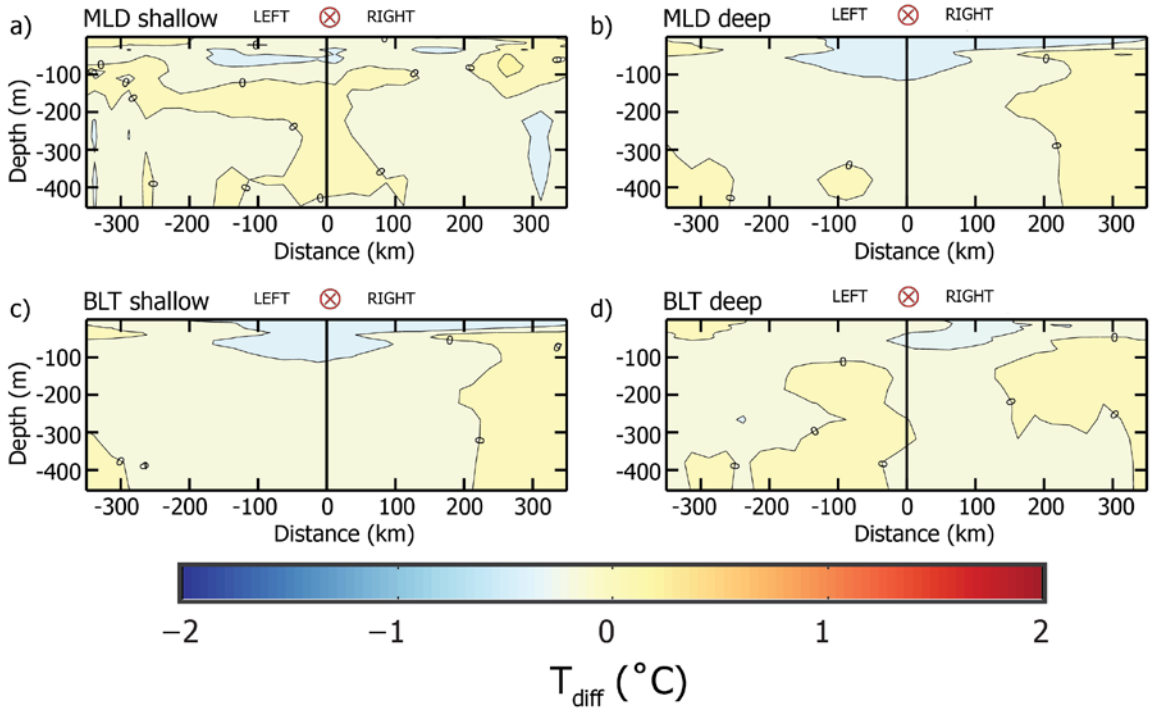

Figure 8-8 FOAM composite TC-induced temperature response for TCs travelling over ocean stratification classes with a) shallow MLD (≤ 20 m); b) deep MLD (> 20 m); shallow BL (≤ 10 m); deep BL (> 10 m) for all TCs in 2011-2015 in the North Atlantic.

The composite TC-induced salinity response in FOAM, shown in Figure 8-9 for different ocean stratification conditions, resulted in different magnitude and compared to the TC composite saline foot print seen Argo (Figure 7-15). The CTCFP in FOAM shows as a large salinity change for TCs over shallow MLD (MLD ≤ 20 m) with salinity increase to the left of the storm track and salinity decrease to the right side of the track. Changes to the left are restricted to the surface layer, while changes to the right occur through the water column, from the surface down to 400 m. Salinity change at the surface are seen also for TCs over deep BL (BL > 10 m) on both sides of the track, but most markedly on to the right of the storms. Salinity decreases from the centre to about 200 km radius and then increase from about 200 km to 400 km.

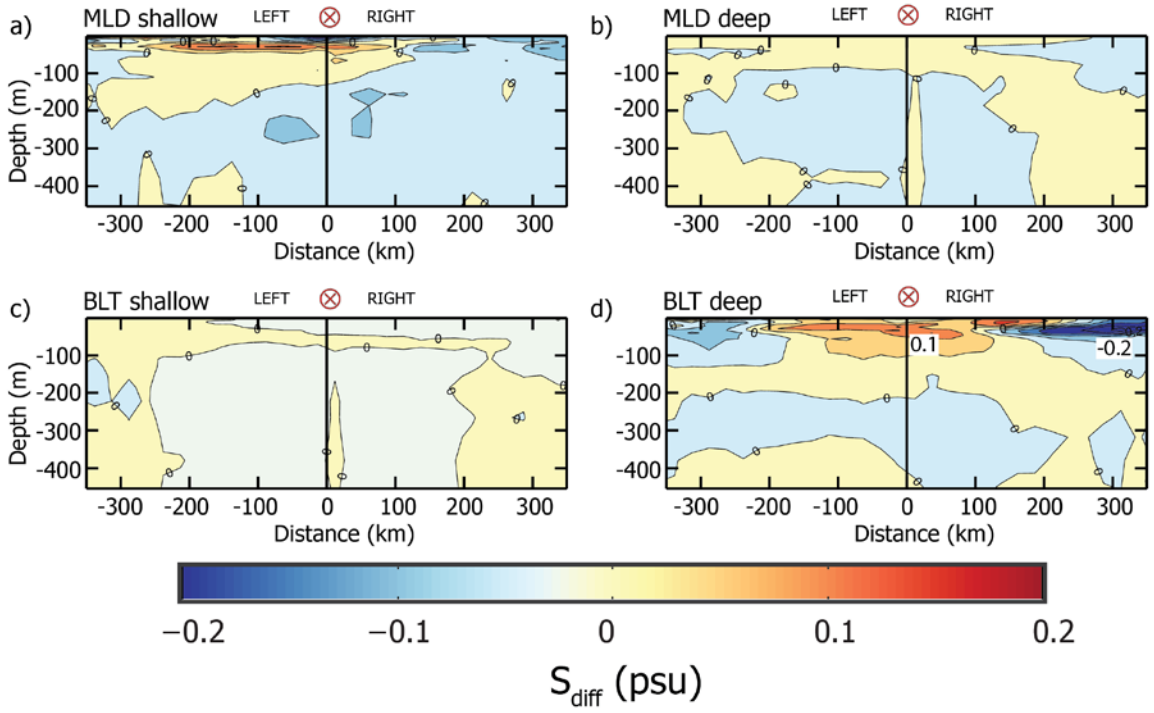

Figure 8-9 North Atlantic (2011-2015) salinity composite TC-induced response for storms travelling over different ocean conditions of MLD (shallow: MLD ≤ 20 m; deep MLD > 20 m) and BL (shallow ≤ 10 m; deep: BL > 10 m).

8.5 Summary and Conclusions

In this chapter, FOAM data were used to study TC-induced changes in the North Atlantic Ocean for TCs in the period 2011 to 2015. Using the CTCFP method developed in this thesis (Chapter 3), this work showed that TC-induced changes in FOAM are less discernible and more smoothed than those observed with the same method applied to in situ observations only (see Chapter 6 and 7). The differences between the data-based CTCFP results and the FOAM-based results are especially marked for TC-induced changes in salinity, which might be an indication that the model is tied too strongly to air-sea fluxes or surface climatology, as has been suggested by *Matthew J. Martin* [2016].

The work in this chapter examined TC-induced changes in FOAM temperature and salinity for TC-Katia (2011) and TC-Gonzalo (2014). Analyses showed that both TCs induced surface cooling about 10-12 days after the passage of the storms of about 2˚C, located predominantly at the western side of the North Atlantic basin and away from the Amazon plume region. These results were similar to results obtained in Chapter 6 using satellite SST and Argo data, suggesting that TC-induced changes in temperature are correctly captured by the FOAM system.

The application of CTCFP to FOAM salinity fields revealed a wealth of information about the magnitude, timing, spatial location and depth profile of TC-induced changes. But overall, the TC-induced changes in salinity in FOAM presents a complex and variable picture, which is not fully consistent with the results obtained when applying CTCFP to data alone. CTCFP in FOAM salinity (Figure 8-9) seemed to capture the TC induced salinity increase over shallow MLD and deep BLT. These results coincide with the results obtained using salinity in situ observations from Argo floats (Figure 7-15). These results would agree with previous works (e.g. Balaguru, 2011), arguing that regions with shallow MLD and deep BLT would results in such pre-storm surface freshwater conditions (i.e. surface river run-off). Therefore, TCs tend to increase surface salinity over those regions.

Results presented in this chapter showed that, while the assimilation in FOAM gives access to gap-free frequent full-depth representations of the ocean, it does not represent some of the responses seen in the data. A possible reason is the scarcity of in situ observations in the open ocean, particularly for salinity. Whilst the assimilation includes both in situ and satellite temperature observations, salinity observations are limited to in situ data only. This may explain why differences between the model and the climatology are larger in the salinity field than in temperature field. It is also possible that the assimilation scheme rejects in situ data located too close to TC events. Or that FOAM is tied too closely to the salinity climatological surfaces fluxes [*Matthew J. Martin*, 2016]. Hence it might be appropriate to test other assimilation techniques, assimilations windows (i.e. from one day to 10 days) and other assimilation increments into the model. Furthermore, it is possible that new improved satellite SSS products (i.e. spatial resolution 45 km and an accuracy of about 0.1 psu) could be assimilated in FOAM in future [*J. Boutin et al.*, 2018; *Olmedo et al.*, 2018]. In which case, the model performance in capturing salinity changes may improve, especially in those regions with large river plumes and strong salinity-controlled stratification, e.g. near the Amazon plume.

Chapter 9

Conclusions and Future Work

9.1 Introduction

This thesis has examined the TC induced ocean response as measured by changes in T and S profiles (0 to 200 m depth) with a particular focus on the role of the latter. This thesis presented a new method to compute the composite TC induced response of the ocean and applied it to carry out three distinct science studies. The aim of this chapter is to highlight the main achievements presented in earlier chapters and to offer conclusions from the combined work. Section 9.2 gives a summary of the achievements of the thesis, and how they relate to the research questions posed in Chapter 1(Section 1.1), that defined the scope for the thesis. The last two sections in this chapter present suggestions for future work (Section 9.3) and some final remarks (9.4).

9.2 Scientific contributions and review of achievements

The work presented through this thesis has brought new scientific knowledge of the TC induced response of the ocean by addressing the research questions presented at the beginning of this thesis (Section 1.2). The following subsections summarise the main achievements and link back to the corresponding research questions.

9.2.1 Research Question 1

Is it possible to devise a method to objectively and systematically compute TC-induced changes in T and S, that can be applied to multiple TCs in any ocean basin, any ocean conditions, and is independent of the sources of the data (e.g. Argo, model, satellite)?

The ability to address the science-driven research questions stated in Section 1.2 depended on the success of creating and validating a new methodology to synthesize observations and enable a complete study of TC induced ocean response. Therefore, the CTCFP method was designed and developed (Chapter 4) and then evaluated in a validation study (Chapter 6) and two further studies (Chapter 7 and Chapter 8). The CTCFP was found to be a suitable tool that objectively and systematically selects all the information available in the vicinity of the location of a TC. The results of the CTCFP for a specific TC event already documented in the literature were comparable with those previous studies. Furthermore, the results here were based on a larger number of observations than those previously reported [e.g. *Grodsky et al.*, 2012]. Therefore, the CTCFP method was shown to provide a reliable methodology to assemble observations and study TC induced changes in the ocean.

Furthermore, the CTCFP brings two additional benefits over previous approaches reported in the literature:

1. It provides the means to make global studies of the TC induced response by computing the composite change in thermal and saline vertical structure for TC locations with similar TC properties (e.g. wind, translational speed, etc.) and ocean conditions (e.g. MLD, BL, etc.).

2. The CTCFP is independent of the data source and can be applied to any datasets. Thus, it makes it possible to compare results obtained from in situ observations, satellite observations or synthetic (i.e. model or assimilated model) datasets using the same methodology.

This thesis used CTCFP to study the TC induced changes in T and S with time and depth (anomalies in average vertical profiles) and in space (anomalies along and across track from the TC centre). However, the CTCFP could be readily adapted to consider further aspects of the TC-ocean systems (e.g. ocean currents, ocean instabilities and fronts, etc.). A number of further applications of the CTCFP method are suggested in Section 9.3.2.

9.2.2 Research Question 2

Are TC induced changes in T always accompanied by changes in S, and if so, what is the nature of the observed changes in S? How robust are previous findings of temperature decreases and salinity increases for TCs crossing over freshwater river plumes?

This thesis (Chapter 6) showed application of the CTCFP method to two TC case studies in 2011 and 2014 in the North Atlantic where strong TC induced ocean responses in T and S had previously been reported in the literature. Our results for these same case studies confirmed that the wake of TCs show changes in both T and S. Our Argo-based analyses showed a TC induced decrease in T of the order of -2.5˚C (cooling) in the case of TC-Katia in 2011. These analyses showed that the cooling extended from the surface down to about 300 m depth. For S, our results showed that TC-Katia (2011) induced a salinity increase. This had been reported already by *Grodsky et al.* [2012] who linked this salinity increase to the passage of the TC over the BL region within the Amazon plume. However, when this thesis studied nearby TC locations, the results for S were inconclusive. This research showed that, when considering all available in situ Argo profiles in the vicinity of TCs, the response can exhibit either an increase or decrease in salinity. So it was not possible to support the conclusions of *Grodsky et al.* [2012] that TCs crossing over the Amazon plume would systematically induce a cooling and a salinity increase.

9.2.3 Research Question 3

Is it possible to detect TC induced ocean response using satellite SST and SSS data?

The CTCFP was also applied to satellite SST and SSS datasets. The resulting composite TC response analyses showed that TC induce SST decrease of as much as 2˚C on average, with a recovery time of about 20 days after the passage of the storm. These results are in agreement with the findings of *I D Lloyd and Vecchi* [2011]. Furthermore, our CTCFP analyses of satellite SST helped to identify regions towards the western side of ocean basins, where it is more likely TC induced cooling to happen.

The CTCFP approach was applied also to products from the Soil Moisture and Ocean Salinity (SMOS) satellite mission but these do not show a clear TC induced response in SSS. Therefore, unlike SST, it was not possible to estimate what is the average SSS recovery time after the passage of a TC. From this work, it is not possible to determine if the absence of TC signature in satellite SSS products is linked to the ocean response in SSS being weaker or less coherent.

9.2.4 Research Question 4

Can we overcome the spatial and temporal limitations of in situ data to understand ocean response to TC in similar ocean conditions but different basins?

In Chapter 7, the CTCFP method was applied to all TCs from 2005-2015 in the North Atlantic, North-East Pacific, North-West Pacific and in the North Indian Ocean. The results based on Argo data demonstrated that the average TC induced response in T at 10 m showed a dependency with the translational speed and the wind speed of the TCs. Chapter 7 also presented evidence that TC induced differences in temperature are greater to the right side of the storm track than on the left. These observation-based results are consistent with conclusions of previous studies based on numerical model datasets. This demonstrated that the CTCFP method is a valuable tool to overcome the sampling limitations of in situ observations in the vicinity of TCs. Applying the CTCFP to a larger number of TC events and ocean conditions indicates that the TC induced ocean response can present both decreases and increases in salinity. This is consistent with the results obtained from the two cases studies in the North Atlantic in Chapter 6, suggesting that it is difficult to anticipate the sign of TC induced salinity changes in the ocean.

9.2.5 Research Question 5

How are TC induced changes in S represented in data-assimilating model systems, and is data assimilation able to overcome the sampling limitations of in situ observations?

This question was addressed in Chapter 8, where the CTCFP was applied to output from the FOAM forecasting system. The work in this thesis found that the average TC induced response in temperature seen in FOAM consists of a cooling, which was similar to the results obtained using in situ and satellite observations. However, the magnitude of the temperature response is lower in FOAM than that found using in situ observations, even though many of these observations are assimilated into the system. For salinity, the TC induced response in FOAM did not replicate the results obtained with CTCFP applied to Argo observations. Therefore, it is concluded that data-assimilating systems like FOAM do not adequately represent the upper ocean response to TC, with possible consequences on ocean feedback and TC forecasting. The problem seems partly linked to the lack of in situ observations, but also to the assimilating scheme and relaxation to climatology which attenuate the ocean response seen in the data. The reason why the FOAM ocean response in temperature compares reasonably well with observations relates to the fact that FOAM assimilates large amount of satellite SST. For salinity, FOAM so far only assimilates in situ observations, although the UK Met Office is actively investigating the value of also assimilating SSS

data from satellites such as SMOS. Applying the CTCFP to a version of FOAM that assimilates SSS satellite data (e.g. from SMOS) could be a worthwhile future study (Section 9.3).

9.3 Future work

The work presented in this thesis showed that the CTCFP method offers an objective common methodology to estimate the TC induced ocean response for different TCs, different conditions and different datasets. In the following sections, suggestions for future work towards improvement of both the CTCFP method and the understanding of the mechanisms driving salinity changes after the passage of a storm.

9.3.1 CTCFP Uncertainty and Sensitivity

The CTCFP method would benefit from sensitivity analyses and from providing uncertainty estimates. This would require a study of the uncertainty resulting from 1) the choice of parameters used to characterise pre- and post-storm states (e.g. choice of search radius, R_{max}, and reference period, t_{ref}); 2) the chosen means to mitigate ocean background variability (e.g. with climatological profiles); 3) the pairing criteria used to combine observations from the same or from the different platforms (i.e. uncertainty of different datasets). These sensitivity analyses would need to be performed in well-monitored ocean regions, where observations are available with fine sampling in space and in time (e.g. ideally at least daily observations). Designing such an experiment from scratch would be very expensive. One way forward could be to apply the CTCFP method to well-studied regions like the North Atlantic sub-tropical gyre or the North East Pacific, where extensive field campaigns took place as part of the Salinity Processes in the Upper Regional Study (SPURS, http://spurs.jpl.nasa.gov) in 2012-2013 for the North Atlantic and 2016-2017 for the Pacific. Assuming a sufficient number of TC events occur in these regions over those periods, this exercise would provide a wealth of information about ocean state and its variability thanks to a wide range of available in situ observations (e.g. CTDs, TSGs, surface drifters, Argo floats, etc.) and dedicated satellite and model products.

With regards to ocean background variability, this thesis used WOA13 as the main source of information to correct individual observations prior to the application of the CTCFP. However, as noted before, it is likely that this approach does not fully remove the ocean natural variability, most notably from short-term variability linked to meandering ocean currents and eddies. One way to approach this would be to better determine the actual ocean background variability within days of the passage of the TC and during periods without TC-activity, using for example multi-sensors

products from different satellite missions (e.g. sea surface height, SST, SSS, winds, currents, ocean colour etc.), and verify the CTCFP also in no TC conditions (e.g. same locations but different years when there was no TC activity).

9.3.2 Additional influences on TC-induced surface changes in the ocean

The work in this thesis shows that upper ocean salinity changes induced by the passage of TCs are more complex and varied than those observed for temperature. Evidence indicates that there is a need to understand TC induced changes in salinity and how they relate to TC intensity. It was not possible within the constraints of this thesis to examine how salinity changes affect TC evolution.

This thesis simplified the influence of TC winds by using the maximum wind speed reported at each TC location. More detailed analyses of wind speed patterns within the storm could however allow the development of more detailed argument supporting the observed evidence of different TC induced responses on either side of the TC tracks. Additionally, more detailed information about the wind speed structure within the TC could reveal more details about the spatial structure of the TC forcing and how this relates to TC induced ocean response.

Another aspect that was not addressed in this thesis is the influence of precipitation, which is typically significant in the case of TCs, but nevertheless assumed to play a minor role in SSS in conditions of intense upper ocean mixing. A future study could however consider the inclusion of detailed rainfall analyses in TC conditions to characterize the potential impact of SSS reduction (freshening) over TC-locations due to precipitation. These additional influences could bring some insights into the TC induced salinity response (or lack of) that were described in this thesis using Argo observations.

The satellite SST have proven a valuable source of observations, providing large scale synoptic views of the ocean surface that complement in situ and model data. The satellite SSS products used in this thesis were useful to map the salinity ocean conditions on a monthly basis, but satellite SSS products could not be used to evaluate the daily SSS variability in the vicinity of the TC. However, activities are continuously undertaken to improve existing satellite SSS products, to reduce the uncertainty of individual measurements, improve calibration methods and extend their usefulness in more extreme conditions (e.g. polar regions, high winds). The ESA funded CCI Salinity (CCI+SSS) project aims to improve existing SSS observations from all relevant L-band satellites (SMOS, Aquarius, SMAP). The new CCI+ SSS products will have higher temporal (3-7 days) and spatial (0.25˚) resolution, and would be well suited to repeat the CTCFP study. These new datasets will include uncertainty characterization of the salinity that would be useful to use in synergy with other

satellite datasets (e.g. synergy of SST and SSS to compute sea surface density maps at daily and 0.25˚ resolution). Furthermore, combining satellite SSS and SST with satellite sea surface height (SSH) and Argo could provide information on upper ocean structure (MLD and BL) on a weekly basis, which would be an improvement from the current information available only as monthly maps based on Argo data only.

9.4 Final Remarks

This thesis developed an innovative method to explore TC-induced changes in the ocean. The results showed that the ocean response to the passage of TCs is varied and complex, and still not fully understood. In terms of the ocean temperature response, analyses from in situ and satellite observations and the FOAM assimilating system model all show a TC induced decrease in T, which might be explained by the TC induced upwelling and turbulent mixing. Although TCs do sometimes induce changes in salinity, the response varies from case to case and shows not clear relation to the underlaying ocean conditions alone (i.e. MLD and BL). Furthermore, changes in temperature following the passage of a TC are not always associated with TC induced changes in salinity. The results presented in this thesis suggest further research is required to understand the sensitivity of the CTCFP method and the links between ocean salinity changes, wind field structure, precipitation and TC intensification. The work with the FOAM model data indicates that existing forecasting systems do not adequately represent the ocean response to TC, which is either attenuated (temperature) or missing (salinity) in the model. Forecasting systems concerned with TC intensity prediction should account for upper ocean changes in both temperature and salinity, which taken together account for the stability of the ocean water column and its potential for overturning. This recommendation would extend to those studies aimed at understanding what would be the consequences upon TC intensity and frequency in a 1.5˚ Global Warming scenario [*Allen*, 2018] where warming and changes in the hydrological cycle will affect both SST and SSS fields.

Appendix A Tropical cyclone FootPrint MATLAB code

```
% Tropical cyclone FootPrint (TCFP)
%
% Description
% Method to charactherize the TC induced changes into the ocean by
% accumulating any available source of information in the surrounding
% of a passing TC. Data set might be: in situ observation (e.g. Argo),
% satellite data (e.g. SST and SSS) or assimilation system model (e.g.
% FOAM). For more detail information, see Chapter 3 in this thesis (see
rerence below to thesis title and author).
%
% Objective:
% 1) Check out that our methodology is matching results of other authors.
% 2) Demonstrate where our method is outperforming other authors work.
%
% Notes from the author
% The code presented in this work was written using MATLAB version
8.1.0.604 (R2013a) and it might be subject to improvements. Do use
% this code with caution and allways revise your own results and
% conclusion as these are your own responsability.
% The author is happy to hear any feedback on the use of the CTCFP code
and its suggentions for improvements.
% Full access to code and snipets are available:
% [1] Upon request to the main author of the thesis
% (rafaelcatany@gmail.com)
% [2] Open source Github to be public upon publication of the main work
% (https://github.com/RCatany/CTCFP)
%
%
% Thesis title: Understanding Tropical cyclone induced changes in the
upper
% temperature and salinity (University of Southampon eprint 2019)
%
% Author: Rafael Jaume Catany (ORCID: https://orcid.org/0000-0002-3561-
5596)
%
%
%
% UPDATE
% LAB option to use SSS dataset of CATDS (LAB = 1, default) or BEC (LAB =
0) (2019/01/12)
% ========================


clear; clc
```

Add script and snippets to your MATLAB path

```
%folder_script = mfilename('fullpath');
```

```
 folder_script = '/Users/rejc1e11/Documents/GitHub/my_git/TCFP/';
 cd (folder_script)
 addpath(genpath(folder_script));

 % Set workspace
 folder_workspace = '/Volumes/NOC/valor/Rafael/';
```

scripts inputs

```
 plot_example = 1;                    % plot example (1) or set to zero
other wise
 save_fig = 0;                        % save figures;other wise set to zero
 climat = 1;                          % remove climatology (climat =1) or
not (climat = 0);

tcmake = 5;                          % (1) TC-BOLAVEN; (2) TC-KATIA; (3) TC-
HUMBERTO (2013); (4) TC-2014; % (5) input any year from 2004 to 2015
 fg_format = 'eps';                   % string with figure format (i.e. png,
eps)
 zoom_in = 0;                         % zoom in (1) or not (0)
 method = 2;                          % Argo sampling all floats within r
(method 1); only same platform sampling (method 2)
 r = 400; r_str = num2str(r);         % (km) radius from TC centre
 t_range = 10;                        % number of days to use in the average
to compute before-TC ocean conditions (for GHRSST only)
 LAB = 1;                             % USE SSS from CATDS laboratory (LAB =
1) or BEC laboratory (LAB = 0)

 % ======

 if LAB == 1
     LAB_str = 'CATDS';
 elseif LAB == 0
     LAB_str = 'BEC';
 else
     clc
     error(' #### Choose the right Laboratory: CATDS (LAB = 0) or BEC (LAB
= 0) #### ')
 end

 % ===
```

Plot specs

```
 plot_specs_raf; % load plot_specs_raf

 if method == 1
     method_str = ['Multi float method ' num2str(method)];
 elseif method == 2
     method_str = ['Single float method ' num2str(method)];
 end
```

=====

Choose TC example to plot

```
if tcmake == 1
    tc = {'bolaven'}; % TC name in Zenghong study
    tc_example = 'TCBOLAVEN';
    iyear = 2012; % input year
    year_str = num2str(iyear);
    basin = 2; % East Pacific Basin, just near by China coast
    [xmin,xmax,ymin,ymax,basin_str]=map_lim_raf(basin);
    fzeng = [2901201, 2901527, 5901989]'; % floats used in Zenghong paper
    % plot study Zenghong study region
    x1 = 120; % min lon
    x2 = 150; % max lon
    y1 = 15; % min lat
    y2 = 30; % max lat

elseif tcmake == 2
    tc = {'irene','katia','maria','ophelia','philippe'}; % TC name
    tc_example = 'TCKATIA';
    iyear = 2011; % input year
    year_str = num2str(iyear);

    basin = 0; % North Atlantic
    [xmin,xmax,ymin,ymax,basin_str]=map_lim_raf(basin);
    fzeng = [6900590, 4900758, 4900818, 4900839]'; % floats used in
Grodsky, 2012
    % plot study Grodsky 2011 study region
    x1 = -70; % min lon
    x2 = -30; % max lon
    y1 = 5; % min lat
    y2 = 30; %max lat

elseif tcmake == 3
    tc = {' '}; % TC name
    tc_example = '';
    fzeng = []';

    iyear = 2013; % input year
    year_str = num2str(iyear);

    basin = 0; % North Atlantic
    [xmin,xmax,ymin,ymax,basin_str]=map_lim_raf(basin);

elseif tcmake == 4 % GRODSKY 2012
    tc = {' '}; % TC name
    tc_example = '';
    fzeng = []'; % floats used in Grodsky, 2012

    iyear = 2014; % input year
    year_str = num2str(iyear);

    basin = 0; % North Atlantic
```

```
    [xmin,xmax,ymin,ymax,basin_str]=map_lim_raf(basin);

 elseif tcmake == 5 % REUL 2014
    tc = {' '}; % TC name
    tc_example = '';
    fzeng = []'; % floats used in Reul, 2014

    iyear = 2015; % input year
    year_str = num2str(iyear);

    basin = 0; % North Atlantic
    [xmin,xmax,ymin,ymax,basin_str]=map_lim_raf(basin);

 end

 fzeng_cell = num2cell(fzeng);
```

```
 Set up folder_out
```

```
 if climat == 1
    folder_anom = [folder_workspace '/argo/argo_anomalies/TCact/noCL/r'
r_str '/' basin_str '/'];
    fn = ['ar_anomalies' num2str(method) '_13dunperturbed_TC'
num2str(iyear) '_CL19552012_' basin_str '_SAMP12'];
    folder_out = [folder_workspace 'bolaven2/' num2str(iyear) '/' ];

 elseif climat == 0
    folder_anom = [folder_workspace '/argo/argo_anomalies/TCact/withCL/r'
r_str '/' basin_str '/'];
    fn = ['ar_anomalies' num2str(method) '_13dunperturbed_TC'
num2str(iyear) '_' basin_str '_SAMP12'];
    folder_out = [folder_workspace 'bolaven2/' num2str(iyear) '/'] ;
 end

 % Create folder output
 foldercheck_raf(folder_out);


 folder_sst = [folder_out 'SST/'];
 foldercheck_raf(folder_sst)
```

```
 Choose out SSS storage depending what data you use (1: SSS CATDS; 2:
BEC)
```

Flat to use SSS CATDS data (LAB = 1), or BEC (LAB = 0)

```
 folder_sss = [folder_out 'SSS/' LAB_str '/'];
 foldercheck_raf(folder_sss);
```

```
 ## Check and Load file with anomalies
```

>> NOTE: Use function: fast_argo_anomalies5.m (e.g. in hurri_ARGOstatisticsANOMALIES.m)

```
Lfn = [folder_anom fn '.mat'];

if exist(Lfn,'file') == 2
    % list of parameters to load
    paramL1 = {'param_out','param_diff'};
    paramL2 = {'basin_str','platform','plat_rare','r','rlon','rlat',...
        'time_hurri','time_cross','time_cross_num','time_MATnum',...

'trans_sp','wind_hurri','name_hurri','plat_repetition','plat_INFO'};
    load (Lfn,paramL1{:});
    load(Lfn,paramL2{:});
else
    warning (['MISSING file with Argo anomalies: ' fn '.mat'])
    warning (['Directory of search: ' folder_anom])

    warning(['Check out you have anomaly filles for ' basin_str '. If you
do not have them just run ar_TCappend2.m'])
    error(['Check that you have Argo anomalies ' method_str ' ' basin_str
' in '  year_str])
    %
end % load mat file with Argo anomalies

% ==================
```

Get the argo floats

```
lon_ar = param_diff.lon_diff;
lat_ar = param_diff.lat_diff;
```

```
============
plat information (wind, trans_sp, RLON, RLAT, etc)
```

```
rlon_plat = plat_INFO.plat_RLON;
rlat_plat = plat_INFO.plat_RLAT;
```

```
============
```

```
whos time_cross lon_ar lat_ar
clc
warning ('REMOVE unwanted zeros. Consider including the followind into
hurri_ARGOstattisticsANOMALIES.m')

ind = lon_ar == 0 & lat_ar == 0;

lon_ar(ind) = NaN;
lat_ar(ind) = NaN;
time_cross(ind) = NaN;
time_cross_num (ind) = NaN;
time_MATnum(ind) = NaN;
plat_repetition(ind) = NaN;

[a,b,c] = size(param_diff.temp_diff);
```

```
 if c > 1
     ind = repmat (ind,[1,1,c]);
 end; clear a b c

 param_diff.temp_diff(ind) = NaN;
 param_diff.salt_diff(ind) = NaN;
 param_diff.rho_diff(ind) = NaN;
 param_diff.pres_diff(ind) = NaN;

 % time hurricane crosssing
 % null_loc = isnan(rlon) & isnan(rlat); % index the empty locations
 % time_hurri = time_MATnum;
 % time_hurri (null_loc) = NaN;
```

```
 Get Argo Cartesian coords
```

```
 [Xp,Yp] =
tangent2TC_fnc_raf2(rlon,rlat,time_hurri,lon_ar,lat_ar,time_cross,r,basin);
```

```
 =======
 Get the original hurricane track (this is because rlon rlat values
have to many NaNs so it plots dots instead of lines)
```

```
 [hurri] = hurri_track5(iyear,basin); % prime hurri parameters
 % ======
 % IBTrACS data FILTERED
 % .......
 % TC filter specs
 trans_sp_MAX = 100;    % max translational speed (m/s)
 distMax2land = 300;      % max distance to land (km)
 time_sampling = -9;    % choose time of the day sampling (00,06,12,18)
 wind_min = 33;           % minimum wind speed (m/s); i.e. hurricanes min
wind = 33 m/s
 % ........
 [lonf,latf,time_hurrif,presf,windf,trans_spf,accelf,naturef,name_strf,name
f,sourcef,dist2landf] = ...

TCfilter(hurri,basin,trans_sp_MAX,distMax2land,wind_min,time_sampling);

 % Get the time_hurri at each location (Note: here you need to filter again
the original time_hurri.
 % It is possible to solve bug by saving variable time_hurri at the time
when anomalies were computed)
 % time_sampling = 12;    % choose time of the day sampling (00,06,12,18)
 %
 % [~,~,time_hurri,~,~,~,~,~,~,~,~,~] = ...
 %
TCfilter(hurri,basin,trans_sp_MAX,distMax2land,wind_min,time_sampling);
 [~,~,~,HH,~,~] = datevec(time_hurrif);
 ind12 = HH==12;
 ind = ~isnan(time_hurri);

 wind2 = nan(size(time_hurri));
```

```
 trans_sp2 = nan(size(time_hurri));

 wind2 (ind) = windf(ind12);
 trans_sp2 (ind) = trans_spf(ind12);

 wind = wind2;
 trans_sp = trans_sp2;

 clear wind2 trasn_sp2 ind ind12

 % ====
 % Assign color to each TC
 X = time_hurrif;
 Y = windf;
 [h1,h2,color_TC] =
plot_oceanTC(X,Y,name_strf,min(time_hurrif(:)),max(time_hurrif(:)),0,50); %
close all
```

```
 ===========
 ## Computation SST and SSS TC-INDUCED changes at each TC-LOCATION
```

```
 sst_bolaven_CHANGES % script (snippet TC CHANGES)

 if iyear >= 2011
     sss_bolaven_CHANGES % script (snippet TC CHANGES (in SMOS))
 end
```

```
 =========
 ## Plot SST and SSS time series at each TC-LOCATION
```

```
 if plot_example == 1
     sst_bolaven_TSERIES % (snippet SST TSERIES)

     if iyear >= 2011
         sss_bolaven_TSERIES % (snippet SST TSERIES)
     end
 end
```

```
 ==========
 Plot float location
```

```
 if plot_example== -9
     leg_str = cat(2,name_hurri, ['daily location (12:00) with a circle of
r = ' r_str ' km']);

     figure(1*method); clf

     clear n
     tc = name_hurri; % Just keeping TCs in  the hurri file
     h2 = zeros(length(tc),1);
     for n = 1 : length(tc)
         hold on
```

```
        h2(n) =
plot(rlon(:,(n)),rlat(:,(n)),marker_style{n},'Color',marker_color{n},'LineW
idth',2,'MarkerSize',8); %h2 = h2(1);
        set(h2(n), 'LineStyle',line_style{n})
        % uncomment the following to place the TC time
        %
text(rlon_p2(:,itc(n)),rlat_p2(:,itc(n)),datestr(time_hurri(:,itc(n)),'dd/m
m'),'BackGroundColor','w','FontWeight','bold')

    end
    [~,h3] = plot_study_region(rlon(:,(1)),rlat(:,(1)),r); % plot study
region in around chosen TC (i.e. TC katia or bolaven)

    % mark the time of the TC's passage (i.e. Katia)
    %
text(rlon_p2(:,itc(2)),rlat_p2(:,itc(2)),datestr(time_hurri(:,itc(2)),'dd/m
m'),'FontWeight','bold','BackGroundColor','w','Position',[0.5 0.5]) % date
katia only
    %
text(rlon(:,1),rlat(:,1),datestr(time_hurri(:,1),'dd/mm'),'FontWeight','nor
mal','BackGroundColor','w') % date katia only

    %
text(rlon_p2(:),rlat_p2(:),datestr(time_hurri(:),'dd/mm'),'BackGroundColor'
,'w','FontWeight','bold') % date all TCs
    % Add legend
    legend([h2;h3],leg_str(:),'Location','NorthEast');
    xlim([xmin xmax]); ylim([ymin ymax]);
    fillmap
    title([basin_str ' Tropical Cyclones in '
num2str(iyear)],'FontWeight','bold','FontSize',12); hold on
    xlabel('Longitude (\circ)','FontWeight','bold'); ylabel('Latitude
(\circ)','FontWeight','bold')
    % Plot limits of the study regoion (Do NOT plot region. It is
confusing to the reader, Christine advised 18122016)
    hold on
    plot([x1 x1],[y1 y2],'k-','LineWidth',2);
    plot([x2 x2],[y1 y2],'k-','LineWidth',2)
    plot([x1 x2],[y1 y1],'k-','LineWidth',2)
    plot([x1 x2],[y2 y2],'k-','LineWidth',2)
    % Zoom in to the study region (i.e. Grodky(2012) is looking into the
Amazon plume)
    if zoom_in == 1
        % figure(1*method); clf
        % h2 = plot(rlon_p(:,itc_p),rlat_p(:,itc_p),'-','LineWidth',3);
%h2 = h2(1);
        clear ind
        ind = (rlon >= x1 & rlon <= x2) & (rlat >= y1 & rlat <= y2);
        rlon(~ind) = NaN;
        rlat(~ind) = NaN;
        time_hurri(~ind) = NaN;
        legend([h2;h3],leg_str(:),'Location','SouthEast');
```

```
        xlim([xmin xmax]); ylim([ymin ymax]);
        fillmap
        title([basin_str ' Tropical Cyclones in '
num2str(iyear)],'FontWeight','bold','FontSize',12); hold on
        xlim([x1 x2]); ylim([y1 y2]);
        grid on
        % grid minor
    end; clear ind

    % =======
    % save figure
    fg_name1 = [folder_out 'ar_dist_TC_' basin_str '_' num2str(iyear)];


    if save_fig == 1
        fg = gcf;
        save_raf(fg,fg_name1)
    end
end

if tcmake == 1 || tcmake == 2
    fzeng_str =  num2str(fzeng(:));
    nfloat = length(fzeng);                    % number of floats picked
up in the paper
    n = 1;                                     % tc number (i.e. n = 2 is
Katia)
    p_bol = platform(:,n);                     % platforms around TC
bolaven
    lon_bol = lon_ar(:,n);
    lat_bol = lat_ar(:,n);

    tar_bol = time_cross(:,n);                % time Argo time which is
the same day when TC is crossing
    tar_bol2 = time_cross_num(:,n);           % Argo sampling time
relative to storm passage around bol
    tar_bol3 = tar_bol+tar_bol2;              % Argo sampling absolute
time (matlab time) arount bol

    fzeng1 = ismember(p_bol,fzeng(1)); % index floats used in the paper
(ID: 2901201)
    fzeng2 = ismember(p_bol,fzeng(2)); % index floats used in the paper
(ID: 2901527)
    fzeng3 = ismember(p_bol,fzeng(3)); % index floats used in the paper
(ID: 5901989)
    bTC = tar_bol < 0; % before TC
    aTC = tar_bol > 0; % after TC
end
```

Plot floats around TC Bolaven

```
if tcmake == 1 || tcmake == 2
```

```
    if plot_example == -999
        figure(1*method);
        hold on
        clear n
        h4 = zeros(length(tc),1);
        for n = 1% 1 : length(tc)
            h4(n) =
plot(lon_bol(:),lat_bol(:),'ko','MarkerFaceColor','y','MarkerSize',8);
        end


        figure
        H = zeros(1,nfloat); % indeces for the legend
        h = H;
        H = logical(H);
        for n = 3%1:nfloat
            fzeng1 = ismember(p_bol,fzeng(n)); % index floats used in the
paper (ID: 2901201)
            Tfloat = sum(fzeng1(:)); % test float is found

            if Tfloat >=1
                hold all
                h5 =
plot(lon_bol(fzeng1),lat_bol(fzeng1),'k','LineStyle',marker_style{n},'Marke
rSize',10); %(ID: 2901201)

                h(1,n) = h5(1);
                H(:,n) = ones;
            end
        end
        h5 = h(H);


        if save_fig == 1
            save_raf(figure(1*method),fg_name1); % save argo distribution
around bolaven
            close
        end
    end
 end
```

```
 Plot 'Other' Argo float (i.e. floats out of range of Katia)
```

R = 1000; % radius of 1000 km from TC % plot Argo around Katia only rlon2 = rlon_p2(:,itc(2)); rlat2 = rlat_p2(:,itc(2)); rlon2 = rlon(:,itc(2)); rlat2 = rlat(:,itc(2));

time_hurri2 = time_hurri(:,itc(2));

% index values only (i.e. no nans) ind = find(~isnan(rlon2) & ~isnan(rlat2)); nloc = length(ind); % numbe of locattions for x = 5 %: nloc ind2 = ind(x); % % Time TC passage [Yy,Mm,Dd,hh,mm,ss] = datevec(time_hurri2(ind2));

```
        [~,ar_floatsT,lon_ar2,lat_ar2,time_num,dist,plat] =
ar_inrange(rlon2(ind2),rlat2(ind2),R,Yy,Mm,Dd);
```

```
        lon_ar3 = squeeze(lon_ar2);
        lat_ar3 = squeeze(lat_ar2);
        time_num3 = squeeze(time_num);
        dist3 = squeeze(dist);
        plat3 = squeeze(plat);
        pp = plat3(dist3<200); pp = unique(pp);
        %lon_other
        figure; hold on
        h_ar = plot(lon_ar3,lat_ar3,'k.');

plot(rlon2(ind2),rlat2(ind2),'ks','MarkerFaceColor','r','MarkerSize',
10)
```

end

% time range unperturbed ocean before TC d1 = time_hurri2(ind2)-10; % upper time limit d2 = time_hurri2(ind2)-3; % ower time limit time_range = d1:d2;

```
% Match float from data base to my ar_sampling
% t = find(plat3== pp(4)); % index a given float
%  t = find(plat3==fzeng(n)); % index a given float
% hold on; plot(lon_ar3(t),lat_ar3(t),'go')

% ony around Katia
% lon_katia = lon_bol(:,2);
% lat_katia = lat_bol(:,2);
% tar_katia = tar_bol(:,2);
% p_katia = p_bol(:,2);
% gind = p_katia == pp(2); sum(gind)
```

```
==========
ARGO Temperature and salinity under Bolaven
```

```
zmax = 400; % maximum depth layer to observe (i.e zmax = 50 is depth = 200
m as in the paper)
MLD_method = 2; % computation of kara MLD
% All_F = 1; % plot all the floats(1)
all_TC = 0; % look all TC in the study region (1) or only to the chose one
(0)


if all_TC == 0
    ind = 1;
end
temp = squeeze(param_out.temp_out);
salt = squeeze(param_out.salt_out);
pres = squeeze(param_out.pres_out);

% Temp and salt differences
temp_d = squeeze(param_diff.temp_diff);
salt_d = squeeze(param_diff.salt_diff);
pres_d = squeeze(param_diff.pres_diff);

% generate a presure variable (is equal in all profiles). It has the same
depth levels as param aand param_diff
```

```
p1 = [min(pres(:)):5:max(pres(:))];
```

Computation Brunt Vaisalta frequency (used the Gibss Sea water tool, TEOS10)

```
clear a b c
[a,b,c] = size(salt);


if c ~= 1
    SALT = reshape(salt,a*b,c);
    TEMP = reshape(temp,a*b,c);
    PRES = reshape(pres,a*b,c);
    LAT = reshape(lat_ar,a*b,1);
    LON = reshape(lon_ar,a*b,1);

    % ========
    % prolocate vars
    Brunt2_ar = nan(a*b,c);
    p_mid_ar = nan(a*b,c); % mid point pres between two depth levels


else
    SALT = reshape(salt,a,b,c);
    TEMP = reshape(temp,a,b,c);
    PRES = reshape(pres,a,b,c);
    LAT = reshape(lat_ar,a,1);
    LON = reshape(lon_ar,a,1);

    % ========
    % prolocate vars
    Brunt2_ar = nan(a,b,c);
    p_mid_ar = nan(a,b,c); % mid point pres between two depth levels

end



[A,B,C] = size(SALT);

ind = find(any(SALT,2) & any(TEMP,2));


for n = 1 : length(ind)
    ind2 = ind(n);

    SALT2 =
gsw_SA_from_SP(SALT(ind2,:),PRES(ind2,:),LON(ind2,:),LAT(ind2,:));

    %     [Brunt2_out, p_mid_out] =
gsw_Nsquared(SALT(ind2,:),TEMP(ind2,:),PRES(ind2,:),LAT(ind2));
    [Brunt2_out, p_mid_out] =
gsw_Nsquared(SALT2,TEMP(ind2,:),PRES(ind2,:),LAT(ind2));
```

```
    Brunt2_ar(ind2,1:length(Brunt2_out)) = Brunt2_out;
    p_mid_ar(ind2,1:length(Brunt2_out)) = p_mid_out;

    clear Brunt2_out p_mid_out
end; clear n ind SALT TEMP PRES LAT

Brunt2_ar = Brunt2_ar .*(60*60);         % Convert cps to cph;

Brunt_ar = nan(size(Brunt2_ar));
ind = Brunt2_ar >= 0;                    % Keep Brunt Vaisala grater than
0 cph (i.e. avoid imaginary number in sqrt)
Brunt_ar(ind) = realsqrt(Brunt2_ar(ind));% Value used in literautre
clear ind

% =======
% Reshape N2_ar to original dimension
Brunt_ar = reshape(Brunt_ar,a,b,c);
Brunt2_ar = reshape(Brunt2_ar,a,b,c);
```

```
====
COMPUTATION OF MIXED LAYER DEPTH (only with raw data not with
anomalies)
```

```
=======
```

```
MLD_method = 1; % (1) Monegut; (2) Kara

if MLD_method == 1
    MLD_method_str = 'mont';
elseif MLD_method == 2
    MLD_method_str = 'kara';
else
    error('You must choose MLD calculation: Montegut (1) or Kara (2)
method')
end

% MLD file name
folder_MLD_data = [folder_out 'MLD_mat/']; % store mat files with MLD
computations
foldercheck_raf(folder_MLD_data);

fn_mld = [folder_MLD_data 'ar' num2str(method) '_r' num2str(r) '_mld_'
MLD_method_str '_' basin_str '_' num2str(iyear) '.mat' ];

% check fn_mld exist
fn_exist = exist (fn_mld,'file');

% ====

if climat == 0
    nTC = length(name_hurri); % number of TCs
```

```
    [nobs,~] = size(lon_ar); % number of obs per TC

    % MLD computation and saving fn_mld
    if fn_exist ~= 2
        % var pre-location
        TT = NaN(nobs,nTC);

        ILD = TT;
        MLD = TT;
        BLT = TT;
        salt_ht =  TT; salt_hd = TT;
        temp_ht = TT; temp_hd = TT;
        rho_ht =  TT; rho_hd = TT;

        if nTC == 1
            iTC = nTC;
            for nprof = 1 : nobs
                S = squeeze(salt(nprof,:))';
                T = squeeze(temp(nprof,:))';
                P = squeeze(pres(nprof,:))';


[ILD(nprof,iTC),MLD(nprof,iTC),BLT(nprof,iTC),salt_ht(nprof,iTC),temp_ht(np
rof,iTC),rho_ht(nprof,iTC),salt_hd(nprof,iTC),temp_hd(nprof,iTC),rho_hd(npr
of,iTC)] =...
                    stratos_fnc4(S,T,P,MLD_method);
            end

        elseif nTC > 1

            for iTC = 1:nTC
                for nprof = 1:nobs

                    S = squeeze(salt(nprof,iTC,:));
                    T = squeeze(temp(nprof,iTC,:));
                    P = squeeze(pres(nprof,iTC,:));


[ILD(nprof,iTC),MLD(nprof,iTC),BLT(nprof,iTC),salt_ht(nprof,iTC),temp_ht(np
rof,iTC),rho_ht(nprof,iTC),salt_hd(nprof,iTC),temp_hd(nprof,iTC),rho_hd(npr
of,iTC)] =...
                        stratos_fnc4(S,T,P,MLD_method);
                end
            end
        end % if statement computing MLD for one TC or for more

        % ====
        % save MLD vars
        vars_mld = {'lon_ar', 'lat_ar', 'ILD', 'MLD', 'BLT', 'salt_ht',
'temp_ht', 'rho_ht', 'salt_hd','temp_hd','rho_hd'};
        save(fn_mld, vars_mld{:});
```

```
    elseif fn_exist == 2
        load (fn_mld)
    end; % MLD computation

elseif climat == 1

    if fn_exist == 2
        load(fn_mld)
    else
        clc
        warning ('Run script for raw data (i.e. climat = 0) to compute the
MLD')
        pause (10)
    end

end
```

```
 Get MLD hw (closest grid point to float) at each Argo profile Before
TC
```

MLD_hawaii file name

```
    fn_MLD_hw = [folder_MLD_data 'MLD_hw_' basin_str '_' num2str(iyear)
'.mat'];

    % check fn_mld exist
    MLD_hw_exist = exist (fn_MLD_hw,'file');

    if  MLD_hw_exist ~= 2
        MLD_hw = nan(size(time_cross));
        BLT_hw = nan(size(time_cross));
        TTD_hw = nan(size(time_cross));
        ILD_hw = nan(size(time_cross));
        temp_hd_hw = nan(size(time_cross)); % temp in MLD
        salt_hd_hw = nan(size(time_cross)); % salt in MLd

        ind = find(~isnan(time_cross));

        for n = 1 : length(ind)

            iX = ind(n);

            TT = time_cross(iX);

            DD = rd_mld_hawaii_month(basin,TT);
            LON = DD.lon_out;
            LAT = DD.lat_out;
            mld_hw = DD.mld;
            blt_hw = DD.blt;
            ttd_hw = DD.ttd;
            ild_hw = DD.ild;
            mlt_hw = DD.mlt;
            mls_hw = DD.mld;
```

```
            MLD_hw (iX) =
interp2(LON',LAT',mld_hw',lon_ar(iX),lat_ar(iX),'nearest');
            BLT_hw (iX) =
interp2(LON',LAT',blt_hw',lon_ar(iX),lat_ar(iX),'nearest');
            TTD_hw (iX) =
interp2(LON',LAT',ttd_hw',lon_ar(iX),lat_ar(iX),'nearest');
            ILD_hw (iX) =
interp2(LON',LAT',ild_hw',lon_ar(iX),lat_ar(iX),'nearest');
            temp_hd_hw (iX) =
interp2(LON',LAT',mlt_hw',lon_ar(iX),lat_ar(iX),'nearest');
            salt_hd_hw (iX) =
interp2(LON',LAT',mls_hw',lon_ar(iX),lat_ar(iX),'nearest');

            clear mld_hw LON LAT DD iX TT
        end; clear ind % Get MLD_hw closest to each Argo float

        % ====
        % save MLD (hawaii) vars
        vars_mld = {'lon_ar', 'lat_ar', 'ILD_hw', 'MLD_hw',
'BLT_hw','TTD_hw', ...
            'salt_hd_hw','temp_hd_hw'};

       save(fn_MLD_hw, vars_mld{:});
    else
        load (fn_MLD_hw);
    end
```

Get MLD_JAMSTEC 10-day (closest grid to float)

```
data_type = 1; % (1) 10days MLD; (2) month; (3) monthly

% MLD_j file name
fn_MLD_j = [folder_MLD_data 'MLD_JAMTEC10d_' basin_str '_' num2str(iyear)
'.mat'];

% check fn_mld exist
MLD_j_exist = exist (fn_MLD_j,'file');

tic
if  MLD_j_exist ~= 2
    MLD_j = nan(size(time_cross));
    temp_hd_j = nan(size(time_cross)); % temp in MLD
    salt_hd_j = nan(size(time_cross)); % salt in MLd

    ind = find(~isnan(time_cross));

    for n = 1 : length(ind)

        iX = ind(n);

        TT = time_cross(iX);
```

```
        [lon_j,lat_j,mld_j,mlt_j,mls_j,mlrho_j,nobs_j,time_out_j,Ndays_j]
= get_mld_jamstec(TT,basin,data_type);

        LON = lon_j;
        LAT = lat_j;

        MLD_j (iX) =
interp2(LON',LAT',mld_j',lon_ar(iX),lat_ar(iX),'nearest');
        temp_hd_j (iX) =
interp2(LON',LAT',mlt_j',lon_ar(iX),lat_ar(iX),'nearest');
        salt_hd_j (iX) =
interp2(LON',LAT',mls_j',lon_ar(iX),lat_ar(iX),'nearest');

        clear mld_j LON LAT DD iX TT lon_j lat_j
    end; clear ind % Get MLD_j closest to each Argo float

    % ====
    % save MLD (hawaii) vars
    vars_mld = {'lon_ar', 'lat_ar', 'MLD_j', ...
        'salt_hd_j','temp_hd_j'};

    save(fn_MLD_j, vars_mld{:});
 else
    load (fn_MLD_j);
 end


 toc
```

```
==========
## STATS TC changes in Argo (ALL TCs)
```

```
 stats_bolaven_ALLTC % % script (snippet) to comput stats including all TC
in a season
```

```
 STATS for each TC
```

nTC= 3; TEMP = squeeze(temp_d(:,nTC,:)); SALT = squeeze(salt_d(:,nTC,:));

bolaven_TC_STATS_fn(iyear,time_cross_num(:,nTC),time_cross(:,nTC),lon_ar(:,nTC),lat_ar(:,nTC),p1,TEMP,SALT,MLD(:,nTC),MLD_hw(:,nTC),MLD_j(:,nTC),BLT(:,nTC),BLT_hw(:,nTC),climat,method)

```
=====
## ghrsst_bolaven_example (make plots of Argo around each TC)
```

```
ghrsst_bolaven_example2         % (script: look at each TC separated)
```

```
==============
NEED TO REVISE THE BELOW CODE
```

```
clc
error('need to review code from here to end')
```

```
 [a,b,c] = size(temp);
 tar_bol2 = repmat(tar_bol2,[1,b]);
 tar_bol3 = repmat(tar_bol3,[1,b]);
```

```
 plot temp and salt under Bol
```

==== Generate a fancy colormap (for F)

```
 [dplot] = cbrewer('div','RdYlBu',60,'cubic'); dplot = flipud(dplot); %
colormap for divergent data

 % =====
 % plot spec
 MLDc = 'k'; % line color for MLD
 if climat == 0
     dT1m = 15; dT1M = 30; dT = 3; % caxis temp diffs
     dS1m = 35; dS1M = 39; dS = 0.4; % caxis salt diffs
 elseif climat ==1
     dT1m = -2; dT1M = 2; dT = 3; % caxis temp diffs
     dS1m = -1; dS1M = 1; dS = 0.2; % caxis salt diffs
 end

 All_F = 0; % plot all the floats available (All_F == 1); other wise plot a
single platform (All_F == 0)
 title_specs = {'FontSize',12,'FontWeight','bold'};
 label_specs = {'fontSize',10,'FontWeight','bold'};
 legend_loc = 'SouthEast'; % location of the legend


 if All_F == 0
     for Flt = 1 : length(fzeng);
         % ====
         % subplot specs (it needs to be reset at each iteration)
         m = 1; n=2; fgx3 = 0; fgx4 = 0;

         % ====
         % plot profiles from each float
         ifloat = ismember(p_bol,fzeng(Flt));
         ifloat_profiles = sum(ifloat(:)); % number of profiles done by
ifloat
         ifloat = find(ifloat);
         Flt_str = num2str(fzeng(Flt));

         % Get data from each float (ifloat)
         itemp = temp(ifloat,:)';
         isalt = salt(ifloat,:)';
         ipres = pres(ifloat,:)';

         itemp_d = temp_d(ifloat,:)';
         isalt_d = salt_d(ifloat,:)';
         ipres_d =  pres_d(ifloat,:)';
```

```
        test = ~isempty(itemp) & ~isempty(isalt) & ~isempty(ipres); %
check floats are full (of data)

        if test == 1
            figure; fg1 = gcf;
            % figure(3*method); clf
            fgx3 = fgx3+1; subplot(m,n,fgx3)
            fg_name3 = [folder_out tc_example '_TEMP_profiles' Flt_str
'_M' num2str(method) '_' basin_str];

            plot(itemp,-ipres,'linewidth',2); hold on
            legend(num2str(time_cross_num(ifloat)),'Location',legend_loc);
xlim([-3 3]);
            plot([0 0],ylim,'k-'); % line 0,0
            title(['Temperature Float ID: ' num2str(fzeng(Flt)) '; method
' num2str(method)],title_specs{:})
            xlabel('Temperature (C\circ)',label_specs{:}); ylabel('De[th
(m)',label_specs{:});

            fgx3 = fgx3+1; subplot(m,n,fgx3)
            plot(itemp_d,-ipres_d,'linewidth',2); hold on
            legend(num2str(time_cross_num(ifloat)),'Location',legend_loc);
xlim([-3 3]);
            plot([0 0],ylim,'k-'); % line 0,0
            title(['Temperature difference Float ID: ' num2str(fzeng(Flt))
'; method ' num2str(method)],title_specs{:})
            xlabel('Temperature (C\circ)',label_specs{:}); ylabel('De[th
(m)',label_specs{:});

            figure; fg2 = gcf;
            %figure(4*method); clf
            fgx4 = fgx4+1; subplot(m,n,fgx4)
            fg_name4 = [folder_out tc_example '_SALT_profiles' Flt_str
'_M' num2str(method)  '_' basin_str];
            plot(isalt,-ipres,'linewidth',2); hold on
            legend(num2str(time_cross_num(ifloat)),'Location',legend_loc);
xlim([-2 2]);
            plot([0 0],ylim,'k-'); % line 0,0
            title(['Salinity Float ID: ' num2str(fzeng(Flt)) '; method '
num2str(method)],title_specs{:})
            xlabel('Salinity (psu)',label_specs{:}); ylabel('De[th
(m)',label_specs{:});

            fgx4 = fgx4+1; subplot(m,n,fgx4)
            plot(isalt_d,-ipres_d,'linewidth',2); hold on
            legend(num2str(time_cross_num(ifloat)),'Location',legend_loc);
xlim([-2 2]);
            plot([0 0],ylim,'k-'); % line 0,0
            title(['Salinity difference Float ID: ' num2str(fzeng(Flt)) ';
method ' num2str(method)],title_specs{:})
            xlabel('Salinity (psu)',label_specs{:}); ylabel('De[th
(m)',label_specs{:});
```

```
            % Save figures
            if save_fig == 1
                save_raf(fg1,fg_name3,fg_format); close (fg1) % save temp
and salt figure
                save_raf(fg2,fg_name4,fg_format); close (fg2) % save temp
and salt diff figure
            end
        end % check ifloat is full and plot the result
    end

 elseif All_F == 1
    figure(3*method); clf
    fgx3 = fgx3+1; subplot(m,n,fgx3)
    fg_name3 = [folder_out 'ar_N_' Flt_str '_' basin_str];
    pcolor(tar_bol2,-pres,temp); shading flat; hold on
    %plot(tar_bol2,-MLD,'-.','LineWidth',2,'Color',MLDc)
    colormap(jet)
    c = colorbar;ylabel(c, 'Temperature (C\circ)');
    caxis([dT1m dT1M])
    title(['Float ID: '
num2str(fzeng(Flt))],'FontWeight','Bold','FontSize',12)

    fgx3 = fgx3+1; subplot(m,n,fgx3)
    pcolor(tar_bol2,-pres,salt); shading flat; hold on
    %plot(tar_bol2,-MLD,'--','LineWidth',2,'Color',MLDc)
    colormap(jet)
    c = colorbar;ylabel(c, 'Salinity (psu)');
    caxis([dS1m dS1M])


    figure(4*method); clf
    fgx4 = fgx4+1; subplot(m,n,fgx4)
    fg_name4 = [folder_out 'ar_D_' Flt_str '_' basin_str];

    pcolor(tar_bol2,-pres_d,temp_d); shading flat; hold on
    %plot(tar_bol2,-MLD,'--','LineWidth',2,'Color',MLDc)
    colormap(french2)
    c = colorbar;ylabel(c, 'Temperature difference (C\circ)');
    caxis([-dT dT])
    title(['Float ID: '
num2str(fzeng(Flt))],'FontWeight','Bold','FontSize',12)

    fgx4 = fgx4+1; subplot(m,n,fgx4)
    pcolor(tar_bol2,-pres,salt_d); shading flat; hold
    %plot(tar_bol2(ifloat,:),-MLD(ifloat'),'--
','LineWidth',2,'Color',MLDc)
    colormap(french2)
    c = colorbar;ylabel(c, 'Salinity difference (psu)');
    caxis([-dS dS])

    if save_fig == 1
```

```
        save_raf(figure(3*method),fg_name3); % save temp and salt figure
        save_raf(figure(4*method),fg_name4); % save temp and salt diff
figure
    end
 end
```

Plot profiles (not pcolors)

```
 title_specs = {'FontSize',12,'FontWeight','bold'};
 legend_specs_s = {'Location','SouthWest'}; % legend temp
 legend_specs_t = {'Location','SouthEast'}; % legend salt
 label_specs = {'fontSize',10,'FontWeight','bold'};

 % Get Tp and Sp from the selected platform (ifloat), p stands for 'prime'
 Tp = temp(ifloat,:)';
 Sp = salt(ifloat,:)';
 Pp = pres(ifloat,:)';

 Tp_d = temp_d(ifloat,:)';
 Sp_d = salt_d(ifloat,:)';
 Pp_d = pres_d(ifloat,:)';

 % profile time relative to the passage of the storm
 tar_bol2p = tar_bol2(ifloat,1);


 figure(3); clf
 fg_name3 = [folder_out tc_example '_temp_M_' num2str(method) '_ID' Flt_str
'_' basin_str];

 h1 = plot(Tp(:,tar_bol2p<0),-Pp(:,tar_bol2p<0),'-o','lineWidth',2); hold
on
 set(h1,'MarkerSize',6,'MarkerFaceColor','k')
 h2 = plot(Tp(:,tar_bol2p>0),-Pp(:,tar_bol2p>0),'-','lineWidth',2);
 title(['Temperature (C\circ) float ID: ' Flt_str '; method '
num2str(method)],title_specs{:})
 xlabel('Temperature (\circ)',label_specs{:}); ylabel('De[th
(m)',label_specs{:});
 legend(num2str(tar_bol2p),legend_specs_t{:})
 grid on

 figure(4); clf
 fg_name4 = [folder_out tc_example '_salt_M_' num2str(method) 'ID' Flt_str
'_' basin_str];

 h1 = plot(Sp(:,tar_bol2p<0),-Pp(:,tar_bol2p<0),'-o','lineWidth',2); hold
on
 set(h1,'MarkerSize',6,'MarkerFaceColor','k')
 h2 = plot(Sp(:,tar_bol2p>0),-Pp(:,tar_bol2p>0),'-','lineWidth',2);
 title(['Salinity (psu) float ID: ' Flt_str '; method '
num2str(method)],'FontWeight','bold')
 legend(num2str(tar_bol2(ifloat)),legend_specs_s{:})
```

```
 xlabel('Salinity (psu)',label_specs{:}); ylabel('De[th
(m)',label_specs{:});
 grid on

 figure(33); clf
 fg_name33 = [folder_out tc_example '_tempD_M_' num2str(method) 'ID'
Flt_str '_' basin_str];

 h1 = plot(Tp_d(:,tar_bol2p<0),-Pp_d(:,tar_bol2p<0),'-o','lineWidth',2);
hold on
 set(h1,'MarkerSize',6,'MarkerFaceColor','k')
 h2 = plot(Tp_d(:,tar_bol2p>0),-Pp_d(:,tar_bol2p>0),'-','lineWidth',2);
 title(['Temperature difference (C\circ) float ID: ' Flt_str '; method '
num2str(method)],'FontWeight','bold')
 legend(num2str(tar_bol2(ifloat)),legend_specs_t{:})
 xlabel('Temperature (\circ)',label_specs{:}); ylabel('De[th
(m)',label_specs{:});
 grid on

 figure(44); clf
 fg_name44 = [folder_out tc_example '_saltD_M_' num2str(method) 'ID'
Flt_str '_' basin_str];

 h1 = plot(Sp_d(:,tar_bol2p<0),-Pp_d(:,tar_bol2p<0),'-o','lineWidth',2);
hold on
 set(h1,'MarkerSize',6,'MarkerFaceColor','k')
 h2 = plot(Sp_d(:,tar_bol2p>0),-Pp_d(:,tar_bol2p>0),'-','lineWidth',2);
 title(['Salinity difference (psu) float ID: ' Flt_str '; method '
num2str(method)],'FontWeight','bold')
 legend(num2str(tar_bol2(ifloat)),legend_specs_s{:})
 xlabel('Salinity (psu)',label_specs{:}); ylabel('De[th
(m)',label_specs{:});
 grid on

 if save_fig == 1
     save_raf(figure(3),fg_name3); % save temp and salt figure
     save_raf(figure(4),fg_name4); % save temp and salt diff figure
     save_raf(figure(33),fg_name33); % save temp and salt figure
     save_raf(figure(44),fg_name44); % save temp and salt diff figure

 end
```

================== END SCRIPT (CTCFP.m) ==================

Bibliography

Allen, M. R., O.P. Dube, W. Solecki, F. Aragón-Durand, W. Cramer, S. Humphreys, M. Kainuma, J. Kala, N. Mahowald, Y. Mulugetta, R. Perez, M. Wairiu, and K. Zickfeld (2018), Framing and Context. In: Global Warming of 1.5°C. An IPCC Special Report on the impacts of global warming of 1.5°C above pre-industrial levels and related global greenhouse gas emission pathways, in the context of strengthening the global response to the threat of climate change, sustainable development, and efforts to eradicate poverty. In Press.*Rep.*

Androulidakis, Y., V. Kourafalou, G. Halliwell, M. Le Hénaff, H. Kang, M. Mehari, and R. Atlas (2016), Hurricane interaction with the upper ocean in the Amazon-Orinoco plume region, *Ocean Dyn.*, 1-30, doi: 10.1007/s10236-016-0997-0.

Balaguru, K., S. Taraphdar, and L. R. Leung (2014), Cyclone-cyclone interactions through the ocean pathway, *Geophysical Research Letters*, 9, doi: 10.1002/2014GL061489.

Balaguru, K., G. R. Foltz, L. R. Leung, and K. A. Emanuel (2016), Global warming-induced upper-ocean freshening and the intensification of super typhoons, *Nature Communications*, *7*, 13670, doi: 10.1038/ncomms13670

http://www.nature.com/articles/ncomms13670#supplementary-information.

Balaguru, K., P. Chang, R. Saravanan, L. R. Leung, Z. Xu, M. Li, and J.-S. Hsieh (2012), Ocean barrier layers' effect on tropical cyclone intensification, *Proceedings of the National Academy of Sciences of the United States of America*, *109*(36), 14343-14347, doi: 10.1073/pnas.1201364109.

Bell, G. D., and M. Chelliah (2006), Leading Tropical Modes Associated with Interannual and Multidecadal Fluctuations in North Atlantic Hurricane Activity, *Journal of Climate*, *19*(4), 590-612, doi: 10.1175/jcli3659.1.

Blanke, B., and P. Delecluse (1993), Variability of the Tropical Atlantic Ocean Simulated by a General Circulation Model with Two Different Mixed-Layer Physics, *Journal of Physical Oceanography*, *23*(7), 1363-1388, doi: doi:10.1175/1520-0485(1993)023<1363:VOTTAO>2.0.CO;2.

Blockley, E. W., A. P. Martin, A. J. McLaren, J. Waters, D. J. Lea, K. A. Mirouze, A. Sellar, and D. Storkey (2014), Recent development of the Met Office operational ocean forecasting system: an overview and assessment of the new Global FOAM forecasts, *Geoscience Model Development*, *7*, 26, doi: doi:10.5194/gmd-7-2613-2014.

Boutin, J., N. Martin, N. Kolodziejczyk, and G. Reverdin (2016), Interannual anomalies of SMOS sea surface salinity, *Remote Sensing of Environment*, *180*, 128-136, doi: http://dx.doi.org/10.1016/j.rse.2016.02.053.

Boutin, J., N. Martin, X. Yin, J. Font, N. Reul, and P. Spurgeon (2012), First Assessment of SMOS Data Over Open Ocean: Part II-Sea Surface Salinity, *Ieee Transactions on Geoscience and Remote Sensing*, *50*(5), 1662-1675, doi: 10.1109/tgrs.2012.2184546.

Boutin, J., N. Martin, G. Reverdin, S. Morisset, X. Yin, L. Centurioni, and N. Reul (2014), Sea surface salinity under rain cells: SMOS satellite and in situ drifters observations, *Journal of Geophysical Research: Oceans*, *119*(8), 5533-5545, doi: 10.1002/2014JC010070.

Boutin, J., J. L. Vergely, S. Marchand, F. D'Amico, A. Hasson, N. Kolodziejczyk, N. Reul, G. Reverdin, and J. Vialard (2018), New SMOS Sea Surface Salinity with reduced systematic errors and improved variability, *Remote Sensing of Environment*, *214*, 115-134, doi: https://doi.org/10.1016/j.rse.2018.05.022.

Boyer, T. P., and S. Levitus (2002), Harmonic analysis of climatological sea surface salinity, doi: 10.1029/2001JC000829.

Boyer, T. P., et al. (2014), 2013 World Ocean Atlas Aids High-Resolution Climate Studies, *Eos, Transactions American Geophysical Union*, *95*(41), 369-370, doi: 10.1002/2014eo410002.

Camargo, S. J., K. A. Emanuel, and A. H. Sobel (2007), Use of a genesis potential index to diagnose ENSO effects on tropical cyclone genesis, *Journal of Climate*, *20*(19), 4819-4834, doi: 10.1175/jcli4282.1.

Carval, T., et al. (2015), Argo User's Manual*Rep.*

Cecil, D. J., and M. Wingo (2009), Comparison of TRMM Rain-Rate Retrievals in Tropical Cyclones, *Journal of the Meteorological Society of Japan*, *87A*, 369-380, doi: 10.2151/jmsj.87A.369.

Chang, Y.-C., G.-Y. Chen, R.-S. Tseng, L. R. Centurioni, and P. C. Chu (2013), Observed near-surface flows under all tropical cyclone intensity levels using drifters in the northwestern Pacific, *Journal of Geophysical Research: Oceans*, *118*(5), 2367-2377, doi: 10.1002/jgrc.20187.

Chang, Y.-C., R.-S. Tseng, P. C. Chu, J.-M. Chen, and L. R. Centurioni (2016), Observed strong currents under global tropical cyclones, *Journal of Marine Systems*, *159*, 33-40, doi: 10.1016/j.jmarsys.2016.03.001.

Chavas, D. R., and K. A. Emanuel (2010), A QuikSCAT climatology of tropical cyclone size, *Geophysical Research Letters*, *37*, doi: 10.1029/2010gl044558.

Chavas, D. R., and K. Emanuel (2014), Equilibrium Tropical Cyclone Size in an Idealized State of Axisymmetric Radiative-Convective Equilibrium*, *Journal of the Atmospheric Sciences*, *71*(5), 1663-1680, doi: 10.1175/jas-d-13-0155.1.

Chavas, D. R., and N. Lin (2016), A Model for the Complete Radial Structure of the Tropical Cyclone Wind Field. Part II: Wind Field Variability, *Journal of the Atmospheric Sciences*, *73*(8), 3093-3113, doi: 10.1175/jas-d-15-0185.1.

Chavas, D. R., N. Lin, W. H. Dong, and Y. L. Lin (2016), Observed Tropical Cyclone Size Revisited, *Journal of Climate*, *29*(8), 2923-2939, doi: 10.1175/jcli-d-15-0731.1.

Cheng, L., J. Zhu, and R. Sriver (2015), Global representation of tropical cyclone induced short term ocean thermal changes using Argo data, *Ocean Science*, *11*, 23, doi: 10.5194/os-11-719-2015.

D'Asaro, E. A., T. B. Sanford, P. P. Niiler, and E. J. Terrill (2007), Cold wake of Hurricane Frances, *Geophysical Research Letters*, *34*(15), doi: 10.1029/2007gl030160.

D'Asaro, E. A., et al. (2014), Impact of Typhoons on the Ocean in the Pacific, *Bulletin of the American Meteorological Society*, *95*(9), 1405-1418, doi: 10.1175/BAMS-D-12-00104.1.

D'Ortenzio, F., D. Iudicone, C. de Boyer Montégut, P. Testor, D. Antonie, S. Marullo, R. Santoleri, and G. Madec (2005), Seasonal variability of the mixed layer depth in the Mediterranean Sea as derived fom in situ profiles, *Geophysical Research Letters*, *32*, doi: doi:10.1029/2005GL022463.

de Boyer Montégut, C. (2004), Mixed layer depth over the global ocean: An examination of profile data and a profile-based climatology, *Journal of Geophysical Research*, *109*(C12), doi: 10.1029/2004jc002378.

Dean, L., K. A. Emanuel, and D. R. Chavas (2009), On the size distribution of Atlantic tropical cyclones, *Geophysical Research Letters*, *36*, 5, doi: 10.1029/2009gl039051.

Domingues, R., G. Goni, F. Bringas, S. K. Lee, H. S. Kim, G. Halliwell, J. Dong, J. Morell, and L. Pomales (2015), Upper ocean response to Hurricane Gonzalo (2014): Salinity effects revealed by targeted and sustained underwater glider observations, *Geophysical Research Letters*, *42*(17), 7131-7138, doi: 10.1002/2015GL065378.

Donlon, C. J., M. Martin, J. Stark, J. Roberts-Jones, E. Fiedler, and W. Wimmer (2012), The Operational Sea Surface Temperature and Sea Ice Analysis (OSTIA) system, *Remote Sensing of Environment*, *116*, 140-158, doi: http://dx.doi.org/10.1016/j.rse.2010.10.017.

Emanuel, K. (2000), A statistical analysis of tropical cyclone intensity, *Monthly Weather Review*, *128*(4), 1139-1152, doi: Doi 10.1175/1520-0493(2000)128<1139:Asaotc>2.0.Co;2.

Emanuel, K. (2003), Tropical cyclones, *Annual Review of Earth and Planetary Sciences*, *31*, 75-104, doi: 10.1146/annurev.earth.31.100901.141259.

Emanuel, K. (2005), Increasing destructiveness of tropical cyclones over the past 30 years, *Nature*, *436*(7051), 686-688, doi: 10.1038/nature03906.

Emanuel, K. (2007), Environmental factors affecting tropical cyclone power dissipation, *Journal of Climate*, *20*(22), 5497-5509, doi: 10.1175/2007jcli1571.1.

Emanuel, K., and R. Rotunno (2012), Self-stratification of tropical cyclone outflow. Part I: Implications for storm structure (vol 68, pg 2236, 2011), *Journal of the Atmospheric Sciences*, *69*(1), 416-416, doi: 10.1175/jas-d-11-0283.1.

Emanuel, K., and A. Sobel (2013), Response of tropical sea surface temperature, precipitation, and tropical cyclone-related variables to changes in global and local forcing, *Journal of Advances in Modeling Earth Systems*, *5*(2), 447-458, doi: 10.1002/jame.20032.

Emanuel, K., C. DesAutels, C. Holloway, and R. Korty (2004), Environmental control of tropical cyclone intensity, *Journal of the Atmospheric Sciences*, *61*(7), 843-858, doi: 10.1175/1520-0469(2004)061<0843:ecotci>2.0.co;2.

Emanuel, K. A. (1986), An Air Sea Interaction Theory for Tropical Cyclones .1. Steady-State Maintenance, *Journal of the Atmospheric Sciences*, *43*(6), 585-604, doi: Doi 10.1175/1520-0469(1986)043<0585:Aasitf>2.0.Co;2.

Emanuel, K. A. (1988), The Maximum Intensity of Hurricanes, *Journal of the Atmospheric Sciences*, *45*(7), 1143-1155, doi: Doi 10.1175/1520-0469(1988)045<1143:Tmioh>2.0.Co;2.

Emanuel, K. A. (1999), Thermodynamic control of hurricane intensity, *Nature*, *401*(6754), 665-669, doi: Doi 10.1038/44326.

Geisler, J. E. (1970), Linear theory of the response of a two layer ocean to a moving hurricane, *Geophysical Fluid Dynamics*, *1*(1-2), 249-272, doi: 10.1080/03091927009365774.

George, J. E., and W. M. Gray (1976), Tropical Cyclone Motion and Surrounding Parameter Relationships, *Journal of Applied Meteorology*, *15*(12), 1252-1264, doi: 10.1175/1520-0450(1976)015<1252:TCMASP>2.0.CO;2.

Gill, A. (1982), Chapter Eight - Gravity Waves in a Rotating Fluid, in *International Geophysics*, edited by G. Adrian E, pp. 247-315, Academic Press.

Gill, A. E. (1982), Chapter One - How the Ocean–Atmosphere System Is Driven, in *International Geophysics*, edited by G. Adrian E, pp. 1-17, Academic Press.

Ginis, I. (2002), Tropical cyclone-ocean interactions, *Atmosphere-Ocean Interactions, Vol 1*, *33*, 83-114.

Ginis, I., and G. Sutyrin (1995), Hurricane-Generated Depth-Averaged Currents and Sea-Surface Elevation, *Journal of Physical Oceanography*, *25*(6), 1218-1242, doi: Doi 10.1175/1520-0485(1995)025<1218:Hgdaca>2.0.Co;2.

Gray, W. M. (1998), The formation of tropical cyclones, *Meteorology and Atmospheric Physics*, *67*(1-4), 37-69, doi: Doi 10.1007/Bf01277501.

Grodsky, S. A., N. Reul, B. Chapron, J. A. Carton, and F. O. Bryan (2017), Interannual surface salinity in Northwest Atlantic shelf, *Journal of Geophysical Research: Oceans*, doi: 10.1002/2016JC012580.

Grodsky, S. A., N. Reul, G. Lagerloef, G. Reverdin, J. A. Carton, B. Chapron, Y. Quilfen, V. N. Kudryavtsev, and H.-Y. Kao (2012), Haline hurricane wake in the Amazon/Orinoco plume: AQUARIUS/SACD and SMOS observations, *Geophysical Research Letters*, *39*, doi: 10.1029/2012gl053335.

Guimbard, S., N. Reul, B. Chapron, M. Umbert, and C. Maes (2017), Seasonal and interannual variability of the Eastern Tropical Pacific Fresh Pool, *Journal of Geophysical Research: Oceans*, *122*(3), 1749-1771, doi: 10.1002/2016jc012130.

Helber, R. W., A. B. Kara, J. G. Richman, M. R. Carnes, C. N. Barron, H. E. Hurlburt, and T. Boyer (2012), Temperature versus salinity gradients below the ocean mixed layer, *Journal of Geophysical Research-Oceans*, *117*, doi: 10.1029/2011jc007382.

Hernandez, O., J. Jouanno, and F. Durand (2016), Do the Amazon and Orinoco freshwater plumes really matter for hurricane-induced ocean surface cooling?, *Journal of Geophysical Research: Oceans*, *121*(4), 2119-2141, doi: 10.1002/2015jc011021.

Hernandez, O., J. Boutin, N. Kolodziejczyk, G. Reverdin, N. Martin, F. Gaillard, N. Reul, and J. L. Vergely (2014), SMOS salinity in the subtropical north Atlantic salinity maximum: 1. Comparison with Aquarius and in situ salinity, *Journal of Geophysical Research: Oceans*, n/a-n/a, doi: 10.1002/2013JC009610.

Hosoda, S., T. Ohira, K. Sato, and T. Suga (2010), Improved description of global mixed-layer depth using Argo profiling floats, *Journal of Oceanography*, *66*(6), 773-787, doi: 10.1007/s10872-010-0063-3.

Jacob, S. D., L. K. Shay, A. J. Mariano, and P. G. Black (2000), The 3D oceanic mixed layer response to Hurricane Gilbert, *Journal of Physical Oceanography*, *30*(6), 1407-1429, doi: Doi 10.1175/1520-0485(2000)030<1407:Tomlrt>2.0.Co;2.

Johnson, D. R., T. P. Boyer, O. K. Baranova, H. E. Z. Garcia, Melissa M.; , and R. A. L. Locarnini, Sydney; Mishonov, Alexey V. (2013), World ocean database 2013, user's manual, *Technical Report Rep.*, 171 pp.

Jullien, S., C. E. Menkes, P. Marchesiello, N. C. Jourdain, M. Lengaigne, A. Koch-Larrouy, J. Lefevre, E. M. Vincent, and V. Faure (2012), Impact of Tropical Cyclones on the Heat Budget of the South Pacific Ocean, *Journal of Physical Oceanography*, *42*(11), 1882-1906, doi: 10.1175/jpo-d-11-0133.1.

Kara, A. B. (2003), Mixed layer depth variability over the global ocean, *Journal of Geophysical Research*, *108*(C3), 24-21-15, doi: 10.1029/2000jc000736.

Kara, A. B., P. A. Rochford, and H. E. Hurlburt (2000), An optimal definition for ocean mixed layer depth, *Journal of Geophysical Research-Oceans*, *105*(C7), 16803-16821, doi: 10.1029/2000jc900072.

Knaff, J. A., and R. M. Zehr (2007

), Reexamination of Tropical Cyclone Wind–Pressure Relationships, 71-88, doi: 10.1175/WAF965.1.

Knapp, K. R., M. C. Kruk, D. H. Levinson, H. J. Diamond, and C. J. Neumann (2010), The international best track archive for climate stewardship (IBTrACS), *Bulletin of the American Meteorological Society*, *91*(3), 363-376, doi: 10.1175/2009BAMS2755.1.

Knutson, T. R., J. L. McBride, J. Chan, K. Emanuel, G. Holland, C. Landsea, I. Held, J. P. Kossin, A. K. Srivastava, and M. Sugi (2010), Tropical cyclones and climate change, *Nature Geosci*, *3*(3), 157-163.

Kumar, B. P., J. Vialard, M. Lengaigne, V. S. N. Murty, G. R. Foltz, M. J. McPhaden, S. Pous, and C. d. B. Montegut (2014), Processes of interannual mixed layer temperature variability in the thermocline ridge of the Indian Ocean, *Climate Dynamics*, *43*(9-10), 2377-2397, doi: 10.1007/s00382-014-2059-y.

Leipper, D. F. (1967), Observed ocean conditions and hurricane hilda, 1964, *Journal of Atmospheric Sciences*, *24*, 182–186.

Leipper, D. F., and D. Volgenau (1972), Hurricane Heat Potential of the Gulf of Mexico, *Journal of Physical Oceanography*, *2*(3), 218-224, doi: 10.1175/1520-0485(1972)002<0218:Hhpotg>2.0.Co;2.

Li, Y., W. Han, W. Wang, M. Ravichandran, T. Lee, and T. Shinoda (2017), Bay of Bengal salinity stratification and Indian summer monsoon intraseasonal oscillation: 2. Impact on SST and convection, *Journal of Geophysical Research: Oceans*, doi: 10.1002/2017JC012692.

Lin, I. I., I.-F. Pun, and C.-C. Wu (2009), Upper-Ocean Thermal Structure and the Western North Pacific Category 5 Typhoons. Part II: Dependence on Translation Speed, *Monthly Weather Review*, *137*(11), 3744-3757, doi: 10.1175/2009MWR2713.1.

Lin, I. I., C.-C. Wu, I.-F. Pun, and D.-S. Ko (2008), Upper-Ocean Thermal Structure and the Western North Pacific Category 5 Typhoons. Part I: Ocean Features and the Category 5 Typhoons' Intensification, *Monthly Weather Review*, *136*(9), 3288-3306, doi: 10.1175/2008MWR2277.1.

Lin, Y., M. Zhao, and M. Zhang (2015), Tropical cyclone rainfall area controlled by relative sea surface temperature, *Nature Communications*, *6*, 6591, doi: 10.1038/ncomms7591.

Lin, Y. C., and L. Y. Oey (2016), Rainfall-enhanced blooming in typhoon wakes, *Scientific Reports*, *6*, 31310, doi: 10.1038/srep31310

http://www.nature.com/articles/srep31310#supplementary-information.

Liu, L. L., and F. Wang (2015), Tropical cyclone-induced vertical water transfer and its variability in the North Atlantic and North Pacific, *Journal of Oceanography*, *71*(4), 401-407, doi: 10.1007/s10872-015-0299-z.

Liu, L. Y., C. Lozano, and D. Iredell (2015), Time-Space SST Variability in the Atlantic during 2013: Seasonal Cycle, *Journal of Atmospheric and Oceanic Technology*, *32*(9), 1689-1705, doi: 10.1175/Jtech-D-15-0028.1.

Liu, Z., J. Xu, B. Zhu, C. Sun, and L. Zhang (2007), The upper ocean response to tropical cyclones in the northwestern Pacific analyzed with Argo data, *Chinese Journal of Oceanology and Limnology*, *25*(2), 123-131, doi: 10.1007/s00343-007-0123-8.

Liu, Z. H., J. P. Xu, C. H. Sun, and X. F. Wu (2014), An upper ocean response to Typhoon Bolaven analyzed with Argo profiling floats, *Acta Oceanologica Sinica*, *33*(11), 90-101, doi: 10.1007/s13131-014-0558-7.

Lloyd, I. D., and G. A. Vecchi (2011), Observational Evidence for Oceanic Controls on Hurricane Intensity, *Journal of Climate*, *24*(4), 1138-1153, doi: 10.1175/2010jcli3763.1.

Lloyd, J., E. Guilyardi, and H. Weller (2011), The role of atmosphere feedbacks during ENSO in the CMIP3 models. Part II: using AMIP runs to understand the heat flux feedback mechanisms, *Climate Dynamics*, *37*(7-8), 1271-1292, doi: 10.1007/s00382-010-0895-y.

Locarnini, R. A., et al. (2013), World Ocean Atlas 2013: Temperature, edited by N. O. D. Center, p. 48, Siver Spring, Maryland.

Madec, G., and M. Imbard (1996), A global ocean mesh to overcome the North Pole singularity, *Climate Dynamics*, *12*(6), 381-388, doi: 10.1007/s003820050115.

Maes, C. (2008), On the ocean salinity stratification observed at the eastern edge of the equatorial Pacific warm pool, *J Geophys Res*, *113*.

Maes, C., and T. J. O'Kane (2014), Seasonal variations of the upper ocean salinity stratification in the Tropics, *Journal of Geophysical Research: Oceans*, *119*(3), 1706-1722, doi: 10.1002/2013JC009366.

Mainelli, M., M. DeMaria, L. K. Shay, and G. Goni (2008), Application of oceanic heat content estimation to operational forecasting of recent Atlantic category 5 hurricanes, *Weather and Forecasting*, *23*(1), 3-16, doi: 10.1175/2007waf2006111.1.

Martin, M. J. (2015), Suitability of satellite sea surface salinity data for assessing and correcting ocean forecasts, *Forecasting Research Technical Report*, *599*.

Martin, M. J. (2016), Suitability of satellite sea surface salinity data for use in assessing and correcting ocean forecasts, *Remote Sensing of Environment*, *180*, 305-319, doi: http://dx.doi.org/10.1016/j.rse.2016.02.004.

Martin, M. J., A. Hines, and M. J. Bell (2007), Data assimilation in the FOAM operational short-range ocean forecasting system: a description of the scheme and its impact, *Quarterly Journal of the Royal Meteorological Society*, *133*(625), 981-995, doi: 10.1002/qj.74.

McIlween, R. (1986), *Basic Meteorology a physical outline*, 457 pp., Van Nostrand Reinhold (UK) Co Ltd, Berkshire, England.

Mei, W., C. Pasquero, and F. Primeau (2012), The effect of translation speed upon the intensity of tropical cyclones over the tropical ocean, *Geophysical Research Letters*, *39*(7), doi: 10.1029/2011GL050765.

Mignot, J., C. de Montegut, A. Lazar, and S. Cravatte (2007), Control of salinity on the mixed layer depth in the world ocean: 2. Tropical areas, *Journal of Geophysical Research-Part C-Oceans*, *112*(C10), doi: 10.1029/2006jc003954.

Miller, B. I. (1958), On the Maximum Intensity of Hurricanes, *Journal of Meteorology*, *15*(2), 184-195, doi: 10.1175/1520-0469(1958)015<0184:otmioh>2.0.co;2.

Monaldo, F. M., T. D. Sikora, S. M. Babin, and R. E. Sterner (1997), Satellite imagery of sea surface temperature cooling in the wake of Hurricane Edouard (1996), *Monthly Weather Review*, *125*(10), 2716-2721, doi: 10.1175/1520-0493(1997)125<2716:siosst>2.0.co;2.

Montegut, C. D., J. Mignot, A. Lazar, and S. Cravatte (2007), Control of salinity on the mixed layer depth in the world ocean: 1. General description, *Journal of Geophysical Research-Oceans*, *112*(C6), 12, doi: 10.1029/2006jc003953.

Mrvaljevic, R. K., et al. (2013), Observations of the cold wake of Typhoon Fanapi (2010), *Geophysical Research Letters*, *40*(2), 316-321, doi: 10.1029/2012GL054282.

Neetu, S., M. Lengaigne, E. M. Vincent, J. Vialard, G. Madec, G. Samson, M. R. R. Kumar, and F. Durand (2012), Influence of upper-ocean stratification on tropical cyclone-induced surface cooling in the Bay of Bengal, *Journal of Geophysical Research-Oceans*, *117*, 12020-12020.

Ninove, F., P. Y. Le Traon, E. Remy, and S. Guinehut (2016), Spatial scales of temperature and salinity vairabilty estimated from Argo observations, *Ocean Science*, *12*, 7.

Nirupama, N. (2013), Is it possible to rank hurricanes in a unique manner?, *Natural Hazards*, *67*(2), 963-968, doi: 10.1007/s11069-013-0560-y.

Olmedo, E., I. Taupier-Letage, A. Turiel, and A. Alvera-Azcárate (2018), Improving SMOS Sea Surface Salinity in the Western Mediterranean Sea through Multivariate and Multifractal Analysis, *Remote Sensing*, *10*(3), 485.

Pailler, K., B. Bourles, and Y. Gouriou (1999), The barrier layer in the western Tropical Atlantic Ocean, *Geophysical Research Letters*, *26*(14), 2069-2072, doi: 10.1029/1999gl900492.

Park, J. J., Y.-O. Kwon, and J. F. Price (2011), Argo array observation of ocean heat content changes induced by tropical cyclones in the north Pacific, *Journal of Geophysical Research-Oceans*, *116*, 12, doi: 10.1029/2011jc007165.

Pielke, R. A., C. Landsea, M. Mayfield, J. Laver, and R. Pasch (2005), Hurricanes and global warming, *Bulletin of the American Meteorological Society*, *86*(11), 1571-+, doi: 10.1175/bams-86-11-1571.

Price, J. F. (1976), Sea-Surface Temperature Response to Hurricane Eloise, *Transactions-American Geophysical Union*, *57*(4), 260-260.

Price, J. F. (1981), Upper ocean response to a hurricane, *Journal of Physical Oceanography*, *11*(2), 153-175, doi: 10.1175/1520-0485(1981)011<0153:uortah>2.0.co;2.

Price, J. F. (1983), Internal Wave Wake of a Moving Storm .1. Scales, Energy Budget and Observations, *Journal of Physical Oceanography*, *13*(6), 949-965, doi: Doi 10.1175/1520-0485(1983)013<0949:Iwwoam>2.0.Co;2.

Price, J. F. (2009), Metrics of hurricane-ocean interaction: vertically-integrated or vertically-averaged ocean temperature?, *Ocean Science*, *5*(3), 351-368.

Price, J. F., J. Morzel, and P. P. Niiler (2008), Warming of SST in the cool wake of a moving hurricane, *Journal of Geophysical Research-Oceans*, *113*(C7), doi: Artn C07010

10.1029/2007jc004393.

Reul, N., Y. Quilfen, B. Chapron, S. Fournier, V. Kurdyavtsev, and R. Sabia (2014), Multisensor observations of the Amazon-Orinoco River plume interactions with hurricanes, *Journal of Geophysical Research: Oceans*, n/a-n/a, doi: 10.1002/2014JC010107.

Reul, N., et al. (2013), Sea Surface Salinity Observations from Space with the SMOS Satellite: A New Means to Monitor the Marine Branch of the Water Cycle, *Surv Geophys*, 1-42, doi: 10.1007/s10712-013-9244-0.

Reynolds, R. W., and D. B. Chelton (2010), Comparisons of Daily Sea Surface Temperature Analyses for 2007–08, *Journal of Climate*, *23*(13), 3545-3562, doi: 10.1175/2010JCLI3294.1.

Reynolds, R. W., T. M. Smith, C. Liu, D. B. Chelton, K. S. Casey, and M. G. Schlax (2007), Daily High-Resolution-Blended Analyses for Sea Surface Temperature, *Journal of Climate*, *20*(22), 5473-5496, doi: doi:10.1175/2007JCLI1824.1.

Roemmich, D., G. C. Johnson, S. Riser, R. Davis, J. Gilson, W. B. Owens, S. L. Garzoli, C. Schmid, and M. Ignaszewski (2009), The Argo Program Observing the Global Ocean with Profiling Floats, *Oceanography*, *22*(2), 34-43, doi: 10.5670/oceanog.2009.36.

Rumyantseva, A., N. Lucas, T. Rippeth, A. Martin, S. C. Painter, T. J. Boyd, and S. Henson (2015), Ocean nutrient pathways associated with the passage of a storm, *Global Biogeochemical Cycles*, *29*(8), 1179-1189, doi: 10.1002/2015GB005097.

Sanford, T. B., J. F. Price, and J. B. Girton (2011), Upper-Ocean Response to Hurricane Frances (2004) Observed by Profiling EM-APEX Floats, *Journal of Physical Oceanography*, *41*(6), 1041-1056, doi: 10.1175/2010JPO4313.1.

Sanford, T. B., P. G. Black, J. R. Haustein, J. W. Feeney, G. Z. Forristall, and J. F. Price (1987), Ocean Response to a Hurricane .1. Observations, *Journal of Physical Oceanography*, *17*(11), 2065-2083, doi: Doi 10.1175/1520-0485(1987)017<2065:Ortahp>2.0.Co;2.

Schade, L. R., and K. A. Emanuel (1999), The ocean's effect on the intensity of tropical cyclones: Results from a simple coupled atmosphere-ocean model, *Journal of the Atmospheric Sciences*, *56*(4), 642-651, doi: Doi 10.1175/1520-0469(1999)056<0642:Toseot>2.0.Co;2.

Schreck, C. J., K. R. Knapp, and J. P. Kossin (2014), The Impact of Best Track Discrepancies on Global Tropical Cyclone Climatologies using IBTrACS, *Monthly Weather Review*, *142*(10), 3881-3899, doi: 10.1175/mwr-d-14-00021.1.

Shay, L. K. (2009), Upper Ocean Structure: Responses to Strong Atmospheric Forcing Events A2 - Steele, John H, in *Encyclopedia of Ocean Sciences (Second Edition)*, edited, pp. 192-210, Academic Press, Oxford.

Shay, L. K., R. L. Elsberry, and P. G. Black (1989), Vertical Structure of the Ocean Current Response to a Hurricane, *Journal of Physical Oceanography*, *19*(5), 649-669, doi: Doi 10.1175/1520-0485(1989)019<0649:Vsotoc>2.0.Co;2.

Shay, L. K., A. J. Mariano, D. Jacob, and E. H. Ryan (1997), Mean and Near-Inertial Ocean Current Response to Hurricane Gilbert, *Journal of Physical Oceanography*, *28*, 32.

Shay, L. K., P. G. Black, A. J. Mariano, J. D. Hawkins, and R. L. Elsberry (1992), Upper ocean response to hurricane Gilbert, *Journal of Geophysical Research-Oceans*, *97*(C12), 20227-20248, doi: 10.1029/92jc01586.

Sprintall, J., and M. Tomczak (1992), Evidence of the barrier layer in the surface layer of the tropics, *Journal of Geophysical Research-Oceans*, *97*(C5), 7305-7316, doi: 10.1029/92jc00407.

Storkey, D., E. W. Blockley, and R. Furner (2010), Forecasting the ocean state using NEMO: The new FOAM system, *Journal of operational Oceanography*, *3*, 13.

Stramma, L., P. Cornillon, and J. F. Price (1986), Satellite observations of sea surface cooling by hurricanes, *Journal of Geophysical Research-Oceans*, *91*(C4), 5031-5035, doi: 10.1029/JC091iC04p05031.

Velden, C., et al. (2006), The Dvorak Tropical Cyclone Intensity Estimation Technique: A Satellite-Based Method that Has Endured for over 30 Years, *Bulletin of the American Meteorological Society*, *87*(9), 1195-1210, doi: 10.1175/BAMS-87-9-1195.

Vigh, L. J. (2015), VDM+: The Enhanced Vortex Message Dataset, edited by N. C. f. A. Research, p. 75, National Center for Atmospheric Research, Boulder, Colorado, USA.

Vincent, E. M., G. Madec, M. Lengaigne, J. Vialard, and A. Koch-Larrouy (2013), Influence of tropical cyclones on sea surface temperature seasonal cycle and ocean heat transport, *Climate Dynamics*, *41*(7-8), 2019-2038.

Vincent, E. M., K. A. Emanuel, M. Lengaigne, J. Vialard, and G. Madec (2014), Influence of upper ocean stratification interannual variability on tropical cyclones, *Journal of Advances in Modeling Earth Systems*, n/a-n/a, doi: 10.1002/2014MS000327.

Vincent, E. M., M. Lengaigne, J. Vialard, G. Madec, N. C. Jourdain, and S. Masson (2012), Assessing the oceanic control on the amplitude of sea surface cooling induced by tropical cyclones, *Journal of Geophysical Research: Oceans*, *117*(C5), C05023, doi: 10.1029/2011JC007705.

Vincent, E. M., M. Lengaigne, G. Madec, J. Vialard, G. Samson, N. C. Jourdain, C. E. Menkes, and S. Jullien (2012), Processes setting the characteristics of sea surface cooling induced by tropical cyclones, *Journal of Geophysical Research-Oceans*, *117*, 2020-2020.

Vissa, N. K., A. N. V. Satyanarayana, and B. P. Kumar (2012), Response of Upper Ocean during passage of MALA cyclone utilizing ARGO data, *International Journal of Applied Earth Observation and Geoinformation*, *14*(1), 149-159, doi: 10.1016/j.jag.2011.08.015.

Wang, X., G. Han, Y. Qi, and W. Li (2011), Impact of barrier layer on typhoon-induced sea surface cooling, *Dynamics of Atmospheres and Oceans*, *52*(3), 367-385, doi: 10.1016/j.dynatmoce.2011.05.002.

Waters, J., D. Lea, A. P. Martin, D. Storkey, and J. While (2013), Describing tge development of the new FOAM-NEMOVAR system in the global 1/4 degree configuration, *Forecasting Research Technical Report*, *578*.

Wells, N. C. (2011), Observations of Winds and Currents, in *The Atmosphere and Ocean*, edited, pp. 147-180, John Wiley & Sons, Ltd.

Wood, V. T., L. W. White, H. E. Willoughby, and D. P. Jorgensen (2013), A New Parametric Tropical Cyclone Tangential Wind Profile Model, *Monthly Weather Review*, *141*(6), 1884-1909, doi: 10.1175/mwr-d-12-00115.1.

Woodruff, J. D., R. L. Sriver, and D. C. Lund (2012), Tropical cyclone activity and western North Atlantic stratification over the last millennium: a comparative review with viable connections, *Journal of Quaternary Science*, *27*(4), 337-343, doi: 10.1002/jqs.1551.

Wyrtki, K. (1981), An estimate of equatorial upwelling in the Pacific, *J Phys Oceanogr*, *11*, 1205 - 1214.

Yanai, M. (1964), Formation of tropical cyclones, *Reviews of Geophysics*, *2*(2), 367-414, doi: 10.1029/RG002i002p00367.

Yang, H., G. Lohmann, W. Wei, M. Dima, M. Ionita, and J. Liu (2016), *Intensification and poleward shift of subtropical western boundary currents in a warming climate*, n/a-n/a pp.

Zhang, H., D. Chen, L. Zhou, X. Liu, T. Ding, and B. Zhou (2016), Upper ocean response to typhoon Kalmaegi (2014), *Journal of Geophysical Research: Oceans*, doi: 10.1002/2016JC012064.

Zhang, H., D. Chen, L. Zhou, X. H. Liu, T. Ding, and B. F. Zhou (2016), Upper ocean response to typhoon Kalmaegi (2014), *Journal of Geophysical Research-Oceans*, *121*(8), 6520-6535, doi: 10.1002/2016jc012064.

Zhao, B., F. Qiao, L. Cavaleri, G. Wang, L. Bertotti, and L. Liu (2017), Sensitivity of typhoon modeling to surface waves and rainfall, *Journal of Geophysical Research: Oceans*, *122*(3), 1702-1723, doi: 10.1002/2016jc012262.

Zweng, M. M., et al. (2013), World Ocean Atlas 2013: Salinity, edited, p. 47.